Effects of Substrate Surface in the Design of VO$_2$ Micro- and Nano-Crystals

By

Samuel Thomas White

Dissertation

Submitted to the Faculty of the

Graduate School of Vanderbilt University

in partial fulfillment of the requirements

for the degree of

DOCTOR OF PHILOSOPHY

in

Physics

May 13, 2022

Nashville, Tennessee

Approved:

Richard F. Haglund, Ph.D.

Joshua D. Caldwell, Ph.D.

Norman H. Tolk, Ph.D.

D. Greg Walker, Ph.D.

Alfredo Gurrola, Ph.D.

To the glory of the LORD God Almighty—Who hath set us the grand puzzle of Science in order that we, by working it, might better exercise our transient stewardship of the Earth and might learn eternally something of its Creator—this small piece of the solution is humbly devoted.

ACKNOWLEDGEMENTS

No great work of man is achieved by one alone, unaided. If this dissertation be not a great a work, at least it is the largest and most onerous I have undertaken, and accordingly has been aided, abetted, assisted, availed, and accomplished altogether by the greatest set of inestimably invaluable individuals. My gratitude, honor, and friendship to:

My research advisor, Dr. Richard Haglund, who has mentored me in the mysterious ways of academia, science, publication, the literature, experiment design, professional etiquette, job applications, and who knows what else besides; who has been exceedingly patient, helpful, and gracious though too many years of my slow plodding through dead ends, changes of direction, unfinished experiments, and general befuddlement; who continually puts the needs of his students before his own.

The students before me, Drs. Eugene Donev, Bob Marvel, Kent Hallman, and Christina McGahan, who got me up to speed on VO_2 in general and on our group's expertise in particular.

A whole host of helpful undergraduates:—Peyton Brown, Ellis Thompson, James Taylor, Ivan Chukhryaev, Silas Bailey, Josh Queen, and Matthew Lu—and graduate students—Jackson Bentley, Jake Grayson, and Adam Cummings—who have lent their hands to multiply my productivity.

Our various collaborators, at home and abroad, who have let me take part in their incredible work or assisted in mine: Prof. Dr. Laura Liu and Dr. Xiaoyang Duan at the University of Stuttgart; Prof. Josh Caldwell, Dr. Thomas Folland, Mingze He, and Joseph Matson from the Vanderbilt School of Engineering; Prof. Yohannes Abate and Alireza Fali at the University of Georgia; Dr. Larry Domash, Dr. Baris Unal, and Dr. Matthew Duff at Triton Systems; Prof. Leonard Feldman and Hussein Hijazi at Rutgers University; Prof. David Hilton and Tenzin Norden at Baylor University; Prof. Ali Shakouri and Sami Alajlouni at Purdue University; and Dr. Hanu Arava at Northwestern University.

The managers of the Vanderbilt Chemistry Powder XRD core, Evan Robinson and Christopher Sharp, for training, advice, and hands-on assistance with somewhat unusual experiments and requests.

The Vanderbilt Institute of Nanoscale Science and Engineering and all its staff, including Drs. Dmitry Koktysh, James McBride, Bo Choi, Kurt Heinrich, Alice Leach, Bill Martinez, Mike Valenti, and Christina McGahan (hey look, she's in here twice!). Huge portions of this work would have been impossible without the facilities, instruments, supplies, help, support, and advice of VINSE; and they've all been a pleasure to work with.

My undergraduate advisors, Prof. Matthew Nee and Prof. Doug Harper, who got me started off on the right foot.

The members of my dissertation committee who have been supportive, helpful, and patient through my long graduate tenure.

My office-mates, Aaron Stevens, Rustam Gatamov, Kyle Godby, Matt Murrow, and Crisel Suarez, who have enlivened my workspace with all manner of amusing, informative, and intriguing conversation.

My parents, Todd and Robin White, who raised me up in the way I should go, fully equipped me to equip myself for any undertaking, and provided for my needs far and above anything I could expect, ask, or deserve.

My brother, Will White, who will insist on encouraging me in spite of my determination to believe myself the least competent of mortals, and who taught me to find enjoyment in hard labor...like cutting down trees with an axe.

My wife, Katie White, with whom I fit so very well, whose presence, affection, and confidence have already proved a great comfort and strength, who has been an invaluable editor, and who has an endless enthusiasm for moving bits of text around in spreadsheets.

My old friends in the Universal Jacobball Senate and the Donut Brigade, who have kept me sane by their innocuous, inexhaustible insanity.

My brothers and sisters in Christ at Living Hope, Covenant Ministries, The Gospel Church, Arts Alive, and throughout my extended family who have taught me, loved me, and earnestly prayed for me.

And last of all, you, my dear reader. For no written work, least of all a work of science, has fulfilled its end until it has been read, understood, and put to some purpose. Thank you for completing this work I started. May you find some small part of it, in some small way, of some small use.

TABLE OF CONTENTS

LIST OF TABLES

LIST OF FIGURES

CHAPTER 1

INTRODUCTION

1.1 Motivation

A vast subset of current (and developing) technologies and devices rely fundamentally on materials with properties that change reversibly in response to certain stimuli: the electric-field driven expansion of piezoelectric actuators, the switchable magnetic moments of hard disk drives, the UV-sensitive chemical reactions in photochromic lenses. Understanding, modulating, and exploiting such behaviors is a perpetual goal of condensed matter physics; reliably producing and precisely designing the materials that exhibit them is a perpetual challenge of materials science.

There are many such technologically-relevant exotic materials which derive their utility from switchable or tunable properties. A large and important subset of these are the phase-change materials (PCMs), which exhibit two or more different phases with distinct properties or behaviors, and form the basis for a wide variety of switches, modulators, sensors, re-writable structures, and actuators. Regarding nomenclature, some authors distinguish between "phase change materials" and "phase transition materials" based on whether the phase transition in question is non-volatile (latching) or volatile (non-latching), respectively,[1] since the term "phase change materials" has been used to refer specifically to materials with a non-volatile crystalline-to-amorphous phase transition.[2] However, this usage is far from consistent across the literature. For the purposes of this work, we use PCM for both and distinguish between "volatile" and "non-volatile" PCMs as needed for clarity.
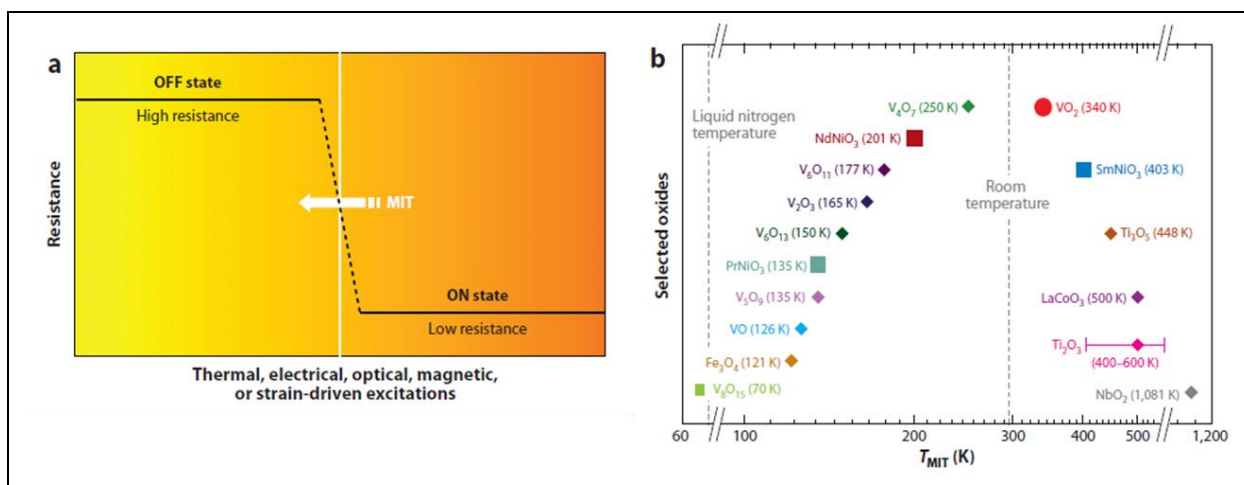
Figure 1.1: Materials with an IMT switch from a high-resistance to a low-resistance state at T_c (a). Many such materials exist, with different T_c (b), but T_c is nearest to room-temperature for VO_2.

Materials with an insulator-metal transition (IMT) are a subclass of PCMs which switch from an insulating, high-resistivity state to a metallic, low-resistivity state at a certain critical temperature (T_c), illustrated in Figure 1a. Many oxides have IMT behavior, with T_c ranging from below 100 K to over 1000 K.[3] Several of these and their respective transition temperatures are plotted in Figure 1b. Different applications have different optimal switching temperatures, but for many uses, as well as for ease of performing experiments, it is desirable that the T_c fall as near as possible to room temperature, which directs our attention to vanadium dioxide (VO_2).

1.2 VO_2 : Structural, Electronic, and Optical Properties

Vanadium is a transition metal with several stable valence charge states (+2, +3, +4, +5),[4] leading to over a dozen different oxides, from the vanadium-rich VO to the oxygen-rich V_2O_5, including the Magnéli series (V_nO_{2n-1}, $3 \leq n \leq 9$) and the Wadsley series (V_nO_{2n+1}, $1 \leq n \leq 6$).[5-6] The complexity of the vanadium oxides makes careful tuning of the oxygen content necessary to produce any given species,[7-8] and most species will oxidize toward the stable V_2O_5 phase under ambient conditions.[9-10] Many of these (including all the Magnéli series except V_7O_{13})[11] have an IMT, with that of VO_2 occurring nearest room temperature at about 340 K (~67°C).[3]

Table 1.1: Space groups and lattice parameters for three common VO_2 phases. Comparing equivalent lattice vectors highlights the overall strain associated with the phase change; compared to R, the insulating phases contract along a_R and b_R, but expand along c_R.

Phase	**R**			**M1**			**M2**		
Space Group	P 42/mnm			P 21/c			C 2/m		
a (Å)	4.5546			5.7517			9.0600		
b (Å)	4.5546			4.5378			5.8000		
c (Å)	2.8514			5.3825			4.5217		
α (°)	90			90			90		
β (°)	90			122.646			91.850		
γ (°)	90			90			90		
	Lattice Vector	*Length (Å)*	*change from R*	*Lattice Vector*	*Length (Å)*	*change from R*	*Lattice Vector*	*Length (Å)*	*change from R*
a_R *axis*	[100]	4.5546	0%	[010]	4.5378	-0.37%	[001]	4.5217	-0.72%
b_R *axis*	[020]	9.1092	0%	[$\bar{1}$0$\bar{2}$]	9.0645	-0.49%	[100]	9.0600	-0.54%
c_R *axis*	[002]	5.7028	0%	[$\bar{1}$00]	5.7517	0.86%	[010]	5.8000	1.70%
Ref	12			13			14		

Discovered in 1959,[15] the VO_2 phase transition incorporates both a structural and an electronic change. Vanadium dioxide manifests several distinct crystalline phases[5] which can be described as distortions of the high-symmetry rutile (R) phase lattice.[16] Figure 2 compares the crystal structure of R with that of two monoclinic phases (M1 and M2).
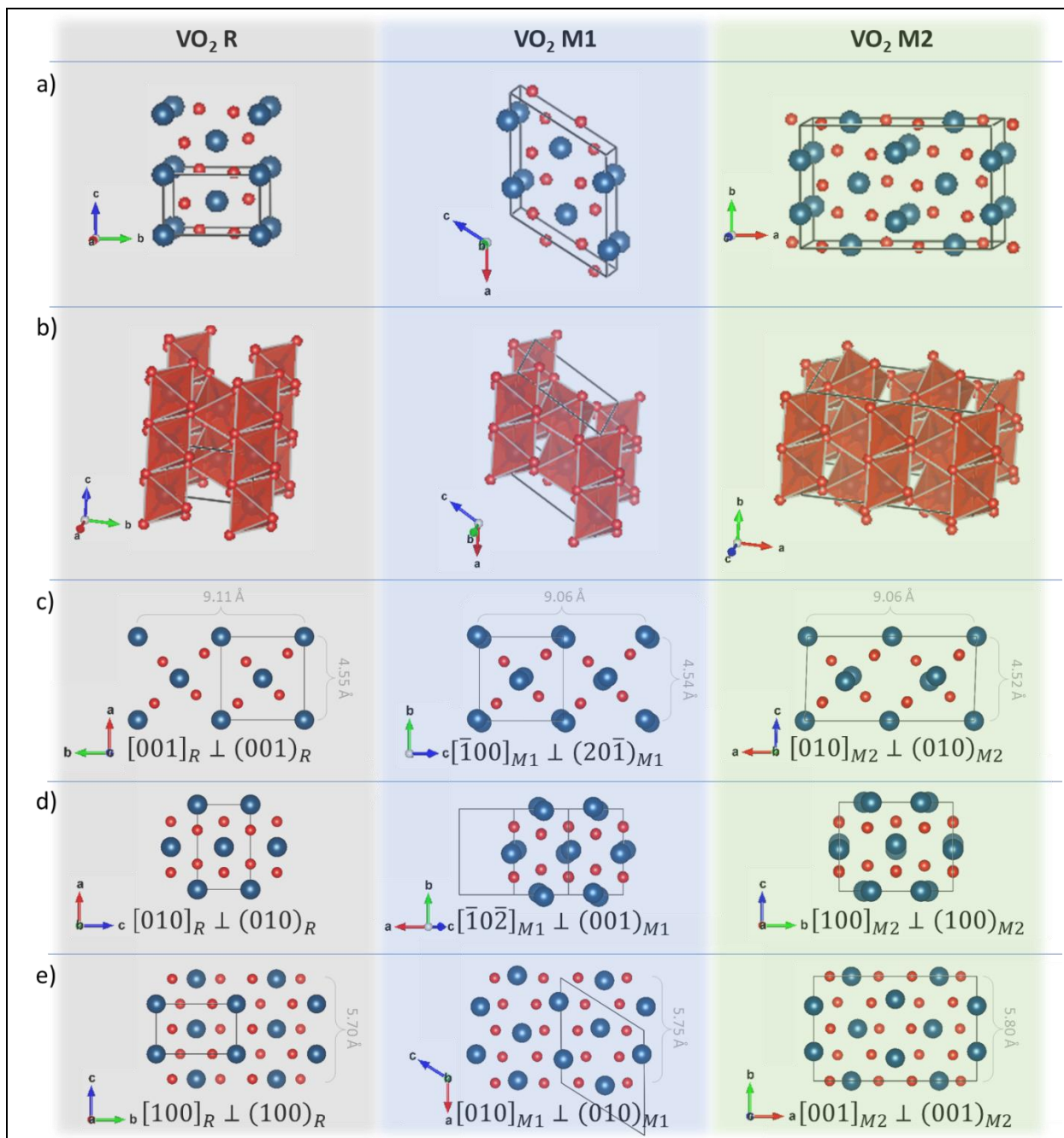
Figure 1.2: Visualizations of the VO_2 crystal lattice in the R, M1, and M2 phases, with vanadium atoms in blue and oxygen atoms in red, and the unit cells outlined in black (a). Each vanadium atom is surrounded by an octahedron of oxygen atoms (b). Viewing the lattice along the c_R (c), b_R (d) and a_R (e) axes highlights the shifting of the vanadium atoms. The vector along which the lattice is viewed and the corresponding plane normal to that vector is indicated under each structure.

figures prepared using VESTA ver. 3.4.7[17]
based on lattice parameters in Table 1

In the R phase, V atoms form straight, equally spaced chains, with each vanadium atom surrounded by an octahedron of oxygen atoms. In M1, pairs of V atoms move closer together,

forming dimers, and tilt slightly away from the rutile c-axis (c_R); due to the consequent decrease in symmetry, the unit cell doubles. Relative to R, the M1 phase expands along c_R (~0.9%) and contracts perpendicular to it (~0.4%). In M2, alternating V chains either pair into dimers (which remain colinear) or tilt relative to c_R (but remain equally spaced); relative to R, M2 expands still further along c_R (~1.7%). Another, triclinic phase (T) is intermediate between M1 and M2. Table 1 summarizes the lattice parameters for M1, M2, and R. The tilting of V-V dimers in these insulating phases eliminates the four-fold rotational symmetry about c_R, giving rise to the possibility of ferroelastic twin domains with a common c_R axis but different V-V dimer tilt directions.[18]

The M1 phase is the most stable VO_2 structure under standard temperature and pressure, but at T_c it undergoes a phase transition to R. This is a first-order phase transition, involving latent heat and hysteretic switching behavior. Both M1 and M2 are insulating (with band gaps of ~0.6-0.7 eV[19-20] and ~0.1-0.6 eV,[21-22] respectively), while R is metallic (classified as a "bad metal", highly lossy and violating the Wiedemann-Franz law)[23] with resistivity lower by a factor of ~10^5, so that the M1-R structural phase transition (SPT) occurs together with the IMT.

The sharp changes in lattice and electronic structure necessitate a corresponding change in optical properties. The change is relatively small in the visible, but much more pronounced in the near IR, where absorption across the band gap disappears and other optical absorptions are shifted due to changes in the band structure.[24-27] Further into the mid-IR, most of the optically active phonons disappear and IR absorption and reflectivity increase due to the dominating Drude response of the metallic free electrons.[28] Recently, Wan *et al.* published VO_2 optical constants from 0.3-30 μm, the broadest range to date.[29]

Across different studies, and across different samples in the same study, the measured optical constants show the same broad trends, but differ in spectral details. Strain,[30] substrate,[31] defects,[32] doping,[33] stoichiometry,[34] and deposition method[29] can all affect the optical constants in different ways, aside from the inherent model-dependence of ellipsometric measurements. To the best of this author's knowledge, all measurements of VO_2 optical constants to date have been performed on thin films; while single crystals would provide a better picture of the bulk VO_2 optical constants, obtaining VO_2 crystals of sufficiently large size and high quality is difficult.

1.3 Nature of the VO₂ Phase Transition

1.3.a Structurally-Driven vs. Electron-Correlation-Driven

The fundamental origin and nature of the VO_2 phase transition has been a subject of study and debate continuously from its discovery to the present day. The primary competing theories are that the IMT is structurally-driven (Peierls) or electron-correlation driven (Mott). According to Peierls' theory, non-interacting electrons in a 1D periodic potential (i.e. a string of equally-spaced ions) are conducting; however, a small energy savings will cause the atoms to dimerize, doubling the lattice period, and inducing a band-gap, thus changing the system into an insulator.[35] On this view, the V-atom chains can be considered as quasi-1D Peierls-like systems. In the early 1970s, Goodenough presented a model to explain the IMT behavior based on changes in orbital overlap consequent upon the V-V pairing, without invoking electron correlations.[36]

On the other hand, only a few years later Zylbersztejn and Mott argued that the insulating phase could only be explained by including the Hubbard intra-atomic correlation energy to account for electron-electron interactions, even stating, "The pairing of the V ions in VO_2 has

only a minor effect on the gap."[37] This idea firmly places VO_2 among the correlated electron materials, a class of materials characterized by the importance (or even dominance) of electron correlations in determining their properties, many of which exhibit exotic behaviors like phase transitions or high-temperature superconductivity.[38] The correlation properties are driven by competition between delocalization due to the kinetic energy of the electrons, and localization due to Coulomb repulsion between electrons.

Due to the two-fold drive to understand the VO_2 phase transition in particular and to develop theoretical frameworks to deal with correlated materials in general, VO_2 became a test bed for materials theory, as different groups sought to explain the VO_2 behavior from first principles. Recently, density functional theory (DFT) calculations have succeeded in reproducing both the electronic and magnetic properties of the M1, M2, and R phases known from experiment, with a consistent set of DFT potentials.[22] It appears that neither the Peierls nor the Mott picture fully describes the VO_2 transition; both structural and electron-correlation driven effects are important.[39] A recent review posits that the VO_2 phase transition is unique among IMTs because it involves a change from a quasi-1D electronic system (in the insulating phase) to a fully 3D electronic system (in the metallic phase).[40]

1.3.b   *Ultrafast Optically-Triggered Transition*

The VO_2 phase transition can also be triggered optically (with fluence on the order of a few mJ/cm^2) ,[41] and the nature of this photo-induced phase transition (PIPT) has itself been the subject of much study, to determine how it may differ from the thermally-induced phase transition and with hopes of disentangling the electronic and lattice degrees of freedom. With long-duration pulses (greater than ns) on the same timescale as thermal and structural effects, this photo-induced phase-transition (PIPT) may not be distinguished from the thermal transition; but ultrafast (sub-ps) measurements can probe the lattice (x-ray, Raman) and electronic structure (optical reflection/transmission) faster than thermalization can occur.

Cavalleri *et al.*, using ultrafast visible pump-probe measurements, observed the transition to occur no faster than ~80 fs, which they attributed to a "structural bottleneck" with the phase transition speed limited by coherent phonons.[42]   On the other hand, Wegkamp *et al.*, using femtosecond time-resolved photoelectron spectroscopy, found that the insulator-metal transition occurred "quasi-instantaneously", and faster than the corresponding structural change, implying the existence of a transient metallic monoclinic (mM) phase.[43] Other measurements have shown the IMT to happen as fast as 26 fs.[44] It was proposed that when ultrafast light above the band gap excites sufficient electrons (~0.05 electrons/formula unit) into the conduction band, the change in Coulomb screening causes both the band gap to collapse and the lattice potential to change, simultaneously initiating both the SPT and IMT, producing the mM phase until enough time has passed for the lattice to relax to R.[45-46] This mM phase was shown to be similar to the M2 phase,[45] and has since been identified with another distinct phase predicted by DFT.[22] Other groups have confirmed the occurrence of a mM phase—in the optically-induced transition by a combination of electron diffraction (for structural information) and IR transmissivity (for electronic information) measurements;[47] in the electrically-induced transition by electron diffraction and electrical transport;[48] and in the thermally-induced transition by electron diffraction and x-ray photoemission.[49] Otto *et al.* used ultrafast electron diffraction measurements to show that both M1-mM and M-R transitions can take place in the same film, albeit at different fluences and timescales.[50]

More recently, however, Vidas *et al.* showed that thermal processes do play a role even at this timescale; carefully accounting for these, they found no evidence for the mM phase at all, and showed that the threshold fluence simply corresponds to the energy of the thermal transition temperature.[51] It is noteworthy that all of the above evidences of a mM phase relied upon electron diffraction measurements, while Vidas *et al.* used x-ray absorption spectroscopy; this difference in technique may help account for the discrepancy. Complicating the picture still further, ultrafast x-ray scattering studies showed that, rather than transitioning from one well-ordered crystal state to another, the initial structural change is an order-disorder transition: on the order of 150 fs, phonons are generated with a broad range of wave vectors, and thus cannot be described in terms of a single order parameter.[52] A full understanding of the behavior of the VO_2 PIPT is still being developed; and sample-to-sample variation,[41] variations in experimental conditions,[51] and phase coexistence on ultrafast timescales[50, 53-54] make it difficult to separate the "true" behavior of bulk VO_2 from the effects of defects and strain.

1.4 Manipulating the Phase Transition

Owing to its strongly-correlated nature and the interplay of electronic and lattice degrees of freedom,[38] the details of the VO_2 phase transition are extremely sensitive to a variety of factors.

1.4.a Strain Effects

Strain (arising from mechanical stress, isotropic pressure, or substrate interactions) directly affects the lattice and (depending on the strain direction) can lower T_c or introduce additional phases M2 and T.[55-56] In bulk VO_2 crystals[57] and in unstrained nanorods,[58] the transition occurs abruptly, near 340 K, and with a single sharp boundary between M-phase and R-phase regions during the transition. However, for epitaxial films grown on TiO_2 substrates, the transition temperature is shifted — down to 300 K on TiO_2 (001) with compressive strain along c_R, or up to 369 K on TiO_2 (110) with tensile strain along c_R.[59] This behavior is intuitively easy to understand in that the crystal lattice along c_R is longer for M1 than R, so compressive strain stabilizes R, and vice-versa. Similarly, the M2 phase can be stabilized in strained epitaxial thin films.[60]

Furthermore, in strained VO_2 films and single crystals, microscale coexisting metallic and insulating phases have been observed during the phase transition. This phase coexistence can persist over a wide temperature range (>70 K),[61] leading to a gradual macroscopic transition. Releasing the film or crystal from substrate-induced strain by growing on a lattice-matched buffer,[62] a van der Waals substrate,[61] or simply removing it from the substrate[58] can restore the sharp transition and steep hysteretic behavior of native VO_2. The nucleation of metallic regions during the phase transition has been linked to and the ferroelastic strain domains,[18, 63] which are themselves affected by strain on (or in) the crystal.[64]

For tensile-strained VO_2 films on TiO_2 (110), alternating, micrometer-scale stripes of M- and R-phase are observed during the transition (Figure 3a). These stripes tend to orient perpendicular to c_R (in the plane of the film), leading to highly anisotropic conductivity during the transition.[65] Similar striped phases appear in strained single crystals[66] and nanorods,[54] and can be manipulated by bending the rods to change the strain distribution (Figure 3b).[58] In high-aspect-ratio nanorods these manifest as lateral stripes,[67] whereas in lower aspect-ratio crystals,

6
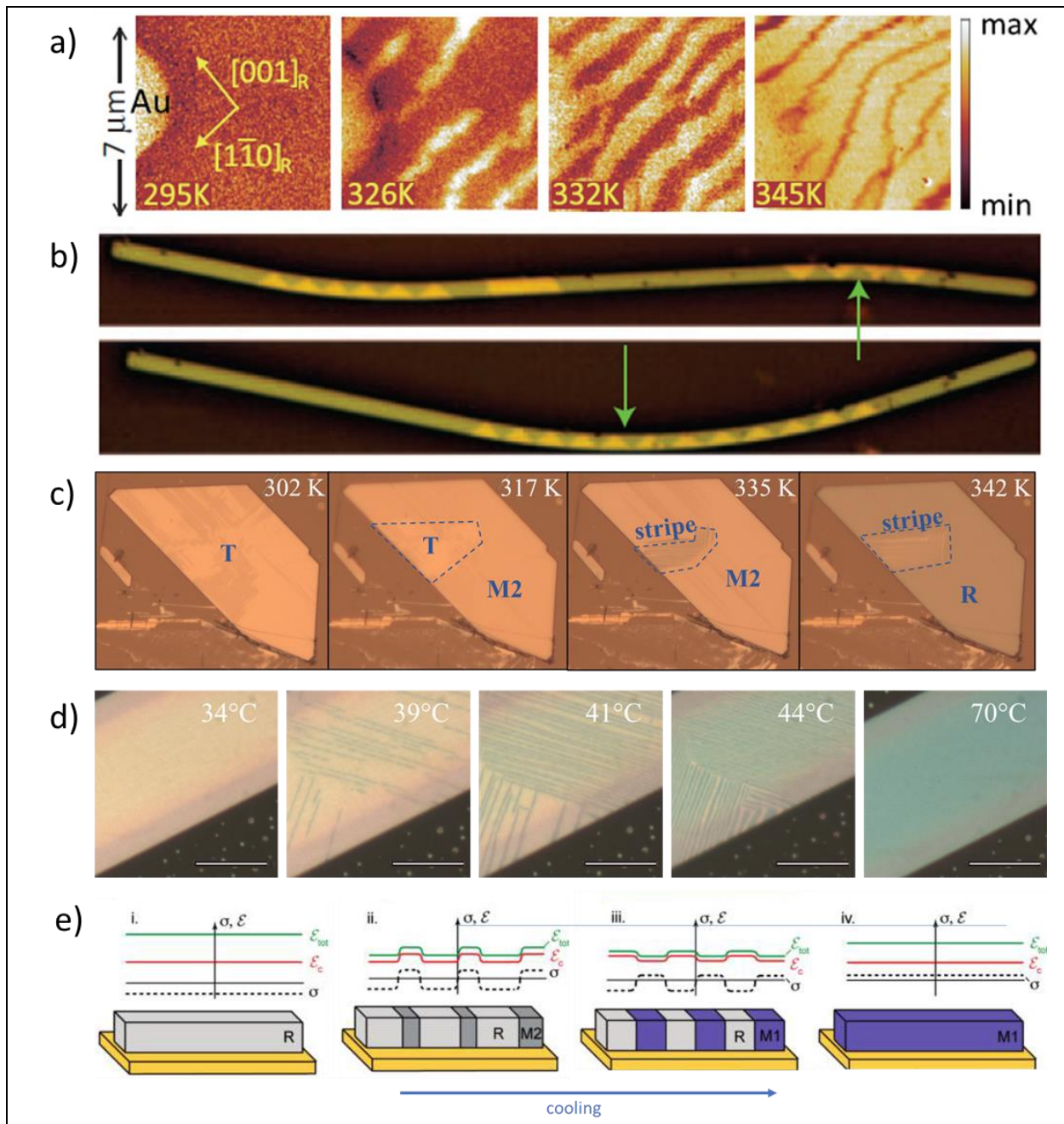
Figure 1.3: Thin films (a) subject to lattice strain from hetero-epitaxy with the substrate exhibit stripes perpendicular to c_R throughout the phase transition. In single crystals, phase coexistence arises due to strain applied by bending (b) or by thermal expansion mismatch with the substrate (c-d). M1, T, M2, and R can all participate in the phase coexistence depending on the strain and temperature. Striped phases arise to minimize the elastic energy density (ε_{tot}) arising due to stress (σ) in individual domains and between the crystal and substrate.

(a) reprinted figure with permission from reference [65]. Copyright 2013 by the American Physical Society. 10.1103/PhysRevLett.111.096602
(b) Reprinted by permission from Springer Nature Customer Service Center GmbH: Springer Nature, reference [58], Copyright 2009.
(e) adapted with permission from reference [67]. Copyright 2010 American Chemical Society

more complex herringbone patterns can be observed[63] (Figure 3c-d). Single crystals adhered to a rigid substrate often exhibit striped phases involving M1, M2 and R, as the increase in length (along c_R) in M2 compensates for the corresponding decrease in R[66-69] (Figure 3e).

Self-organized phase coexistence is observed in the ultrafast PIPT as well as the steady-state thermally-induced transition. Strain apparently plays a similar role here as in the thermally-induced transition, and local regions that become metallic at the lowest temperatures also undergo the PIPT at the lowest fluence.[54] On the other hand, another study observed a metallic stripe oriented *along* the c_R-direction (perpendicular to the lateral stripes observed in the thermally-induced transition)[53] suggesting that there are some differences in the nucleation behavior under ultrafast optical excitation.

1.4.b Doping Effects

Dopants and defects also play an important role. Figure 4 shows a schematic diagram showing qualitatively how doping, oxygen content, and strain all affect the stable phases.[40] Substitutional doping with metal atoms both contributes to local lattice strain and adds electrons or holes.[70] Like strain, it can shift T_c and stabilize other phases such as M2, depending on the valence charge state of the dopant ion. Some dopants (like W) decrease T_c, while others (Cr, Al) stabilize the M2 phase, resulting in a doping/temperature phase diagram qualitatively similar to the strain/temperature phase diagram.[71] Oxygen stoichiometry plays a similar role,[72-73] as long as the deficiency or surplus of oxygen is not so large as to convert VO_2 into another vanadium oxide.
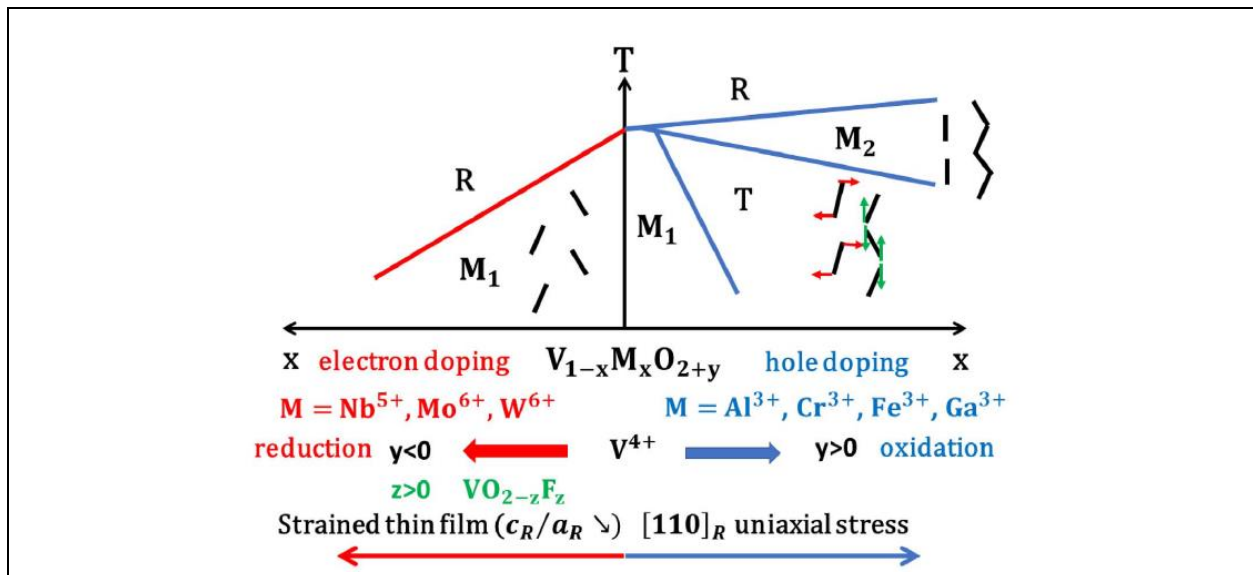
Figure 1.4: Doping, strain, and oxygen stoichiometry all result in a similar phase diagram for VO_2. Doping with electrons, Nb, Mo, or W, oxygen deficiency, compressive strain along c_R or tensile strain along a_R decrease the temperature for the M1-R transition; doping with holes, Al, Cr, Fe, or Ga, oxygen surplus, and tensile strain along c_R or compressive strain along a_R stabilize the T and M2 phases between M1 and R.

Interstitial doping with H atoms (which penetrate channels along the c_R axis of the R phase),[74] can produce still other distinct phases.[75] Electron-doping via contact with metals of different work functions can also slightly increase or decrease the transition temperature.[76] Individual dopant atoms,[77] oxygen vacancies,[78] surface roughness[79] and other localized and extended defects[80] (as well as grain boundaries in thin films)[81-82] also serve as nucleation sites for the phase transition, affecting the slope and width of hysteresis curves.

1.4.c Morphological Effects

From a practical standpoint, it is useful to relate the VO_2 transition properties (contrast in transmission, reflection or resistivity, T_c, hysteresis width and slope, intermediate phase changes) to its nanoscale and microscale morphology, though these effects can usually be attributed to combinations of the strain and defect effects discussed in the preceding paragraphs.

Polycrystalline thin films are composed of densely-packed crystalline grains (~10s-100s of nm in size) which may have either random or preferred orientations, depending on how well the substrate lattice matches the VO_2 lattice. Grain size and film density varies with deposition method.[83] In thin films, the phase transition proceeds percolatively,[84-85] as individual grains switch one-by-one. Somewhat surprisingly, this percolation is not entirely stochastic, but can be highly reproducible;[86] the critical temperature for any given grain may differ randomly from its neighbors, affected by its size, stoichiometry, and defects.[83, 87-89] A film with more uniform grains should exhibit a sharper transition, and *vice versa*. Electrical probes of the phase transition will show a drop in resistivity when enough grains have switches to form a conductive channel between the probes,[90] while optical measurements yield an ensemble average of the properties of all the grains in the sampled volume. X-ray holography[91-92] measurements reveal the presence of different VO_2 phases and other vanadium oxides on the nanoscale even at room temperature. Varying film thickness can affect T_c, especially in epitaxial films where strain is most prominent near the substrate surface.[93-94]

Unstrained single crystals, by contrast, come closer to representing true bulk VO_2. In addition to the strain and dopant effects discussed above, the phase transition in VO_2 single crystals is sensitive to their size and shape. Crystals thinned by Ar-ion milling to less than 5 nm thick showed a decreased T_c due to increasing strain;[95] and microbeams with decreasing width (~30 μm down to ~1 μm) exhibit increasing hysteresis width (due to fewer nucleation sites) and faster phase transitions due to better thermal exchange.[96] On the other hand, O'Callahan *et al.* found that ultrafast transition times in VO_2 micro-crystals are uncorrelated with size, suggesting that local defects, dopants, and strain have stronger effects than size alone.[41]

Size effects become particularly pronounced in VO_2 nanoparticles (~100s of nm and smaller). At this size scale, the number of defects (and thus nucleation sites) in a single nanoparticle is low enough that the phase transition is difficult to nucleate, broadening the hysteretic behavior,[97] and scattering and plasmon resonances in the visible and near-IR affect the optical properties.[98] Also, Lopez *et al.* showed that W-doping is much more effective at decreasing T_c in nanoparticles embedded in SiO_2,[99] though the reason for this has not been fully explained.

1.5 Engineering VO₂ for Applications

The variety of different properties (optical, electrical, magnetic, lattice) which change across the phase transition, coupled to the variety of means to induce the transition (thermal, electrical, optical, mechanical, chemical), render VO$_2$ an extremely versatile material for applications and devices. The change in IR optical behavior as a function of temperature is being exploited in "smart" thermochromic windows,[100] passive thermal control for spacecraft,[101] and IR stealth coatings.[102-104] The possibility of ultrafast all-optical switching is attractive for photonics; several ultrafast optical devices have been demonstrated, including tunable ring resonators[105] and in-waveguide switches.[106] The conductivity change, coupled with the hysteretic properties, has enabled electronic devices based on the phase transition, including field-effect transistors, memristors,[107] and neural network components.[108]

Still more varied, creative applications abound: chemical sensors, microscale thermometers, and nanoactuators.[107] Recently, the combination of VO$_2$ with two-dimensional (2D) materials has begun to be explored, with demonstrations of photodetectors,[109-110] optical and electrical rectifiers,[111] field-effect transistors,[112] and reconfigurable planar metasurfaces.[113] This diverse array of potential VO₂-based devices—each with its own requirements for morphology, form factor, fabrication processes, T_c, hysteresis width and sharpness, switching speed, and operating environment—requires a similarly broad set of techniques to fabricate and process different forms of high-quality VO$_2$.

The complexity of the V-O phase diagram and the sensitivity of VO$_2$ switching behavior to so many intrinsic and extrinsic factors (outlined briefly above) provide, at the same time, an excellent opportunity to engineer VO$_2$ to suit specific needs and a significant challenge to find the narrow window of parameter space required to produce the desired behavior.

Thin-film VO$_2$ is perhaps the most well-developed form; recipes exist for producing VO$_2$ thin films via sputtering, sol-gel, pulsed laser deposition, chemical vapor deposition,[114] and atomic layer deposition (ALD).[115] Thin films have the advantages of compatibility with wafer-scale growth and lithographic patterning (both liftoff[116] and etch[117-118] processes), precise thickness control, simple integration into heterostructures, and robustness to repeated on-off cycles.[119] On the other hand, micro-scale single crystals offer bulk VO$_2$ lattice, well-defined orientation, smooth crystal facets, and sharp metal-insulator boundaries; however, large crystals tend to break due to stress after many repeated heating cycles. Nanoparticles exhibit unique size-dependent properties, and may perform better than thin films when heavily doped. While growth of VO$_2$ thin films has been thoroughly explored,[114] and large-scale preparation of nanoparticles is rapidly developing,[120] growth of large, high-quality single crystals is still difficult and offers wide room for exploration.

1.6 Overview

Whatever the desired form of VO$_2$, and whatever the selected growth method, many critical process parameters must be finely tuned and controlled. Understanding not only the effects of each parameter on the final product, but also the underlying physics affecting the final product is critical to realizing the full potential of VO$_2$, and, by extension, other PCMs.

This work examines the various mechanisms by which the growth substrate (a process parameter common to all but a few VO$_2$ growth methods) can affect (and be leveraged to

control) different forms of vanadium dioxide prepared by different methods. Chapter 2 examines vapor-transport growth of large VO_2 single crystals, differentiating the roles of lattice match, chemical reactions, and surface/interface energies. Chapter 3 examines the formation of nanoparticles via solid state dewetting, driven primarily by interface energies, and the role of W-dopants on the dewetting behavior. To illustrate the utility of these advances, two different applications areas are explored. A new platform for reconfigurable metamaterials (Chapters 4 and 5) is demonstrated by coupling large, low-aspect-ratio VO_2 microcrystals to 2D materials; thermochromic coatings based on VO_2 thin films (Chapter 6) can potentially benefit from W-doping, micro-patterning, and nanoparticle formation. Finally, the Appendix presents additional technical details and insights into the processes and analysis techniques employed.

This work specifically highlights substrate choice as a valuable strategy for engineering VO_2 for applications, with interactions at the substrate-VO_2 interface driving changes in orientation, morphology, chemical composition, and strain state. Though substrate is but one of many critical growth parameters, it is a common consideration in vastly different processes; the interactions studied here (lattice match, chemical reactions, and surface/interface energies) play similar roles for single crystals or thin films, from the nm- to the mm-scale, regardless of the specific growth method employed. The results presented here advance our understanding of these important effects, and point the way to exploiting them to improve cutting-edge technologies.

1.7 References

1.   Lyu, X. R.; Hessler, A.; Wang, X.; Cao, Y. Z.; Song, L. X.; Ludwig, A.; Wuttig, M.; Taubner, T., Combining Switchable Phase-Change Materials and Phase-Transition Materials for Thermally Regulated Smart Mid-Infrared Modulators. *Adv. Opt. Mater.* **2021,** *9* (16), 8.
2.   Raoux, S., Phase Change Materials. *Annual Review of Materials Research* **2009,** *39*, 25-48.
3.   Yang, Z.; Ko, C. Y.; Ramanathan, S., Oxide Electronics Utilizing Ultrafast Metal-Insulator Transitions. In *Annual Review of Materials Research, Vol 41*, Clarke, D. R.; Fratzl, P., Eds. Annual Reviews: Palo Alto, 2011; Vol. 41, pp 337-367.
4.   Properties of the Elements. In *CRC Handbook of Chemistry and Physics*, 102nd ed.; Rumble, J. R., Ed. CRC Press: Boca Raton, 2021.
5.   Bahlawane, N.; Lenoble, D., Vanadium Oxide Compounds: Structure, Properties, and Growth from the Gas Phase. *Chem. Vapor Depos.* **2014,** *20* (7-9), 299-311.
6.   Wriedt, H. A., The O-V (Oxygen-Vanadium) system. *Bulletin of Alloy Phase Diagrams* **1989,** *10* (3), 271-277.
7.   Lee, M. H.; Kalcheim, Y.; del Valle, J.; Schuller, I. K., Controlling Metal-Insulator Transitions in Vanadium Oxide Thin Films by Modifying Oxygen Stoichiometry. *ACS Appl. Mater. Interfaces* **2021,** *13* (1), 887-896.
8.   Lee, S.; Meyer, T. L.; Park, S.; Egami, T.; Lee, H. N., Growth control of the oxidation state in vanadium oxide thin films. *Appl. Phys. Lett.* **2014,** *105* (22), 4.
9.   Occhiuzzi, M.; Cordischi, D.; Dragone, R., Reactivity of some vanadium oxides: An EPR and XRD study. *Journal of Solid State Chemistry* **2005,** *178* (5), 1551-1558.
10.   Yang, Y.; Wei, W.; Wang, S. X.; Huang, T. T.; Yuan, M. H.; Zhang, R.; Yang, W. L.; Zhang, T. N.; Sun, Y.; Yuan, Y. J.; Yu, Z. T.; Chen, X.; Dai, N., Suppression of Photoinduced Surface Oxidation of Vanadium Dioxide Nanostructures by Blocking Oxygen Adsorption. *ACS Omega* **2019,** *4* (18), 17735-17740.

11.   Schwingenschlogl, U.; Eyert, V., The vanadium Magneli phases $V_{(n)}O_{(2n-1)}$. *Ann. Phys.-Berlin* **2004,** *13* (9), 475-510.

12.   McWhan, D. B.; Marezio, M.; Remeika, J. P.; Dernier, P. D., X-ray-diffraction study of metallic VO_2. *Phys. Rev. B* **1974,** *10* (2), 490-495.

13.   Longo, J. M.; Kierkegaard, P.; Ballhausen, C.; Ragnarsson, U.; Rasmussen, S.; Sunde, E.; Sørensen, N., A refinement of the structure of VO_2. *Acta Chem. Scand* **1970,** *24* (2), 420-426.

14.   Ghedira, M.; Chenavas, J.; Marezio, M., Cation disproportionation and pairing in the insulating T phase of $V_{0.985}Al_{0.15}O_2$. *Journal of Physics C-Solid State Physics* **1977,** *10* (11), L309-L314.

15.   Morin, F. J., Oxides which show a metal-to-insulator transition at the Neel temperature. *Phys. Rev. Lett.* **1959,** *3* (1), 34-36.

16.   Bruckner, W., Structural relations between the VO_2 phases. *Cryst. Res. Technol.* **1981,** *16* (3), K28-K31.

17.   Momma, K.; Izumi, F., VESTA 3 for three-dimensional visualization of crystal, volumetric and morphology data. *J. Appl. Crystallogr.* **2011,** *44*, 1272-1276.

18.   Tselev, A.; Meunier, V.; Strelcov, E.; Shelton, J., William A.; Luk'yanchuk, I. A.; Jones, K.; Proksch, R.; Kolmakov, A.; Kalinin, S. V., Mesoscopic metal-insulator transition at ferroelastic domain walls in VO_2. *ACS Nano* **2010,** *4* (8), 4412-4419.

19.   Berglund, C. N.; Guggenheim, H. J., Electronic Properties of VO_2 near the Semiconductor-Metal Transition. *Physical Review* **1969,** *185* (3), 1022-1033.

20.   Cavalleri, A.; Rini, M.; Chong, H. H. W.; Fourmaux, S.; Glover, T. E.; Heimann, P. A.; Kieffer, J. C.; Schoenlein, R. W., Band-Selective Measurements of Electron Dynamics in VO_2 Using Femtosecond Near-Edge X-Ray Absorption. *Phys. Rev. Lett.* **2005,** *95* (6), 067405.

21.   Okimura, K.; Azhan, N. H.; Hajiri, T.; Kimura, S.; Zaghrioui, M.; Sakai, J., Temperature-dependent Raman and ultraviolet photoelectron spectroscopy studies on phase transition behavior of VO_2 films with M1 and M2 phases. *J. Appl. Phys.* **2014,** *115* (15), 6.

22.   Xu, S.; Shen, X.; Hallman, K. A.; Haglund, R. F.; Pantelides, S. T., Unified band-theoretic description of structural, electronic, and magnetic properties of vanadium dioxide phases. *Phys. Rev. B* **2017,** *95* (12), 7.

23.   Lee, S.; Hippalgaonkar, K.; Yang, F.; Hong, J. W.; Ko, C.; Suh, J.; Liu, K.; Wang, K.; Urban, J. J.; Zhang, X.; Dames, C.; Hartnoll, S. A.; Delaire, O.; Wu, J. Q., Anomalously low electronic thermal conductivity in metallic vanadium dioxide. *Science* **2017,** *355* (6323), 371-374.

24.   Cueff, S.; Li, D. F.; Zhou, Y.; Wong, F. J.; Kurvits, J. A.; Ramanathan, S.; Zia, R., Dynamic control of light emission faster than the lifetime limit using VO_2 phase-change. *Nat. Commun.* **2015,** *6*, 6.

25.   Kakiuchida, H.; Jin, P.; Nakao, S.; Tazawa, M., Optical properties of vanadium dioxide film during semiconductive-metallic phase transition. *Jpn. J. Appl. Phys. Part 2 - Lett. Express Lett.* **2007,** *46* (4-7), L113-L116.

26.   Kana, J. B. K.; Ndjaka, J. M.; Vignaud, G.; Gibaud, A.; Maaza, M., Thermally tunable optical constants of vanadium dioxide thin films measured by spectroscopic ellipsometry. *Opt. Commun.* **2011,** *284* (3), 807-812.

27.   Verleur, H. W.; Barker, A. S.; Berglund, C. N., Optical Properties of VO_2 between 0.25 and 5 eV. *Physical Review* **1968,** *172* (3), 788-798.

28.   Barker, A. S.; Verleur, H. W.; Guggenheim, H. J., Infrared Optical Properties of Vanadium Dioxide Above and Below the Transition Temperature. *Phys. Rev. Lett.* **1966,** *17* (26), 1286-1289.

29.   Wan, C. H.; Zhang, Z.; Woolf, D.; Hessel, C. M.; Rensberg, J.; Hensley, J. M.; Xiao, Y. Z.; Shahsafi, A.; Salman, J.; Richter, S.; Sun, Y. F.; Qazilbash, M. M.; Schmidt-Grund, R.; Ronning, C.; Ramanathan, S.; Kats, M. A., On the Optical Properties of Thin-Film Vanadium Dioxide from the Visible to the Far Infrared. *Ann. Phys.-Berlin* **2019,** *531* (10), 7.

30.   Nazari, M.; Zhao, Y.; Kuryatkov, V. V.; Fan, Z. Y.; Bernussi, A. A.; Holtz, M., Temperature dependence of the optical properties of VO_2 deposited on sapphire with different orientations. *Phys. Rev. B* **2013,** *87* (3), 7.

31.   Guo, Y. F.; Zhang, Y. Z.; Zhang, L. M.; Lv, X. R.; Wu, L. N.; Cao, Y. Z.; Song, L. X., Study of the phase transition properties and electronic band structures of VO_2 thin films grown on different substrates. *Mater. Res. Express* **2019,** *6* (2), 9.

32.   Guinneton, F.; Sauques, L.; Valmalette, J. C.; Cros, F.; Gavarri, J. R., Role of surface defects and microstructure in infrared optical properties of thermochromic VO_2 materials. *J. Phys. Chem. Solids* **2005,** *66* (1), 63-73.

33.   Paone, A.; Sanjines, R.; Jeanneret, P.; Schuler, A., Temperature-dependent multiangle FTIR NIR-MIR ellipsometry of thermochromic VO_2 and $V_{1-x}W_xO_2$ films. *Sol. Energy* **2015,** *118*, 107-116.

34.   Jiang, M.; Li, Y. M.; Li, S. T.; Zhou, H. J.; Cao, X.; Bao, S. H.; Gao, Y. F.; Luo, H. J.; Jin, P., Room Temperature Optical Constants and Band Gap Evolution of Phase Pure M_1-VO_2 Thin Films Deposited at Different Oxygen Partial Pressures by Reactive Magnetron Sputtering. *J. Nanomater.* **2014,** *2014*, 6.

35.   Peierls, R. E., *More surprises in theoretical physics / Rudolf Peierls*. Princeton University Press: Princeton, N.J, 1991.

36.   Goodenough, J. B., The two components of the crystallographic transition in VO_2. *Journal of Solid State Chemistry* **1971,** *3* (4), 490-500.

37.   Zylbersztejn, A.; Mott, N. F., Metal-insulator transition in vanadium dioxide. *Phys. Rev. B* **1975,** *11* (11), 4383-4395.

38.   Basov, D. N.; Averitt, R. D.; van der Marel, D.; Dressel, M.; Haule, K., Electrodynamics of correlated electron materials. *Rev. Mod. Phys.* **2011,** *83* (2), 471-541.

39.   Qazilbash, M. M.; Schafgans, A. A.; Burch, K. S.; Yun, S. J.; Chae, B. G.; Kim, B. J.; Kim, H. T.; Basov, D. N., Electrodynamics of the vanadium oxides VO_2 and V_2O_3. *Phys. Rev. B* **2008,** *77* (11), 10.

40.   Pouget, J. P., Basic aspects of the metal -insulator transition in vanadium dioxide VO_2: a critical review. *C. R. Phys.* **2021,** *22* (1), 37-87.

41.   O'Callahan, B. T.; Jones, A. C.; Park, J. H.; Cobden, D. H.; Atkin, J. M.; Raschke, M. B., Inhomogeneity of the ultrafast insulator-to-metal transition dynamics of VO_2. *Nat. Commun.* **2015,** *6*, 8.

42.   Cavalleri, A.; Dekorsy, T.; Chong, H. H. W.; Kieffer, J. C.; Schoenlein, R. W., Evidence for a structurally-driven insulator-to-metal transition in VO_2: A view from the ultrafast timescale. *Phys. Rev. B* **2004,** *70* (16), 4.

43.   Wegkamp, D.; Herzog, M.; Xian, L.; Gatti, M.; Cudazzo, P.; McGahan, C. L.; Marvel, R. E.; Haglund, R. F.; Rubio, A.; Wolf, M.; Stahler, J., Instantaneous Band Gap Collapse in Photoexcited Monoclinic VO_2 due to Photocarrier Doping. *Phys. Rev. Lett.* **2014,** *113* (21), 5.

44.   Jager, M. F.; Ott, C.; Kraus, P. M.; Kaplan, C. J.; Pouse, W.; Marvel, R. E.; Haglund, R. F.; Neumark, D. M.; Leone, S. R., Tracking the insulator-to-metal phase transition in VO_2 with few-femtosecond extreme UV transient absorption spectroscopy. *Proc. Natl. Acad. Sci. U. S. A.* **2017,** *114* (36), 9558-9563.

45.   Tao, Z. S.; Zhou, F. R.; Han, T. R. T.; Torres, D.; Wang, T. Y.; Sepulveda, N.; Chang, K.; Young, M.; Lunt, R. R.; Ruan, C. Y., The nature of photoinduced phase transition and metastable states in vanadium dioxide. *Sci Rep* **2016,** *6*, 10.

46.   Wegkamp, D.; Stahler, J., Ultrafast dynamics during the photoinduced phase transition in VO_2. *Prog. Surf. Sci.* **2015,** *90* (4), 464-502.

47.   Morrison, V. R.; Chatelain, R. P.; Tiwari, K. L.; Hendaoui, A.; Bruhacs, A.; Chaker, M.; Siwick, B. J., A photoinduced metal-like phase of monoclinic VO2 revealed by ultrafast electron diffraction. *Science* **2014,** *346* (6208), 445-448.

48.   Sood, A.; Shen, X. Z.; Shi, Y.; Kumar, S.; Park, S. J.; Zajac, M.; Sun, Y. F.; Chen, L. Q.; Ramanathan, S.; Wang, X. J.; Chueh, W. C.; Lindenberg, A. M., Universal phase dynamics in VO2 switches revealed by ultrafast operando diffraction. *Science* **2021,** *373* (6552), 352-+.

49.   Laverock, J.; Kittiwatanakul, S.; Zakharov, A. A.; Niu, Y. R.; Chen, B.; Wolf, S. A.; Lu, J. W.; Smith, K. E., Direct Observation of Decoupled Structural and Electronic Transitions and an Ambient Pressure Monocliniclike Metallic Phase of VO2. *Phys. Rev. Lett.* **2014,** *113* (21), 5.

50.   Otto, M. R.; de Cotret, L. P. R.; Valverde-Chavez, D. A.; Tiwari, K. L.; Emond, N.; Chaker, M.; Cooke, D. G.; Siwick, B. J., How optical excitation controls the structure and properties of vanadium dioxide. *Proc. Natl. Acad. Sci. U. S. A.* **2019,** *116* (2), 450-455.

51.   Vidas, L.; Schick, D.; Martinez, E.; Perez-Salinas, D.; Ramos-Alvarez, A.; Cichy, S.; Batlle-Porro, S.; Johnson, A. S.; Hallman, K. A.; Haglund, R. F.; Wall, S., Does VO_2 Host a Transient Monoclinic Metallic Phase? *Phys. Rev. X* **2020,** *10* (3), 12.

52.   Wall, S.; Yang, S.; Vidas, L.; Chollet, M.; Glownia, J. M.; Kozina, M.; Katayama, T.; Henighan, T.; Jiang, M.; Miller, T. A.; Reis, D. A.; Boatner, L. A.; Delaire, O.; Trigo, M., Ultrafast disordering of vanadium dimers in photoexcited VO_2. *Science* **2018,** *362* (6414), 572-576.

53.   Donges, S. A.; Khatib, O.; O'Callahan, B. T.; Atkin, J. M.; Park, J. H.; Cobden, D.; Raschke, M. B., Ultrafast Nanoimaging of the Photoinduced Phase Transition Dynamics in VO_2. *Nano Lett.* **2016,** *16* (5), 3029-3035.

54.   Huber, M. K.; Plankl, M.; Eisele, M.; Marvel, R. E.; Sandner, F.; Kornt, T.; Schuller, C.; Haglund, R. F.; Huber, R.; Cocker, T. L., Ultrafast Mid-Infrared Nanoscopy of Strained Vanadium Dioxide Nanobeams. *Nano Lett.* **2016,** *16* (2), 1421-1427.

55.   Cao, J.; Gu, Y.; Fan, W.; Chen, L. Q.; Ogletree, D. F.; Chen, K.; Tamura, N.; Kunz, M.; Barrett, C.; Seidel, J.; Wu, J., Extended Mapping and Exploration of the Vanadium Dioxide Stress-Temperature Phase Diagram. *Nano Lett.* **2010,** *10* (7), 2667-2673.

56.   Park, J. H.; Coy, J. M.; Kasirga, T. S.; Huang, C. M.; Fei, Z. Y.; Hunter, S.; Cobden, D. H., Measurement of a solid-state triple point at the metal-insulator transition in VO_2. *Nature* **2013,** *500* (7463), 431-434.

57.   Liu, M. K.; Sternbach, A. J.; Wagner, M.; Slusar, T. V.; Kong, T.; Bud'ko, S. L.; Kittiwatanakul, S.; Qazilbash, M. M.; McLeod, A.; Fei, Z.; Abreu, E.; Zhang, J. D.; Goldflam, M.; Dai, S. Y.; Ni, G. X.; Lu, J. W.; Bechtel, H. A.; Martin, M. C.; Raschke, M. B.; Averitt, R. D.; Wolf, S. A.; Kim, H. T.; Canfield, P. C.; Basov, D. N., Phase transition in bulk single crystals and thin films of VO_2 by nanoscale infrared spectroscopy and imaging. *Phys. Rev. B* **2015,** *91* (24), 10.

58.   Cao, J.; Ertekin, E.; Srinivasan, V.; Fan, W.; Huang, S.; Zheng, H.; Yim, J. W. L.; Khanal, D. R.; Ogletree, D. F.; Grossmanan, J. C.; Wu, J., Strain engineering and one-dimensional organization of metal-insulator domains in single-crystal vanadium dioxide beams. *Nat. Nanotechnol.* **2009,** *4* (11), 732-737.

59.   Muraoka, Y.; Ueda, Y.; Hiroi, Z., Large modification of the metal-insulator transition temperature in strained VO_2 films grown on TiO_2 substrates. *J. Phys. Chem. Solids* **2002,** *63* (6-8), 965-967.

60.   Quackenbush, N. F.; Paik, H.; Wahila, M. J.; Sallis, S.; Holtz, M. E.; Huang, X.; Ganose, A.; Morgan, B. J.; Scanlon, D. O.; Gu, Y.; Xue, F.; Chen, L. Q.; Sterbinsky, G. E.; Schlueter, C.; Lee, T. L.; Woicik, J. C.; Guo, J. H.; Brock, J. D.; Muller, D. A.; Arena, D. A.; Schlom, D. G.; Piper, L. F. J., Stability of the M2 phase of vanadium dioxide induced by coherent epitaxial strain. *Phys. Rev. B* **2016,** *94* (8), 6.

61.   Pendse, S.; Jiang, J.; Zhang, L. F.; Guo, Y. W.; Chen, Z. Z.; Hu, Y.; Lu, Z. H.; Li, S. M.; Feng, J.; Lu, T. M.; Shi, J., Tuning phase transition kinetics via van der Waals epitaxy of single crystalline VO_2 on hexagonal-BN. *J. Cryst. Growth* **2020,** *543*, 5.

62.   Lee, D.; Lee, J.; Song, K.; Xue, F.; Choi, S. Y.; Ma, Y. J.; Podkaminer, J.; Liu, D.; Liu, S. C.; Chung, B.; Fan, W. J.; Cho, S. J.; Zhou, W. D.; Lee, J.; Chen, L. Q.; Oh, S. H.; Ma, Z. Q.; Eom, C. B., Sharpened VO_2 Phase Transition via Controlled Release of Epitaxial Strain. *Nano Lett.* **2017,** *17* (9), 5614-5619.

63.   McGahan, C.; Gamage, S.; Liang, J. R.; Cross, B.; Marvel, R. E.; Haglund, R. F.; Abate, Y., Geometric constraints on phase coexistence in vanadium dioxide single crystals. *Nanotechnology* **2017,** *28* (8), 9.

64.   Tselev, A.; Strelcov, E.; Luk'yanchuk, I. A.; Budai, J. D.; Tischler, J. Z.; Ivanov, I. N.; Jones, K.; Proksch, R.; Kalinin, S. V.; Kolmakov, A., Interplay between Ferroelastic and Metal-Insulator Phase Transitions in Strained Quasi-Two-Dimensional VO_2 Nanoplatelets. *Nano Lett.* **2010,** *10* (6), 2003-2011.

65.   Liu, M. K.; Wagner, M.; Abreu, E.; Kittiwatanakul, S.; McLeod, A.; Fei, Z.; Goldflam, M.; Dai, S.; Fogler, M. M.; Lu, J.; Wolf, S. A.; Averitt, R. D.; Basov, D. N., Anisotropic Electronic State via Spontaneous Phase Separation in Strained Vanadium Dioxide Films. *Phys. Rev. Lett.* **2013,** *111* (9), 5.

66.   Tselev, A.; Luk'yanchuk, I. A.; Ivanov, I. N.; Budai, J. D.; Tischler, J. Z.; Strelcov, E.; Kolmakov, A.; Kalinin, S. V., Symmetry Relationship and Strain-Induced Transitions between Insulating M1 and M2 and Metallic R phases of Vanadium Dioxide. *Nano Lett.* **2010,** *10* (11), 4409-4416.

67.   Jones, A. C.; Berweger, S.; Wei, J.; Cobden, D.; Raschke, M. B., Nano-optical Investigations of the Metal-Insulator Phase Behavior of Individual VO₂ Microcrystals. *Nano Lett.* **2010,** *10* (5), 1574-1581.

68.   Sohn, J. I.; Joo, H. J.; Kim, K. S.; Yang, H. W.; Jang, A. R.; Ahn, D.; Lee, H. H.; Cha, S.; Kang, D. J.; Kim, J. M.; Welland, M. E., Stress-induced domain dynamics and phase transitions in epitaxially grown VO₂ nanowires. *Nanotechnology* **2012,** *23* (20), 6.

69.   Zhang, S. X.; Chou, J. Y.; Lauhon, L. J., Direct Correlation of Structural Domain Formation with the Metal Insulator Transition in a VO₂ Nanobeam. *Nano Lett.* **2009,** *9* (12), 4527-4532.

70.   Tan, X. G.; Yao, T.; Long, R.; Sun, Z. H.; Feng, Y. J.; Cheng, H.; Yuan, X.; Zhang, W. Q.; Liu, Q. H.; Wu, C. Z.; Xie, Y.; Wei, S. Q., Unraveling Metal-insulator Transition Mechanism of VO₂ Triggered by Tungsten Doping. *Sci Rep* **2012,** *2*, 6.

71.   Pouget, J., P.; Launois, H., Metal-insulator phase transition in VO₂. *J. Phys. Colloques* **1976,** *37* (C4), 49-57.

72.   Zhang, S. X.; Kim, I. S.; Lauhon, L. J., Stoichiometry Engineering of Monoclinic to Rutile Phase Transition in Suspended Single Crystalline Vanadium Dioxide Nanobeams. *Nano Lett.* **2011,** *11* (4), 1443-1447.

73.   Zhang, Z.; Zuo, F.; Wan, C. H.; Dutta, A.; Kim, J.; Rensberg, J.; Nawrodt, R.; Park, H. H.; Larrabee, T. J.; Guan, X. F.; Zhou, Y.; Prokes, S. M.; Ronning, C.; Shalaev, V. M.; Boltasseva, A.; Kats, M. A.; Ramanathan, S., Evolution of Metallicity in Vanadium Dioxide by Creation of Oxygen Vacancies. *Phys. Rev. Appl.* **2017,** *7* (3), 13.

74.   Lin, J.; Ji, H.; Swift, M. W.; Hardy, W. J.; Peng, Z. W.; Fan, X. J.; Nevidomskyy, A. H.; Tour, J. M.; Natelson, D., Hydrogen Diffusion and Stabilization in Single-Crystal VO₂ Micro/Nanobeams by Direct Atomic Hydrogenation. *Nano Lett.* **2014,** *14* (9), 5445-5451.

75.   Chen, S.; Wang, Z. W.; Fan, L. L.; Chen, Y. L.; Ren, H.; Ji, H.; Natelson, D.; Huang, Y. Y.; Jiang, J.; Zou, C. W., Sequential insulator-metal-insulator phase transitions of VO₂ triggered by hydrogen doping. *Phys. Rev. B* **2017,** *96* (12), 6.

76.   Duan, X. Y.; White, S. T.; Cui, Y. Y.; Neubrech, F.; Gao, Y. F.; Haglund, R. F.; Liu, N., Reconfigurable Multistate Optical Systems Enabled by VO2 Phase Transitions. *ACS Photonics* **2020,** *7* (11), 2958-2965.

77.   Braham, E. J.; Sellers, D.; Emmons, E.; Villarreal, R.; Asayesh-Ardakani, H.; Fleer, N. A.; Farley, K. E.; Shahbazian-Yassar, R.; Arroyave, R.; Shamberger, P. J.; Banerjee, S., Modulating the Hysteresis of an Electronic Transition: Launching Alternative Transformation Pathways in the Metal-Insulator Transition of Vanadium(IV) Oxide. *Chem. Mat.* **2018,** *30* (1), 214-224.

78.   Appavoo, K.; Lei, D. Y.; Sonnefraud, Y.; Wang, B.; Pantelides, S. T.; Maier, S. A.; Haglund, R. F., Role of Defects in the Phase Transition of VO₂ Nanoparticles Probed by Plasmon Resonance Spectroscopy. *Nano Lett.* **2012,** *12* (2), 780-786.

79.   Wang, C. Q.; Shao, J.; Liu, X. L.; Chen, Y.; Xiong, W. M.; Zhang, X. Y.; Zheng, Y., Phase transition characteristics in the conductivity of VO₂(A) nanowires: size and surface effects. *Phys. Chem. Chem. Phys.* **2016,** *18* (15), 10262-10269.

80.   Fan, W.; Cao, J.; Seidel, J.; Gu, Y.; Yim, J. W.; Barrett, C.; Yu, K. M.; Ji, J.; Ramesh, R.; Chen, L. Q.; Wu, J., Large kinetic asymmetry in the metal-insulator transition nucleated at localized and extended defects. *Phys. Rev. B* **2011,** *83* (23), 7.

81.   Aliev, R. A.; Andreev, V. N.; Kapralova, V. M.; Klimov, V. A.; Sobolev, A. I.; Shadrin, E. B., Effect of grain sizes on the metal-semiconductor phase transition in vanadium dioxide polycrystalline thin films. *Phys. Solid State* **2006,** *48* (5), 929-934.

82.   Jian, J.; Zhang, W. R.; Jacob, C.; Chen, A. P.; Wang, H.; Huang, J. J.; Wang, H. Y., Roles of grain boundaries on the semiconductor to metal phase transition of VO_2 thin films. *Appl. Phys. Lett.* **2015,** *107* (10), 5.

83.   Marvel, R. E.; Harl, R. R.; Craciun, V.; Rogers, B. R.; Haglund, R. F., Influence of deposition process and substrate on the phase transition of vanadium dioxide thin films. *Acta Mater.* **2015,** *91*, 217-226.

84.   Rozen, J.; Lopez, R.; Haglund, R. F.; Feldman, L. C., Two-dimensional current percolation in nanocrystalline vanadium dioxide films. *Appl. Phys. Lett.* **2006,** *88* (8), 3.

85.   Qazilbash, M. M.; Tripathi, A.; Schafgans, A. A.; Kim, B. J.; Kim, H. T.; Cai, Z. H.; Holt, M. V.; Maser, J. M.; Keilmann, F.; Shpyrko, O. G.; Basov, D. N., Nanoscale imaging of the electronic and structural transitions in vanadium dioxide. *Phys. Rev. B* **2011,** *83* (16), 7.

86.   Huffman, T. J.; Lahneman, D. J.; Wang, S. L.; Slusar, T.; Kim, B. J.; Kim, H. T.; Qazilbash, M. M., Highly repeatable nanoscale phase coexistence in vanadium dioxide films. *Phys. Rev. B* **2018,** *97* (8), 6.

87.   Ruzmetov, D.; Zawilski, K. T.; Narayanamurti, V.; Ramanathana, S., Structure-functional property relationships in rf-sputtered vanadium dioxide thin films. *J. Appl. Phys.* **2007,** *102* (11), 7.

88.   Kang, L. T.; Xie, L. L.; Chen, Z.; Gao, Y. F.; Liu, X. G.; Yang, Y. Z.; Liang, W., Asymmetrically modulating the insulator-metal transition of thermochromic VO_2 films upon heating and cooling by mild surface-etching. *Appl. Surf. Sci.* **2014,** *311*, 676-683.

89.   Narayan, J.; Bhosle, V. M., Phase transition and critical issues in structure-property correlations of vanadium oxide. *J. Appl. Phys.* **2006,** *100* (10), 6.

90.   del Valle, J.; Vargas, N. M.; Rocco, R.; Salev, P.; Kalcheim, Y.; Lapa, P. N.; Adda, C.; Lee, M. H.; Wang, P. Y.; Fratino, L.; Rozenberg, M. J.; Schuller, I. K., Spatiotemporal characterization of the field-induced insulator-to-metal transition. *Science* **2021,** *373* (6557), 907-+.

91.   Johnson, A. S.; Conesa, J. V.; Vidas, L.; Perez-Salinas, D.; Gunther, C. M.; Pfau, B.; Hallman, K. A.; Haglund, R. F.; Eisebitt, S.; Wall, S., Quantitative hyperspectral coherent diffractive imaging spectroscopy of a solid-state phase transition in vanadium dioxide. *Sci. Adv.* **2021,** *7* (33), 8.

92.   Vidas, L.; Gunther, C. M.; Miller, T. A.; Pfau, B.; Perez-Salinas, D.; Martinez, E.; Schneider, M.; Guhrs, E.; Galiani, P.; Valvidares, M.; Marvel, R. E.; Hallman, K. A.; Haglund, R. F.; Eisebitt, S.; Wall, S., Imaging Nanometer Phase Coexistence at Defects During the Insulator-Metal Phase Transformation in VO_2 Thin Films by Resonant Soft X-ray Holography. *Nano Lett.* **2018,** *18* (6), 3449-3453.

93.   Hu, K.; Yang, Y. J.; Hong, B.; Zhao, J. T.; Luo, Z. L.; Li, X. G.; Zhang, X. M.; Gu, Y. L.; Gao, X. Y.; Gao, C., Thickness-dependent anisotropy of metal-insulator transition in (110)-VO_2/TiO_2 epitaxial thin films. *J. Alloy. Compd.* **2017,** *699*, 575-580.

94.   Nagashima, K.; Yanagida, T.; Tanaka, H.; Kawai, T., Stress relaxation effect on transport properties of strained vanadium dioxide epitaxial thin films. *Phys. Rev. B* **2006,** *74* (17), 4.

95.   Fadlelmula, M. M.; Surmeli, E. C.; Ramezani, M.; Kasirga, T. S., Effects of Thickness on the Metal-Insulator Transition in Free-Standing Vanadium Dioxide Nanocrystals. *Nano Lett.* **2017,** *17* (3), 1762-1767.

96.   Yoon, J.; Kim, H.; Chen, X.; Tamura, N.; Mun, B. S.; Park, C.; Ju, H., Controlling the Temperature and Speed of the Phase Transition of VO_2 Microcrystals. *ACS Appl. Mater. Interfaces* **2016,** *8* (3), 2280-2286.

97.   Lopez, R.; Haynes, T. E.; Boatner, L. A.; Feldman, L. C.; Haglund, R. F., Size effects in the structural phase transition of VO_2 nanoparticles. *Phys. Rev. B* **2002,** *65* (22), 5.

98.   Nishikawa, K.; Kishida, Y.; Ito, K.; Tamura, S.; Takeda, Y., Near-infrared localized surface plasmon resonance of self-growing W-doped VO_2 nanoparticles at room temperature. *Appl. Phys. Lett.* **2017,** *111* (19), 5.

99.   Lopez, R.; Haynes, T. E.; Boatner, L. A.; Feldman, L. C.; Haglund, R. F., Temperature-controlled surface plasmon resonance in VO_2 nanorods. *Opt. Lett.* **2002,** *27* (15), 1327-1329.

100.   Vu, T. D.; Chen, Z.; Zeng, X. T.; Jiang, M.; Liu, S. Y.; Gao, Y. F.; Long, Y., Physical vapour deposition of vanadium dioxide for thermochromic smart window applications. *J. Mater. Chem. C* **2019,** *7* (8), 2121-2145.
101.   Sun, K.; Riedel, C. A.; Urbani, A.; Simeoni, M.; Mengali, S.; Zalkovskij, M.; Bilenberg, B.; de Groot, C. H.; Muskens, O. L., VO_2 Thermochromic Metamaterial-Based Smart Optical Solar Reflector. *ACS Photonics* **2018,** *5* (6), 2280-2286.
102.   Feng, L. L.; Liu, Y. M.; Yao, L.; Sun, R.; He, J. H., Infrared Stealth and Multi-Band Compatible Stealth Materials. *Prog. Chem.* **2021,** *33* (6), 1044-1058.
103.   Lang, F. P.; Wang, H.; Zhang, S. J.; Liu, J. B.; Yan, H., Review on Variable Emissivity Materials and Devices Based on Smart Chromism. *Int. J. Thermophys.* **2018,** *39* (1), 20.
104.   Ulpiani, G.; Ranzi, G.; Shah, K. W.; Feng, J.; Santamouris, M., On the energy modulation of daytime radiative coolers: A review on infrared emissivity dynamic switch against overcooling. *Sol. Energy* **2020,** *209*, 278-301.
105.   Haglund, R. F.; Hallman, K. A.; Miller, K. J.; Weiss, S. M.; Ieee, Picosecond Optical Switching in Silicon Photonics Using Phase-Changing Vanadium Dioxide. In *2019 Conference on Lasers and Electro-Optics*, IEEE: New York, 2019.
106.   Hallman, K. A.; Miller, K. J.; Baydin, A.; Weiss, S. M.; Haglund, R. F., Sub-Picosecond Response Time of a Hybrid VO_2:Silicon Waveguide at 1550 nm. *Adv. Opt. Mater.* **2021,** *9* (4), 8.
107.   Shi, R.; Shen, N.; Wang, J. W.; Wang, W. J.; Amini, A.; Wang, N.; Cheng, C., Recent advances in fabrication strategies, phase transition modulation, and advanced applications of vanadium dioxide. *Appl. Phys. Rev.* **2019,** *6* (1), 27.
108.   Oh, S.; Shi, Y. H.; del Valle, J.; Salev, P.; Lu, Y. C.; Huang, Z. S.; Kalcheim, Y.; Schuller, I. K.; Kuzum, D., Energy-efficient Mott activation neuron for full-hardware implementation of neural networks. *Nat. Nanotechnol.* **2021,** *16* (6), 680-687.
109.   Luo, H.; Wang, B. L.; Wang, E. Z.; Wang, X. W.; Sun, Y. F.; Li, Q. Q.; Fan, S. S.; Cheng, C.; Liu, K., Phase-transition modulated, high-performance dual-mode photodetectors based on WSe_2/VO_2 heterojunctions. *Appl. Phys. Rev.* **2019,** *6* (4), 11.
110.   Zhou, J. Y.; Xie, M. Z.; Ji, H.; Cui, A. Y.; Ye, Y.; Jiang, K.; Shang, L. Y.; Zhang, J. Z.; Hu, Z. G.; Chu, J. H., Mixed-Dimensional Van der Waals Heterostructure Photodetector. *ACS Appl. Mater. Interfaces* **2020,** *12* (16), 18674-18682.
111.   Oliva, N.; Casu, E. A.; Yan, C.; Krammer, A.; Rosca, T.; Magrez, A.; Stolichnov, I.; Schueler, A.; Martin, O. J. F.; Ionescu, A. M., Van der Waals MoS_2/VO_2 heterostructure junction with tunable rectifier behavior and efficient photoresponse. *Sci Rep* **2017,** *7*, 8.
112.   Yamamoto, M.; Nouchi, R.; Kanki, T.; Hattori, A. N.; Watanabe, K.; Taniguchi, T.; Ueno, K.; Tanaka, H., Gate-Tunable Thermal Metal-Insulator Transition in VO_2 Monolithically Integrated into a WSe_2 Field-Effect Transistor. *ACS Appl. Mater. Interfaces* **2019,** *11* (3), 3224-3230.
113.   Follan, T. G.; Fali, A.; White, S. T.; Matson, J. R.; Liu, S.; Aghamiri, N. A.; Edgar, J. H.; Haglund, R. F.; Abate, Y.; Caldwell, J. D., Reconfigurable infrared hyperbolic metasurfaces using phase change materials. *Nat. Commun.* **2018,** *9*, 7.
114.   Nag, J.; Haglund, R. F., Synthesis of vanadium dioxide thin films and nanoparticles. *J. Phys.-Condens. Mat.* **2008,** *20* (26), 14.
115.   Prasadam, V. P.; Bahlawane, N.; Mattelaer, F.; Rampelberg, G.; Detavernier, C.; Fang, L.; Jiang, Y.; Martens, K.; Parkin, I. P.; Papakonstantinou, I., Atomic layer deposition of vanadium oxides: process and application review. *Mater. Today Chem.* **2019,** *12*, 396-423.
116.   Haglund, R. F.; Lopez, R.; Suh, J. Y.; Feldman, L. C.; Haynes, T. E.; Boatner, L. A. In *Fabricating arrays of vanadium dioxide nanodisks by focused ion-beam lithography and pulsed laser deposition*, Conference on Photon Processing in Microelectronics and Photonics III, San Jose, CA, Jan 26-29; Spie-Int Soc Optical Engineering: San Jose, CA, 2004; pp 601-610.
117.   Lee, T.; Efremov, A.; Ham, Y. H.; Yun, S. J.; Min, N. K.; Hong, M.; Kwon, K. H., Etching characteristics and mechanism of vanadium dioxide in inductively coupled Cl_2/Ar plasma. *J. Micro-Nanolithogr. MEMS MOEMS* **2009,** *8* (2), 5.

118.   Yamin, T.; Wissberg, S.; Cohen, H.; Cohen-Taguri, G.; Sharoni, A., Ultrathin Films of VO_2 on r-Cut Sapphire Achieved by Postdeposition Etching. *ACS Appl. Mater. Interfaces* **2016,** *8* (23), 14863-14870.
119.   Long, S. W.; Cao, X.; Li, N.; Xin, Y. C.; Sun, G. Y.; Chang, T. C.; Bao, S. H.; Jin, P., Application-oriented VO2 thermochromic coatings with composite structures: Optimized optical performance and robust fatigue properties. *Sol. Energy Mater. Sol. Cells* **2019,** *189*, 138-148.
120.   Malarde, D.; Johnson, I. D.; Godfrey, I. J.; Powell, M. J.; Cibin, G.; Quesada-Cabrera, R.; Darr, J. A.; Carmalt, C. J.; Sankar, G.; Parkin, I. P.; Palgrave, R. G., Direct and continuous hydrothermal flow synthesis of thermochromic phase pure monoclinic VO_2 nanoparticles. *J. Mater. Chem. C* **2018,** *6* (43), 11731-11739.

CHAPTER 2

SUBSTRATE CHEMISTRY AND LATTICE EFFECTS IN VAPOR TRANSPORT GROWTH OF VANADIUM
DIOXIDE MICROCRYSTALS

2.1 Publication Citation

It is reproduced here, with minor formatting changes, with the permission of all authors and the
publisher.

2.2 Abstract

Vapor-phase transport is a rapid, inexpensive method of growing nano- and micro-scale
single crystals of vanadium dioxide, a correlated-electron material with a metal-insulator-
transition at ~70°C. Many growth parameters—including time, temperature, precursor, ambient
conditions, and substrate—have been explored, and a variety of crystal morphologies has been
produced, with most emphasis given to oriented nanowires. However, a comprehensive strategy
for predicting/controlling the crystal morphology is still evolving. Here, we investigate the role
of the substrate in platelet growth, highlighting three important types of interactions: chemical
reactions at the surface, lattice matching effects, and surface energy. We present results on four
different cuts of sapphire (Al_2O_3) and three of yttria-stabilized zirconia (YSZ) to differentiate the
roles of these mechanisms. Each has significant effects; chemical reactions leading to Al-doped
VO_2 on Al_2O_3 and formation of YVO_4 on YSZ, lattice match producing preferred orientations on
both, and high surface energy promoting growth of larger microcrystals. We suggest a
framework for relating crystal morphology, orientation and doping to substrate properties, in
order to use intentional choice of substrate to engineer the size, shape, orientation, and strain
state of VO_2 single crystals, a crucial step toward realizing VO_2-crystal-based devices.

2.3 Introduction

Vanadium dioxide (VO_2) remains among the most promising reconfigurable materials [1-6]
with tunable optical and electrical properties. Its first-order phase transition from an insulating
monoclinic phase (M1) to a metallic rutile phase (R) is accompanied by an orders-of-magnitude
change in resistivity, sharp change in optical constants, and ~1% change in lattice strain
(shrinking along the c_R-axis, expanding normal to it, see Supporting Information, section *a*,

Figure S1 and Table S1). This phase transition occurs at the readily-accessible temperature of ~70°C and can be initiated optically on a femtosecond timescale;[7] moreover, its critical temperature (T_c) and hysteretic response can be tuned via local strain, particle size, and doping, [8] increasing its versatility. VO_2 has been employed in sundry devices, from passive thermal control coatings[9] to ultrafast photonic modulators[10] and the complex physics underlying the phase transition—the role of the structural vs. the electronic transition and the difference between thermal and optical excitation—have made it an ideal subject in the study of correlated-electron materials.[2]

Bulk VO_2 single crystals—while less robust and less viable for large-scale applications than thin films—offer high crystalline quality, smooth faceted faces, and, in the absence of substrate strain, sharp, single-domain switching. When subject to strain, VO_2 single crystals exhibit ferroelasticity, with strain-sensitive twin domains that form additional nucleation sites for the phase transition[11] and generate complex patterns of coexisting of metallic and insulating domains.[12] A broad range of applications requiring single-crystal VO_2 have been proposed or demonstrated. Nanowires have been used for nano-actuators, tiny optically-readable thermometers, nanoscale gas sensors, thermal rectifiers, and more.[4] Microplatelets have received less attention, but proved to be an ideal platform to demonstrate reconfigurable index-based control of hyperbolic phonon-polaritons in hexagonal boron nitride.[13]

The sensitivity of the VO_2 phase transition to so many factors—size and shape, strain state, dopants, and crystals defects—and the variety of potential applications, each with its own specific requirements, necessitate the development of growth techniques that can engineer VO_2 crystals to have desired properties. In the last two decades, vapor transport methods have gained popularity as a way to produce high-quality nano- and micro-scale crystals at low cost and in a short time.[11, 14-28] Numerous growth parameters—including time, temperature, precursors, ambient conditions, and substrate—constitute a set of potential tools for tailoring the resulting crystals. The choice of growth substrate, in particular, has been shown to affect crystal size, shape, and orientation (see Supporting Information, section *b* and Table S2 for a detailed review of the growth substrates investigated heretofore and their effects). These effects can broadly be separated into two groups: those arising due to lattice match, and those arising from chemical reactions between the substrate and VO_2 precursor materials. The former have received by far the most attention, and have been exploited to produce highly oriented nanowires of several varieties, while the latter, though not unknown,[26, 29] are often overlooked.

In this paper, we explore the possibilities for substrate-driven engineering of vapor-transport-grown VO_2 single crystals, highlighting the importance of surface energy and chemical reactions at the V_2O_5/substrate interface, in addition to the lattice matching effects which have already begun to be exploited. We show that Al-doping occurs in VO_2 crystals grown on the commonly-used substrate Al_2O_3, and go on to identify the lattice-match conditions which lead to preferred orientations on four different Al_2O_3 surface planes. We further add to the library of VO_2-crystal-growth substrates by introducing YSZ, showing again the effects of chemical reactions and lattice match. Finally, comparing the growth habits of platelet-like and wire-like VO_2 crystals, our results suggest that strong lattice match disfavors the growth of crystals with low in-plane aspect ratios, while high surface energy favors the growth of large-area crystals, often with low aspect ratios. Choice of substrate is a powerful but complex tool for designing VO_2 crystals, with surface energy, lattice matching, and chemical effects acting in concert to determine important properties of the resulting crystals.

2.4 Experimental Section

Single crystals of VO$_2$ were grown by the vapor-phase transport method. Vanadium pentoxide (V$_2$O$_5$) powder (Sigma-Aldrich, ≥99.6% trace metal basis) was loaded into one end of a quartz boat (100 mm x 17 mm x 10 mm, MTI) encrusted with a coat of vanadium oxide crystals from previous growths. Growth substrates were placed in the boat at varying distances from the precursor powder, tilted relative to the horizontal by leaning against the side of the boat (see Supporting Information, section *c*, Figure S2 for an image of the prepared boat before and after growth). Two filled boats were placed end-to-end inside a small quartz tube (235 mm x 26 mm dia.), which was then centered in a quartz tube furnace (Lindberg Blue M) at room temperature. The tube was evacuated with a vacuum pump and Ar gas was flowed at 25 sccm to achieve a stable pressure of 1.7 torr. Flow direction was from precursor toward substrates. The furnace was heated to 810°C, held at that temperature for 1-4 hrs., and allowed to cool back to room temperature. As the temperature ramps up, the precursor melts and the gas flow carries resulting vanadia vapor to the substrates. Holding the system at a high temperature allows VO$_2$ to grow through a droplet assisted growth mechanism. Droplets of melted precursor condense onto the substrate, out of which VO$_2$ wires crystallize.[16, 19, 26]

Substrates, listed in Table 1, were purchased from MTI as wafers or pre-cut chips, all polished on both sides. Wafers were cut into chips using a dicing saw or manually cleaved with a diamond scribe. Substrates were used as-received from the supplier without additional cleaning, as we found that cleaning had no significant effect on growth results.

Table 2.1: Substrates used in this work			
Substrate	**Formula**	**Orientation**	**Wafer Size**
Quartz	SiO$_2$	z-cut (0001)	100 mm diameter x 0.5 mm
Sapphire	Al$_2$O$_3$	c-cut (0001)	100 mm diameter x 0.65 mm
		r-cut (1$\bar{1}$02)	2" diameter x 0.5 mm
		a-cut (11$\bar{2}$0)	10x10x0.5 mm
		m-cut (10$\bar{1}$0)	10x10x0.5 mm
YSZ	ZrO$_2$:Y$_2$O$_3$ (92:8)	(100)	10x10x0.5 mm
		(111)	10x10x0.5 mm
		(110)	10x10x0.5 mm

Polarized optical microscopy was used to image the crystals and the ferroelastic twins. A Raman microscope (Thermo Scientific DXR, 532 nm) was used to distinguish the phases of VO$_2$ and to identify other species formed during growth. An x-ray diffractometer (XRD) (Rigaku Smart Lab, Cu Kα source) was used to perform standard θ-2θ measurements (scan 2θ from 20°-100°, 0.01° steps, 10 °/min) and pole figure measurements (fix 2θ, scan α 0°-90° in 1° or 3° steps, scan β 0°-360° in 1° or 3° steps at 60 °/min or 150 °/min) to identify out-of-plane and in-plane crystal orientations, respectively. Energy dispersive spectroscopy (EDS) measurements were carried out with a scanning electron microscope (SEM, Zeiss Merlin with Gemini II

column) at 20kV, 3nA, and a working distance of 8.5mm. Elemental analysis was performed with proprietary Oxford Instruments AZtec software.

2.5 Results and Discussion

The following experimental results are divided into three subsections—considering first the chemical and lattice-match effects of sapphire substrates, then those of yttria-stabilized zirconia (YSZ), and lastly comparing the crystal sizes and growth habits across different substrates. Raman spectroscopy shows that VO_2 crystals grown on sapphire are in the M2 phase, and EDS (Figure 1) shows the presence of Al-dopants. Pole figure measurements (Figure 2) allow determination of crystal orientation and lattice-matching with the substrate (Table 2), including an orientation on c-cut (Figure 3) that is different (with better lattice match) than has been previously reported. Likewise, Raman spectra indicate the presence of ZrO_2 and YVO_4 on YSZ substrates after growth, and pole figures show preferred orientation (Figure 4). Comparison of crystal size across substrates (Figure 5) shows that maximum crystal size tends to increase with substrate surface energy.

2.5.a Growth on Sapphire

We examine VO_2 crystal growth on the following different cuts of sapphire (Al_2O_3): c-(0001), r- ($1\bar{1}02$), a- ($11\bar{2}0$), and m-cut ($10\bar{1}0$). Among typical VO_2 substrates, sapphire provides a good lattice match—domain-matching epitaxy of thin films on c-cut sapphire is well established,[30] and epitaxial single crystals have been observed on c-, r-, a-, and m-cuts. Titanium dioxide (TiO_2) would offer a still better lattice match, but lower cost has rendered Al_2O_3 a common growth substrate, making its often-overlooked Al-doping (see discussion below) a relevant issue. This, and a better-characterized surface energy, make sapphire of interest for this study.

On all the sapphire substrates, the vast majority of VO_2 crystals (30 out of 34 sampled) are in the secondary monoclinic phase (M2) at room temperature, rather than the typical M1. Figure 1a compares Raman spectra from a representative VO_2 crystal grown on sapphire above (M2-phase, yellow curve) and below (T-phase, red curve) room temperature to that of a crystal grown on quartz at room temperature (M1-phase, blue curve). It is well known that tensile strain along the c_R axis,[31] or compressive strain normal to it[32] can stabilize the M2 phase, and some reports observing M2-phase crystals on sapphire substrates have attributed this to substrate-induced strain.[33-34] However, the M2 phase can also be stabilized by Al-doping,[29] and molten vanadia is known to be corrosive to refractory oxides, including Al_2O_3.[35-37] Moreover, Nag *et al.* found that VO_2 films made with pulsed laser deposition (PLD) at high temperatures (~500°C) show a thin interlayer of nonstoichiometric Al, V and O,[38] and Strelcov *et al.* have intentionally doped VO_2 crystals with Al by growing them on a thin film of Al_2O_3.[29] To determine which of the two mechanisms (strain or doping) is primarily responsible, we analyzed Raman spectra from a VO_2 crystal after removing it from the substrate with flexible adhesive tape. Thus freed from substrate strain, the crystal remained in the M2-phase, supporting the idea that doping is responsible for stabilizing this phase in our samples. As further confirmation, EDS measurements (Figure 1b) demonstrate the presence of Al in another VO_2 crystal removed from its substrate in the same manner.

We conclude that during the growth process, a small amount of the Al_2O_3 substrate is dissolved into molten vanadia droplets, and a small fraction of Al atoms is incorporated into the VO_2 lattice as it crystallizes from the droplet. We also note that etch pits appeared in many of the sapphire substrates after growth, which we attribute to the corrosive action of molten vanadia on the substrate (Supporting Information, section *d*, Figure S3).

Figure 2.1. VO_2 crystals grown on sapphire are in the M2-phase at room temperature due to Al-doping. a) Raman spectra comparing a VO_2 crystal grown on sapphire, above (yellow) and below (red) the M2-T phase transition, to an M1-phase VO_2 crystal grown on quartz. b) EDS spectrum showing Al-doping of a crystal grown on sapphire.
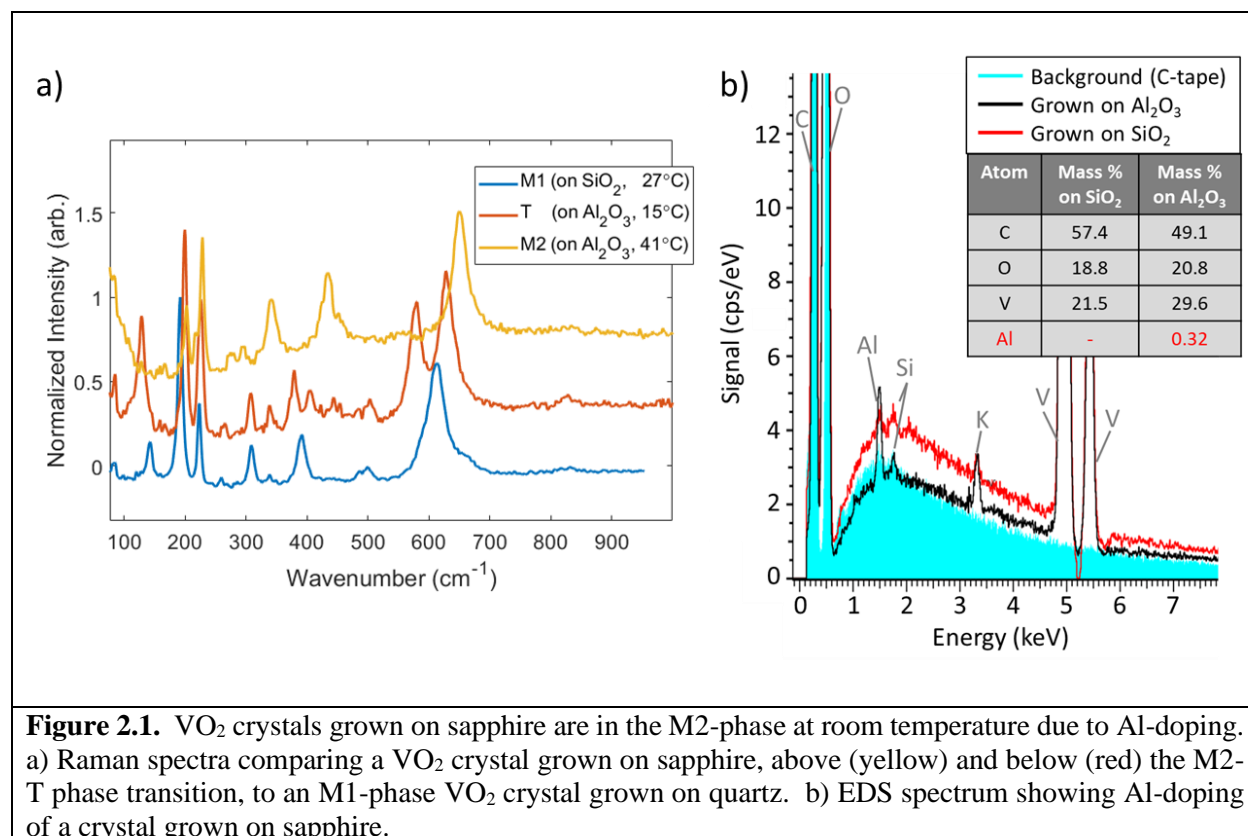
While the orientation of the substrate does not seem to affect the doping and room-temperature phase of the crystals, it has a drastic impact on the morphology and orientation of the crystals. Figure 2 shows optical microscope images of some VO_2 crystals grown on sapphire substrates. Across multiple growth attempts on identical substrates, and even across a given sample, a variety of crystal sizes, shapes, and orientations can be observed; but on all substrates, these crystals can broadly be grouped into two categories: crystals exhibiting a preferred orientation relative to each other and the substrate, and crystals with seemingly random orientation. The former (exemplified in Figure 2) tend to be fairly uniform on a given substrate, to be long and narrow in shape, and to have facets non-parallel to the substrate surface, with cross-sectional shape determined by lattice orientation and energetically-favored bounding facets. The latter (see Supporting Information, section *e*, Figure S4) are more varied in shape, size, and orientation, but tend to have lower aspect ratios and to lie flat with their largest facets parallel to the substrate surface.

Figure 2.2. Microscope images of VO₂ crystals on the four sapphire cuts illustrate the preferred orientation of crystal growth. Insets (upper): XRD pole figures show preferred orientation on all four samples. Insets (lower): diagrams illustrating crystal lattice orientation of epitaxial crystals, shown with typical $(001)_R$ growth axis and $(110)_R$ side facets.
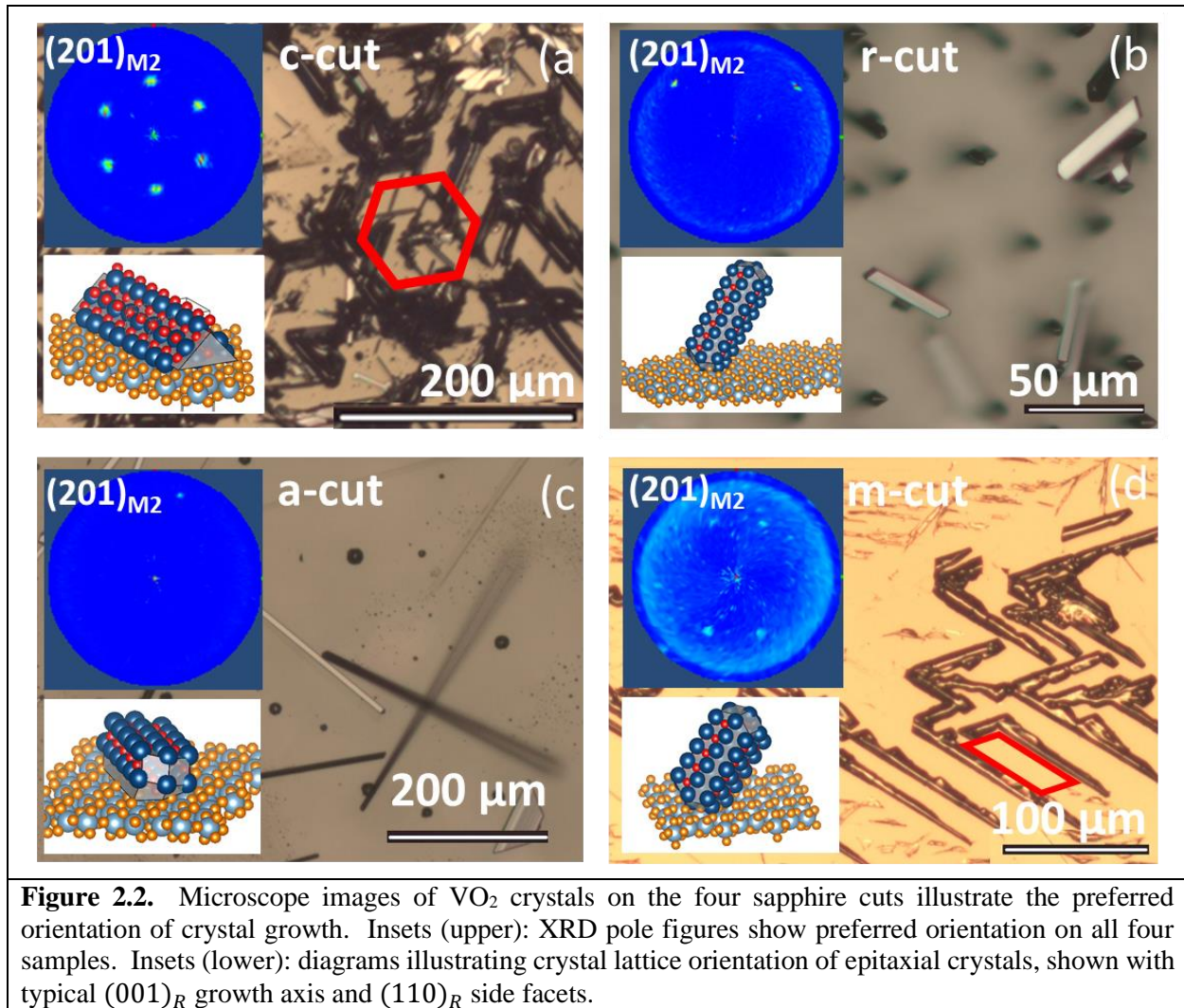
Powder XRD pole figure measurements provide a quantitative measurement of the orientations of a given crystalline plane in a sample; in our case, not for an individual single crystal, but of all the crystals on a sample in aggregate. The upper insets in Figure 2 show pole figures for the $(201)_{M2}$ plane—equivalent to the $(110)_R$ or $(01\bar{1})_{M1}$ planes in other phases— which is usually the favored plane for side-facets of VO₂ crystals.[27] Comparing the four pole figures in Figure 2, it is noticeable that they all have in common a peak at the center of the figure, corresponding to the normal to the substrate. This indicates that all of the samples have some VO₂ crystals with their $(201)_{M2}$ planes parallel to the substrate surface. These can be identified with the less-uniform, flat-lying, lower-aspect-ratio crystals present in all the samples, as noted above. Apart from this common central peak, each substrate presents a unique pattern corresponding to the preferred orientations of VO₂ crystals on that substrate. On c-cut sapphire (Figure 2a), a six-fold symmetry is evident, arising from the six-fold symmetry of the c-plane in the hexagonal sapphire lattice. On m-cut, likewise, a clear two-fold symmetry emerges from the two-fold symmetry of the substrate. Interestingly, the two-fold rotational symmetries of the a- and r-planes are not reflected in the corresponding VO₂ pole figures—it may be that asymmetry in the growth conditions (tilted sample and unidirectional vapor flow) caused one orientation to

be preferred, or that random fluctuations and sparse coverage resulted in one orientation occurring so infrequently as to be lost in noise. The different orientations determined for each substrate (see discussion below) are illustrated in the lower insets in Figure 2, assuming the energetically favorable $(001)_R$ growth axis and $(110)_R$ side facets.

Figure 2.3: Orientation analysis for VO$_2$ crystals grown on c-cut sapphire. (a) Pole figures for the $\{201\}_{M2}$ and $\{104\}_{Al_2O_3}$ sets of planes show their respective orientations and symmetries. Taking a circle cut (constant-α, panel b) or a line cut (constant-β, panel c) shows the in-plane orientation or out-of-plane tilt, respectively. A closer look at the $\{201\}_{M2}$ data (panel b, inset) reveals that each peak is split by ~6° in β. This data allows quantitative determination of the relative orientations of the VO$_2$ and Al$_2$O$_3$ lattices (d).

By comparing these pole figures for VO$_2$ crystal planes to similar ones for the substrate planes, it is possible to determine the preferred orientation(s) of the VO$_2$ crystals relative to the substrate lattice. Figure 3 details such an analysis for crystals grown on c-cut sapphire (corresponding analysis for other substrates is found in the Supporting Information, section *f*, Figures S5-S7 and Table S3). For simplicity, from this point forward we reference the VO$_2$ crystals planes according to the equivalent planes of the R-phase, since this is the phase of the crystals during growth, and thus the phase relevant for lattice-match considerations affecting the growth. The pole figure (Figure 3a) for $\{110\}_R$ has a peak at $\alpha = 90°$ ($\{110\}_R$ parallel to substrate) and six at $\alpha = 45°$ ($\{100\}_R$ parallel to substrate) and $\beta = 3° + n(60°)$ (n=0,1,2,3,4,5), the six-fold symmetry reflecting the hexagonal lattice of the $\{0001\}_{Al_2O_3}$ plane. A pole figure for $\{10\bar{1}4\}_{Al_2O_3}$ on the same sample has three peaks at $\alpha = 52°$ and $\beta = 33° + n(120°)$ (n=0,1,2), as expected for these planes relative to $\{0001\}_{Al_2O_3}$. Comparing these, the $\{110\}_R$ planes appear with $\Delta\beta = \pm90°$ relative to $\{10\bar{1}4\}_{Al_2O_3}$, consistent with the orientation $\{010\}_R \parallel \{11\bar{2}0\}_{Al_2O_3}$ (Figure 3d, left), which is equivalent to that reported in previous studies on single crystals[25] and thin films.[39] However, looking more closely at the $\{110\}_R$ pole figure (Figure 3b), it appears that each peak is split into two, with a separation of ~6° in β. This can be explained if instead $\{011\}_R \parallel \{11\bar{2}0\}_{Al_2O_3}$ (Figure 3d, right), the 6° splitting arising because $\{011\}_R$ are separated from $\{010\}_R$ by $\pm57°$ as noted in one study on thin films.[40] Moreover, we find that this orientation yields better lattice match (see Table S2): 0.6% (-3.2%) mismatch normal (parallel) to the matched plane, as opposed to 3.7% (-5.2%) for the conventional orientation. The results

of orientation analysis on other cuts of Al_2O_3, including lattice mismatch calculations, are summarized in Table 2. Except on a-cut, (see discussion accompanying Supporting Information, Figure S7) the crystallographic orientation is derived from multiple peaks in the XRD pole figures for both $\{201\}_{M2}$ and $\{220/021\}_{M2}$ sets of planes, guaranteeing a unique orientation. Lattice mismatch is calculated by finding the percent difference between matched plane spacings (or lattice vector lengths) d, with VO_2 crystallographic parameters drawn from the literature.[41]

Al$_2$O$_3$ Cut	Crystal Orientation	Lattice Mismatch $(\frac{d_R - d_{Al_2O_3}}{d_{Al_2O_3}})$	d_R (Å)	$d_{Al_2O_3}$ (Å)
c-cut $\{0001\}$	$\{100\}_R \parallel \{0001\}_{Al_2O_3}$ $\{011\}_R \parallel \{11\bar{2}0\}_{Al_2O_3}$	Normal to matched plane: 0.6 %	$\{01\bar{1}\}_R$: $(2.42) \times 1$	$\{11\bar{2}0\}_{Al_2O_3}$: $(2.40) \times 1$
		Along matched plane: -3.2%	$\langle 01\bar{1}\rangle_R$: $(5.37) \times 3$	$\langle 10\bar{1}0\rangle_{Al_2O_3}$: $(8.32) \times 2$
r-cut $\{1\bar{1}02\}$	$\{011\}_R \parallel \{1\bar{1}02\}_{Al_2O_3}$ $\langle 100\rangle_R \parallel \langle 1\bar{2}10\rangle_{Al_2O_3}$	Along matched vector: -5.2%	$\langle 100\rangle_R$: $(4.55) \times 1$	$\langle 1\bar{2}10\rangle_{Al_2O_3}$: $(4.81) \times 1$
		Normal to matched vector: 3.7%	$\langle 01\bar{1}\rangle_R$: $(5.37) \times 3$	$\langle \bar{1}01\bar{1}\rangle_{Al_2O_3}$: $(15.53) \times 1$
a-cut $\{11\bar{2}0\}$	$\{210\}_R \parallel \{11\bar{2}0\}_{Al_2O_3}$ $\langle 1\bar{2}3\rangle_R \parallel \langle 0001\rangle_{Al_2O_3}$	Along matched vector: 1.4%	$\langle 1\bar{2}3\rangle_R$: $(13.30) \times 1$	$\langle 0001\rangle_{Al_2O_3}$: $(13.12) \times 1$
		Normal to matched vector: -1.6%	$\{30\bar{1}\}_R^\dagger$: $(2.18) \times 5$	$\{2\bar{1}\bar{1}0\}_{Al_2O_3}^\dagger$: $(2.77) \times 4$
m-cut $\{10\bar{1}0\}$	$\{031\}_R \parallel \{10\bar{1}0\}_{Al_2O_3}$ $\langle 100\rangle_R \parallel \langle 0001\rangle_{Al_2O_3}$	Along matched vector: 4.2%	$\langle 100\rangle_R$: $(4.55) \times 3$	$\langle 0001\rangle_{Al_2O_3}$: $(13.12) \times 1$
		Normal to matched vector: 0.8%	$\langle 0\bar{1}3\rangle_R$: $(9.69) \times 1$	$\langle 1\bar{2}10\rangle_{Al_2O_3}$: $(4.81) \times 2$

Table 2.2: Observed orientation and calculated lattice match for VO_2 crystals grown on various cuts of sapphire

† These planes are not normal to the substrate surface, so the lattice match condition relates to the period of their *intersections* with the substrate plane, equal to $d/\sin(\theta)$ where θ is the angle between the plane and the surface.

2.5.b Growth on YSZ

Yttria-stabilized zirconia (YSZ) is a form of zirconia (ZrO_2) stabilized in its cubic phase by doping with yttria (Y_2O_3). Ceramic YSZ is of interest as a refractory material for solid-oxide fuel cells, high-temperature turbine coatings, and nuclear reactor fuel matrices,[42] and erbium-doped single-crystal YSZ has been used for up-conversion luminescence.[43] YSZ thin films have been used as a buffer layer to grow epitaxial VO_2 films on Si substrates,[44] suggesting that the YSZ and VO_2 lattices may be close enough to result in preferred orientation.

After a growth on YSZ, the entire substrate (initially transparent) is covered with a dark film, as well as assorted VO_2 crystals (Figure 4a). Analysis of this dark film with Raman spectroscopy (Figure 4b, blue curve) clearly shows peaks belonging to yttrium vanadate (YVO_4, red curve) and zirconia (ZrO_2, yellow curve). At high temperatures, YSZ is known to become unstable, tending to form yttria-rich and yttria-poor domains;[45] moreover, near 800°C, vanadia is known to react with yttria in YSZ to form yttrium vanadate,[46-47] as we observe. By removing VO_2 crystals from the substrate with adhesive tape, it is observed that the layer of YVO_4/ZrO_2

underlies the VO_2 crystals (Supporting Information, section *g*, Figure S8). From this, and the uniformity of the YVO_4/ZrO_2 layer, we hypothesize that, rather than forming individual droplets, molten vanadia completely wets the YSZ surface during growth and reacts with the substrate; VO_2 crystals then grow atop the resulting YVO_4 layer. The VO_2 crystals grown thus tend to be large (tens to hundreds of micrometers in width), which we attribute to the aforementioned surface wetting, and to have rough surfaces, as seen in the optical micrographs (Figures 4a, c-e). All the crystals sampled are in the usual M1 phase at room temperature.

Figure 2.4: (a) Microscope image of VO_2 crystals grown on YSZ, and a dark film covering the substrate. (b) Raman spectra of the background film after growth (blue) show it to be composed of YVO_4 (red) and ZrO_2 (yellow). (c-e) Microscope images of VO_2 crystals grown on the three YSZ cuts investigated suggest preferred orientation, confirmed by XRD pole figures (insets).
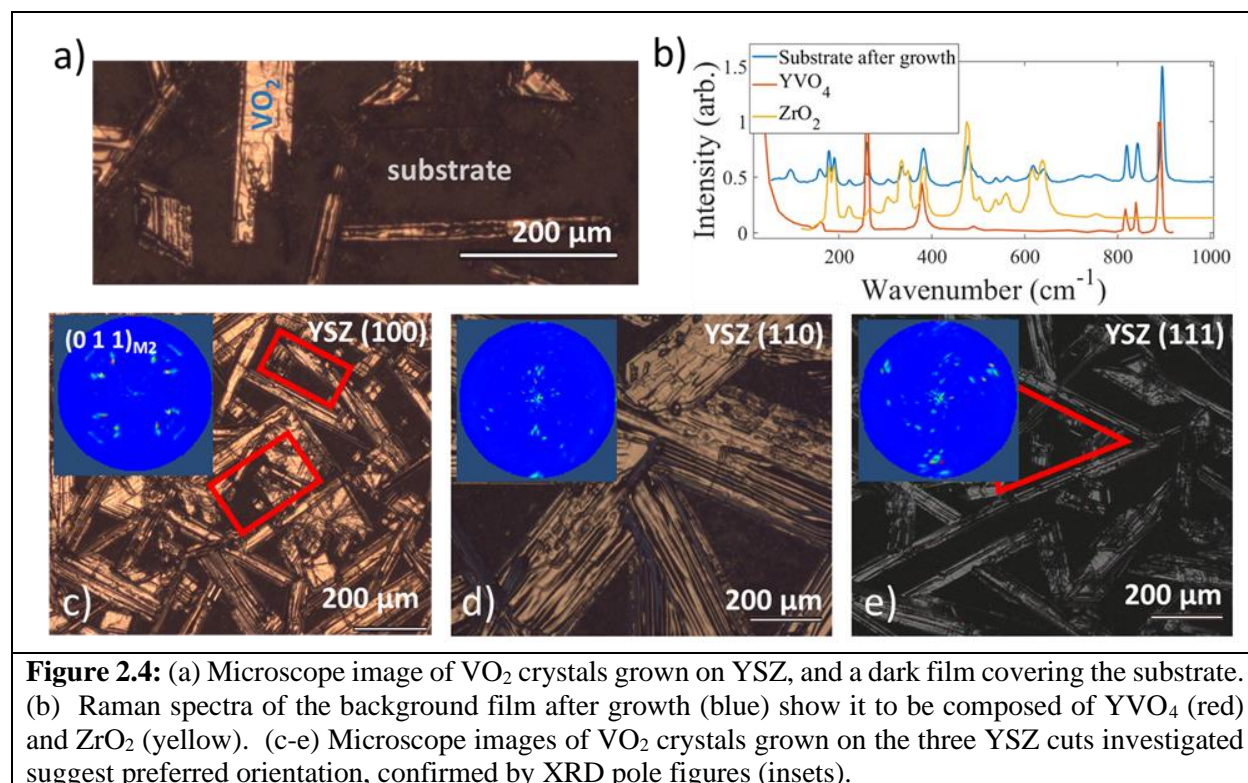
On each of the three cuts of YSZ, there is clear evidence of preferred orientation. While none of these grow out-of-plane (as on some cuts of sapphire), the in-plane growth axis $(001)_R$ tends to orient along certain directions, causing groups of crystals to form rectangular or triangular patterns (Figure 4c-e). Pole figures confirm this qualitative observation, showing distinct and complex patterns with 4-fold, 2-fold, and 3-fold symmetry reflecting the respective symmetries of the (100), (110), and (111) planes of cubic YSZ. Determining a definite lattice-match relation to the substrate, however, is complicated by the fact that a layer (or layers) of YVO_4 and ZrO_2 lies between the VO_2 crystals and the substrate. Pole figure measurements for distinctive planes of these materials (Supporting Information, section *h*, Figure S9) show that they, too, have definite preferred orientations relative to the underlying YSZ. This suggests that the situation is one of multilayer heteroepitaxy, where the lower-symmetry YVO_4 and ZrO_2 may have multiple distinguishable orientations relative to the higher-symmetry substrate, leading to the complex peak-splitting patterns observed for VO_2. A full analysis of the orientation and lattice mismatch of each layer is beyond the scope of this paper.

2.5.c Substrate Effects on Nanowire/Microplatelet Size
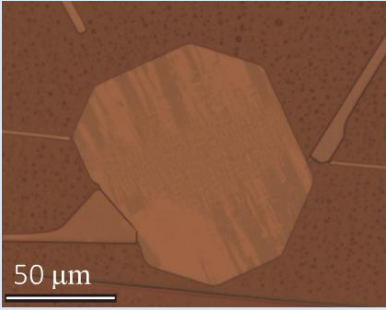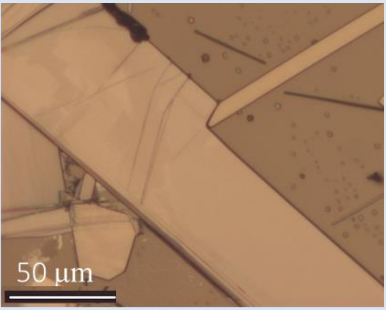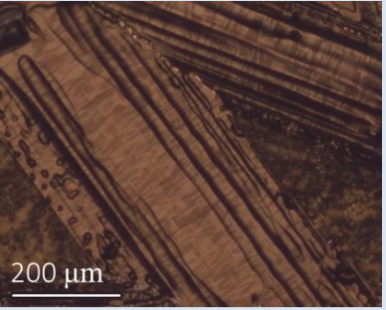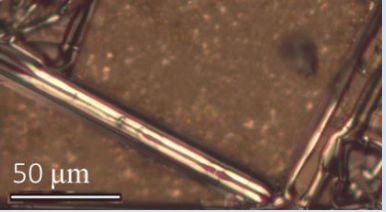
	(a) Qtz	(b) Al₂O₃	(c) YSZ
Platelets	50 µm	50 µm	200 µm
Wires	20 µm	20 µm	50 µm
γ	0.18 J/m² [48]	0.80 J/m² [49]	1.46 J/m² [50]

Figure 2.5: Examples of platelet- and wire-shaped VO$_2$ microcrystals. The platelets shown are representative of the largest we have produced. On every substrate, both morphologies are observed, with a range of sizes; but the largest crystals on sapphire tend to be slightly larger than those on quartz, while the crystals on YSZ far exceed either of the others in size. This size ordering follows the surface energies (γ) of the substrates (extrapolated to 810°C). Note the different scale bars in each image.

The size and aspect ratio of VO$_2$ crystals are affected by growth conditions (time, temperature, pressure, precursor), but are difficult to precisely control. Generally, increasing the flux of precursor vapor (by increasing the amount of precursor or placing samples closer to the precursor source) will result in larger crystals with a lower aspect ratio, and vice-versa. Though we have attempted to optimize for the growth of larger crystals, the resulting crystal sizes vary drastically due to variables such as sample orientation, residual precursor, or stochastic precursor droplet aggregation. Our results emphasize that the substrate also strongly affects whether high-aspect-ratio nanowires or low-aspect-ratio microplatelets are preferred (Figure 5). On quartz (Figure 5a), both forms are observed, often coexisting on the same sample (see Supporting Information, section *i*, Figure S10 for a discussion of the crystal growth results on quartz). Which predominates is somewhat random, but strongly affected by the growth parameters. The largest crystals are often in excess of 50 by 50 µm. On sapphire (Figure 5b), nanowires and microplatelets (in some cases even larger than any seen on quartz) are again observed to coexist; but, as noted above, the nanowires tend to exhibit preferred orientation and to have facets non-parallel to the substrate (with some exceptions, nanowires with parallel and non-parallel facets can both be seen in Figure 5b), while the microplatelets (like those on quartz) seem to have no preferred orientation in-plane and always have facets parallel to the substrate. The former is attested in the literature, with most studies of epitaxial VO$_2$ crystals on sapphire exhibiting

nanowire growth; the latter have not been reported. This suggests that epitaxy on sapphire disfavors low-aspect ratio growth, presumably because the increased contact area increases the total amount of lattice mismatch strain; whereas those crystals which form without epitaxy are free from this constraint, much like those that grow on a substrate with no lattice matching. Crystals grown on YSZ, on the other hand (Figure 5c), tend to be larger with a low aspect ratio. Most of these crystals are larger than on any other substrate we investigated, and a few are larger than any yet reported to be grown by vapor-transport methods, in excess of 1mm in length.

In addition to chemical reactions and lattice matching effects, a third interaction is likely to play a strong role in determining the crystal morphologies that are possible on a given substrate: surface/interface energies and the wettability of the substrate by molten V_2O_5. This will affect the size and shape of precursor droplets, and thus also the resulting crystals. Figure 5 presents representative surface energies (where available) for the different substrates used in this study. It is noteworthy that the surface energy increases in the order $\gamma_{qtz} < \gamma_{Al_2O_3} < \gamma_{YSZ}$, the same order followed by maximum microcrystal size. This suggests that substrate surface energy is a key factor in determining the size of VO_2 crystals grown by this method: greater surface energy leads to better wetting by V_2O_5 precursor, which in turn results in larger V_2O_5 droplets, more substrate coverage, and, ultimately, larger crystals. We consider this a topic well worth further investigation, hypothesizing that for the growth of large-area microplatelets, high surface energy is more important than good lattice match.

2.5.d Summary of Experimental Results

Lattice-matching effects result in preferred orientation on all cuts of sapphire and YSZ, though non-oriented crystals also appear in most cases. On sapphire, at least, it appears that oriented crystals are more likely than their non-oriented counterparts to have high aspect ratios, which we attribute to the effects of lattice-induced strain. On YSZ, preferred orientation arises from multilayer heteroepitaxy, with highly-oriented ZrO_2/YVO_4 lying between VO_2 and the substrate. Chemical effects also play a prominent role, though they have received less attention heretofore. Molten vanadia can be highly reactive, even with refractory oxides like Al_2O_3 and YSZ. On Al_2O_3 substrates, this results in etching of the substrate and Al-doping of the VO_2 crystals; this doping, rather than substrate-induced strain, is primarily responsible for these crystals relaxing to the M2, instead of the M1, phase when cooled to room temperature. On YSZ substrates, YVO_4 is formed at the substrate surface, forming a lattice-matched buffer layer between the substrate and VO_2, and representing (to the best of our knowledge) a novel method for the growth of YVO_4 films. We have also identified a third possible mechanism of substrate influence—its wettability by molten vanadia. Substrates with higher surface energies tend to grow larger crystals because the precursor vapor can more fully wet the substrate surface. This may also have an impact on the crystal morphology, and is a ripe area for further study.

2.6 Conclusions

After over sixty years of research, a great deal of progress has been made in the fabrication of high-quality VO_2, but as its phase-transition behaviors are so exquisitely sensitive to its crystallite size, grain boundaries, dopants, strain states, and lattice defects, the ability to finely control its morphology is critical. Single crystal VO_2, while offering a better platform to study its bulk properties and enabling device architectures difficult or impossible to achieve with

thin films, are still hard to produce controllably and to reproduce consistently. Some progress has been made in the growth of highly-uniform, oriented nanowires; but large, low-aspect-ratio crystals suitable for optical experiments or 2D-material platforms are harder to obtain.

Figure 2.6: Schematic diagram depicting the different substrate properties that affect VO_2 crystal growth. Effects observed in this study are marked in white, those predicted for TiO_2 (an example case) in red.
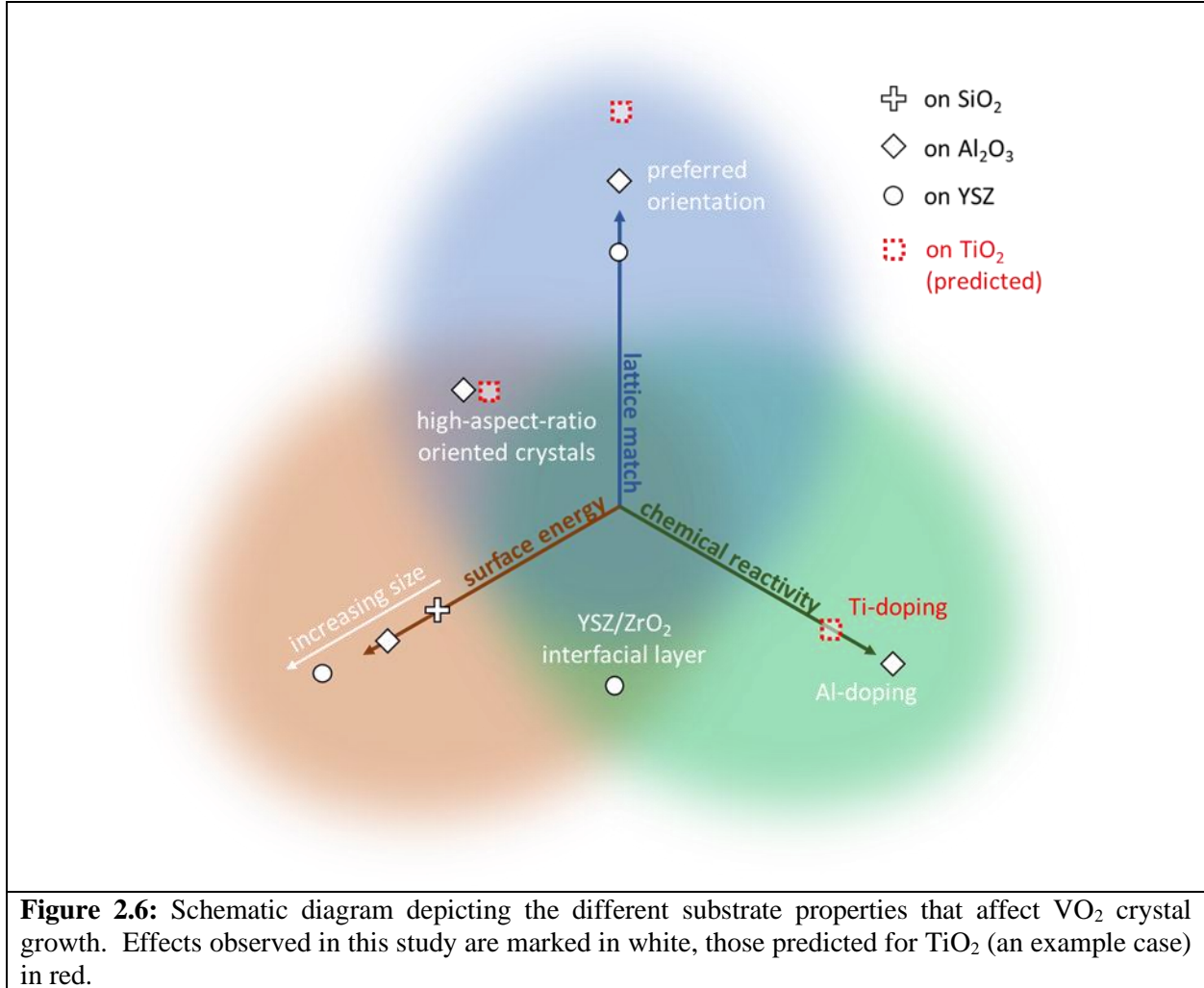
Among the dizzying array of growth parameters that can be tuned to influence crystal growth, choice of substrate is a simple but powerful tool to engineer crystal morphology, as has been shown with lattice-match-oriented nanowires. Based on our results and a survey of other studies, we suggest a three-fold paradigm for evaluating substrates to be used in VO_2 crystal growth (illustrated in Figure 6)—lattice match, which affects orientation, shape, and aspect ratio; chemical reactions with molten V_2O_5, which can result in doping of VO_2, changes to the substrate surface, or generation of interfacial species; and surface energy, which affects wetting of the surface by V_2O_5 precursor and thus the size and substrate coverage of VO_2 crystals.

Applying this paradigm can help to predict the results of VO_2 crystal growth, identify otherwise hard-to-find effects (such as small doping concentrations), and, ultimately, identify substrates likely to yield desired crystal properties. For example, TiO_2 is generally considered

the ideal substrate for epitaxial VO_2 growth, due to its rutile crystal structure and excellent lattice match with VO_2 (see Supporting Information, section *j*, Table S4). We would expect that to result in highly-oriented, high-aspect-ratio crystals, as have indeed been observed.[26-27] Additionally, there is potential for a slight amount of Ti-doping; and though studies on TiO_2 surface energy are few, there is evidence that V_2O_5 wets the surface well (see discussion in the Supporting Information, section *j*). Or, for yet another example, we predict that the growth of large, low-aspect ratio crystals would be favored by substrates with high surface energy, low reactivity with VO_2, and little or no lattice match to VO_2. We anticipate that these considerations will help to guide further advancements in VO_2 crystal growth and engineering.

2.7 Acknowledgements

2.8 References

1. Dai, S.; Tymchenko, M.; Yang, Y.; Ma, Q.; Pita-Vidal, M.; Watanabe, K.; Taniguchi, T.; Jarillo-Herrero, P.; Fogler, M. M.; Alù, A.; Basov, D. N., Manipulation and Steering of Hyperbolic Surface Polaritons in Hexagonal Boron Nitride. *Advanced Materials* **2018,** *30* (16), 5.
2. Zebo, Z.; Jianing, C.; Yu, W.; Ximiao, W.; Xiaobo, C.; Pengyi, L.; Jianbin, X.; Weiguang, X.; Huanjun, C.; Shaozhi, D.; Ningsheng, X., Highly Confined and Tunable Hyperbolic Phonon Polaritons in Van Der Waals Semiconducting Transition Metal Oxides. *Advanced Materials* **2018,** *30* (13), 1705318.
3. Shao, Z. W.; Cao, X.; Luo, H. J.; Jin, P., Recent progress in the phase-transition mechanism and modulation of vanadium dioxide materials. *NPG Asia Mater.* **2018,** *10*, 851-605.
4. Shi, R.; Shen, N.; Wang, J. W.; Wang, W. J.; Amini, A.; Wang, N.; Cheng, C., Recent advances in fabrication strategies, phase transition modulation, and advanced applications of vanadium dioxide. *Appl. Phys. Rev.* **2019,** *6* (1), 27.
5. Liu, M.; Sternbach, A. J.; Basov, D. N., Nanoscale electrodynamics of strongly correlated quantum materials. *Reports on Progress in Physics* **2017,** *80* (1), 014501.
6. Yang, Z.; Ko, C. Y.; Ramanathan, S., Oxide Electronics Utilizing Ultrafast Metal-Insulator Transitions. In *Annual Review of Materials Research, Vol 41*, Clarke, D. R.; Fratzl, P., Eds. Annual Reviews: Palo Alto, 2011; Vol. 41, pp 337-367.
7. Wegkamp, D.; Stahler, J., Ultrafast dynamics during the photoinduced phase transition in VO_2. *Prog. Surf. Sci.* **2015,** *90* (4), 464-502.
8. Nag, J.; Haglund, R. F., Synthesis of vanadium dioxide thin films and nanoparticles. *J. Phys.-Condes. Matter* **2008,** *20* (26), 264016.

9.   Vu, T. D.; Chen, Z.; Zeng, X. T.; Jiang, M.; Liu, S. Y.; Gao, Y. F.; Long, Y., Physical vapour deposition of vanadium dioxide for thermochromic smart window applications. *J. Mater. Chem. C* **2019,** *7* (8), 2121-2145.

10.   Hallman, K. A.; Miller, K. J.; Baydin, A.; Weiss, S. M.; Haglund, R. F., Sub-Picosecond Response Time of a Hybrid VO2:Silicon Waveguide at 1550 nm. *Advanced Optical Materials* **2021,** *9* (4).

11.   Tselev, A.; Strelcov, E.; Luk'yanchuk, I. A.; Budai, J. D.; Tischler, J. Z.; Ivanov, I. N.; Jones, K.; Proksch, R.; Kalinin, S. V.; Kolmakov, A., Interplay between Ferroelastic and Metal-Insulator Phase Transitions in Strained Quasi-Two-Dimensional VO$_2$ Nanoplatelets. *Nano Lett.* **2010,** *10* (6), 2003-2011.

12.   McGahan, C.; Gamage, S.; Liang, J. R.; Cross, B.; Marvel, R. E.; Haglund, R. F.; Abate, Y., Geometric constraints on phase coexistence in vanadium dioxide single crystals. *Nanotechnology* **2017,** *28* (8), 085701.

13.   Folland, T. G.; Fali, A.; White, S. T.; Matson, J. R.; Liu, S.; Aghamiri, N. A.; Edgar, J. H.; Haglund, R. F.; Abate, Y.; Caldwell, J. D., Reconfigurable infrared hyperbolic metasurfaces using phase change materials. *Nat. Commun.* **2018,** *9*, 4371.

14.   Cheng, C.; Guo, H.; Amini, A.; Liu, K.; Fu, D.; Zou, J.; Song, H. S., Self-assembly and horizontal orientation growth of VO$_2$ nanowires. *Sci Rep* **2014,** *4*, 5456.

15.   Cheng, C.; Liu, K.; Xiang, B.; Suh, J.; Wu, J. Q., Ultra-long, free-standing, single-crystalline vanadium dioxide micro/nanowires grown by simple thermal evaporation. *Appl. Phys. Lett.* **2012,** *100* (10), 103111.

16.   Cheng, Y.; Wong, T. L.; Ho, K. M.; Wang, N., The structure and growth mechanism of VO$_2$ nanowires. *J. Cryst. Growth* **2009,** *311* (6), 1571-1575.

17.   Guiton, B. S.; Gu, Q.; Prieto, A. L.; Gudiksen, M. S.; Park, H., Single-crystalline vanadium dioxide nanowires with rectangular cross sections. *J. Am. Chem. Soc.* **2005,** *127* (2), 498-499.

18.   Kim, I. S.; Lauhon, L. J., Increased yield and uniformity of vanadium dioxide nanobeam growth via two-step physical vapor transport process. *Cryst. Growth Des.* **2012,** *12* (3), 1383-1387.

19.   Kim, M. W.; Ha, S. S.; Seo, O.; Noh, D. Y.; Kim, B. J., Real-time structural and electrical characterization of metal-insulator transition in strain-modulated single-phase VO$_2$ wires with controlled diameters. *Nano Lett.* **2016,** *16* (7), 4074-4081.

20.   Lin, J.; Ji, H.; Swift, M. W.; Hardy, W. J.; Peng, Z. W.; Fan, X. J.; Nevidomskyy, A. H.; Tour, J. M.; Natelson, D., Hydrogen Diffusion and Stabilization in Single-Crystal VO$_2$ Micro/Nanobeams by Direct Atomic Hydrogenation. *Nano Lett.* **2014,** *14* (9), 5445-5451.

21.   Loffler, S.; Auer, E.; Weil, M.; Lugstein, A.; Bertagnolli, E., Impact of growth temperature on the crystal habits, forms and structures of VO$_2$ nanocrystals. *Appl. Phys. A-Mater. Sci. Process.* **2011,** *102* (1), 201-204.

22.   Maeng, J.; Kim, T. W.; Jo, G.; Lee, T., Fabrication, structural and electrical characterization of VO$_2$ nanowires. *Mater. Res. Bull.* **2008,** *43* (7), 1649-1656.

23.   Sidorov, A. I.; Lyubimov, V. Y.; Nashchekin, A. V., Morphological features of vanadium dioxide microcrystals grown from the gas phase. *Tech. Phys. Lett.* **2007,** *33* (11), 955-957.

24.   Sohn, J. I.; Joo, H. J.; Ahn, D.; Lee, H. H.; Porter, A. E.; Kim, K.; Kang, D. J.; Welland, M. E., Surface-stress-induced mott transition and nature of associated spatial phase transition in single crystalline VO$_2$ nanowires. *Nano Lett.* **2009,** *9* (10), 3392-3397.

25.   Sohn, J. I.; Joo, H. J.; Porter, A. E.; Choi, C. J.; Kim, K.; Kang, D. J.; Welland, M. E., Direct observation of the structural component of the metal-insulator phase transition and growth habits of epitaxially grown VO$_2$ nanowires. *Nano Lett.* **2007,** *7* (6), 1570-1574.

26.   Strelcov, E.; Davydov, A. V.; Lanke, U.; Watts, C.; Kolmakov, A., In situ monitoring of the growth, intermediate phase transformations and templating of single crystal VO$_2$ nanowires and nanoplatelets. *Acs Nano* **2011,** *5* (4), 3373-3384.

27.   Wang, L. X.; Ren, H.; Chen, S.; Chen, Y. L.; Li, B. W.; Zou, C. W.; Zhang, G. B.; Lu, Y. L., Epitaxial Growth of Well-Aligned Single-Crystalline VO$_2$ Micro/ Nanowires Assisted by Substrate Facet Confinement. *Cryst. Growth Des.* **2018,** *18* (7), 3896-3901.

28.   Wu, J. Q.; Gu, Q.; Guiton, B. S.; de Leon, N. P.; Lian, O. Y.; Park, H., Strain-induced self organization of metal-insulator domains in single-crystalline VO_2 nanobeams. *Nano Lett.* **2006,** *6* (10), 2313-2317.

29.   Strelcov, E.; Tselev, A.; Ivanov, I.; Budai, J. D.; Zhang, J.; Tischler, J. Z.; Kravchenko, I.; Kalinin, S. V.; Kolmakov, A., Doping-based stabilization of the M2 phase in free-standing VO_2 nanostructures at room temperature. *Nano Lett.* **2012,** *12* (12), 6198-6205.

30.   Narayan, J.; Bhosle, V. M., Phase transition and critical issues in structure-property correlations of vanadium oxide. *J. Appl. Phys.* **2006,** *100* (10), 103524.

31.   Cao, J.; Gu, Y.; Fan, W.; Chen, L. Q.; Ogletree, D. F.; Chen, K.; Tamura, N.; Kunz, M.; Barrett, C.; Seidel, J.; Wu, J., Extended Mapping and Exploration of the Vanadium Dioxide Stress-Temperature Phase Diagram. *Nano Lett.* **2010,** *10* (7), 2667-2673.

32.   Pouget, J. P.; Launois, H.; Dhaenens, J. P.; Merenda, P.; Rice, T. M., Electron localization induced by uniaxial stress in pure VO_2. *Phys. Rev. Lett.* **1975,** *35* (13), 873-875.

33.   Jones, A. C.; Berweger, S.; Wei, J.; Cobden, D.; Raschke, M. B., Nano-optical Investigations of the Metal-Insulator Phase Behavior of Individual VO_2 Microcrystals. *Nano Lett.* **2010,** *10* (5), 1574-1581.

34.   Sohn, J. I.; Joo, H. J.; Kim, K. S.; Yang, H. W.; Jang, A. R.; Ahn, D.; Lee, H. H.; Cha, S.; Kang, D. J.; Kim, J. M.; Welland, M. E., Stress-induced domain dynamics and phase transitions in epitaxially grown VO_2 nanowires. *Nanotechnology* **2012,** *23* (20), 205707.

35.   Katz, J. D.; Hurley, G., Etching alumina with molten vanadium pentoxide. *J. Am. Ceram. Soc.* **1990,** *73* (7), 2151-2152.

36.   Safdar, M.; Frischat, G. H.; Salge, H., Etching of Al_2O_3 surfaces with molten V_2O_5. *J. Am. Ceram. Soc.* **1974,** *57* (2), 106-106.

37.   Sequeira, C. A. C.; Chen, Y.; Marquis, F. D. S., Solubility of silica and alumina in sodium sulphate-sodium vanadate-vanadium pentoxide melts. In *High Temperature Corrosion in Molten Salts*, Sequeira, C. A. C., Ed. Trans Tech Publications Ltd: Switzerland, 2003; Vol. 7, pp 335-348.

38.   Nag, J.; Payzant, E. A.; More, K. L.; Haglund, R. F., Enhanced performance of room-temperature-grown epitaxial thin films of vanadium dioxide. *Appl. Phys. Lett.* **2011,** *98* (25), 251916.

39.   Wong, F. J.; Zhou, Y.; Ramanathan, S., Epitaxial variants of VO_2 thin films on complex oxide single crystal substrates with 3m surface symmetry. *J. Cryst. Growth* **2013,** *364*, 74-80.

40.   Chen, C. H.; Zhu, Y. H.; Zhao, Y.; Lee, J. H.; Wang, H. Y.; Bernussi, A.; Holtz, M.; Fan, Z. Y., VO_2 multidomain heteroepitaxial growth and terahertz transmission modulation. *Appl. Phys. Lett.* **2010,** *97* (21), 211905.

41.   McWhan, D. B.; Marezio, M.; Remeika, J. P.; Dernier, P. D., X-ray-diffraction study of metallic VO_2. *Phys. Rev. B* **1974,** *10* (2), 490-495.

42.   Cousland, G. Investigation of material properties of yttria-stabilised zirconia using experimental techniques and first-principles calculations. PhD Doctorate, University of Sydney, Sydney, Australia, 2014.

43.   Wang, X. Y.; Tan, X. J.; Xu, S. L.; Liu, F. H.; Goodman, B. A.; Deng, W., Preparation and up-conversion luminescence of Er-doped yttria stabilized zirconia single crystals. *J. Lumines.* **2020,** *219*, 116896.

44.   Gupta, A.; Aggarwal, R.; Gupta, P.; Dutta, T.; Narayan, R. J.; Narayan, J., Semiconductor to metal transition characteristics of VO_2 thin films grown epitaxially on Si (001). *Appl. Phys. Lett.* **2009,** *95* (11), 111915.

45.   Butz, B.; Schneider, R.; Gerthsen, D.; Schowalter, M.; Rosenauer, A., Decomposition of 8.5 mol.% Y_2O_3-doped zirconia and its contribution to the degradation of ionic conductivity. *Acta Mater.* **2009,** *57* (18), 5480-5490.

46.   Hertl, W., Vanadia reactions with yttria stabilized zirconia. *J. Appl. Phys.* **1988,** *63* (11), 5514-5520.

47.   Susnitzky, D. W.; Hertl, W.; Carter, C. B., Vanadia-induced transformations in yttria-stabilized zirconia. *Ultramicroscopy* **1989,** *30* (1-2), 233-241.

48.   Janczuk, B.; Zdziennicka, A., A study on the components of surface free-energy of quartz from contact-angle measurements. *J. Mater. Sci.* **1994,** *29* (13), 3559-3564.
49.   Rhee, S. K., Critical surface energies of Al_2O_3 and graphite. *J. Am. Ceram. Soc.* **1972,** *55* (6), 300-303.
50.   Tsoga, A.; Nikolopoulos, P., Surface and grain-boundary energies in yttria-stabilized zirconia (YSZ-8 mol %). *J. Mater. Sci.* **1996,** *31* (20), 5409-5413.

2.9 Supporting Information

2.9.a VO₂ Crystal Lattice and Phases

Figure S1 compares the unit cells of the M1, M2, and R phases of VO_2. The corresponding lattice parameters refenced throughout this work are presented in Table S1.

Figure 2.S1: Schematic diagram of the VO_2 crystal structure in its M1, M2, and R phases. The unit cell for R is overlaid (in green) on the M1 and M2 structures as a guide to the eye.
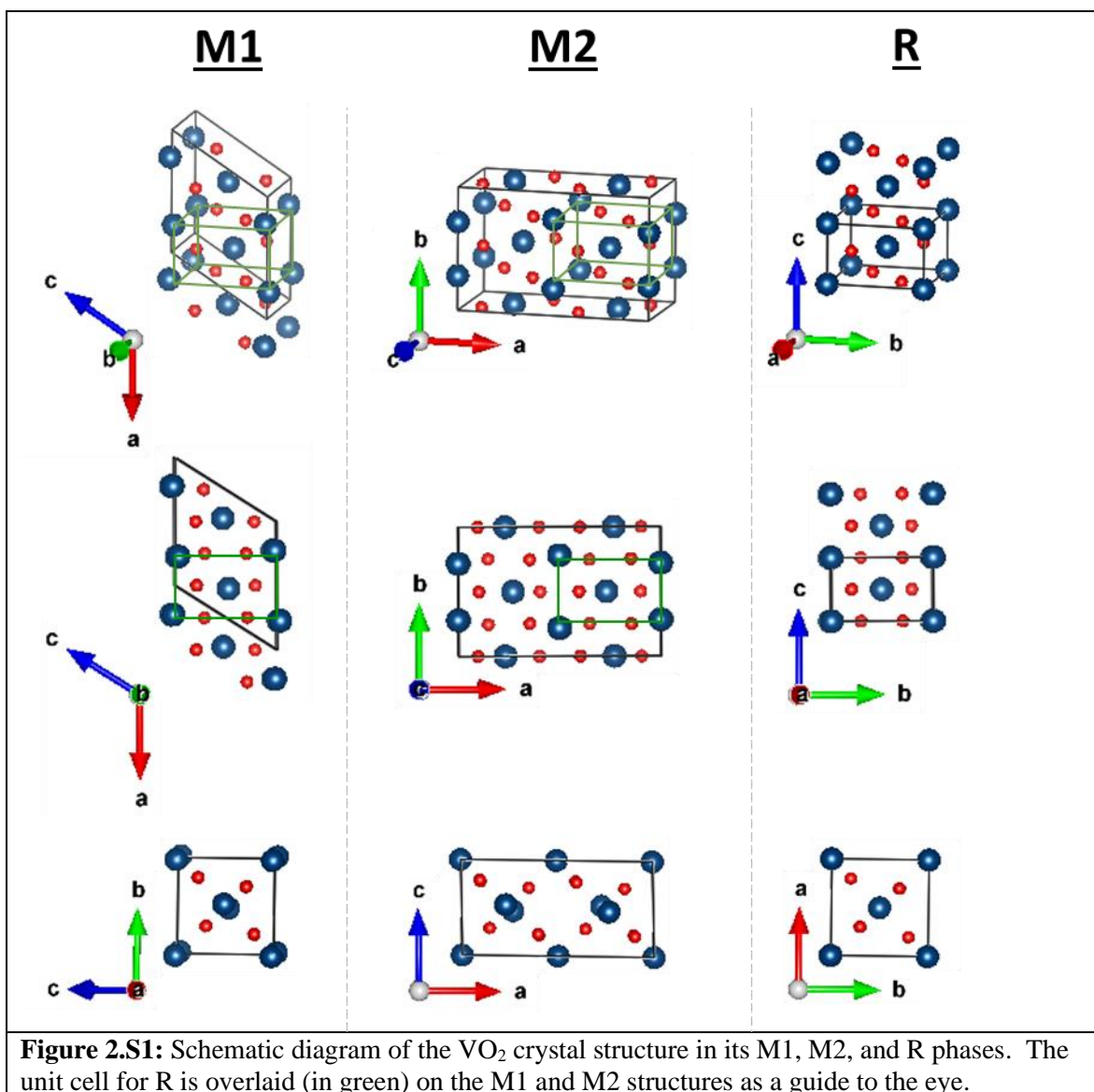
Table 2.S1: Lattice parameters for the M1, M2, and R VO_2 phases								
Phase	**Space Group**	**a (Å)**	**b (Å)**	**c (Å)**	**α(°)**	**β(°)**	**γ(°)**	**Ref.**
M1	P 2₁/c	5.7517	4.5378	5.3825	90	122.646	90	1
M2	C 2/m	9.0600	5.8000	4.5217	90	91.850	90	2
R	P 4₂/m n m	4.5546	4.5546	2.8514	90	90	90	3

2.9.b Review of Progress in Vapor Transport Growth

The optimization of different parameters involved in vapor transport growth has progressed significantly. This method was first developed using VO_2 as a precursor,[4-11] but V_2O_5 has become the standard precursor powder because of its lower melting point. VO_2 melts at 1967ºC, so using V_2O_5, which melts at about 690ºC, allows for a larger flux of vapor making for a more efficient growth.[12-13] Results of previous growths also show that varying growth conditions affects the morphology of the products. Higher temperatures tend to yield denser nanowires which may show directional growth or even larger nanoplatelets, whereas at lower temperatures, fewer, more loosely attached nanowires tend to form.[8, 14] In at least one study, use of a two-step method, wherein oxygen flow is introduced after the initial temperature ramp, yielded a higher density of nanowires as well.[7]

Choice of substrate has been extensively explored as a parameter of crystal growth. Several studies have focused on the effects of lattice match, showing that varying the lattice structure of the substrate may alter the shape and orientation of VO_2 crystals. Table S2 summarizes substrates that have been used and how lattice match affects the crystals they yield. Generally, VO_2 crystals tend to grow along the rutile c-axis $[001]_R$ with facets along the low-surface-energy $\{110\}_R$ family of planes.[11]

The most commonly used substrates for VO_2 crystal growth are silicon and silica. Vanadium dioxide crystals grown on pure SiO_2 tend to grow in specific directions depending on the cut used (with $[001]_R$ aligned to $\langle 2\bar{1}\bar{1}0\rangle_{SiO_2}$ on z-cut SiO_2[14] and to $\langle 1\bar{1}00\rangle_{SiO_2}$ on x-cut).[12] Silicon oxide on Si, pure Si, and Si_3N_4 have produced crystals with unique structural characteristics, but with random orientation in the plane of the substrate.[4-5, 15-17] Growth on TiO_2 (100) and TiO_2 (110) also results in crystals with different structural characteristics, having unique cross-sectional shapes, unusual crystal facets parallel to the substrate, and specific in-plane orientation.[11] Another widely-used substrate is Al_2O_3. In addition to varying structural characteristics, crystals grown on Al_2O_3 show definite evidence of preferred growth direction relative to the substrate, depending on the cut used.[6, 10] On c-cut, crystals grow at 60º angles relative to each other,[6] whereas in r-cut and a-cut, crystals grow directionally out of plane relative to the substrate.[10] Across different crystalline substrates, the arrangement of atoms on the surface affects the shape and morphology of the crystals on a micron-scale.

Other substrate-dependent effects during crystal growth play a significant role in determining the properties of the resulting VO_2 crystals. In particular, chemical interactions between the substrates and vanadium precursors affect the growth mechanism. On substrates with SiO_2 at the surface, a eutectic region forms between newly formed VO_x droplets and VO_2 wires which dissolves a small amount of surrounding material, embedding the wire into the substrate. This facilitates unobstructed growth which leads to larger crystals,[4, 17] and firmly clamps the crystals to the substrate. On TiO_2 substrates, the precursor vapor wets the surface during growth instead of forming droplets.[17] These observations show that interfacial

interactions between liquid vanadium oxides and the substrate surface changes the growth mechanism on these substrates, which may result in different crystal morphologies. In addition, some crystals grown on Al_2O_3 and SiO_2 have been shown to exist in the M2 phase at room temperature.[7, 9, 18] Although this has often been attributed to substrate-induced strain, the M2 phase persists in crystals removed from Al_2O_3 substrates (and thus relieved of substrate-induced strain). Moreover, the M2 phase has also been stabilized by aluminum doping,[19] which suggests the possibility of a chemical effect.

Table 2.S2: Summary of substrate effects on VO₂ crystal growth		
Substrate	**Evidence of Lattice Match / Orientation**	**Evidence of Chemistry Effects**
SiO_2 z-cut $(0001)_{SiO_2}$	$[001]_R \parallel \langle 2\bar{1}\bar{1}0 \rangle_{SiO_2}$ $\{110\}_R \parallel \{0001\}_{SiO_2}$ [14]	Molten V_2O_5 forms eutectic with SiO_2; eutectic layer facilitates growth; resulting VO_2 crystals embedded in SiO_2 [4, 17]
SiO_2 x-cut $(11\bar{2}0)_{SiO_2}$	$[001]_R \parallel \langle 1\bar{1}00 \rangle_{SiO_2}$ $\{110\}_R \parallel \{11\bar{2}0\}_{SiO_2}$ [12]	
SiO_2 (amorphous) on Si	$\{110\}_R$ [4, 17] and $\{011\}_R$ [4] parallel to substrate; square-cross section [4, 16]; random orientation in plane [17]	
Si (w/ native oxide)	Random orientation in plane [6]	Si-assisted reduction: $2V_2O_5(l) + Si(s) \rightarrow 4VO_2(s) + SiO_2$ Leads to small, dense nuclei [17]
Si_3N_4	Rectangular cross section; $\{110\}_R$ parallel to substrate [5]	Higher density of nanowires compared to SiO_2 substrates [5]
GaN $(0001)_{GaN}$	In-plane orientation reflects hexagonal substrate symmetry [17]	Molten vanadia wets GaN surface [17]
TiO_2 $(110)_{TiO_2}$	Triangular cross section; exposed facets are $\{100\}_R$ planes; $[001]_R \parallel \langle 001 \rangle_{TiO_2}$ $\{110\}_R \parallel \{110\}_{TiO_2}$ [11]	Molten vanadia wets TiO_2 surface [17]
TiO_2 $(100)_{TiO_2}$	Rectangular cross section; exposed facets are $\{100\}_R$ planes; $[001]_R \parallel \langle 001 \rangle_{TiO_2}$ $\{100\}_R \parallel \{100\}_{TiO_2}$ [11]	
Al_2O_3 c-cut $(0001)_{Al_2O_3}$	Triangular cross-section [10-11], $[001]_R \parallel \langle 11\bar{2}0 \rangle_{Al_2O_3}$ $\{100\}_R \parallel \{0001\}_{Al_2O_3}$ [10],	M2 phase stabilized at room temperature, attributed to strain effects [7, 9]
Al_2O_3 r-cut $(1\bar{1}02)_{Al_2O_3}$	Square-cross section [10]; growth axis out of plane, 60° relative to substrate surface, unique in-plane orientation [7, 10]	
Al_2O_3 a-cut $(11\bar{2}0)_{Al_2O_3}$	Square-cross section; growth axis out of plane, 3-fold in-plane orientation symmetry [10]	
Al_2O_3 m-cut $(10\bar{1}0)_{Al_2O_3}$	Nanoblocks and nanowires appear to exhibit preferred orientation [20]	
Al_2O_3 (amorphous) on SiO_2		Al-doping stabilizes M2-phase at room temperature [19]

2.9.c Sample and Precursor Loading

Figure 2.S2: (top) Sample boats loaded with V_2O_5 precursor powder upstream, and growth substrates downstream. (bottom) After growth, the precursor has been consumed and substrates are covered with deposited material.
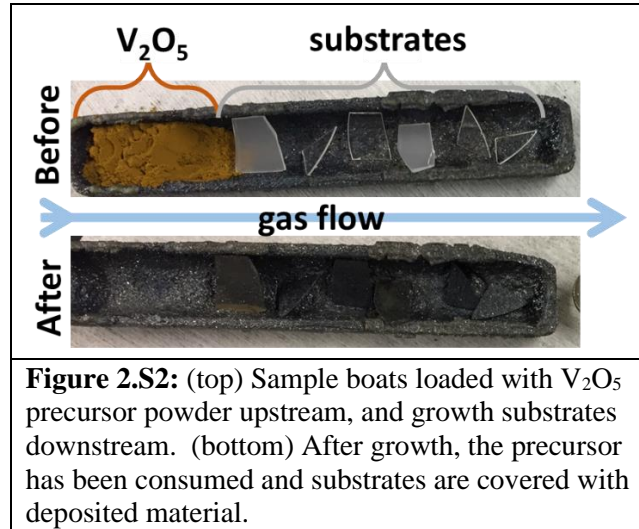
Figure S2 shows an example of the samples before and after the growth process. Orange vanadium pentoxide (V_2O_5) powder is loaded into one end of the boat, and growth substrates into the other. During the growth process, V_2O_5 vapor is carried to the substrates by a directional gas flow. After growth, the V_2O_5 is consumed and the substrates are darkened with a coating of VO_2 crystals.

2.9.d Etch Pits in Sapphire

Figure 2.S3: After crystal growth, etch pits can often be observed in the sapphire substrate.
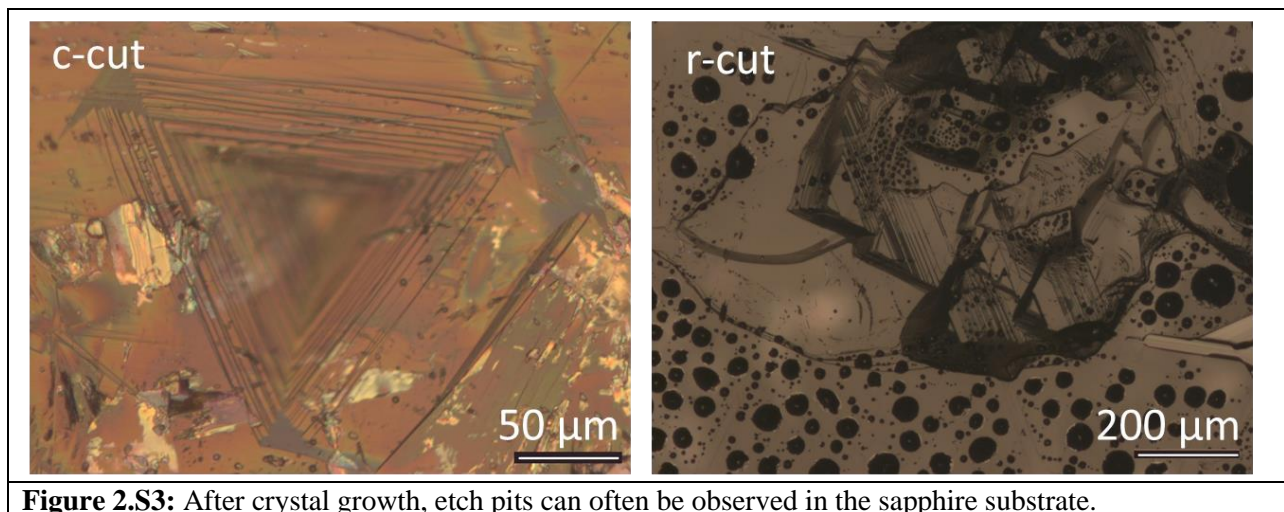
After the growth process, pits can be observed in the sapphire substrate, examples of which are shown in Figure S3. These have a similar appearance to etch pits in sapphire,[21] with a

tendency to have stepped edges and to be shaped differently on different cuts, reflecting the difference in etch rates on different lattice planes. These pits are not observed on untreated substrates, or on substrates heated in the absence of V_2O_5 precursor. We attribute them to the corrosive action of molten V_2O_5, which has been used to etch Al_2O_3 surfaces.[22-23]

2.9.e Examples of Large, Flat, Low-Aspect-Ratio Microcrystals on Sapphire
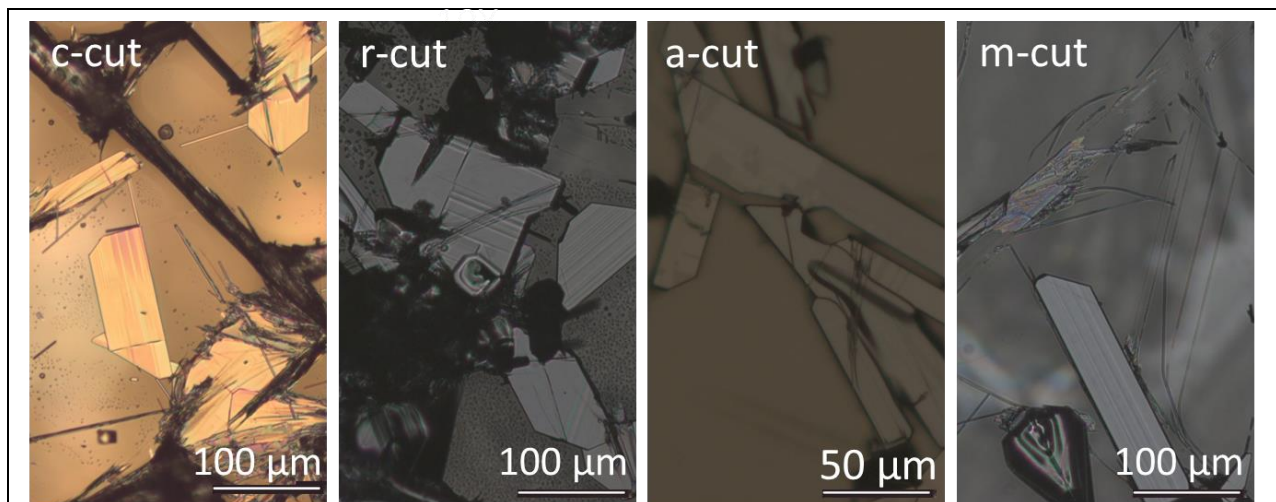
Figure 2.S4: On each cut of sapphire, some crystals grow with large areas, low aspect ratios, and faces parallel to the substrate.

As discussed in the main text, both highly-oriented nanowires and un-oriented micro-platelets can be observed on each cut of sapphire. Examples of the latter are shown in Figure S4.

2.9.f Analysis of Pole Figures on Other Cuts of Sapphire

Figure 2.S5: Additional XRD pole-figures (left) and constant-α cuts from the pole figures (right) were used in determining the VO₂ crystal orientation on r-cut sapphire. Higher-resolution scans (a, left, inset) show that the $\{201\}_{M2}$ peaks are single peaks rather than doublets.
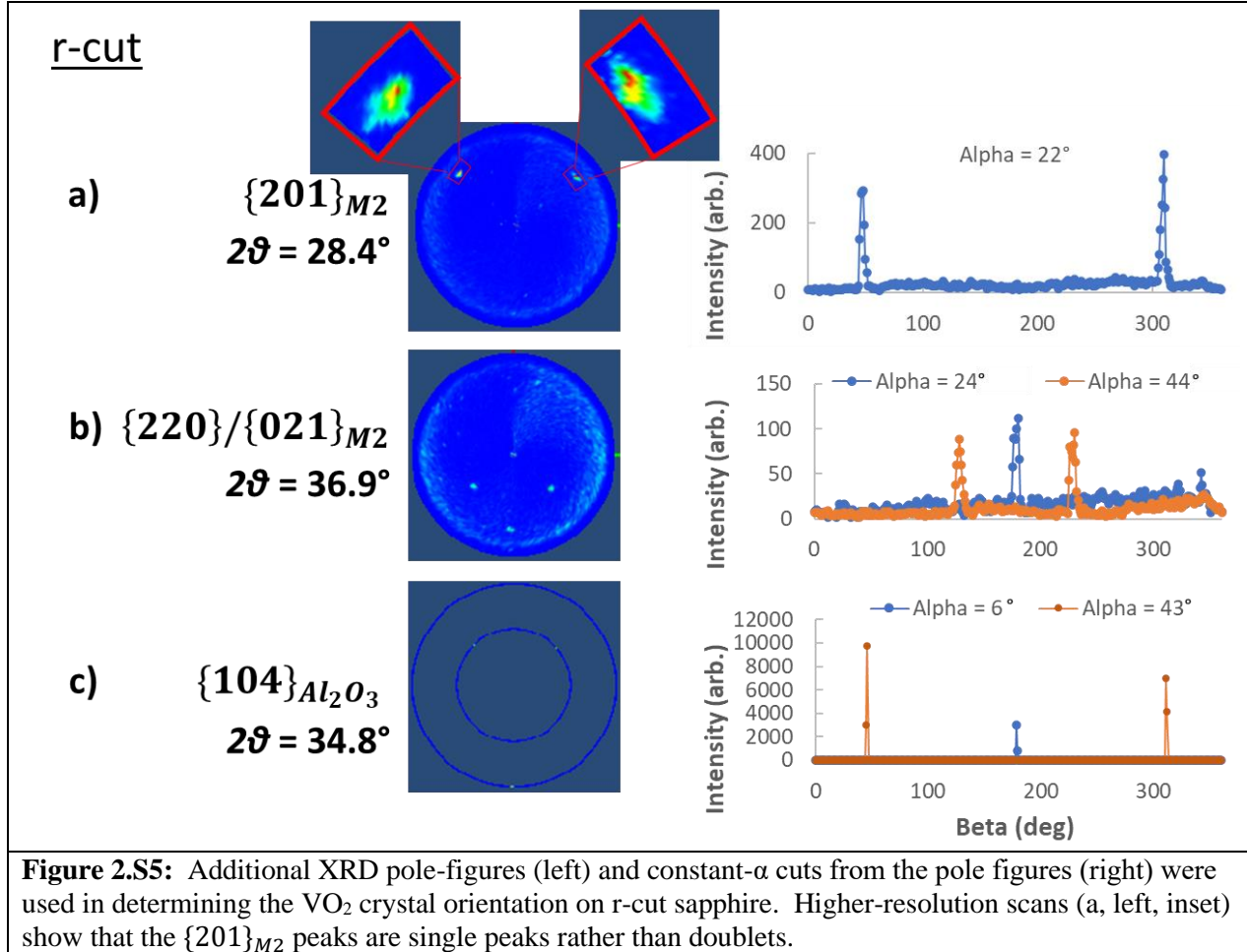
On r-cut Al₂O₃, the $\{201\}_{M2} \equiv \{110\}_R$ family of planes shows one peak at α=90° ($\{110\}_R$ parallel to substrate) and two at α=22° with β=-2°±48°. The $\{220\}/\{021\}_{M2} \equiv \{011\}_R$ planes show four clear peaks: α=90°, α=45° with β=-1°±129°, and α=24° with β=180°. These four peaks correspond to the two $\{110\}_R$ peaks at α=22°. On the other hand, no $\{011\}_R$ peaks are observed that correspond to the $\{110\}_R$ peak at α=90°, which implies that these crystals have no in-plane orientation. Thus, some of the VO₂ crystals on r-cut Al₂O₃ have $\{110\}_R$ parallel to the substrate with no in-plane orientation, while others have $\{011\}_R$ parallel to the substrate with one unique in-plane orientation. To establish the substrate orientation, $\{104\}_{Al_2O_3}$ peaks are observed at α=43° with β=-2°±48° and α=6° with β=178°. This establishes the orientation of the VO₂ crystals relative to the substrate, as listed in Table 2 of the main text.

Notably, this orientation is not the one that would yield the smallest lattice mismatch theoretically. If instead the orientation was $\langle 11\bar{1} \rangle_R \parallel \langle 0\bar{2}2\bar{1} \rangle_{Al_2O_3}$, the calculated mismatch would be only 0.3% (1.4%). This orientation is very close to that we observe, having only a ±2.5° shift in β; however, this would lead to a 5° peak splitting, which is not observed in our data, even with higher-resolution measurements (Figure S5a, insets).

Figure 2.S6: Additional XRD pole-figures (left) and constant-α cuts from the pole figures (right) were used in determining the VO_2 crystal orientation on m-cut sapphire.
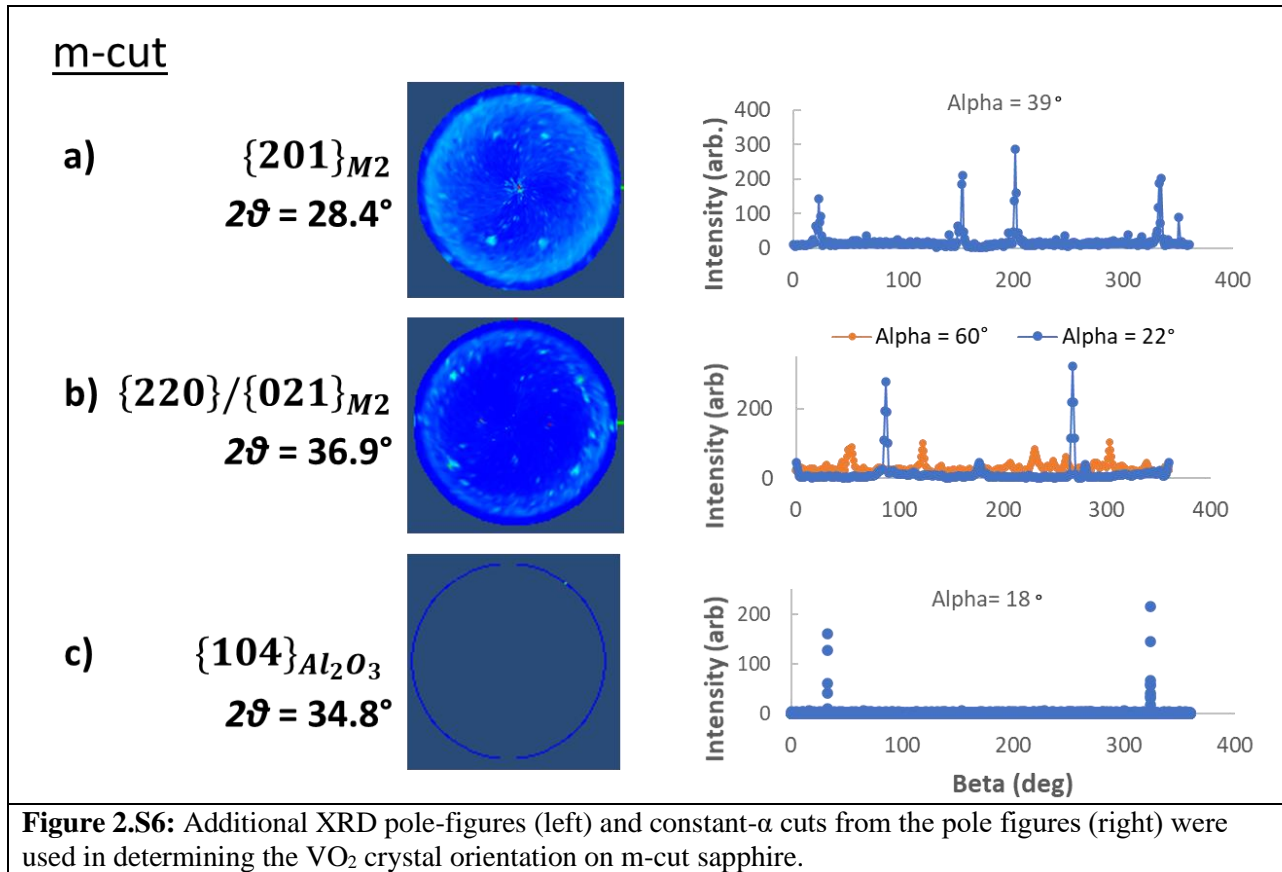
On m-cut Al_2O_3, the $\{201\}_{M2} \equiv \{110\}_R$ family of planes shows one peak at α=90° ($\{110\}_R$ parallel to substrate) and four at α=39° with β=±24° or β=±155°. The $\{220\}/ \{021\}_{M2} \equiv \{011\}_R$ planes show four clear peaks, all at α=21° with β=1°±54° or β=1°±125°. These four peaks correspond to the two $\{110\}_R$ peaks at α=39°, and arise from VO_2 crystals in two symmetry-equivalent orientations, which can be fully identified by comparison to the substrate $\{104\}_{Al_2O_3}$ peaks at α=18° and β=-2°±34° (see main text, Table 2). Once again, no $\{011\}_R$ peaks can be identified to correspond to the $\{110\}_R$ peaks at α=90°, indicating that the crystals with $\{110\}_R$ parallel to the substrate have no definite in-plane orientation.

Table 2.S3: M2 VO_2 peaks observed in θ-2θ measurements on a-cut sapphire
$\{201\}/\{20\bar{1}\}$
$\{220\}/\{021\}$
$\{400\}/\{002\}$
$\{401\}/\{202\}$
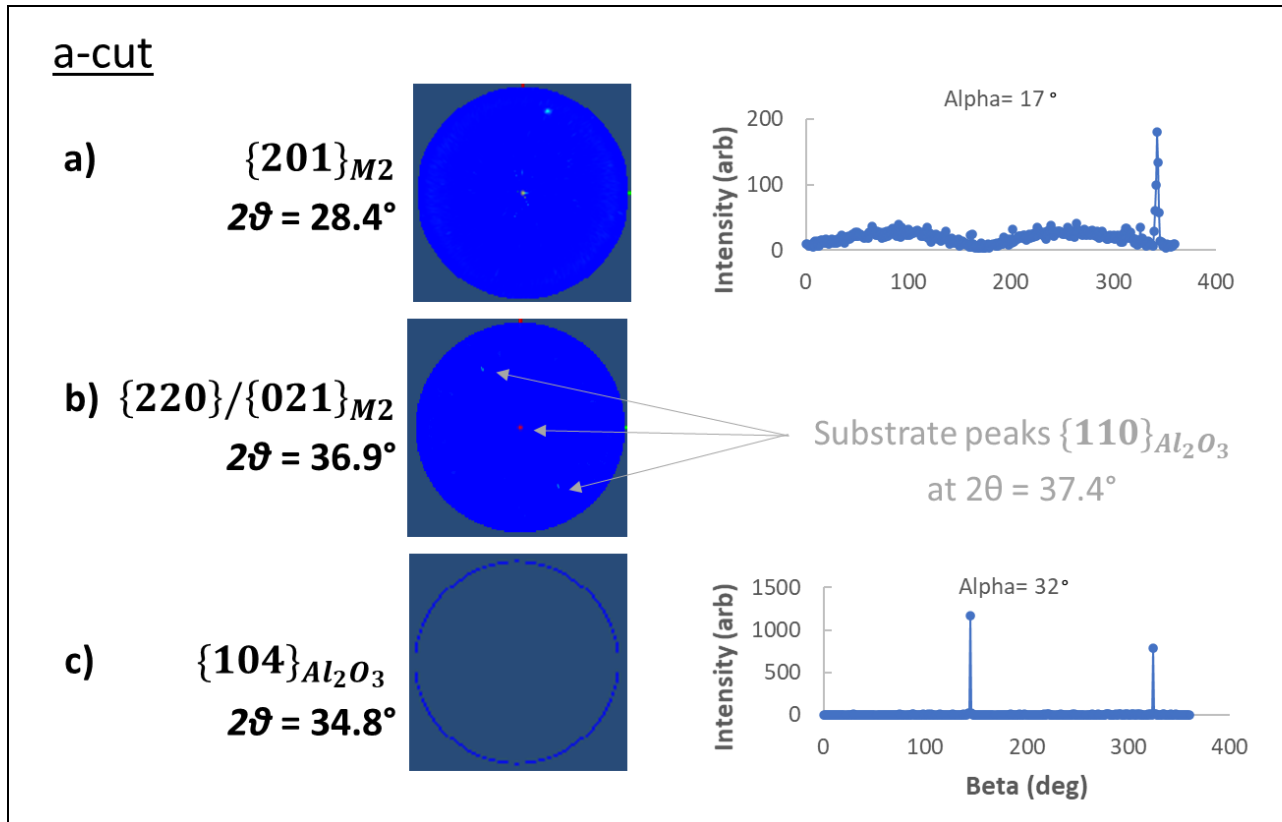
Figure 2.S7: Additional XRD pole-figures (left) and constant-α cuts from the pole figures (right) were used in determining the VO_2 crystal orientation on a-cut sapphire. The peaks that appear in the $\{220\}/\{021\}_{M2}$ pole figure (at $2\theta = 36.9°$) are positioned where $\{110\}_{Al_2O_3}$ peaks (at $2\theta = 37.4°$) would be expected, and are likely the result of bleed-over from those reflections.

On a-cut Al_2O_3, the $\{201\}_{M2} \equiv \{110\}_R$ family of planes shows, as usual, one peak at α=90° ($\{110\}_R$ parallel to substrate), but only one other peak, at α=17° with β=-17°. Given the substrate symmetry, at least two peaks at α=17° would be expected for a sufficiently large sample of crystals; however, this sample was more sparsely covered with VO_2 than the others, and it may be that the corresponding symmetric peak was simply too weak to be observed. Similarly, no peaks are observed due to the $\{220\}/\{021\}_{M2} \equiv \{011\}_R$ family of planes. The peaks that do appear in the pole figure (Figure S6b) can be assigned to bleed-over from the (much more intense) $\{110\}_{Al_2O_3}$ peaks which have a similar 2θ value. All of the $\{011\}_R$ peaks, being intrinsically less intense than the $\{110\}_R$, are simply too weak to be observed. However, to fully determine the orientation which produced the one $\{110\}_R$ peak at α=17° requires additional information. Standard θ-2θ measurements reveal all the VO_2 planes which are parallel to the substrate surface. Table S3 lists all the M2-VO_2 planes identified in θ-2θ measurements on a-cut Al_2O_3. Some of these may correspond to crystals with no in-plane orientation (as appears to be typical of the $\{201\}/\{20\bar{1}\}_{M2}$ planes), or to loose, randomly oriented crystals, but we can identify one that is consistent with $\{110\}_R$ peak at α=17°, which makes it possible to identify that orientation.

2.9.g Evidence that a YVO4 Layer Underlies VO2 Crystals on YSZ

Figure 2.S8: On YSZ, the substrate is covered by both VO2 crystals (c) and a dark film composed of ZrO2 and YVO4 (a). When a VO2 crystal is removed, the same film is observed beneath (b). Raman spectroscopy (d) shows that the material under (red) and around (yellow) the crystal is the same.
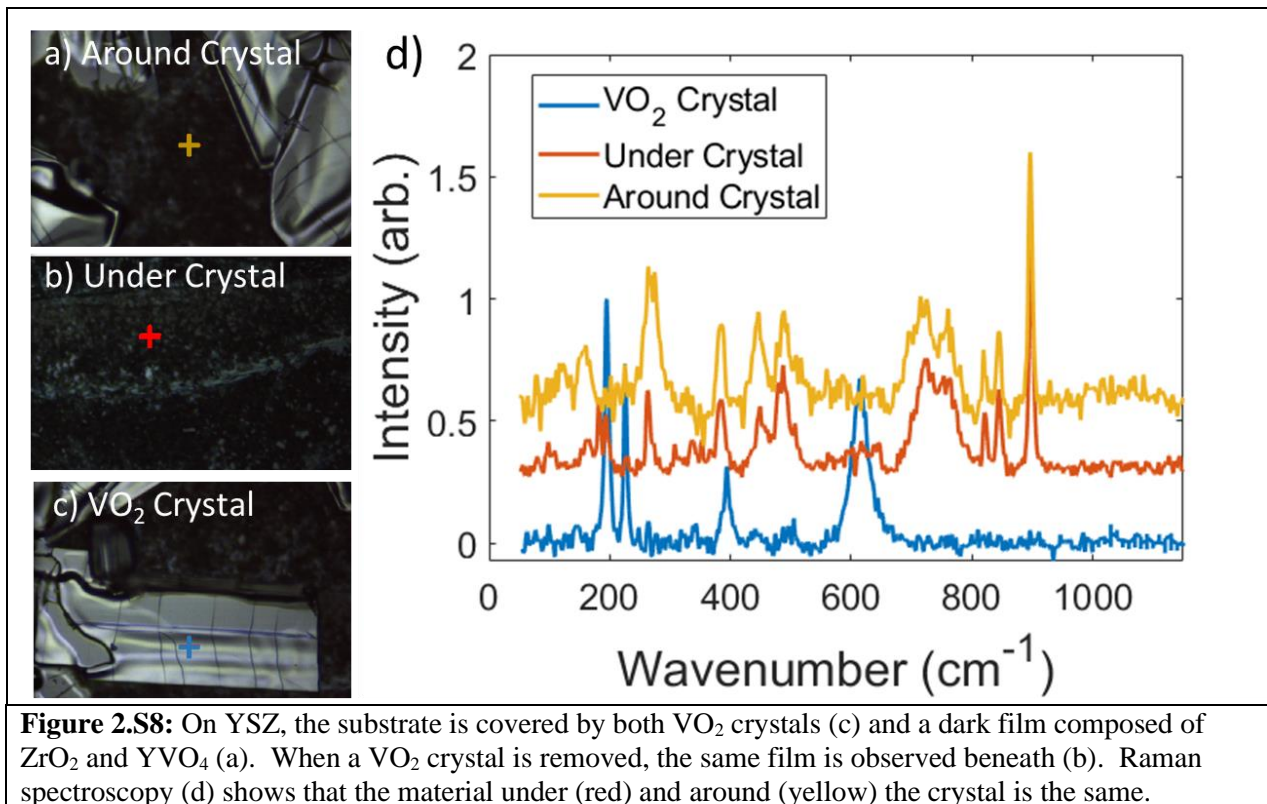
As discussed in the main text, YSZ substrates are covered in a dark, granular film after the crystal growth process. Raman spectroscopy showed this film to be composed of ZrO_2 and YVO_4. To determine whether this film covers the entire substrate or only that portion not occupied by VO_2 crystals, we remove a VO_2 crystal with adhesive tape and examine the material underneath. The crystal (Figure S7c) exhibits the characteristic Raman spectrum of VO_2 (Figure S7d, blue trace); once it has been removed, the area underneath it has the same visual appearance (Figure S7b) and Raman spectrum (Figure S7d, red trace) as the film that appears elsewhere on the exposed substrate (Figure S7a and S7d, red trace). This shows that the ZrO_2/YVO_4 film covers the entire substrate before VO_2 crystals form above it.

2.9.h Pole Figures for YVO₄, ZrO₂, on YSZ

	(100)-cut	(110)-cut	(111)-cut
M1 VO₂	$\{011\}_{M1}$ $2\theta = 27.9°$	$\{011\}_{M1}$ $2\theta = 27.9°$	$\{011\}_{M1}$ $2\theta = 27.9°$
YVO₄	$\{100\}_{YVO_4}$ $2\theta = 25.1°$	$\{100\}_{YVO_4}$ $2\theta = 25.1°$	$\{100\}_{YVO_4}$ $2\theta = 25.1°$
ZrO₂		$\{110\}_{ZrO_2}$ $2\theta = 24.5°$	$\{11\bar{1}\}_{ZrO_2}$ $2\theta = 28.2°$
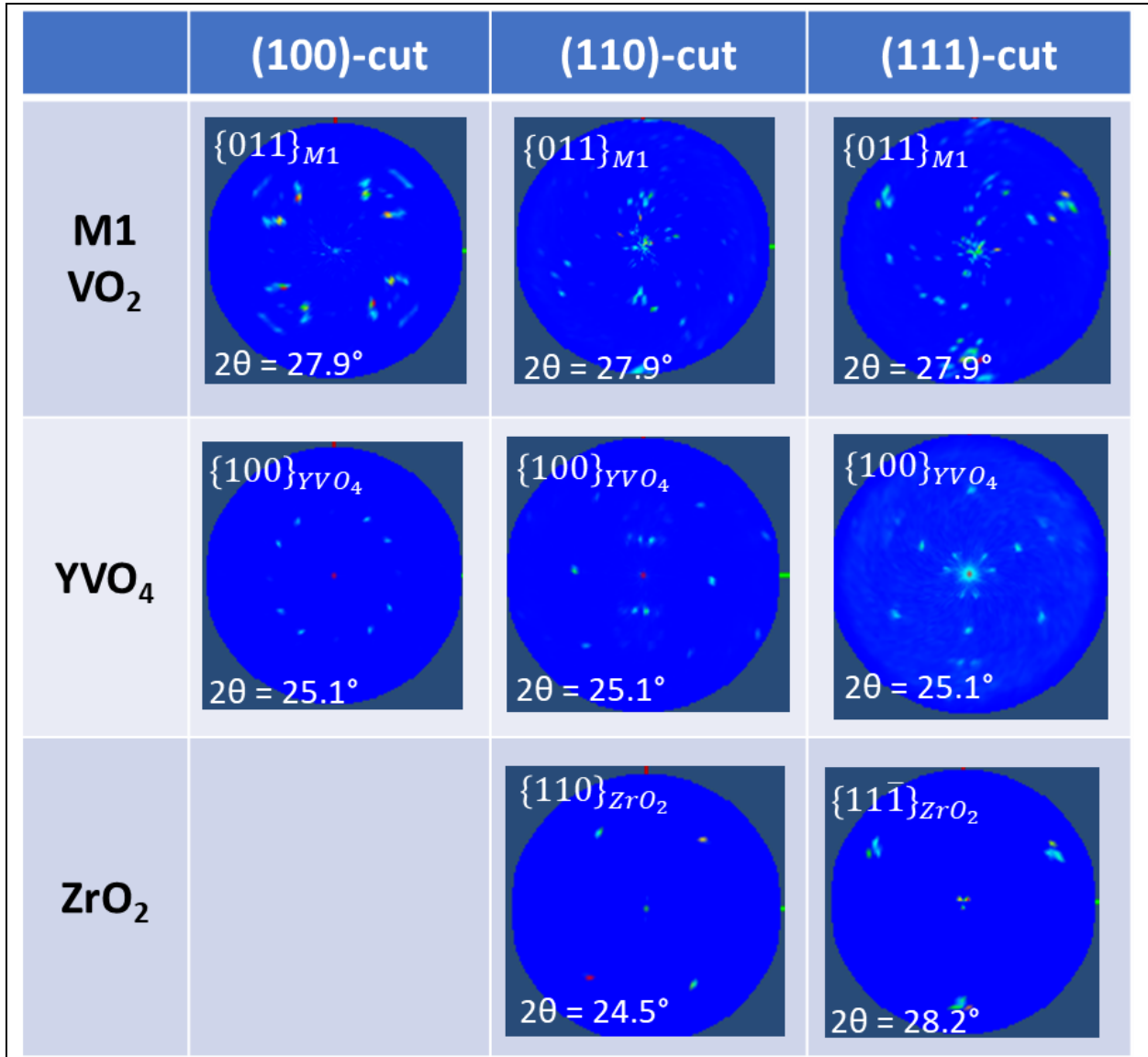
Figure 2.S9: Additional pole figures for growths on all cuts of YSZ show evidence of preferred orientation for VO₂, YVO₄, and ZrO₂.

Figure S9 compares the pole figures for the VO₂ $\{011\}_{M1} \equiv \{1\bar{1}0\}_R$ family of planes to representative low-index planes belonging to YVO₄ and ZrO₂. Both YVO₄ and ZrO₂ exhibit sharp peaks in well-defined patterns, with a high degree of symmetry reflecting the symmetry of the substrate plane: 4-fold on (100)-cut, 2-fold on (110)-cut, and 3-fold on (111)-cut. This shows that the YVO₄ and ZrO₂ are highly-oriented, likely due to a heteroepitaxial relationship to the substrate and each other. Notably, the pole-figure patterns become progressively more complex from ZrO₂ to YVO₄ to VO₂. We hypothesize that atop the YSZ substrate is an yttria-depleted ZrO₂ layer, heteroepitaxial to the substrate, but with multiple distinct orientations

arising from its decreased symmetry. Above the ZrO_2 layer, the yttria reacts with V_2O_5 to form a YVO_4 layer, in turn oriented with respect to the ZrO_2. Multiple symmetry-allowed orientations lead to multiplicatively more peaks in the pole-figure pattern. VO_2 crystals grown on the YSZ layer in turn have preferred orientations relative to it. Finally, we note that since the $\{011\}_{M1}$ and $\{11\bar{1}\}_{ZrO_2}$ planes have similar 2θ values (27.9° and 28.2°, respectively) is it possible that some bleed-over from the more-intense ZrO_2 peaks contributes to the VO_2 pole figures.

2.9.i Growth Results on Quartz

Quartz is perhaps the most commonly-used and well-characterized substrate for VO_2 crystal growth by vapor-phase transport. As a baseline comparison for our crystals on other substrates, we present a sample grown on z-cut (0001) quartz. On this cut of quartz, crystals may exhibit a preferred orientation with six-fold symmetry,[14] as noted above; and as on all SiO_2 substrates, VO_2 crystals will be embedded slightly in substrate due to formation of a eutectic during growth.[17]
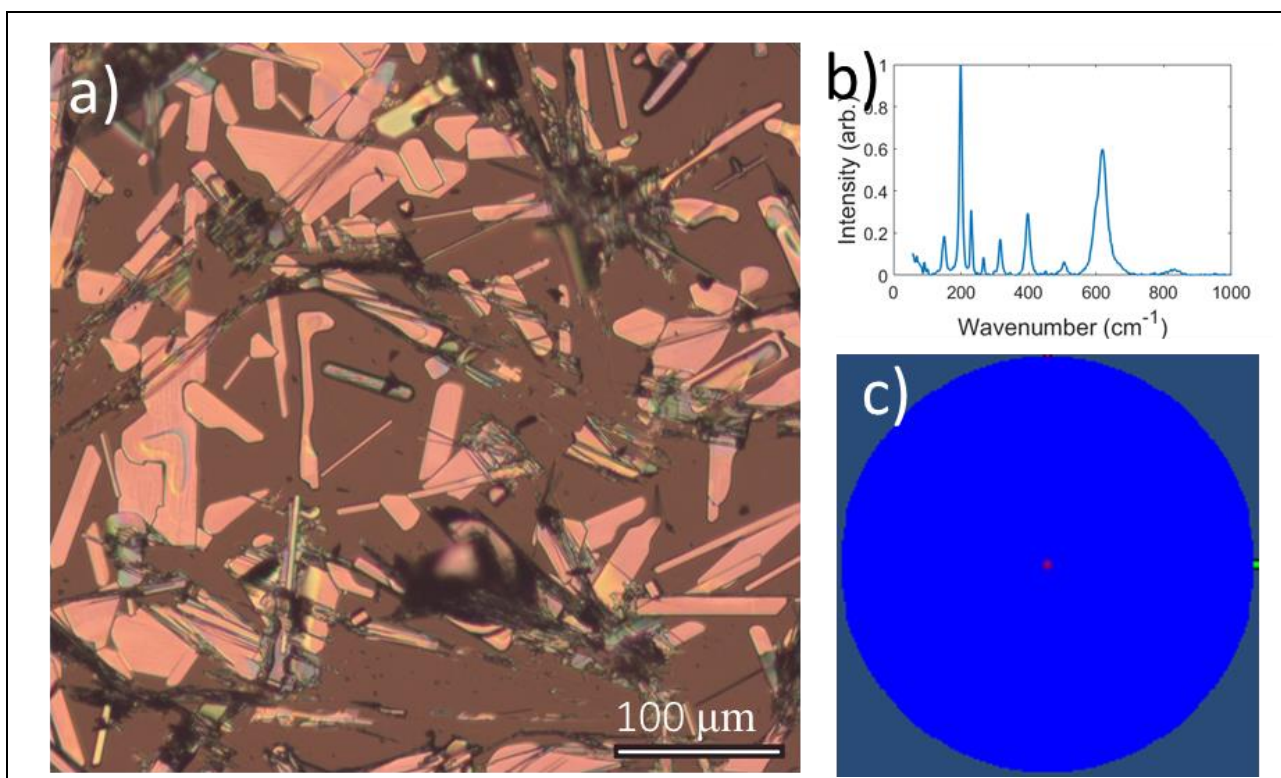
Figure 2.S10: Examples of typical VO_2 crystals grown on quartz. Optical microscopy (a) shows that a variety of sizes and shapes appear, with no clear preferred orientation. Raman microscopy (b) shows the vast majority of crystals to be in the M1 phase at room temperature. Pole figure measurements (c) show that the $\{011\}_{M1}$ planes tend to be parallel to the substrate, but do not have a preferred orientation in-plane.

Figure S10 shows example data of our VO_2 crystals grown on z-cut quartz. Polarized optical microscopy (Figure S10a) shows that the crystals lie flat, with upper facets parallel to the

substrate surface. The crystals are well adhered to the substrate—due to being embedded into the quartz, as mentioned above—and the substrate-induced strain results in complex ferroelastic twin domains (observed as light and dark mazelike patterns in the microscope image).[24] There is no obvious preferred orientation, and our crystals are more reminiscent of those others have observed on SiO_2 thermal oxides on Si,[4, 17] than the oriented nanowires observed on z-cut quartz.[14] As we observed in our sapphire growths, it is likely possible for both oriented nanowires and non-oriented microplatelets to form, especially under different growth conditions. Raman microscopy (Figure S10b) shows that the majority of VO_2 crystals on quartz are in the M1 phase at room temperature, though some are in the T phase due to the influence of substrate strain.
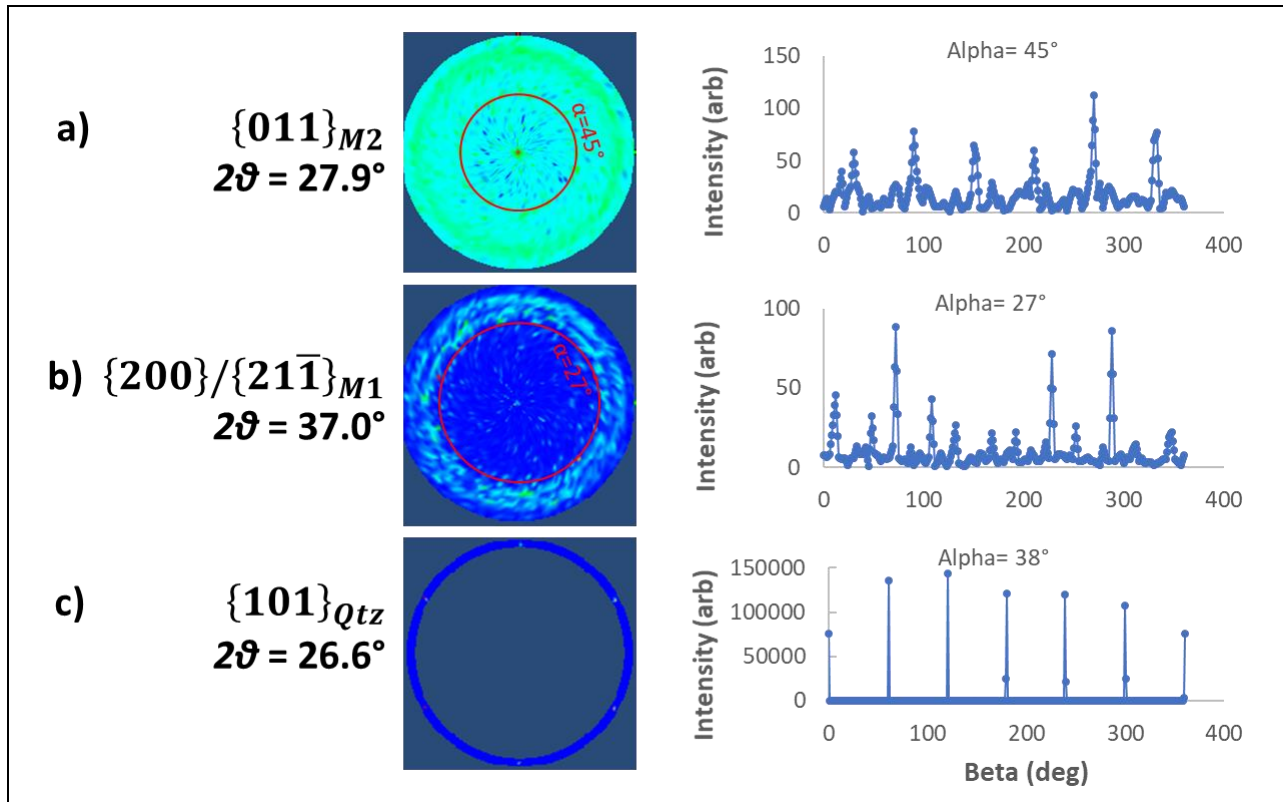
Figure 2.S11: Pole figures (left) for quartz show bright rings, corresponding to crystals with a certain plane parallel to the substrate, but no in-plane orientation. Constant-alpha cuts (right) show some distinct peaks, suggesting a degree of preferred orientation; but no singe orientation can be identified to satisfy the peaks observed for both $\{011\}_{M2}$ and $\{200\}/\{21\bar{1}\}_{M1}$.

Pole figure measurements (Figure S10c) show that the vast majority of $\{011\}_{M1} \equiv \{1\bar{1}0\}_R$ planes tend to be parallel to the substrate ($\alpha=90°$). Replotting this figure on a log scale (Figure S11a) reveals an additional bright ring at $\alpha=45°$ with brighter spots appearing with a six-fold symmetry (reflective of the six-fold symmetry of the z-cut quartz substrate). Another bright ring in this figure at very low α is background noise present in all pole figures, usually too weak to appear on the scale used. The $\{200\}/\{21\bar{1}\}_{M1} \equiv \{011\}_R$ planes show peaks, of variable intensity, at $\alpha=27°$ with six-fold symmetry: $\beta=12°+n*60°$ and $\beta=48°+n*60°$ (n=0, 1, 2, 3, 4, 5).

However, no VO_2 orientation can be identified to satisfy both $\{011\}_R$ at α=27° and $\{1\bar{1}0\}_R$ at either α=90° or α=45°. We conclude that most of our VO_2 crystals on quartz grow with $\{1\bar{1}0\}_R$ parallel to the substrate with no preferred in-plane orientation, while some crystals grow in at least two distinct orientations. Additional measurements will be required to identify the latter.

2.9.j Titanium Dioxide Substrate Properties

For this study, we chose two substrates that exemplify both chemical and lattice-matching effects in a well-understood case (Al_2O_3) as well as a novel one (YSZ). To similarly analyze all common VO_2 growth substrates is beyond the scope of this work, but one in particular deserves mention. Though more expensive, titanium dioxide (TiO_2) is commonly regarded as the best substrate for heteroepitaxial VO_2 growth because it has the same rutile crystal structure with very similar lattice parameters ($a_{R,TiO_2} = 4.593$Å and $c_{R,TiO_2} = 2.959$Å,[25] compared to $a_{R,VO_2} = 4.555$Å and $c_{R,VO_2} = 2.851$Å [3]), and has produced highly-oriented films [26-27] and crystals.[11] Table S4 presents predicted lattice mismatch values for epitaxial VO_2 on several low-index planes of TiO_2. Compared to the values calculated for VO_2 on Al_2O_3 (Table 1 of the main text), these are for the most part comparable or better, with one notable exception: the percent lattice match for VO_2 on c-cut Al_2O_3 (according to the orientation we observed) is better than that on $\{110\}_{TiO_2}$ or $\{100\}_{TiO_2}$ (the two cuts of TiO_2 used previously for single-crystal VO_2 growth). Although this represents multi-domain heteroepitaxy on Al_2O_3 as opposed to single-domain on TiO_2, lattice match on sapphire suffices for our purposes.

Table 2.S4: Predicted orientation and lattice match for VO_2 crystals grown on various cuts of TiO_2

Substrate Plane	Crystal Orientation	Lattice Mismatch ($\frac{d_{VO_2} - d_{TiO_2}}{d_{TiO_2}}$)	d_{VO_2} (Å)	d_{TiO_2} (Å)
$\{110\}_R \parallel \{110\}_{TiO_2}$	$[001]_R \parallel \langle001\rangle_{TiO_2}$	-3.6%	2.851	2.959
	$[\bar{1}10]_R \parallel \langle\bar{1}10\rangle_{TiO_2}$	-0.8%	6.442	6.496
$\{100\}_R \parallel \{100\}_{TiO_2}$	$[001]_R \parallel \langle001\rangle_{TiO_2}$	-3.6%	2.851	2.959
	$[010]_R \parallel \langle010\rangle_{TiO_2}$	-0.8%	4.555	4.593
$\{001\}_R \parallel \{001\}_{TiO_2}$	$[100]_R \parallel \langle100\rangle_{TiO_2}$	-0.8%	4.555	4.593
	$[010]_R \parallel \langle010\rangle_{TiO_2}$	-0.8%	4.555	4.593
$\{011\}_R \parallel \{011\}_{TiO_2}$	$[100]_R \parallel \langle100\rangle_{TiO_2}$	-0.8%	4.555	4.593
	$[01\bar{1}]_R \parallel \{01\bar{1}\}_{TiO_2}$	-1.6%	5.374	5.464

As with Al_2O_3 and YSZ, there is a possibility of chemical reaction between TiO_2 and V_2O_5. Studies on TiO_2-supported V_2O_5 catalysts show that at high temperatures vanadia catalyzes the TiO_2 anatase-to-rutile transition, and V^{4+} is incorporated into the rutile TiO_2 lattice, yielding $V_xTi_{1-x}O_2$ at the interface.[28-30] Also, V_2O_5 is reported to react with titania-stabilized zirconia (TiSZ) to produce $TiVO_4$.[31] On the other hand, several corrosion studies on Ti-containing thermal barrier coatings suggest that TiO_2 is less reactive with vanadia than some other metal oxides, including alumina.[32-34] The possibility of chemical reactions occurring at the

TiO$_2$-V$_2$O$_5$ interface during crystal growth certainly deserves further study, but sapphire provides a better example of substrate-vanadia reactions for this study.

There are few experimental studies of the TiO$_2$ surface energy, but computational studies predict values ranging from 0.3 to 1.8 J/m^2 for the $\{110\}_{TiO_2}$ plane, depending on the calculation method, and higher for other planes.[35-38] The highest of these predicted values are larger than those used in our study, and might lead to good substrate wetting, as observed in one crystal growth study.[17]

2.9.k SI References

1.   Longo, J. M.; Kierkega, P., A refinement of structure of VO$_2$. *Acta Chem. Scand.* **1970,** *24* (2), 420-426.
2.   Ghedira, M.; Chenavas, J.; Marezio, M., Cation disproportionation and pairing in the insulating T phase of V$_{0.985}$Al$_{0.15}$O$_2$. *Journal of Physics C-Solid State Physics* **1977,** *10* (11), L309-L314.
3.   McWhan, D. B.; Marezio, M.; Remeika, J. P.; Dernier, P. D., X-ray-diffraction study of metallic VO$_2$. *Phys. Rev. B* **1974,** *10* (2), 490-495.
4.   Cheng, Y.; Wong, T. L.; Ho, K. M.; Wang, N., The structure and growth mechanism of VO$_2$ nanowires. *J. Cryst. Growth* **2009,** *311* (6), 1571-1575.
5.   Guiton, B. S.; Gu, Q.; Prieto, A. L.; Gudiksen, M. S.; Park, H., Single-crystalline vanadium dioxide nanowires with rectangular cross sections. *J. Am. Chem. Soc.* **2005,** *127* (2), 498-499.
6.   Kim, I. S.; Lauhon, L. J., Increased yield and uniformity of vanadium dioxide nanobeam growth via two-step physical vapor transport process. *Cryst. Growth Des.* **2012,** *12* (3), 1383-1387.
7.   Kim, M. W.; Ha, S. S.; Seo, O.; Noh, D. Y.; Kim, B. J., Real-time structural and electrical characterization of metal-insulator transition in strain-modulated single-phase VO$_2$ wires with controlled diameters. *Nano Lett.* **2016,** *16* (7), 4074-4081.
8.   Maeng, J.; Kim, T. W.; Jo, G.; Lee, T., Fabrication, structural and electrical characterization of VO$_2$ nanowires. *Mater. Res. Bull.* **2008,** *43* (7), 1649-1656.
9.   Sohn, J. I.; Joo, H. J.; Ahn, D.; Lee, H. H.; Porter, A. E.; Kim, K.; Kang, D. J.; Welland, M. E., Surface-stress-induced mott transition and nature of associated spatial phase transition in single crystalline VO$_2$ nanowires. *Nano Lett.* **2009,** *9* (10), 3392-3397.
10.   Sohn, J. I.; Joo, H. J.; Porter, A. E.; Choi, C. J.; Kim, K.; Kang, D. J.; Welland, M. E., Direct observation of the structural component of the metal-insulator phase transition and growth habits of epitaxially grown VO$_2$ nanowires. *Nano Lett.* **2007,** *7* (6), 1570-1574.
11.   Wang, L. X.; Ren, H.; Chen, S.; Chen, Y. L.; Li, B. W.; Zou, C. W.; Zhang, G. B.; Lu, Y. L., Epitaxial Growth of Well-Aligned Single-Crystalline VO$_2$ Micro/ Nanowires Assisted by Substrate Facet Confinement. *Cryst. Growth Des.* **2018,** *18* (7), 3896-3901.
12.   Cheng, C.; Guo, H.; Amini, A.; Liu, K.; Fu, D.; Zou, J.; Song, H. S., Self-assembly and horizontal orientation growth of VO$_2$ nanowires. *Sci Rep* **2014,** *4*, 5456.
13.   Cheng, C.; Liu, K.; Xiang, B.; Suh, J.; Wu, J. Q., Ultra-long, free-standing, single-crystalline vanadium dioxide micro/nanowires grown by simple thermal evaporation. *Appl. Phys. Lett.* **2012,** *100* (10), 103111.
14.   Loffler, S.; Auer, E.; Weil, M.; Lugstein, A.; Bertagnolli, E., Impact of growth temperature on the crystal habits, forms and structures of VO$_2$ nanocrystals. *Appl. Phys. A-Mater. Sci. Process.* **2011,** *102* (1), 201-204.
15.   Jiang, L. L.; Wei, M. D.; Ye, B. H.; Wei, K. M., VO$_2$ rods with a rectangular cross-section. *J. Cryst. Growth* **2008,** *310* (19), 4301-4304.
16.   Lin, J.; Ji, H.; Swift, M. W.; Hardy, W. J.; Peng, Z. W.; Fan, X. J.; Nevidomskyy, A. H.; Tour, J. M.; Natelson, D., Hydrogen Diffusion and Stabilization in Single-Crystal VO$_2$ Micro/Nanobeams by Direct Atomic Hydrogenation. *Nano Lett.* **2014,** *14* (9), 5445-5451.

17.   Strelcov, E.; Davydov, A. V.; Lanke, U.; Watts, C.; Kolmakov, A., In situ monitoring of the growth, intermediate phase transformations and templating of single crystal VO_2 nanowires and nanoplatelets. *Acs Nano* **2011,** *5* (4), 3373-3384.

18.   Jones, A. C.; Berweger, S.; Wei, J.; Cobden, D.; Raschke, M. B., Nano-optical Investigations of the Metal-Insulator Phase Behavior of Individual VO_2 Microcrystals. *Nano Lett.* **2010,** *10* (5), 1574-1581.

19.   Strelcov, E.; Tselev, A.; Ivanov, I.; Budai, J. D.; Zhang, J.; Tischler, J. Z.; Kravchenko, I.; Kalinin, S. V.; Kolmakov, A., Doping-based stabilization of the M2 phase in free-standing VO_2 nanostructures at room temperature. *Nano Lett.* **2012,** *12* (12), 6198-6205.

20.   Choi, S.; Kim, B. J.; Lee, Y. W.; Yun, S. J.; Kim, H. T., Synthesis of VO_2 nanowire and observation of metal-insulator transition. *Jpn. J. Appl. Phys.* **2008,** *47* (4), 3296-3298.

21.   Zhang, L. Y.; Sun, J. F.; Zuo, H. B.; Yuan, Z. Y.; Zhou, J.; Xing, D. W.; Han, J. C., Tridimensional morphology and kinetics of etch pit on the {0001} plane of sapphire crystal. *Journal of Solid State Chemistry* **2012,** *192*, 60-67.

22.   Katz, J. D.; Hurley, G., Etching alumina with molten vanadium pentoxide. *J. Am. Ceram. Soc.* **1990,** *73* (7), 2151-2152.

23.   Safdar, M.; Frischat, G. H.; Salge, H., Etching of Al_2O_3 surfaces with molten V_2O_5. *J. Am. Ceram. Soc.* **1974,** *57* (2), 106-106.

24.   Tselev, A.; Strelcov, E.; Luk'yanchuk, I. A.; Budai, J. D.; Tischler, J. Z.; Ivanov, I. N.; Jones, K.; Proksch, R.; Kalinin, S. V.; Kolmakov, A., Interplay between Ferroelastic and Metal-Insulator Phase Transitions in Strained Quasi-Two-Dimensional VO_2 Nanoplatelets. *Nano Lett.* **2010,** *10* (6), 2003-2011.

25.   Burdett, J. K.; Hughbanks, T.; Miller, G. J.; Richardson, J. W.; Smith, J. V., Structural electronic relationships in inorganic solids - powder neutron-diffraction studies of the rutile and anatase polymorphs of titanium-dioxide at 15 and 295-K. *J. Am. Chem. Soc.* **1987,** *109* (12), 3639-3646.

26.   Muraoka, Y.; Ueda, Y.; Hiroi, Z., Large modification of the metal-insulator transition temperature in strained VO_2 films grown on TiO_2 substrates. *J. Phys. Chem. Solids* **2002,** *63* (6-8), 965-967.

27.   Sambi, M.; Sangiovanni, G.; Granozzi, G.; Parmigiani, F., Growth and the structure of epitaxial VO_2 at the $TiO_2(110)$ surface. *Phys. Rev. B* **1997,** *55* (12), 7850-7858.

28.   Vejux, A.; Courtine, P., Interfacial reactions between V_2O_5 and TiO_2 (anatase) - role of structural-properties. *Journal of Solid State Chemistry* **1978,** *23* (1-2), 93-103.

29.   Saleh, R. Y.; Wachs, I. E.; Chan, S. S.; Chersich, C. C., The interaction of V_2O_5 with TiO_2(anatase) - catalyst evolution with calcination temperature and o-xylene oxidation. *J. Catal.* **1986,** *98* (1), 102-114.

30.   Haber, J.; Nowak, P., A catalysis related electrochemical study of the V_2O_5/TiO_2 (rutile) system. *Langmuir* **1995,** *11* (3), 1024-1032.

31.   Habibi, M. H.; Guo, S. M., The hot corrosion behavior of plasma sprayed zirconia coatings stabilized with yttria, ceria, and titania in sodium sulfate and vanadium oxide. *Mater. Corros.* **2015,** *66* (3), 270-277.

32.   Liu, H.; Cai, J.; Zhu, J. H., Hot corrosion behavior of $BaLa_2Ti_3O_{10}$ thermal barrier ceramics in V_2O_5 and $Na_2SO_4 + V_2O_5$ molten salts. *Coatings* **2019,** *9* (6), 351.

33.   She, Y. J.; Guo, Y. W.; Tan, Z. X.; Liao, K., $Na_2SO_4 + V_2O_5$ corrosion behavior of $BaNd_2Ti_3O_{10}$ for thermal barrier coating applications. *Coatings* **2020,** *10* (9), 901.

34.   Singh, G.; Kumar, S.; Kumar, R., Comparative study of hot corrosion behavior of thermal sprayed alumina and titanium oxide reinforced alumina coatings on boiler steel. *Mater. Res. Express* **2020,** *7* (2), 026527.

35.   Barnard, A. S.; Zapol, P.; Curtiss, L. A., Modeling the morphology and phase stability of TiO_2 nanocrystals in water. *J. Chem. Theory Comput.* **2005,** *1* (1), 107-116.

36.   Labat, F.; Baranek, P.; Adamo, C., Structural and electronic properties of selected rutile and anatase TiO_2 surfaces: An ab initio investigation. *J. Chem. Theory Comput.* **2008,** *4* (2), 341-352.

37.   Lazzeri, M.; Vittadini, A.; Selloni, A., Structure and energetics of stoichiometric TiO_2 anatase surfaces. *Phys. Rev. B* **2001,** *63* (15), 155409.

38.   Okeke, G.; Hammond, R. B.; Antony, S. J., Effects of heat treatment on the atomic structure and surface energy of rutile and anatase TiO_2 nanoparticles under vacuum and water environments. *Chem. Eng. Sci.* **2016,** *146*, 144-158.

CHAPTER 3

FORMATION AND CONTROL OF W-DOPED VANADIUM DIOXIDE NANOPARTICLES VIA SOLID-STATE
DEWETTING

3.1 Publication Citation

Material in this chapter is being prepared for publication as follows:

Samuel T. White, James R. Taylor, Ivan Chukhryaev, Silas Bailey, Joshua M. Queen,
James R. McBride, Richard F. Haglund, Jr.
Nano Letters

It is reproduced here, with minor formatting changes, with the permission of all authors.

3.2 Abstract

Vanadium dioxide (VO_2) nanoparticles (NPs) have strong potential in smart windows, passive thermal radiators, and reconfigurable metasurfaces, for which a change in emissivity, reflectivity or transmission with temperature is essential. A major challenge in these applications is preparing uniform layers of nanoparticles (NPs), over large areas, with well-defined size distributions and low transition temperatures (T_c). Here we describe the growth and transition properties of randomly-distributed VO_2 NPs (undoped and tungsten-doped) formed by solid-state dewetting of VO_2 thin films. Sizes and size distributions are controlled by anneal time, as particles grow via Smoluchowski aggregation then become oxidized into V_2O_5; shapes are determined by interfacial energies between VO_2 (V_2O_5) and the substrate. Tungsten dopants concentrate at the nanoparticle surface and increase the energy required for dewetting and aggregation. These results improve our ability to engineer VO_2 NPs and yield valuable insights into VO_2-substrate interactions and the behavior of W-dopants in VO_2 nanoparticles.

3.3 Introduction

Vanadium dioxide (VO_2) has long been a focus of study because of its metal-to-insulator phase transition (MIT).[1] The sharp change in optical constants associated with this transition has enabled many devices,[2] from ultrafast optical modulators[3] to passive thermal control films (as for "smart windows").[4-5] Though the latter is among the most mature of VO_2-based devices, it still faces the challenge of optimizing spectral behavior[6] and transition temperature T_c without loss of contrast between the hot and cold states. It is often desirable to decrease the transition temperature of pure VO_2 from $T_c \approx 68°C$ to room temperature (for human habitation) or lower (for unmanned spacecraft). Certain substitutional dopants (such as tungsten) can lower T_c, but generally do so at the cost of decreased contrast.[7-8] Annealing treatments can improve the transition behavior of W-doped thin films[9] and nanoparticles[10] by improving crystallinity.

Moreover, VO$_2$ nanoparticles may overcome this doping-related loss of contrast, as one study has produced tungsten-doped VO$_2$ nanoparticles embedded in an SiO$_2$ matrix with $T_c \approx$ -20°C without significant loss of contrast.[11]

Various methods exist for producing VO$_2$ nanoparticles.[12-14] Electron-beam lithography offers the best control of particle size, shape, and spacing,[15] but is slow and expensive. Hydrothermal processes, on the other hand, are amenable to large-scale production,[16] and can yield a variety of different nanoparticle morphologies, but can be hard to reproduce, involve high-pressure processes, and can be difficult to adhere to substrate.[13-14] Several studies have shown that, under certain annealing conditions, solid VO$_2$ thin films can dewet from Si (with native oxide) substrates to form roughly hemispherical nanoparticles.[17-20] Figure 1b compares nanoparticle sizes from these studies, and shows that the nanoparticle radius increases linearly with the thickness of the original film, as expected according to the theory of solid-state dewetting.[21-22] This behavior is remarkably consistent across different film-deposition methods (ALD, PLD, sputtering, and vapor transport), because it is governed entirely by the surface/interface energies of/between the substrate and film. It has also been shown that W-doped nanoparticles can be formed similarly from W-doped films.[23]
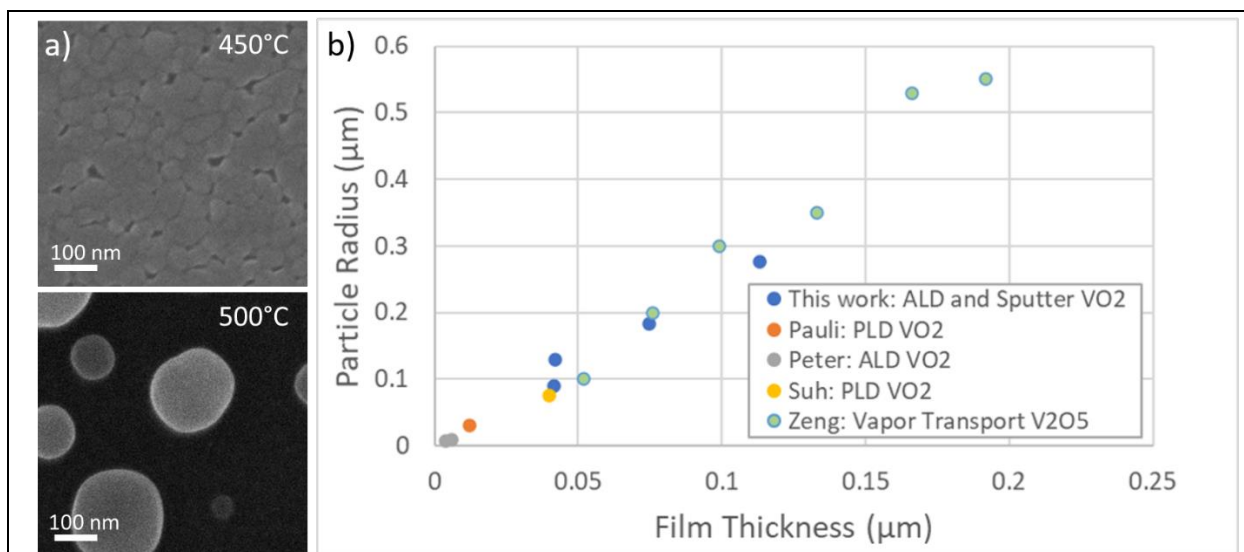
Figure 3.1: Polycrystalline thin films (a, upper) spontaneously dewet to form hemispherical nanoparticles (a, lower) when annealed at a higher temperature. Across multiple studies producing films by different methods, the dewetting process results in nanoparticles with a radius that scales linearly with initial film thickness (b).

Solid-state dewetting, then, is a quick and reliable method of producing single-particle-thick layers of VO$_2$ nanoparticles, with its scalability mainly limited by that of the film deposition method. Although some progress has been made in controlling nanoparticle growth by this method (notably relating the particle size to film thickness),[20] a more comprehensive understanding of the growth process and greater ability to control the nanoparticle characteristics are required to make it fully useful. Moreover, the role of W-doping on the nanoparticle formation process and resulting effects on transition behavior need clarification. Here, we investigate the effect of annealing time on the size and size distribution of VO$_2$ nanoparticles.

We show that after initial dewetting they grow by Smoluchowski aggregation, which provides an additional way to tune average nanoparticle size and results in well-defined size distributions. We further show how this process differs in the case of W-doped nanoparticles. Tungsten doping fundamentally changes the dewetting/aggregation process, but does not reduce the transition temperature of nanoparticles any more than in corresponding thin films. These developments help render solid-state dewetting a viable route to producing nanoparticulate thermochromic films.

3.4 Results and Discussion

First, to investigate how the dewetting proceeds over time, we present SEM images of ALD VO_2 films annealed for progressively longer periods (Figure 2a). Starting as a polycrystalline film, the individual grains coarsen (5 min and 8 min) until they pull apart into discrete particles (~10 min). At longer times, these particles continue to grow (10-20 min). Eventually (30 min and beyond), the low-pressure oxygen environment oxidizes the nanoparticles fully into V_2O_5, drastically changing their shape and size. Figure 2b shows how average nanoparticle size varies with anneal time, with the three different regimes (grain coarsening, nanoparticle aggregation, and oxidation) represented with different colors (green, blue, orange). The intermediate stage can be well described by Smoluchowski aggregation: when pairs of randomly-moving particles collide, they merge into a single, larger-volume particle. Assuming no collisions between three or more particles simultaneously, no spatial correlation between particles, and a time-independent, homogeneous kernel to the Smoluchowski equation, it is possible to derive a scale-invariant particle size distribution (PSD) $F(\varphi)$ for long times.[24-25] For three-dimensional particles constrained to a two-dimensional surface,

$$F(\varphi) = \frac{3W}{\Gamma(\alpha+1)} (W\varphi)^{3\alpha+1} e^{-(W\varphi)^3} \qquad \text{(Equation 1)}$$

where $\varphi = \frac{r}{\bar{r}}$ is the scale-invariant particle size, Γ is the gamma function, and

$$W = \frac{\Gamma(\alpha+\frac{4}{3})}{\Gamma(\alpha+1)} \qquad \text{(Equation 2)}$$

Note that $F(\phi)$ involves only one free parameter, α, the diffusion coefficient exponent, which describes the mass-dependence of the diffusion coefficient, as

$$D = D_0 m^{-\alpha} \qquad \text{(Equation 3)}$$

where D is the diffusion coefficient, D_0 is a constant, and m is the particle mass. The exponent α is system-dependent, but typically varies from 0 to 2.[25] The function $F(\phi)$ reproduces well the shape of our measured PSDs, as shown in Figure 2c, showing that our particle growth proceeds via Smoluchowski aggregation rather than Ostwald ripening (which produces a qualitatively different PSD).[26]

Figure 3.2: As anneal time increases (a), films first coarsen (green), then dewet into separate particles which grow larger over time (blue), and finally oxidize into V_2O_5(orange). The increase of particle size over time (b) and the resulting size distribution (c) can be qualitatively explained by Smoluchowski aggregation.
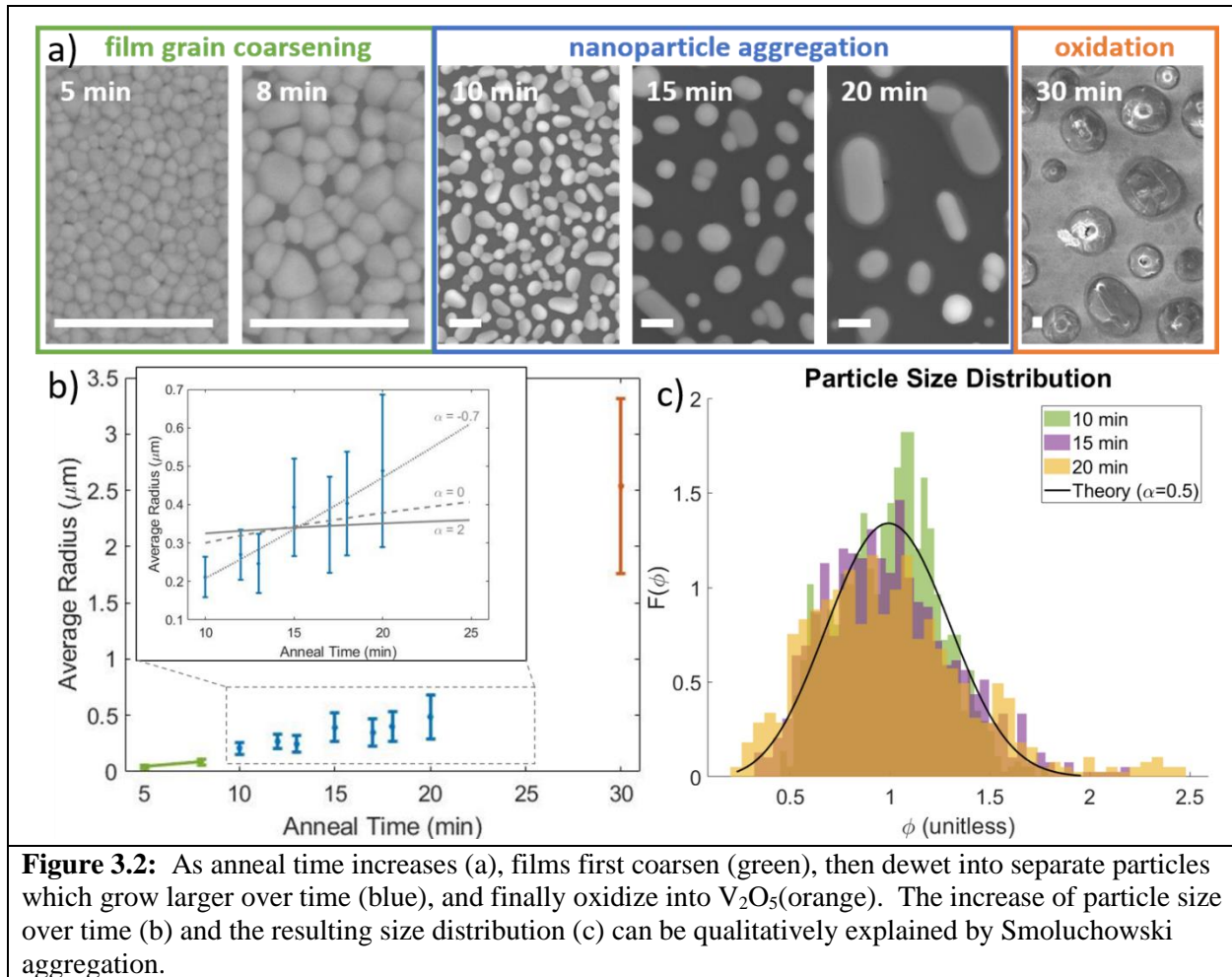
The theory of Smoluchowski aggregation also predicts the time-dependence of the average particle radius $\bar{r}$

$$\bar{r}(t) = \frac{W}{(q\pi b_0)^{\frac{1}{3}}} t^{\frac{1}{3(1+\alpha)}} \qquad \text{(Equation 4)}$$

where q is a geometrical factor accounting for the particle shape ($q = \frac{2}{3}$ for a perfect hemisphere) and b_0 is a scaling factor relating to initial conditions. Ideally, we could quantitatively measure α for our system by fitting our PSD to Eqn. 1 or our radius-vs-time data to Eqn. 4. However, we find that fitting the PSDs yields values of α varying from <0 to >1, while fitting the radius-vs-time data (Figure 2b inset) yields $\alpha = -0.7$ which would imply that larger particles diffuse faster than smaller particles. These discrepancies likely arise due to characteristics of the system not fully accounted for in the model assumption, most notably the possibility of multiple particles colliding simultaneously, and the change in particle shape due to formation of V_2O_5. Further discussion of this point can be found in the Supporting Information, section *b*.

At longer anneal times (~20 min and above), the particle morphology begins to change, exhibiting a "skirt" or "pedestal" around the particle perimeter, with a smaller contact angle θ on the substrate surface (Figure 3). This has previously been attributed to the formation of V_2O_5 at the nanoparticle surface due to over-oxygenation.[19] X-ray diffraction (XRD) measurements (Supporting Information, section *c*) and optical hysteresis measurements (Supporting Information, section *f*) show that characteristic VO_2 lattice planes and switching behavior disappear at long times, indicating that a non-VO_2 species is indeed formed at long times, though additional measurements would be needed to confirm unequivocally that it is V_2O_5 and not another vanadium oxide.
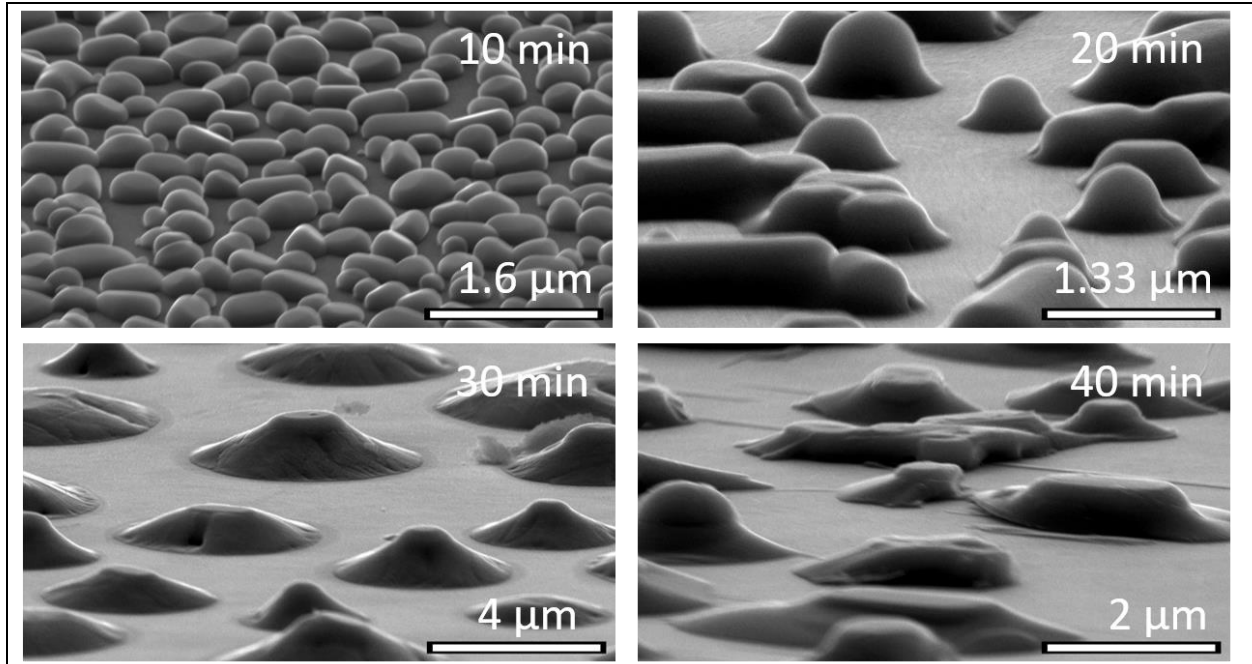
Figure 3.3: As anneal time increases beyond 10 min, another species begins to form. This species (hypothesized to be V_2O_5) has a lower contact angle and forms a "skirt" around the nanoparticle. At long anneal times, this species dominates over the VO_2

Tilted SEM images (Figure 3) allow us to measure the contact angle between the nanoparticles and substrate. Contact angle θ obeys the Young-Laplace equation

$$\gamma_{Si} = \gamma_i + \gamma_{VO_2}\cos(\theta) \qquad \text{(Equation 5)}$$

where γ_{Si} and γ_{VO_2} are the surface energies of the Si substrate and VO_2, respectively, and γ_i is the interface energy between them. Using literature values for $\gamma_{Si} = 39$ mJ/m^2 (experimental, from reference,[27] for p-type, B-doped Si(100) with native oxide, interpolated for Si with resistivity 0.1-1 Ωcm), $\gamma_{V_2O_5} = 90$ mJ/m^2 (experimental, from reference,[28] average of tabulated values), and $\gamma_{VO_2} = 320$ mJ/m^2 (theoretical, average from references [29] and, [30] for (110) rutile planes, which our XRD measurements in the Supporting Information, section *c*, show to be parallel to the substrate), we can calculate the interface energy at different time steps (Table 1).

Since surface energies vary with temperature, and since no experimental surface energy values are available for VO₂, these values are merely approximations, but they represent (to the best of our knowledge) the first approximations to the VO₂/Si and V₂O₅/Si interface energies.

Table 3.1: Measured contact angles and calculated interface energies for VO₂ and V₂O₅ nanoparticles on Si.

	10min	15min	20min	30min	40min
$\theta(°)$	122 ± 2	47 ± 2	42 ± 2	33 ± 1	29 ± 2
γ_i (mJ/m²)	210	x	x	x	-40

Uncertainties on contact angle measurements represent one standard error of the mean (refer to Supporting Information for details on the contact angle measurement). The contact angle is initially large (yielding $\gamma_i \approx 210$ mJ/m²), corresponding to its value for VO₂. As annealing proceeds and V₂O₅ begins to form, the contact angle decreases, asymptotically approaching its value for V₂O₅ (with $\gamma_i \approx -40$ mJ/m²). Intermediate values for γ_i are not listed, as they do not represent actual interfacial energies for either species.
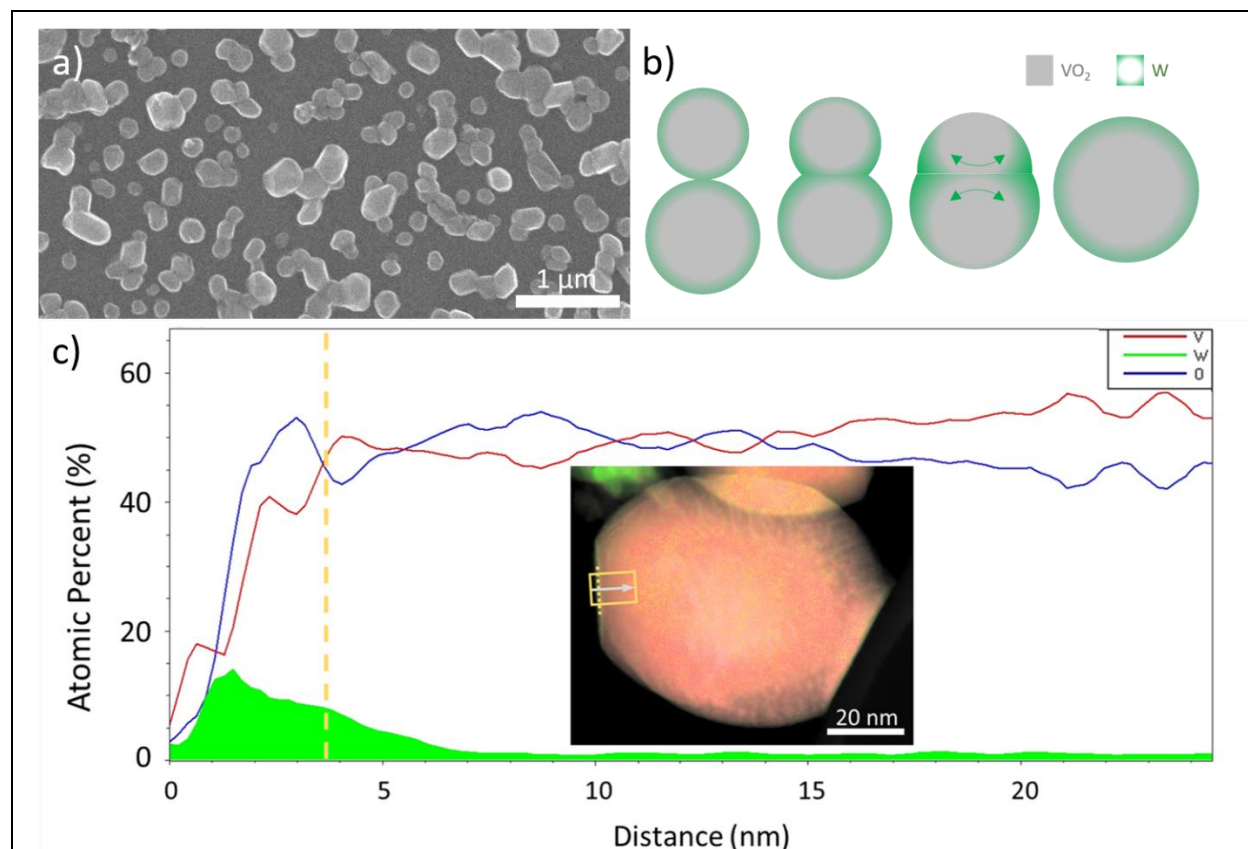
Figure 3.4: Tungsten-doped dewetted nanoparticles (a) are more strongly faceted and tend to group into clusters. Energy-dispersive spectroscopy in TEM (c) shows that the tungsten dopants are concentrated at the nanoparticle surface. For two such particles to aggregate, the W-dopants must be extruded from the interfacial region (c), increasing the energy barrier to nanoparticle aggregation.

Tungsten-doped VO_2 films also form nanoparticles through dewetting, but with two significant qualitative differences (Figure 4). First, W-doped films require a higher temperature to dewet; undoped films dewet at 500°C, but W-doped films require at least 600°C. When annealed at ≥600°C, both doped and undoped samples develop a rough film on revealed areas of the substrate (between nanoparticles), which we attribute to oxidation of the substrate (see Supporting Information, section *d* for comparison of doped and un-doped films annealed at different temperatures). Second, unlike the well-separated, nearly hemispherical nanoparticles that form from undoped films, W-doped form particles that are distinctly faceted and clustered together (Figure 4a).

Energy dispersive x-ray spectroscopy (EDS) in a scanning transmission electron microscope (STEM) allows us to map out the distribution of W-atoms in some of these nanoparticles (Figure 4c). We find that the W concentration is highest at the outside edge (the first ~5-10 nm) of the nanoparticles, and decreases toward the center (additional examples in other nanoparticles, and a reference measurement on an un-doped nanoparticle, are presented in the Supporting Information, section *e*). Based on this observation, we conclude that both the higher dewetting temperature and the clustering behavior in W-doped films result from the W-rich boundary layer on the nanoparticle surface (Figure 4b). Coalescence of two crystalline particles generally involves an energy barrier associated with the atomic rearrangement necessary to incorporate one into the crystal lattice of the other;[31] the W-rich surface layer increases this barrier by the amount of energy necessary to move those W-atoms from the interface to the surface of the new, larger particle. Thus a higher temperature is required to overcome this increased energy barrier; and at any given point during the aggregation process, there are likely to be more particles that have met, but not fully merged into a single particle (hence the "clustering" noted above).

Finally, Figure 5 compares the phase transition behavior in doped and un-doped samples annealed at different conditions to produce contiguous films (yellow) or nanoparticles (red). Additional optical hysteresis curves for an undoped VO_2 film at various stages of dewetting can be found in Supporting Information, Figure S10. For undoped VO_2, there are two distinct differences in behavior for films vs nanoparticles: increased width and decreased contrast. The increased width of the hysteresis loop is a known effect in VO_2 nanoparticles due to their lower density of transition-nucleating defects.[32] The loss of contrast is due mainly to increased scattering from particles as their size approaches the wavelength of visible/near-IR light used for hysteresis measurements. For W-doped VO_2, the hysteresis loop does not broaden appreciably because the W-dopants themselves form transition-nucleating defects, but the loss of contrast due to increased scattering still occurs (this effect is less pronounced for the 5% W-doped sample shown because it is less fully-dewetted than its undoped and 8%-doped counterparts, see Supporting Information, section *d*). We observe no difference in T_c for W-doped films vs. nanoparticles. It is noteworthy that while W-doped films have poorer contrast than undoped films (as expected), this trend does not hold for nanoparticles; however, firm conclusions about the actual switching contrast of doped vs. undoped nanoparticles cannot be drawn without more fully accounting for scattering and particle size.
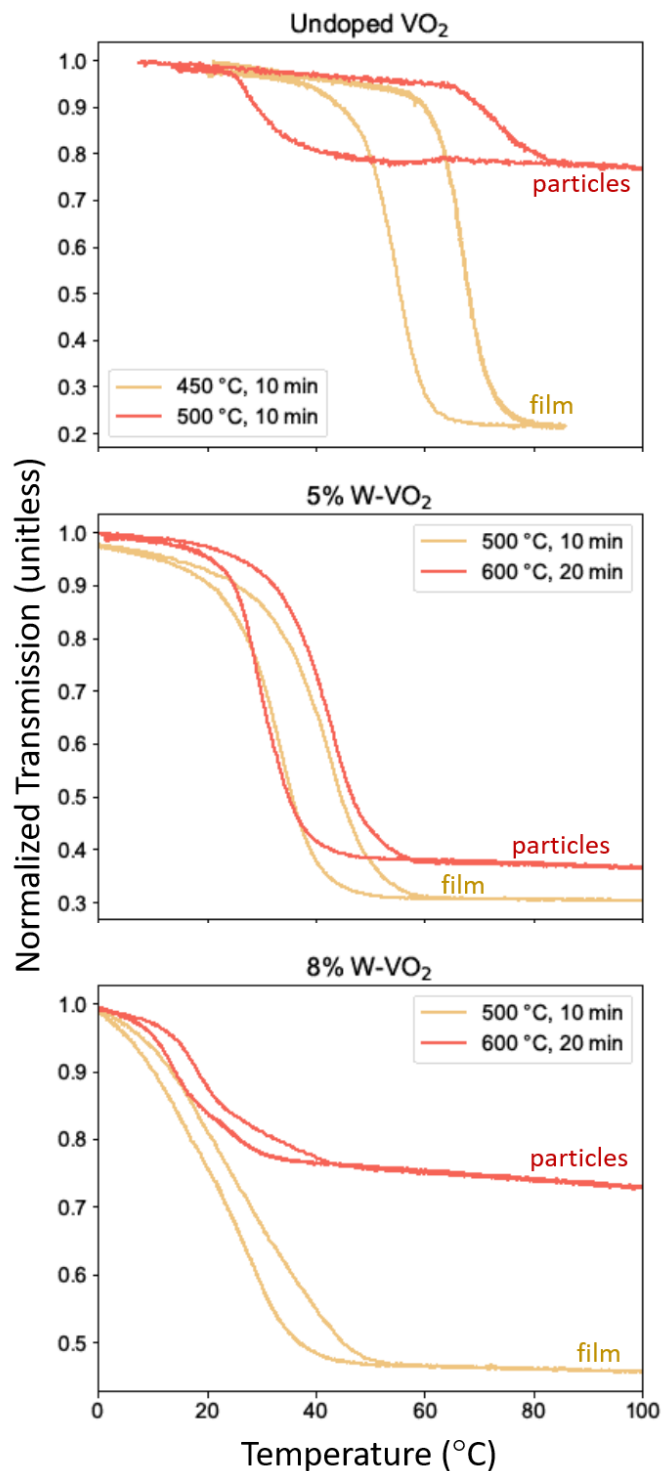
Figure 3.5: The hysteresis loop for undoped VO_2 nanoparticles (red) has greater width (due to fewer nucleating defects) and lower contrast (due to increased scattering) than for a corresponding thin film (yellow). In doped nanoparticles, the contrast is again decreased due to scattering (to differing amounts in each sample), but the transition temperature and hysteresis width are unchanged.

3.5 Conclusions

In conclusion, solid-state dewetting of VO_2 thin films is a viable method of rapidly producing large-scale, single-particle-thick films of VO_2 and W-doped VO_2 nanoparticles. We have shown that the average nanoparticle size can be adjusted not only by varying initial film thickness, but also by adjusting the anneal time — as the nanoparticles grow over time through Smoluchowski aggregation. This results in a well-defined particle-size distribution characteristic of the aggregation process. We also report estimates of the interfacial energies between VO_2/V_2O_5 and Si with a native oxide. These insights will be crucial to the design of actual devices based on dewetted-VO_2 nanoparticles. Despite the potential of W-doped VO_2 nanoparticles to enhance the performance of thermochromics, there has been little study on the dewetting process in W-doped VO_2 films. We have shown that nanoparticles formed by this method have a particularly high W-concentration on their surface, leading to an increased energy barrier to particle aggregation. Understanding this is an important step to improving the fabrication of dewetted, W-doped nanoparticles, and, more importantly, to understanding the effects of W-dopants on the VO_2 phase transition itself.

3.6 Acknowledgements

3.7 References

1.   Pouget, J. P., Basic aspects of the metal -insulator transition in vanadium dioxide VO_2: a critical review. *C. R. Phys.* **2021,** *22* (1), 37-87.
2.   Shi, R.; Shen, N.; Wang, J. W.; Wang, W. J.; Amini, A.; Wang, N.; Cheng, C., Recent advances in fabrication strategies, phase transition modulation, and advanced applications of vanadium dioxide. *Appl. Phys. Rev.* **2019,** *6* (1), 27.
3.   Hallman, K. A.; Miller, K. J.; Baydin, A.; Weiss, S. M.; Haglund, R. F., Sub-Picosecond Response Time of a Hybrid VO_2:Silicon Waveguide at 1550 nm. *Adv. Opt. Mater.* **2021,** *9* (4), 8.
4.   Lang, F. P.; Wang, H.; Zhang, S. J.; Liu, J. B.; Yan, H., Review on Variable Emissivity Materials and Devices Based on Smart Chromism. *Int. J. Thermophys.* **2018,** *39* (1), 20.
5.   Ulpiani, G.; Ranzi, G.; Shah, K. W.; Feng, J.; Santamouris, M., On the energy modulation of daytime radiative coolers: A review on infrared emissivity dynamic switch against overcooling. *Sol. Energy* **2020,** *209*, 278-301.
6.   Gao, Y. F.; Luo, H. J.; Zhang, Z. T.; Kang, L. T.; Chen, Z.; Du, J.; Kanehira, M.; Cao, C. X., Nanoceramic VO_2 thermochromic smart glass: A review on progress in solution processing. *Nano Energy* **2012,** *1* (2), 221-246.
7.   Chae, B. G.; Kim, H. T., Effects of W doping on the metal-insulator transition in vanadium dioxide film. *Physica B* **2010,** *405* (2), 663-667.

8. Mao, Z. P.; Wang, W.; Liu, Y.; Zhang, L. P.; Xu, H.; Zhong, Y., Infrared stealth property based on semiconductor (M)-to-metallic (R) phase transition characteristics of W-doped VO_2 thin films coated on cotton fabrics. *Thin Solid Films* **2014,** *558*, 208-214.

9. Huang, Z. Y.; Wu, Z. M.; Ji, C. H.; Dai, J. H.; Xiang, Z. H.; Wang, D.; Dong, X.; Jiang, Y. D., Improvement of phase transition properties of magnetron sputtered W-doped VO_2 films by post-annealing approach. *J. Mater. Sci.-Mater. Electron.* **2020,** *31* (5), 4150-4160.

10. Zou, J.; Chen, X. Y.; Xiao, L., Phase transition performance recovery of W-doped VO_2 by annealing treatment. *Mater. Res. Express* **2018,** *5* (6), 9.

11. Lopez, R.; Haynes, T. E.; Boatner, L. A.; Feldman, L. C.; Haglund, R. F., Temperature-controlled surface plasmon resonance in VO_2 nanorods. *Opt. Lett.* **2002,** *27* (15), 1327-1329.

12. Nag, J.; Haglund, R. F., Synthesis of vanadium dioxide thin films and nanoparticles. *J. Phys.-Condens. Mat.* **2008,** *20* (26), 14.

13. Zeng, W.; Chen, N.; Xie, W. G., Research progress on the preparation methods for VO_2 nanoparticles and their application in smart windows. *Crystengcomm* **2020,** *22* (5), 851-869.

14. Zhang, Y. Q.; Xiong, W. M.; Chen, W. J.; Zheng, Y., Recent Progress on Vanadium Dioxide Nanostructures and Devices: Fabrication, Properties, Applications and Perspectives. *Nanomaterials* **2021,** *11* (2), 48.

15. Zhu, Z. H.; Evans, P. G.; Haglund, R. F.; Valentine, J. G., Dynamically Reconfigurable Metadevice Employing Nanostructured Phase-Change Materials. *Nano Lett.* **2017,** *17* (8), 4881-4885.

16. Malarde, D.; Johnson, I. D.; Godfrey, I. J.; Powell, M. J.; Cibin, G.; Quesada-Cabrera, R.; Darr, J. A.; Carmalt, C. J.; Sankar, G.; Parkin, I. P.; Palgrave, R. G., Direct and continuous hydrothermal flow synthesis of thermochromic phase pure monoclinic VO_2 nanoparticles. *J. Mater. Chem. C* **2018,** *6* (43), 11731-11739.

17. Pauli, S. A.; Herger, R.; Willmott, P. R.; Donev, E. U.; Suh, J. Y.; Haglund, R. F., X-ray diffraction studies of the growth of vanadium dioxide nanoparticles. *J. Appl. Phys.* **2007,** *102* (7), 6.

18. Peter, A. P.; Martens, K.; Rampelberg, G.; Toeller, M.; Ablett, J. M.; Meersschaut, J.; Cuypers, D.; Franquet, A.; Detavernier, C.; Rueff, J. P.; Schaekers, M.; Van Elshocht, S.; Jurczak, M.; Adelmann, C.; Radu, I. P., Metal-Insulator Transition in ALD VO_2 Ultrathin Films and Nanoparticles: Morphological Control. *Adv. Funct. Mater.* **2015,** *25* (5), 679-686.

19. Suh, J. Y.; Lopez, R.; Feldman, L. C.; Haglund, R. F., Semiconductor to metal phase transition in the nucleation and growth of VO_2 nanoparticles and thin films. *J. Appl. Phys.* **2004,** *96* (2), 1209-1213.

20. Zeng, W.; Lai, H. J.; Chen, T. Y.; Lu, Y. H.; Liang, Z. H.; Shi, T. T.; Chen, K.; Liu, P. Y.; Xie, F. Y.; Chen, J.; Xu, J. B.; Chen, Q. L.; Xie, W. G., Size and crystallinity control of dispersed VO_2 particles for modulation of metal-insulator transition temperature and hysteresis. *Crystengcomm* **2019,** *21* (38), 5749-5756.

21. Leroy, F.; Borowik, L.; Cheynis, F.; Almadori, Y.; Curiotto, S.; Trautmann, M.; Barbe, J. C.; Muller, P., How to control solid state dewetting: A short review. *Surf. Sci. Rep.* **2016,** *71* (2), 391-409.

22. Thompson, C. V., Solid-State Dewetting of Thin Films. *Annual Review of Materials Research* **2012,** *42* (1), 399-434.

23. Nishikawa, K.; Kishida, Y.; Ito, K.; Tamura, S.; Takeda, Y., Near-infrared localized surface plasmon resonance of self-growing W-doped VO_2 nanoparticles at room temperature. *Appl. Phys. Lett.* **2017,** *111* (19), 5.

24. Meakin, P., Diffusion-limited droplet coalescence. *Physica A* **1990,** *165* (1), 1-18.

25. Sholl, D. S.; Skodje, R. T., Late-stage coarsening of adlayers by dynamic cluster coalescence. *Physica A* **1996,** *231* (4), 631-647.

26. Woehl, T. J.; Park, C.; Evans, J. E.; Arslan, I.; Ristenpart, W. D.; Browning, N. D., Direct Observation of Aggregative Nanoparticle Growth: Kinetic Modeling of the Size Distribution and Growth Rate. *Nano Lett.* **2014,** *14* (1), 373-378.

27. Narayan, S. R.; Day, J. M.; Thinakaran, H. L.; Herbots, N.; Bertram, M. E.; Cornejo, C. E.; Diaz, T. C.; Kavanagh, K. L.; Culbertson, R. J.; Ark, F. J.; Ram, S.; Mangus, M. W.; Islam, R., Comparative

Study of Surface Energies of Native Oxides of Si(100) and Si(111) via Three Liquid Contact Angle Analysis. *MRS Adv.* **2018,** *3* (57-58), 3379-3390.
28.   Overbury, S. H.; Bertrand, P. A.; Somorjai, G. A., The Surface Composition of Binary Systems. Prediction of Surface Phase Diagrams of Solid Solutions. *Chem. Rev.* **1975,** *75* (5), 547-560.
29.   Wang, L. X.; Ren, H.; Chen, S.; Chen, Y. L.; Li, B. W.; Zou, C. W.; Zhang, G. B.; Lu, Y. L., Epitaxial Growth of Well-Aligned Single-Crystalline VO_2 Micro/ Nanowires Assisted by Substrate Facet Confinement. *Cryst. Growth Des.* **2018,** *18* (7), 3896-3901.
30.   Mellan, T. A.; Grau-Crespo, R., Density functional theory study of rutile VO2 surfaces. *J. Chem. Phys.* **2012,** *137* (15), 8.
31.   Mu, Z.; Tang, R. K.; Liu, Z. M., Construction of Inorganic Bulks through Coalescence of Particle Precursors. *Nanomaterials* **2021,** *11* (1), 24.
32.   Lopez, R.; Haynes, T. E.; Boatner, L. A.; Feldman, L. C.; Haglund, R. F., Size effects in the structural phase transition of VO_2 nanoparticles. *Phys. Rev. B* **2002,** *65* (22), 5.

3.8 Supporting Information

3.8.a Experimental

        Thin films of undoped VO_2 were produced by atomic layer deposition (ALD) in a PicoSun R-200 system from water and tetrakis[ethylmethylamino] vanadium (TEMAV) precursors for 2500 pulse cycles. Each precursor was flowed at 150 sccm in 5 sec pulses spaced 1 sec apart. Substrate was held at 150°C, TEMAV bottle at 70°C, and valve block at 100°C. ALD film thickness was measured by spectroscopic ellipsometry (JA Woollam M-2000VI) to be 111±2 nm. All ALD samples were cut from two 4-in. wafers prepared in the same way. Tungsten-doped VO_2 films (and corresponding undoped control films) were prepared with RF magnetron sputtering in an Angstrom Amod multimode deposition tool, at ~280 W, in 6 mtorr Ar (20 sccm) and O_2 (1 sccm). Films were deposited from metal W:V alloy targets, with 0:100 wt%, 5:95 wt% and 8:92 wt% compositions, for 450 sec, 1000 sec, and 630 sec, respectively. Sputtered film thickness was measured with a Bruker Dektak 150 stylus profilometer to be 87±4 nm, 75±4 nm, and 110±10 nm, respectively. For both ALD and sputtered films, a post-deposition annealing process (450°C, 250 mtorr O_2, 10 min) was required to adjust stoichiometry and crystallinity in order to produce switching VO_2 thin films. Dewetting was controlled by adjusting the temperature and time of the annealing process.

        Films and nanoparticles at each set of anneal conditions were observed with scanning electron microscopy (SEM), using a Zeiss Merlin SEM with Gemini II Column, an in-lens detector, and ~2 kV electron voltage. For undoped samples, grain/nanoparticle sizes and distributions were extracted using the open-source software ImageJ. The raw images were first converted to greyscale, then converted to black and white using a threshold function, and finally inverted to yield black particles on a white background. ImageJ's built-in particle analysis tool was then used to detect, count, and measure the area of each particle (after scaling the image based on a scale bar produced by the SEM software). For anneal times under 15 minutes, many grains/particles were still in contact with neighboring particles, though divided by a clear grain boundary. In order for the software to distinguish such grain/particles, it was necessary to mark some of the boundaries manually with a black line. Figure S1 demonstrates this markup process, with the raw (or purely computer-processed) images on the left, and the manually adjusted images on the right. The effective radius of each particle is calculated from its measured area by assuming each grain/particle is a spheric section (with a circular cross-section). From this data, a

normalized distribution of nanoparticle sizes and other statistical analyses are performed using Matlab software.

Figure 3.S1: In samples with grains/particles that are in contact, the grain boundaries are often missed by the thresholding and particle analysis algorithms, making it necessary to adjust the images by hand. Raw SEM images (5 and 8 min) and threshold-processed images (10 and 12 min) are shown on the left; their adjusted counterparts on the right.
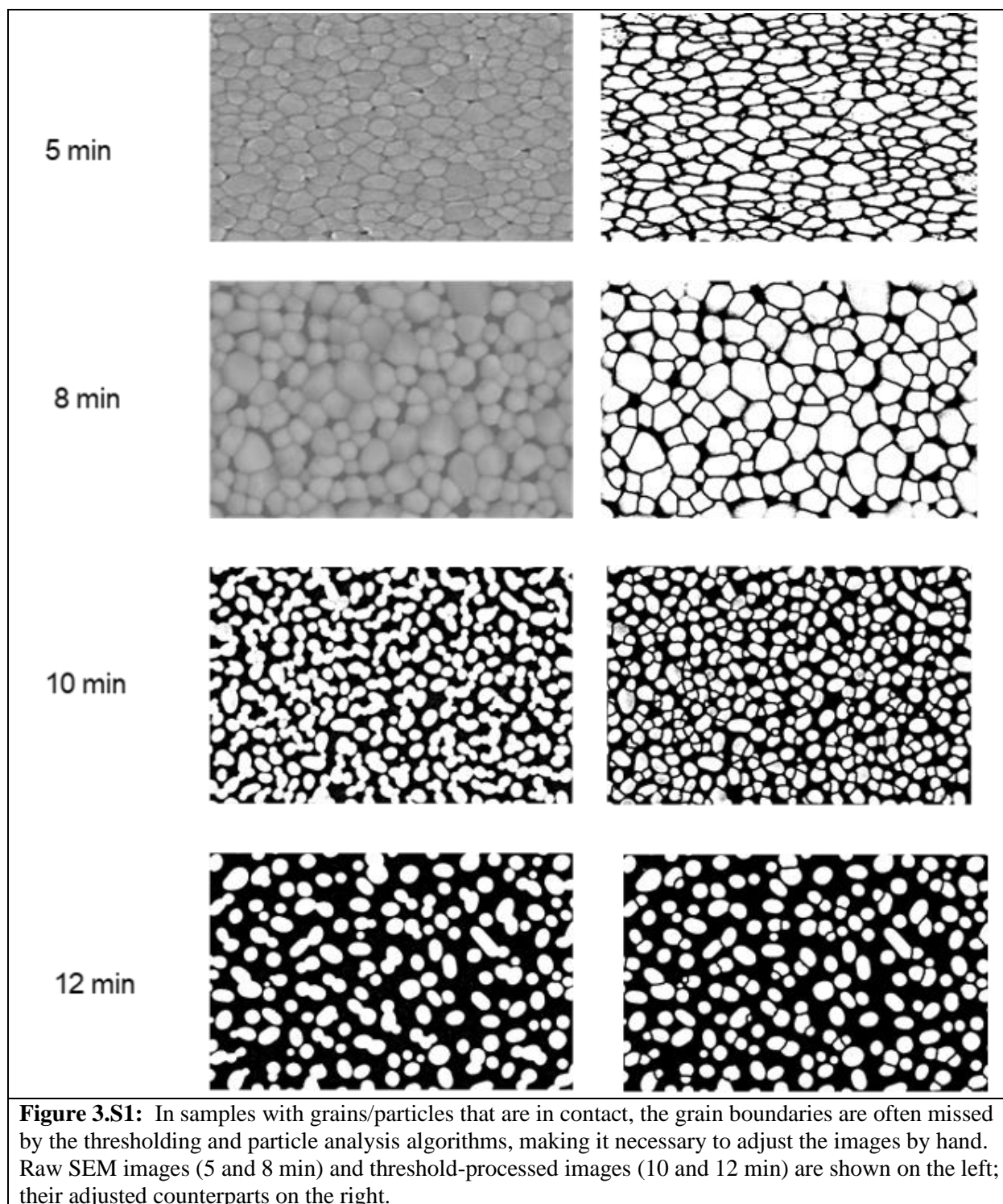
Tilted SEM images were collected at an angle of 20.5°(for the 10-min sample) and 10° (for all others) above the plane of the surface, with the rotation axis parallel to the horizontal axis of the SEM images. Contact angles were measured manually using an angle measurement tool in ImageJ, measuring the tangent of the nanoparticle relative to the horizontal at its corner (examples of these angle measurements are shown in Figure S2a). For each anneal time, angles are measured for multiple particles and averaged to give the reported contact angle. Since these images are not collected exactly edge-on, but at a slight tilt, a geometric correction must be applied to find the actual contact angle. If the true contact angle is θ, the measured angle is θ', and the tilt of the viewing axis above the substrate plane is ϕ, then

$$\theta = \arccos \frac{\cos\theta' + \cos\phi - 1}{\cos\phi} \qquad \text{(Equation 1)}$$

Figure 3.S2: To extract contact angles, the angle between the horizontal and the particle tangent was measured at its point of contact with the surface, for several particles at each time step (a, yellow marks). The particles can be modeled as sections of a sphere cut by the plane of the substrate surface (b). When viewed along a direction not parallel to the surface (c), the apparent height of that section changes, affecting the measured contact angle.

To derive this correction, consider a sphere of radius R centered at the origin of a coordinate system: $R^2 = x^2 + y^2 + z^2$. Let the z-axis represent the viewing angle of our SEM image. The nanoparticle is a spheric section formed by the intersection of this sphere with the substrate plane. Let this plane be parallel to the x-axis, inclined relative to the z-axis by the viewing angle ϕ, and a distance $d = R - h$ from the origin. Then the plane can be represented $y = \frac{R-h}{cos\phi} - \frac{sin\phi}{cos\phi} z$ for all x, the spheric section has height h above the substrate plane, and the vector $R\hat{n} = Rsin\phi\hat{z} + Rcos\phi\hat{y}$ is the radial vector normal to the substrate plane. Figure S2b shows a schematic of this scenario.

When viewed along the substrate plane (Figure S2c), the particle appears as the section (height h) of a circle (radius R). When viewed along the z-axis, however, it appears as the projection of the 3D spheric section onto the xy-plane. The intersection of the sphere and substrate plane is given by $R^2 = x^2 + (R - h)^2 + \frac{1}{sin^2\phi}[y - (R - h)cos\phi]^2$, a circle in 3D space, but an ellipse projected onto the xy-plane. This ellipse has a centerline $y = (R - h)cos\phi$. The projection of our particle (Figure S2d) is then bounded below by the bottom half of this ellipse and above by a circular section with radius R and height $h' = R - (R - h)cos\phi$.

The contact angle of a circular section is given by $\theta = arccos\frac{h}{R}$. Applying this to the actual and apparent particle cross-sections, and using the above equation relating h and h', we can solve for the actual contact angle θ in terms of the apparent angle θ', yielding Equation 1 above.

An x-ray diffractometer (XRD) (Rigaku Smart Lab, Cu Kα source) was used to perform standard θ-2θ measurements (scan 2θ from 20°-80°, 0.01°steps, 10°/min). Optical hysteresis measurements were performed with a custom setup using a white-light tungsten halogen lamp (~3000 K color temperature) and an amplified InGaAs photodiode. Transmission electron microscopy (TEM) and scanning transmission electron microscope energy dispersive spectroscopy (STEM-EDS) measurements were acquired on a Tecnai Osiris TEM/STEM operating at 200 kV. Drift-corrected STEM-EDS maps were acquired with a 1 nA probe current and rendered using Bruker Esprit version 1.9. Nanoparticle samples were prepared for TEM by scraping them off of the substrate with a razor blade, mixing them with IPA into a slurry, dipping a TEM grid into the slurry, and allowing it to dry. Some nanoparticles thus adhered to the grid.

3.8.b PSD Fitting Results

Particle size distributions (PSD) were extracted from SEM images for VO_2 films annealed at different lengths of time (5-30 min), and used to calculate average particle radius $\bar{r}$ and standard deviation $\Delta\bar{r}$ (plotted in the main text, Figure 2b). The diffusion coefficient exponent α and 95% confidence interval $\Delta\alpha$ are extracted by fitting each PSD to the theoretical distribution $F(\varphi)$ using the "maximum likilhood estimates" function in MATLAB, with α as a free parameter. The measured PSDs and best fit $F(\varphi)$ curves are plotted in Figure S3a. For comparison, they are plotted with $F(\varphi)$ for a constant $\alpha = 0.5$ in Figure S3b. To quantify how well each experimental PSD matches the shape of the theory, we compare $\Delta\bar{r}$, skewness, and kurtosis to $F(\varphi)$ with the corresponding value of α. The results are summarized in Table S1.

Figure 3.S3: The measured particle size distributions can be well fit by the predicted function $F(\varphi)$ with α as the only fit parameter (a). For comparison, using a constant value of $\alpha = 0.5$ qualitatively reproduces the PSD (b). The values of α obtained by fitting experimental PSDs vary over time due to physical effects not accounted for in the model (c). A higher value of α corresponds to a narrower distribution (d). A log-log plot of particle radius vs anneal time (e) produces the same value of $\alpha \approx -0.7$ as the curve fit presented in the main text.

As noted in the main text, α varies considerably across the different data sets, though it should be a constant for a given system (VO$_2$ on Si at 500°C). Figure S3c shows the extracted values of α as a function of anneal time. Qualitatively, a higher value of α corresponds to a sharper, narrower distribution, and vice versa (see Figure S3d). At short (<10 min) and long (>20 min) anneal times, $\alpha \approx 0.3$, but during the timeframe where particle aggregation dominates (10-20 min), α appears to decrease from ~1 to ~ -0.2. On the other hand, fitting the radius vs.

time data (main text, Figure 2b) yielded a value of $\alpha \approx -0.7$. To confirm this fit value, the slope of a log-log plot of radius vs time (Figure S3e) also yields $\frac{1}{3(1+\alpha)} = 1.16$, or $\alpha \approx -0.7$. These discrepancies can be explained in terms of deviations of our system from the model. Initially, the PSD will be similar to that of the as-deposited film, and governed by the physics of film deposition rather than by the aggregation. At short times, when particles are small and closely packed, the probability of more than two particles colliding simultaneously is high; while at longer times, the formation of V_2O_5, which both wets Si better and has a lower density, causes the particle radii to be larger than they would be otherwise. Both of these effects will cause the measured particle radii to grow faster than our model would predict, explaining the poor value of α obtained from fitting the radius vs time data. The extracted values of α at intermediate times (~13-18 min) are probably the best approximation, and suggest that $\alpha \approx 0.2 - 0.3$ for this system.

Table 3.S1: Fit results and statistical analysis of PSDs.

PSD	α	$\Delta\alpha$	$\bar{r}$	$\Delta\bar{r}$	Kurtosis	Skewness
5 min	0.23	0.10	0.04	0.01	2.9	0.27
$F(\varphi)$	0.23	-	-	0.01	2.6	0.11
8 min	0.35	0.16	0.09	0.03	3.3	0.61
$F(\varphi)$	0.35	-	-	0.03	2.7	0.09
10 min	0.99	0.15	0.21	0.05	2.5	0.10
$F(\varphi)$	0.99	-	-	0.05	2.8	0.04
12 min	1.12	0.22	0.27	0.06	2.7	0.05
$F(\varphi)$	1.12	-	-	0.06	2.8	0.04
13 min	0.29	0.11	0.25	0.08	11.0	1.99
$F(\varphi)$	0.29	-	-	0.08	2.6	0.10
15 min	0.25	0.10	0.39	0.13	3.2	0.57
$F(\varphi)$	0.25	-	-	0.12	2.6	0.11
17 min	0.02	0.13	0.35	0.12	3.2	0.38
$F(\varphi)$	0.02	-	-	0.12	2.5	0.13
18 min	0.18	0.10	0.40	0.13	3.1	0.58
$F(\varphi)$	0.18	-	-	0.13	2.6	0.11
20 min	-0.17	0.07	0.49	0.20	4.1	0.86
$F(\varphi)$	-0.17	-	-	0.18	2.4	0.15
30 min	0.37	0.17	2.54	0.78	2.7	0.32
$F(\varphi)$	0.37	-	-	0.76	2.7	0.09

The standard deviations $\Delta\bar{r}$ agree very well between the actual distributions and the best-fit PSDs, showing that the theory well describes the spread of particle sizes we observe. Kurtosis measures how large the "tails" of the distribution are relative to a Gaussian (for which kurtosis = 3); a sharper peak with heavy tails has a larger kurtosis, and vice-versa. All of our calculated distributions $F(\varphi)$ have a sub-Gaussian kurtosis (slightly lighter tails than a Gaussian); in each of the measured distributions, kurtosis is slightly higher. Skewness is a measure of asymmetry in a distribution, zero for a Gaussian distribution. $F(\varphi)$ has a positive skewness reflecting the heavier tail toward larger radii. In the measured distributions, skewness is still higher than predicted, and varies sample-to-sample more than the kurtosis. The deviation of skewness and

kurtosis from the expected may be due in part to the failures of our assumptions cited above; but since the skewness and kurtosis (unlike the fitted values of α) don't follow any clear trends with anneal time, their variation is probably due more to noise in the data. Performing this analysis on a larger sample size could improve the statistics and clarify these differences. The 13-min sample is clearly an outlier, with exceptionally large kurtosis (11) and skewness (1.99). Its unusual shape can be easily seen in the distribution (Figure S3a and S3b, green curve) with a sharp peak below $\varphi = 1$. This is again attributed to random variation, resulting in an unusual concentration of smaller-than-average particles in the sampled area.

3.8.c *XRD Measurements on VO₂ Nanoparticles*

X-ray diffraction spectra (Figure S4a) show peaks corresponding to VO_2 (marked in purple) as well as to the silicon substrate (black) and the steel sample stage (grey). Only one VO_2 plane can be identified: the XRD peaks at $2\theta = 25.2°$, $2\theta = 27.9°$, and $2\theta = 57.6°$ corresponding to the $\{011\}$ family of planes in M1-phase VO_2. This suggests that the nanoparticles tend to orient with the $\{011\}$ planes parallel to the substrate; this is the lowest-surface-energy plane for VO_2, and commonly forms bounding facets on VO_2 crystals. However, as this is the strongest reflection in VO_2, small proportions of other orientations could be present and below the noise level. The absence of corresponding peaks for M2- and R-phase VO_2 ($\{20\bar{1}\}_{M2}$ at $2\theta = 27.4°$, $\{201\}_{M2}$ at $2\theta = 28.3°$, and $\{110\}_R$ at $2\theta = 27.7°$) shows that we have phase-pure M1 VO_2.

This $\{011\}_R$ peak evolves as a function of anneal time (Figure S4b). Peak height, center position, and breadth (Figure S4c) are extracted by fitting to a sum of two Lorentz peaks, (peak splitting arises from the presence of Cu $K_{\alpha1}$ and $K_{\alpha2}$ lines in the X-ray source). Solid lines (black error bars) represent the lower-angle peak, and dotted lines (grey error bars) the higher. Initially, the peaks are very weak and broad (overlapping to the point of being indistinguishable), due to poor crystallinity of as-deposited VO_2. At intermediate anneal times, the intensity increases as the VO_2 becomes more crystalline and as the crystalline nanoparticles grow larger. At long times, the intensity decreases and peaks broaden (becoming indistinguishable) again, as the VO_2 is transformed into V_2O_5. The absence of any additional XRD peaks corresponding to V_2O_5 suggests that the V_2O_5 formed by oxidation is highly amorphous.

3.8.d *Undoped and W-Doped Films Annealed at Different Temperatures and Times*

Figures S5, S6, and S7 demonstrate the results of different annealing conditions tested on undoped, 5 wt% W-doped, and 8 wt% W-doped sputtered films. Annealing at 450°C for 10 minutes is the standard annealing protocol to produce switching thin films, and in each case results in a polycrystalline film with small, densely packed grains. In undoped samples, dewetting begins to occur at 500°C, 10 min; at 20 min, the nanoparticles have grown through aggregation and begin to be surrounded by "skirts" or "puddles" of V_2O_5; by 40 min, the particles are fully converted into V_2O_5 with a markedly different shape. At 600°C, particles are fully V_2O_5 by even 10 min. In doped samples, on the other hand annealing at 500°C for any amount of time does not lead to dewetting, but only grain coarsening. Significant dewetting is not observed until 600°C, 20 min.
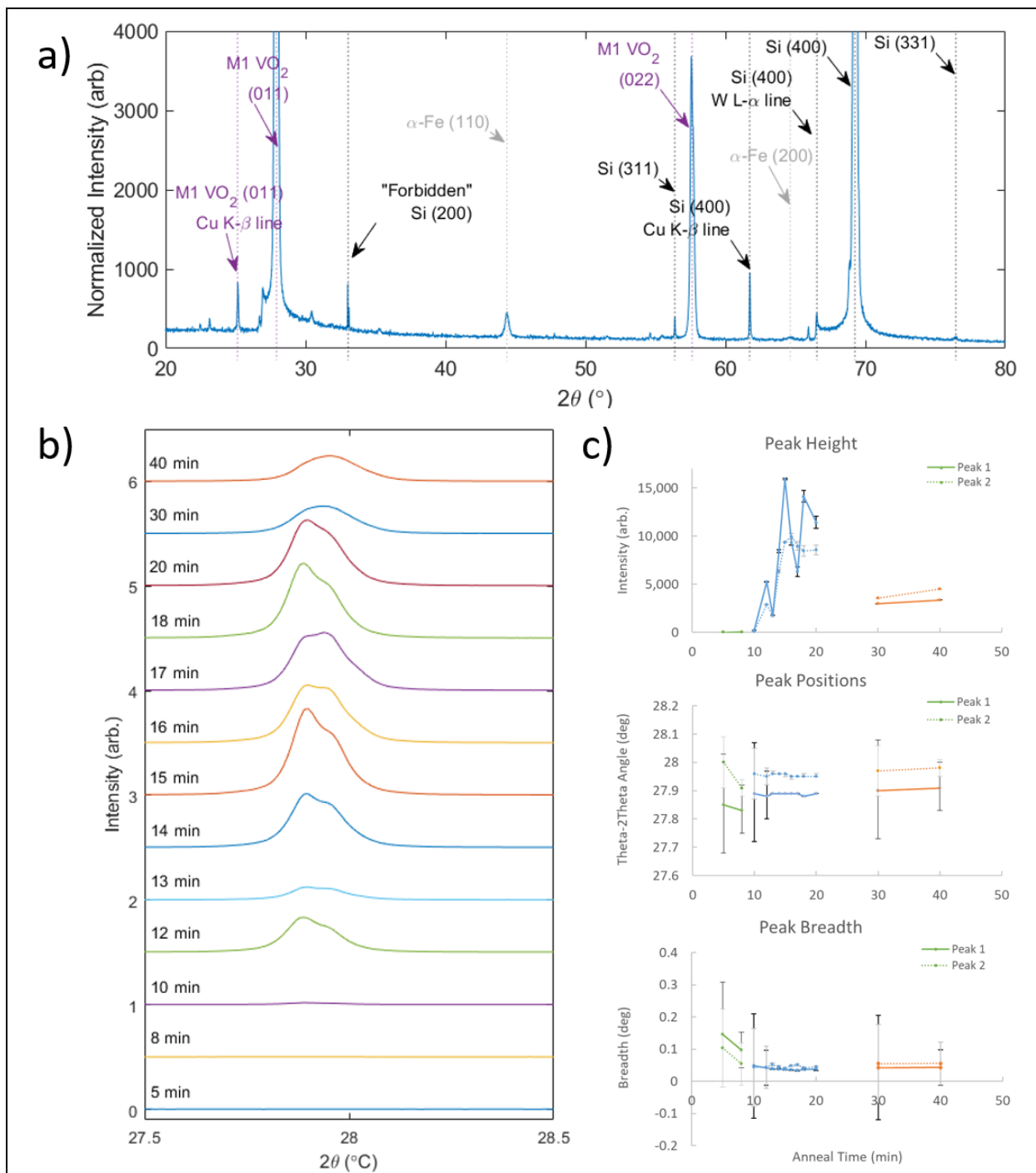
Figure 3.S4: XRD spectra (a) show the presence of (011)-oriented M1-phase VO$_2$. The corresponding peak changes as a function of anneal time (b), revealing information about the change in crystallinity over time (c).

	10 minutes	20 minutes	40 minutes
450°			
500°C			
600°			
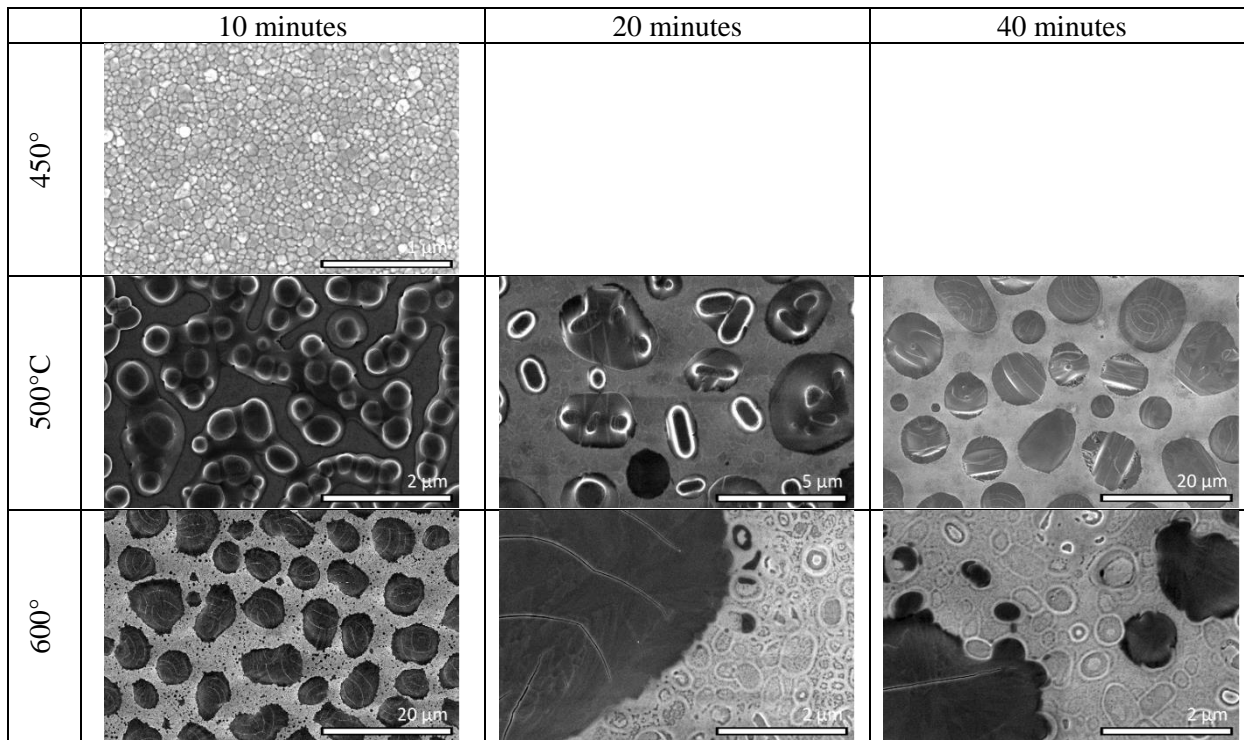
Figure 3.S5: Undoped VO$_2$ annealed, from top to bottom, at 450, 500, and 600°C, and from left to right, for 10, 20, and 40 minutes.

	10 minutes	20 minutes	40 minutes
450°			
500°			
600°			
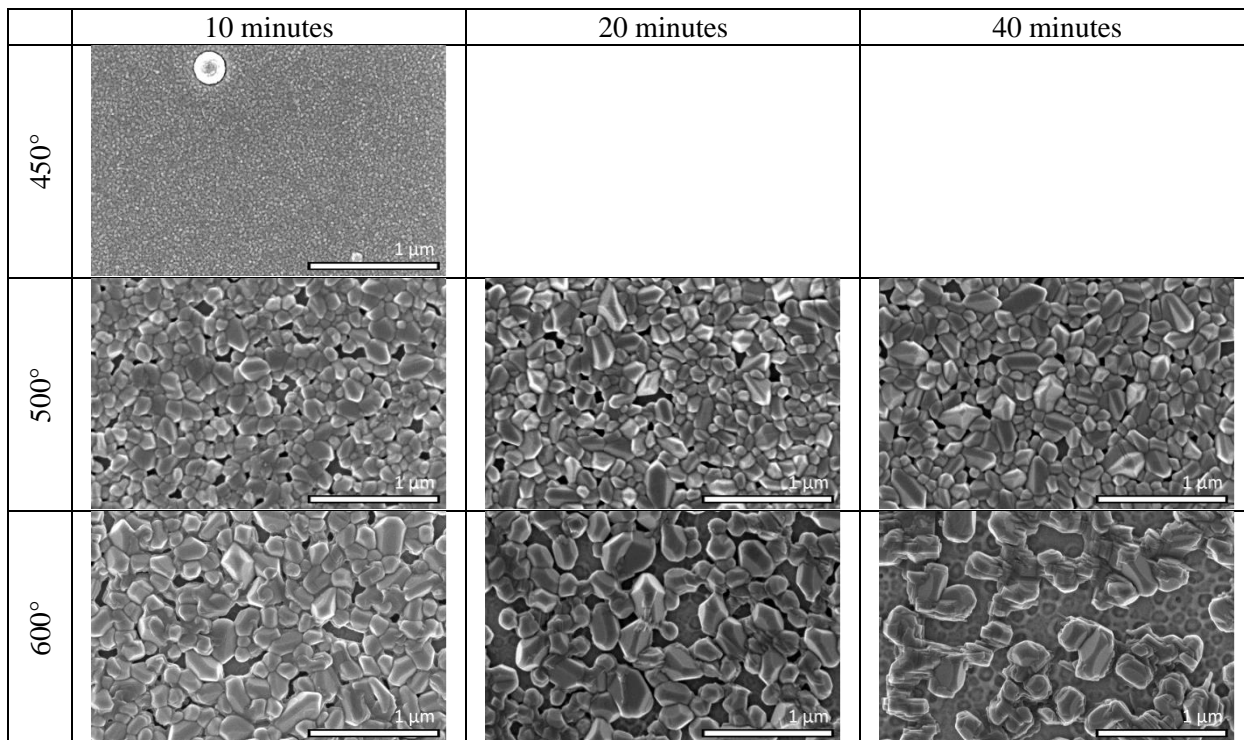
Figure 3.S6: 5 wt.% VO$_2$ annealed, from top to bottom, at 450, 500, and 600 °C, and from left to right, for 10, 20, and 40 minutes.

	10 minutes	20 minutes	40 minutes
450°			
500°			
600°			
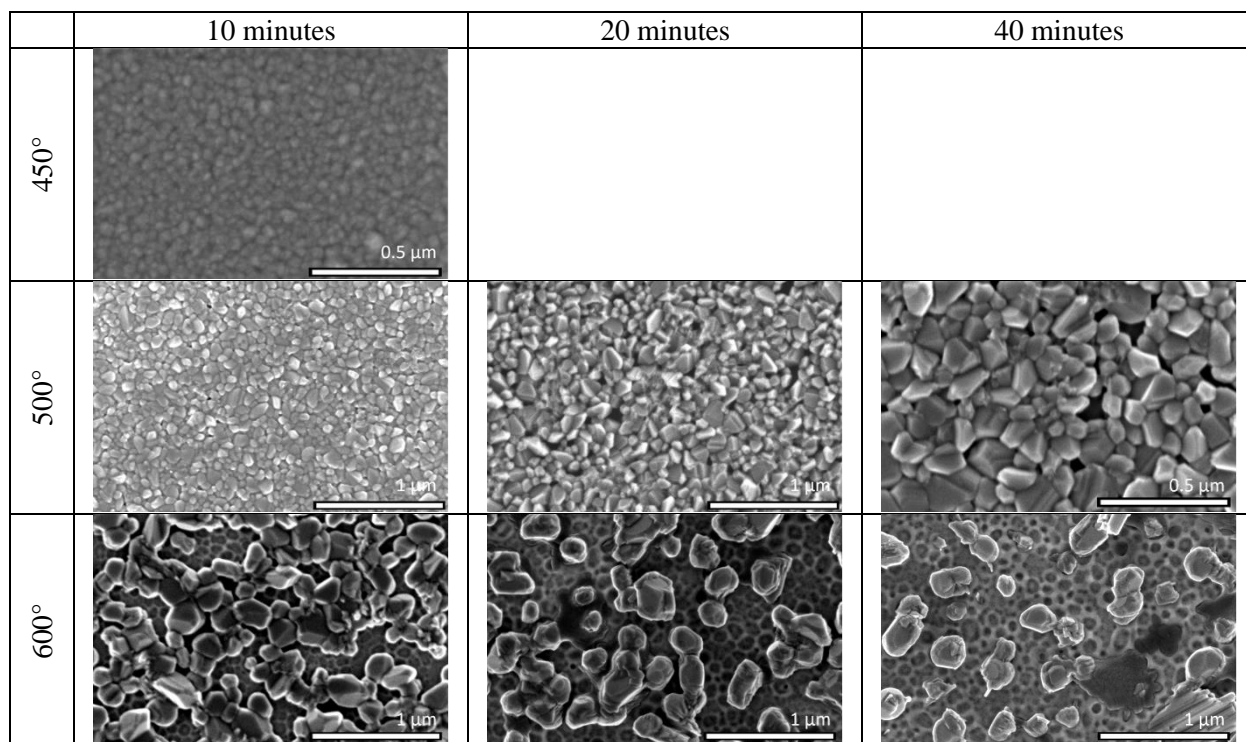
Figure 3.S7: 8 wt.% VO_2 annealed, from top to bottom, at 450, 500, and 600 °C, and from left to right, for 10, 20, and 40 minutes.
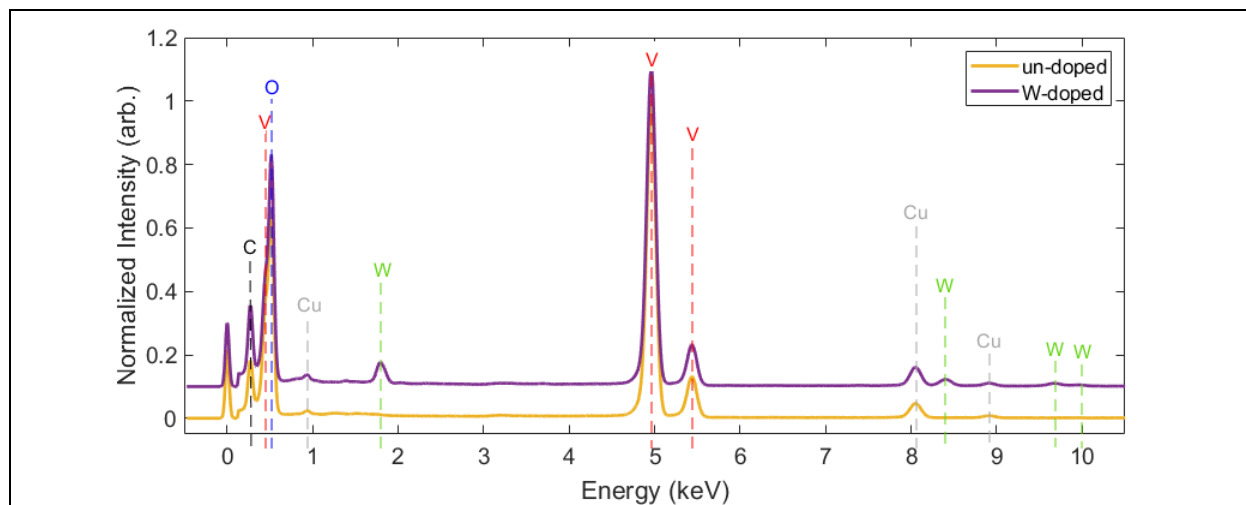
Figure 3.S8: EDS spectra confirm the presence of W in the doped nanoparticle (purple) as opposed to the undoped (yellow).

3.8.e Additional TEM Data

Energy dispersive spectroscopy (EDS) performed in a transmission electron microscope (TEM) allows for determination of the atomic species present in our nanoparticles. Figure S8 compares EDS spectra for an individual undoped (yellow) and W-doped (purple) nanoparticle.
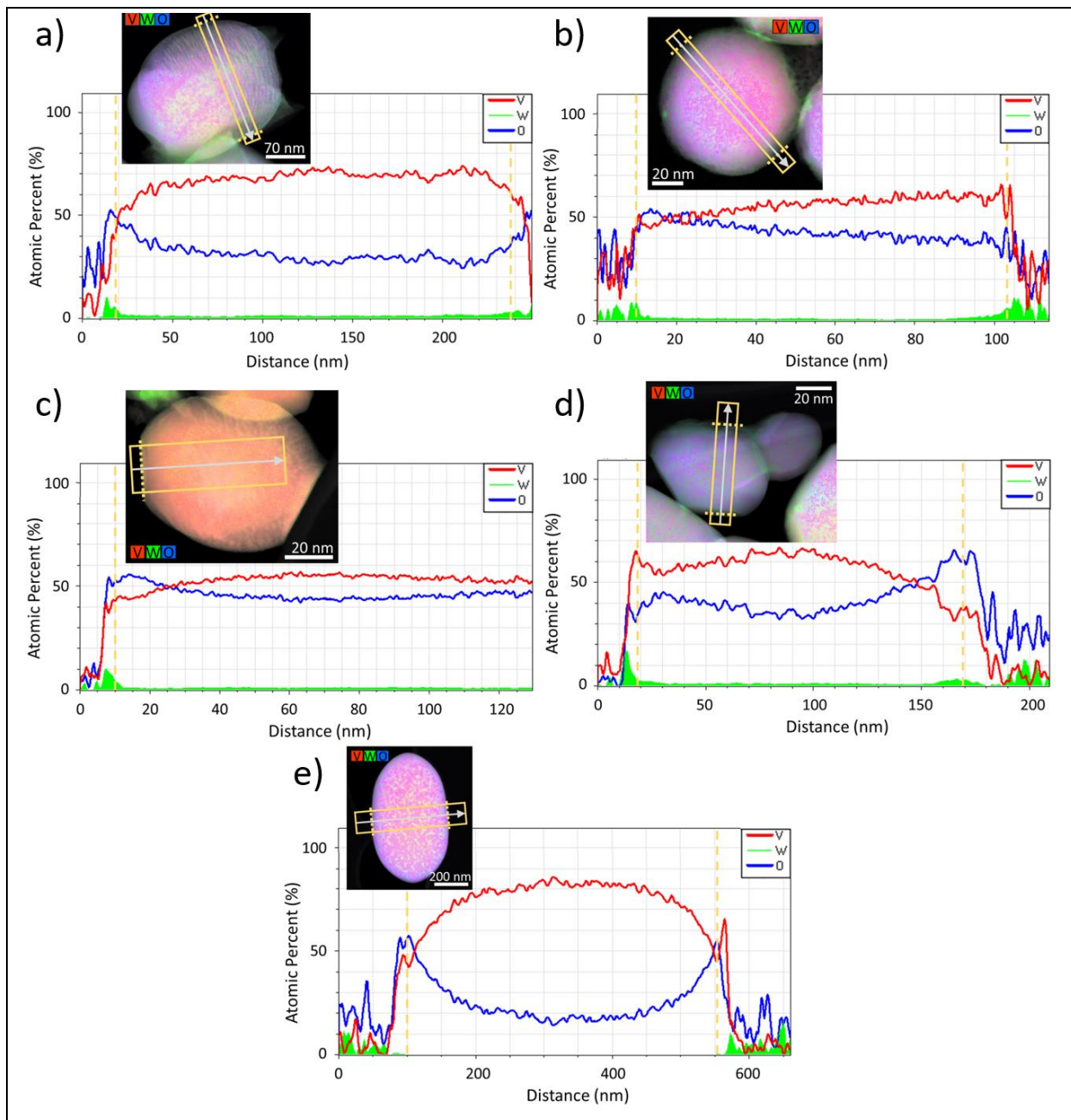
Figure 3.S9: Line scans taken from EDS maps (insets) for doped (a-d) and undoped (e) nanoparticles show that W and O both are present in higher concentrations at the nanoparticle surface.

In both samples, clear peaks are identified corresponding to V and O (from the VO_2), and from C and Cu (from the TEM grid). In the W-doped sample, additional peaks appear corresponding to W, as expected. By fitting the EDS spectra, the relative amounts of each element can be quantitatively determined, with the exception of V and O which have significant spectral overlap making them hard to deconvolve. Thus, we can accurately measure the W:V ratio, but not the V:O ratio. Averaging across 10 separate EDS maps (each containing one or

more nanoparticles), we measure the W:V ratio to be 3.3±0.3 : 97±3 (average±3σ), which is notably larger than the 2.4:97.6 ratio in the original sputtering target.

Furthermore, EDS maps show the distribution of atoms withing the nanoparticles with sub-nm spatial resolution. Figure S9 shows four EDS maps for doped nanoparticles (a-d) and one for an undoped nanoparticle (e). As pointed out in the main text, linescans (marked by yellow boxes along the direction of the grey arrow) show that the tungsten concentration is highest within the first few nm of the nanoparticle edges (marked by broken yellow lines), but is lower and constant throughout the bulk of the particle. On the other hand, no tungsten signal is observed within the un-doped nanoparticle, as expected. Note that random noise, amplified by the calculation of atomic%, results in nonzero signal for all elements outside the particle boundaries. Although we cannot rely upon these measurements for accurate values of the O:V ratio, it is interesting to note that in each case the atomic% O is also higher at the edges and lower inside the particles. This behavior shows most strongly in the undoped nanoparticle. This is likely due to oxidization of the particle surface as annealing progresses.

3.8.f Additional Hysteresis Data

Figure S10 shows optical reflectance hysteresis measurements for undoped samples at progressively longer anneal times. At short times (when the samples are still polycrystalline films), the hysteresis loops are more narrow, with a two-step transition on the cooling curve (due to simultaneously sampling regions that have coarsened to different degrees). Once dewetting has occurred (~10 min), the hysteresis loop becomes much broader, as discussed in the main text. As aggregation continues and the particles grow larger (approaching the size scale of visible/near-IR light), contrast decreases, due mainly to increased scattering. At long times (≥20 min), contrast is further decreased by oxidization of VO_2 into V_2O_5
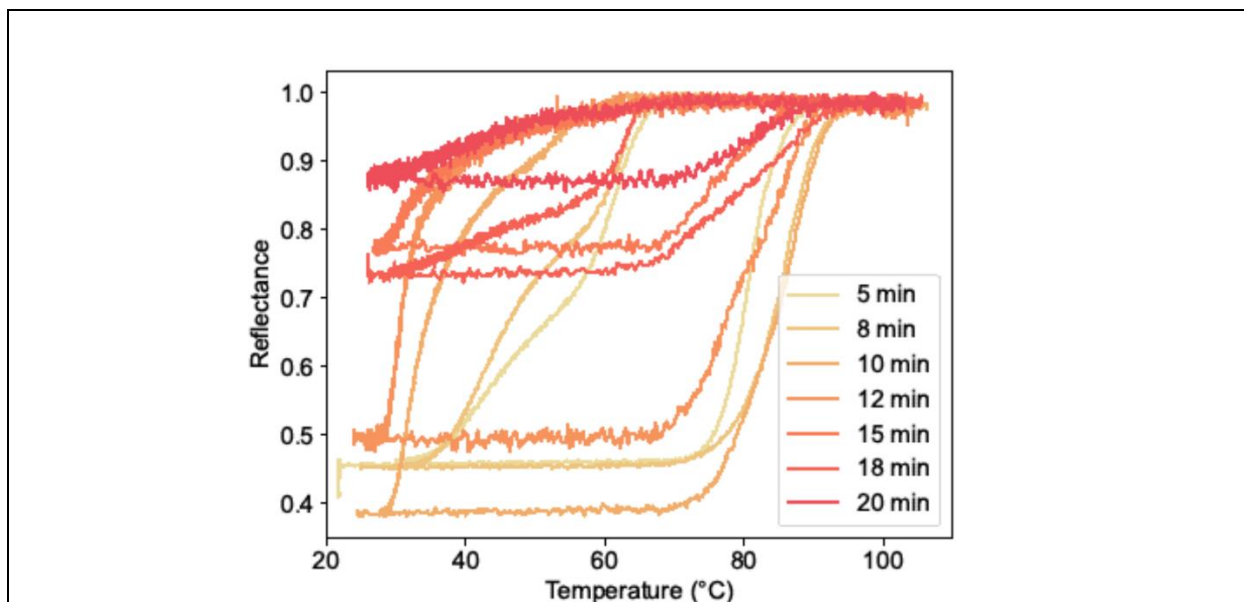
Figure 3.S10: Hysteresis loops for undoped samples, as anneal time increases, first show an increase in hysteresis width (due to the formation of nanoparticles) and then a decreased contrast (due to scattering).

CHAPTER 4

RECONFIGURABLE INFRARED HYPERBOLIC METASURFACES USING PHASE CHANGE MATERIALS

4.1 Publication Citation

4.2 Abstract

Metasurfaces control light propagation at the nanoscale for applications in both free-space and surface-confined geometries. However, dynamically changing the properties of metasurfaces can be a major challenge. Here we demonstrate a reconfigurable hyperbolic metasurface comprised of a heterostructure of isotopically enriched hexagonal boron nitride (hBN) in direct contact with the phase-change material (PCM) single-crystal vanadium dioxide (VO_2). Metallic and dielectric domains in VO_2 provide spatially localized changes in the local dielectric environment, enabling launching, reflection and transmission of hyperbolic phonon phonon polaritons (HPhPs) at the PCM domain boundaries, and tuning the wavelength of (HPhPs) propagating in hBN over these domains by a factor of 1.6. We show that this system supports in-plane HPhP refraction, thus providing a prototype for a class of planar refractive optics. This approach offers reconfigurable control of in-plane HPhP propagation and exemplifies a generalizable framework based on combining hyperbolic media and PCMs to design optical functionality.

4.3 Introduction

Optical near and far fields can be manipulated by scattering light into the resonant modes of nanostructured materials, which collectively form optical metasurfaces.[1-3] Historically, metallic polaritonic elements[4] have been used, which are highly absorbing[5] and typically exhibit limited tuning due to the geometric dependence of optical resonances. True reconfigurability – that is, complete changing of the optical response – therefore becomes challenging, as it requires arbitrarily changing the shape of individual elements of the structure, dynamically controlling the local dielectric environment, or controlling the optical properties of the polaritonic material itself.

In this regard, phase change materials (PCMs) offer an appealing approach to introducing true reconfigurability as they undergo significant changes in optical properties upon exposure to external stimuli.[6-7] Examples of PCM's are vanadium dioxide (VO_2) ,[8-11] and germanium antimony telluride (GeSbTe) glasses,[6, 12] which undergo dielectric to metallic phase transitions upon heating or pulsed-laser excitation. For VO_2 this is a volatile (non-latching) phase transition, whereas GeSbTe undergoes a non-volatile (latching) transition. By integrating PCMs and polaritonic materials, changes in optical properties induced by such a phase transition can provide the means to control the polariton dispersion by changing the local dielectric environment in which the evanescent polaritonic near-fields propagate. Thus they can be exploited to realize reconfigurable metasurfaces.[6, 12-17] However, one of the phases of PCMs is typically metallic and/or exhibits high optical losses. Consequently, in previous studies of surface-confined polaritons, such as surface plasmon (SPPs) or surface phonon polaritons (SPhPs), the propagation was restricted to spatial regions over the PCM where a low-loss dielectric phase was present.[6, 12] This makes concepts such as nanophotonic waveguides, grating couplers and focusing elements extremely difficult to realize in PCM-surface-polariton-based systems, despite the opportunities available.

Here we exploit two key changes in approach that overcome these previous limitations. First, we significantly reduce losses in polariton propagation by using isotopically enriched hexagonal boron nitride[18-19] (hBN), a natural hyperbolic[20-24] medium that supports low-loss hyperbolic phonon polaritons (HPhPs). Secondly, by exploiting hyperbolic polaritons instead of the surface-confined variety,[6, 12-16] the polaritons remain sensitive to local changes in the dielectric function of the ambient environment,[25] while the electromagnetic near-fields are strongly confined to the volume of the hyperbolic material.[20-21, 26] This means that HPhPs can interact with spatially localized phase transitions of the PCM, yet do not suffer significant optical losses from this interaction, and thus should propagate over both metallic and dielectric phases. Crucially, we show this to be the case and that the difference in the local dielectric environment between the metallic and dielectric domains results in a large change in the HPhP wavelength in the hBN over each domain, which in turn results in the refraction of the polariton when transmitting across the PCM phase domain boundaries. This means that the combination of hyperbolic media and PCMs employed here can be used to create refractive optical elements and waveguides,[27] as well as components benefitting from full optical functionalities that to this point have been limited to far-field optics. We demonstrate such concepts using electromagnetic modelling, showing that PCM-HPhP heterostructures can be designed as optical resonators[20, 28] and metasurfaces,[29-30] as well as refractive near-field components, such as waveguides and lenses. This combination of PCMs with hyperbolic media opens a whole new toolset for near-field optical design and structuring. Significantly, for reversible PCM transitions, any of these designs can be fully reconfigured using either thermal changes or approaches based on laser writing. Finally, by exploiting the increasingly wide range of different PCMs and hyperbolic materials and metamaterials, such as transition metal oxides,[31] these effects can be realized over an extended range of frequencies.

4.4 Results

4.4.a Near-Field Measurements of Hyperbolic Polaritons

Figure 4.1: Actively reconfigurable hyperbolic metasurface device. (a) shows a device and experimental schematic, in which hBN has been transferred on top of a VO$_2$ single crystal and polaritons are imaged by the s-SNOM tip (b) shows an optical microscope image of the heterostructure (c-e) s-SNOM images of the optical near-field at 1450cm^{-1} (6.9 µm) at various temperatures, showing HPhPs propagating over both metallic and dielectric VO$_2$ domains. The complex patterns that form are the consequence of multiple interference from the different domains. The arrows show the following: purple highlights tip-launched modes reflected from the hBN edge, while blue designates the HPhP propagating interior to the hBN from the edge of the VO$_2$ crystal (boundary with air, suspended hBN). The red highlights the same propagation characteristics as the blue arrow, except for HPhPs propagating over the metallic VO$_2$ domains. Finally, the orange and green arrows designate HPhPs propagating within the hBN from the domain boundaries between the dielectric and metallic domains of the VO$_2$, with the orange (green) propagating over the dielectric (metallic) domains. In (e) the black dashed line indicates the edge of the VO$_2$ metallic domain, extrapolated from the domain outside the hBN crystal.

The prototype device (Fig. 1a,b) consists of a 24-nm thick flake of ^{10}B-enriched hBN (~99% enriched)[18-19] transferred using low-contamination transfer techniques onto a single crystal of VO$_2$ grown on quartz. We use scattering-type scanning near-field optical microscopy (s-SNOM) to directly map and visualize the evanescent optical fields on the structure, corresponding to polaritonic waves of compressed wavelength λ_p, propagating primarily within the volume of the hBN slab (see Fig. 1a). In s-SNOM images, HPhPs can be observed in two ways: first, polaritons launched by the light scattered off of the s-SNOM tip propagate to, and reflect back from sample boundaries (e.g. a flake edge) creating interference fringes with spacing $\lambda_p/2$, which are scattered back to free-space by the tip and detected.[21, 32-33]

Alternatively, polaritons can be directly launched from sample edges and propagate across the surface to interfere with the incident field at the tip, producing fringes with spacing λ_{p}.[18, 34] Thus, in s-SNOM maps, a superposition of both so-called 'tip-launched' and 'edge-launched' fringes may be observed and are interpreted by considering the fringe spacing from individual waves ($\lambda_{\mathrm{p}}/2$ vs λ_{p}) and the direction of polariton propagation.

4.4.b Controlling Hyperbolic Polaritons Using a PCM

The presence of both tip- (wavelength $\lambda_{\mathrm{p}}/2$, purple line in the *x*-direction) and edge-launched (wavelength λ_{p}, light blue line in the *y*-direction) HPhPs can be readily observed in the hBN (Fig. 1c) slab transferred on top of the VO$_2$ single crystal. Here, this is visualized via the near-field amplitude s-SNOM image collected using a 1450 cm^{-1} excitation laser at room temperature. The observation of both tip- and edge-launched modes in the *x*-direction, while only edge-launched modes being apparent along the *y*-direction derives from the properties of the boundaries in the heterostructure sample, namely the edges of the hBN and VO$_2$ crystals. As in previous experiments[18, 21, 34] the edge of the hBN crystal provides for both high reflection of tip-launched HPhPs as well as a sharp edge for direct initiation of edge-launched modes (*x*-direction). In contrast, the small size (440 nm thickness, 6.5 µm width) of the VO$_2$ crystal provides sufficient momentum to robustly scatter into HPhP modes at the VO$_2$ crystal edges (bottom/top edges in Fig. 1c) .[18, 34] However, the interface between VO$_2$ and air at the crystal edge provides a significantly reduced reflection coefficient, which suppresses tip-launched waves, an effect observed in prior work.[12, 25] A more detailed discussion of the occurrence of both tip- and/or edge-launched modes in the s-SNOM images is available in Supplementary Note 1.

Propagation of HPhPs is strongly influenced by the local dielectric environment,[25, 29] so we investigated the influence of the VO$_2$ phase transition by measuring the s-SNOM response of the sample as a function of temperature, traversing the full dielectric-to-metal transition from 60°C to 80°C.[11] The sample was heated in-situ inside the s-SNOM microscope on a custom-built heating stage. Individual VO$_2$ domains are directly observed with s-SNOM due to the dielectric contrast between domains, with metallic (dielectric) VO$_2$ appearing as bright (dark) regions (Fig. 1d).[8-11] As the device is heated further (Fig. 1e), the hBN-supported HPhPs are observed to propagate over both the metallic and dielectric domains of VO$_2$, for appreciable propagation distances in both regions. This contrasts with an earlier work focused on surface polaritons and PCMs, where the polaritons propagated for only a few cycles over the dielectric phase and were entirely precluded from propagation over the metallic regions.[12] We attribute this difference to the volume-confinement of the local electromagnetic near-fields of HPhPs supported within the low-loss hBN,[18, 20-21] which prevents the polaritonic fields from being absorbed by the lossy metallic phase of VO$_2$. After heating to high temperatures and performing these s-SNOM measurements, allowing the device to cool to room temperature resets the VO$_2$ crystal to its dielectric state, after which the sample can be reheated to get a different PCM domain pattern (see Supplementary Fig. 2). This allows us to reconfigure our device to study the propagation of HPhPs in a range of different geometries and at different frequencies within the same device. The large permittivity difference between metallic and insulating phases of VO$_2$ therefore presents an excellent platform to manipulate and control polariton propagation within hyperbolic materials.

When the s-SNOM maps the evanescent fields of propagating HPhP waves in the presence of multiple interfaces, complex images result from the superposition of the waves

launched, transmitted across and reflected by each domain boundary, crystal edge and the s-SNOM tip. The simplest polaritons to identify are the modes launched from the edge of the VO_2 crystal, as they form straight fringes aligned parallel to the crystal edge. Due to the difference in local dielectric environment, these HPhPs possess different polariton wavelengths λ_p above each domain. Here the HPhP mode launched by the VO_2 crystal edge over the dielectric (metallic) domain is highlighted by the light blue (red) arrow in Figs. 1 c and d, and demonstrate that the HPhP wavelength is modified from $\lambda/12.9$ to $\lambda/20.4$ by the PCM at 1450cm^{-1} between these domains, serving as the first report of the dispersion of HPhPs being tuned by a PCM. Propagation lengths $(1/e)$ are approximately 2.83 µm (5.2 cycles) and 0.8 µm (2.5 cycles) in the dielectric and metallic phases at this frequency respectively, which is comparable to propagation lengths in naturally abundant hBN (~3.1 and 2.5 µm at the same wavevectors respectively).[21] Furthermore, in Fig. 1 d-e, s-SNOM images show that HPhPs are directly launched in the hBN over the boundaries between the dielectric (orange arrow) and metallic (green arrow) domains, despite there being no appreciable change in the topography of the VO_2 crystal (Supplementary Note 2 and Supplementary Fig. 3).
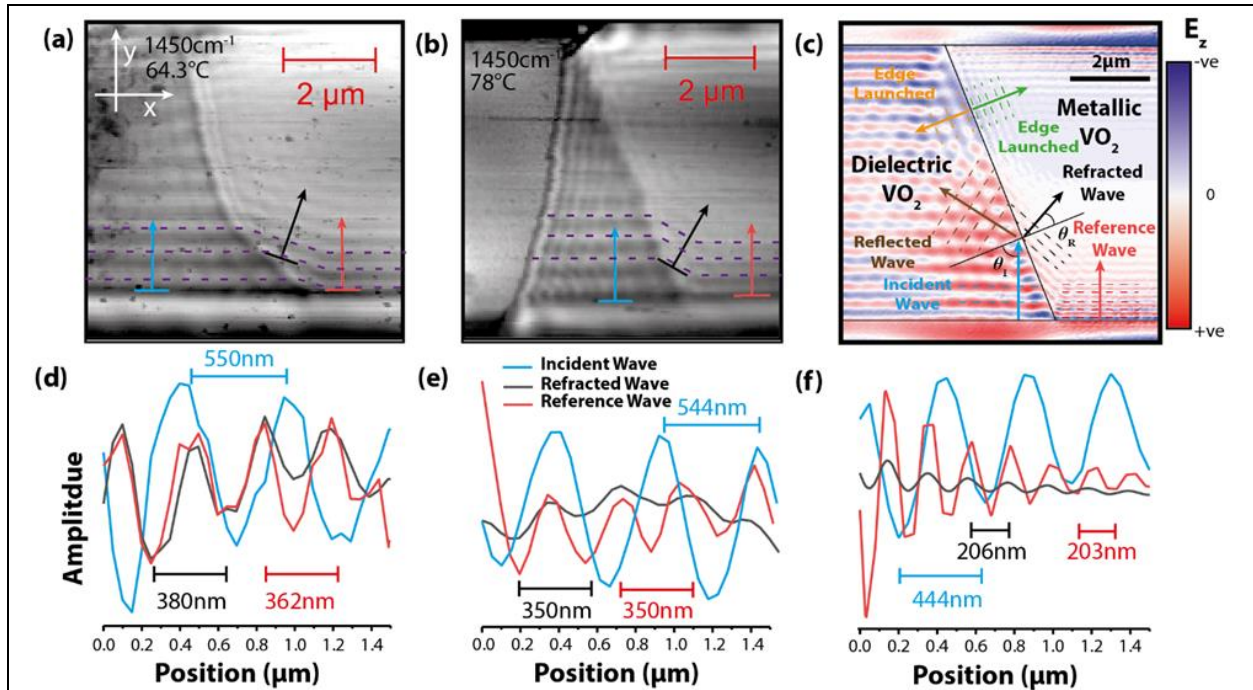
Figure 4.2: Hyperbolic polariton refraction on a hBN-VO_2 heterostructure. (a)-(b) show two s-SNOM maps of the near-field amplitude in the region of the domain boundary showing refraction. Purple dashes show the distorted phase front that propagates over the boundary. (c) shows an electromagnetic-field simulation of the geometry in (b), showing reflected, refracted and edge-launched waves. (d)-(f) show line profiles from (a)-(c) respectively, showing refraction of the wave.

Whilst past work has shown that PCM domain boundaries can serve to launch polaritons[12], here they are launched and propagated over both phases, with a different wavelength over each, promising the potential for dynamically reconfiguring HPhP properties and propagation. Note that the VO_2 domains appear to change size when underneath the hBN (as

seen by following the black dashed line in Fig. 1e). This arises from hyperlensing by the hBN[35-36], which acts to magnify light scattered into a hyperbolic medium, and can give rise to spatial regions on the edge of a domain where the wavelength appears not to change (seen to the left of the blue arrow in Fig. 1e).

4.4.c Refraction of Hyperbolic Polaritons

This heterostructure also enables the transmission of polaritons across the aforementioned domain boundaries. To simplify s-SNOM images and subsequent analysis, domain geometries with only a single boundary are required. As the positions of domain boundaries induced via thermal cycling of the VO_2 phase transition are naturally quasi-random, we implemented multiple heating and cooling cycles (the same process as Supplementary Fig. 2) to achieve single dielectric-metal interfaces on the VO_2 crystal for study. Examples are shown in Figs. 2a,b (also Supplementary Note 3 and Supplementary Fig. 4). Such 'reconfiguring' of the metasurface has been repeated more than eight times in our experiments, with no appreciable change in the dielectric properties of either of the two phases of VO_2 or the hBN flake, demonstrating the repeatability of this process.

Of particular interest is the polariton wave front that propagates away from the VO_2 crystal edge in the *y*-direction (purple dashed line with black arrows in Fig. 2 a,b): it meets the domain boundary and distorts, propagating in a direction that is not normal either to the domain or crystal edge. This is a signature of planar polariton refraction as the wave changes direction due to the local change in dielectric environment. Whilst planar polariton refraction has been reported previously for plasmon polaritons,[37] this is the first direct observation of refraction for hyperbolic polaritons, and the first to study such polariton refraction as a function of incident (transmitted) polariton angle.

If a hyperbolic polariton traverses the boundary between metallic and insulating VO_2 domains, the angle of propagation changes to conserve momentum in accordance with Snell's law:[38]

$$\frac{\sin(\theta_I)}{\sin(\theta_R)} = \frac{n_2}{n_1} \qquad \text{(Equation 1)}$$

where n_1 and n_2 are the wave-effective indices in the first and second media, and θ_I and θ_R are the corresponding angles of incidence and refraction. To demonstrate that the experimentally measured images are due to refraction, we compare the results in Fig. 2b to a simplified electromagnetic simulation (Fig. 2c). In the simulation we excite the structure with plane waves (45° incidence), and at the edges of the VO_2 crystal, polaritonic waves are launched that propagate across the surface, mimicking edge-launched polaritons. Note that we ignore the tip-sample interaction in these simulations. Instead, HPhPs excited at the edge of the VO_2 crystal (blue) propagate in the *y*-direction within the dielectric phase. When these HPhPs approach the angled dielectric-metallic domain boundary (black line), some of the wave will be reflected (brown) and some will be transmitted across the boundary (black) and refracted due to the mismatch in wavevectors for the HPhPs supported over the two PCM domains. The simulation also shows waves launched directly from the domain boundary (orange and green) in Figs. 1c and d. The refracted wave will not propagate normal to either the edge of the crystal or the domain boundary but will have the same polariton wavelength as the wave launched in the hBN by scattering of incident light from the metallic VO_2 crystal edge. This is indeed what is shown in our experiments by the corresponding line profiles provided in Fig. 2d-f. However, the wave reflected by the metal-dielectric domain boundary is not observed experimentally due to interference with the edge-launched mode shown in light blue. Despite this, the good agreement

between Fig. 2b and c shows clear evidence of HPhP refraction. We note that whilst in principle these effects should be observable also with a tip-launched waves in s-SNOM images, during our experiments, we were unable to form a VO_2 domain boundary sufficiently close to the flake edge (seen in Fig. 1b) to study this effect.

4.4.d *Quantifying Polariton Manipulation*

To quantify the change in the polariton wavevector and HPhP refraction induced by the VO_2 domains and to quantify the ability to reconfigure the metasurface, we systematically studied the polariton wavelength dependence on incident frequency and refracted angle in different domain geometries. In the first case, we systematically recorded s-SNOM images at several monochromatic incident laser frequencies in both metallic and dielectric domains, and subsequently extracted the polariton wavelength through Fourier analysis (see Supplementary Note 3 and Supplementary Fig. 5) of the s-SNOM maps, as has been reported previously.[18, 21, 32-33] The experimentally extracted polariton wavevector (symbols) agrees well with numerical calculations of the HPhP dispersion for thin hBN slabs on a substrate consisting of either the dielectric or metallic phase of VO_2 (Fig. 3a and b). In our assignment of the points in Fig. 3a and b, we consider both tip- and edge-launched modes, above both metallic and dielectric VO_2, which can be observed in Supplementary Fig. 5. Again, this dramatic change in wavevector between domains at the same incident frequency is attributable to the large change in dielectric constant in VO_2 between the two PCM states, which further compresses the polariton wavelength.
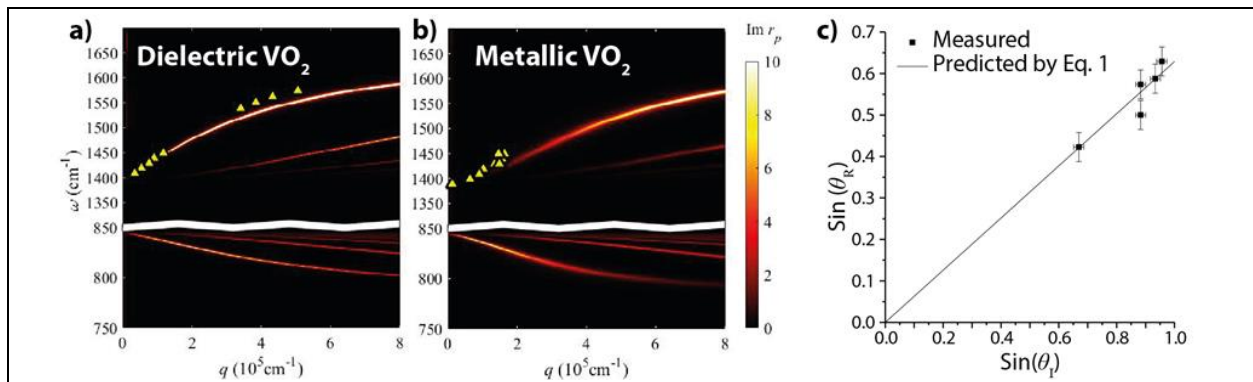
Figure 4.3: Hyperbolic polariton dispersion in VO_2 over both dielectric (a) and metallic (b) domains compared to numerical calculations. The horizontal white line shown in figure (a) and (b) indicates a break in the graph, between upper (1394-1650cm^{-1}) and lower (785-845cm^{-1}) Reststrahlen bands. From the measured dispersion, the angle of refracted waves at 1450cm^{-1} can be computed for a given incident angle and compared against experimentally measured results in (c). There has been no fitting in this result. The x and y error bars in (c) represent the standard deviation of measurements of incident ($\pm 1°$) and refracted ($\pm 2°$) angles respectively.

From the measured change in polariton wavelength, we calculated the ratio of the indices of refraction, n_1/n_2 to determine the expected angle of refraction for the HPhP waves from Eq. (1), and compared this to the refracted angle extracted from the s-SNOM images in Fig. 2 and Supplementary Fig. 4, to test the adherence to Snell's law for HPhPs (Fig 3c). This result is consistent with numerical simulations at a range of different angles and frequencies (see

78

Supplementary Note 4 and Supplementary Fig. 6) confirming that Snell's law holds for HPhPs propagating across domain boundaries. Systematic investigation of polariton propagation and refraction at multiple angles was not possible in prior work[37] and thus, the results presented here demonstrate that the tools and concepts of refractive optics are applicable in near-field optical designs as well. Indeed, the repeatable nature of both the change in polariton wavelength and Snell's law demonstrates that this platform can steer polariton propagation by proper design of the local dielectric environment.

4.4.e Towards Refractive Near-Field Optics

The ability to control HPhPs propagating across phase-domain boundaries opens several possibilities for engineering lithography-free metasurfaces and near-field optics. As an example motivated by prior work,[12] we investigated the possibility for creating rewritable nanoresonators using this technique, where a periodic array of metallic square domains is created inside the VO_2 crystal underneath the hBN (inset Fig 4a). In Fig. 4a we show the numerically calculated reflection spectrum from a hBN crystal on top of a dielectric VO_2 (blue curve), VO_2 patterned with metallic and dielectric domains (red curve), and hBN on top of such a patterned VO_2 structure (black curve). In the simulated spectra for the hBN on top of patterned VO_2, we observe peaks corresponding to a series of HPhP modes. Whilst these peaks are relatively small in amplitude (as this geometry has not been optimized for an intense resonant response), these modes can be tuned in frequency by changing the width and periodicity of the metallic domain (see Supplementary Note 5 and Supplementary Fig. 7 for a complete discussion). Thus, in principle, by controlling the size and shape of the metallic domain, one can realize a resonant response that previously was only observed in nanofabricated structures of hBN.[20, 39-41] This implies that such resonators can be realized without the additional induced losses that are incurred with most nanofabrication approaches.[42-44] Such resonators could also be achieved experimentally by adding titanium to change the local phase transition properties of VO_2.[45]
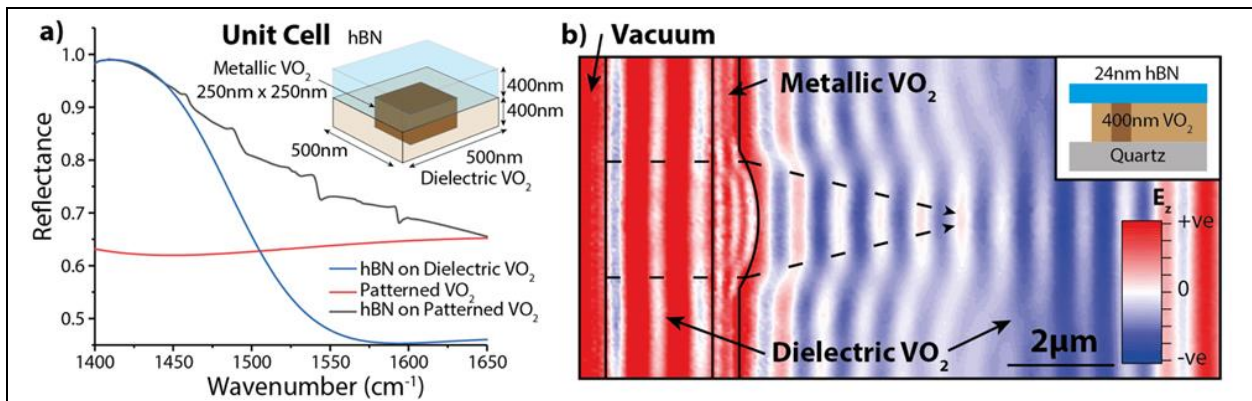
Figure 4.4: Schematic of refractive planar optics and reconfigurable resonators using phase-change materials (a) shows a tunable polariton metasurface of hBN and VO_2, which consists of a continuous film of hBN 400nm thick on top of 400nm of VO_2. By patterning the VO_2 with metallic domains we can excite a rewritable reflection profile, which cannot be generated from either of the materials alone. The pitch is 500nm, with a particle length 250nm. (B) shows a simulation of a refractive polariton lens, which uses a semi-circular domain of metallic VO_2 to launch polariton waves at 1418cm^{-1}.

Refraction of HPhPs across boundaries also enlarges the toolbox for near-field optics to include those of conventional refractive systems, such as in-plane lenses, whereby polaritons are focused to a point via refraction. A simulation of such a lens is shown in Fig. 4b, where HPhPs are launched into hBN at the left crystal edge and propagate inward to a region over a hemispherical VO_2 metallic domain, after which they are focused to a spot in the area over the dielectric VO_2. Here the combination of hyperbolic media and PCMs is critical, because for conventional surface polaritons, the high losses of the PCM metallic state would preclude polariton propagation and thus the polariton refraction required to induce focusing. While experimentally we demonstrate the principle of this reconfigurable nano-optics platform using heterostructures comprising thin slabs of hBN on VO_2 single crystals, this approach can readily be generalized to other materials. To demonstrate this, we have simulated a nanophotonic waveguide using both VO_2 and GeSbTe[12] as the underlying PCMs (See Supplementary Note 6 and Supplementary Fig. 8). The non-volatile nature of the phase transition in GeSbTe,[12] where both states of the PCM are stable at room temperature, offers significant benefits for laser-writing-based approaches aimed at realizing complicated nanophotonic architectures. Although the device we present here is a conceptual prototype, our system could be realized in practice and scaled by using VO_2 or GeSbTe films grown by sputtering, and boron nitride grown by metal organic chemical vapor deposition.[46] There remain numerous material challenges – such as the growth of high quality, large area hBN – in realizing such a system, but this provides a route to achieving scalable reconfigurable devices.

4.5 Discussion

We have experimentally demonstrated that the dispersion of HPhPs can be controlled using the permittivity changes inherent in the different phases of PCMs. This enables the direct launching, reflection, transmission and refraction of HPhP waves at the domain boundaries between the different phases of the PCM, due to the large change in HPhP wavelength (here, by a factor of 1.6) that occurs for modes propagating in the hBN over each of these domains. Thermally cycling of the hBN-VO_2 heterostructure creates a range of domain-boundary geometries in the PCM, enabling the demonstration of various near-field phenomena. By inducing well-defined domain structures, it will be possible to design reconfigurable HPhP resonators and refractive optics in a planar, compact format at dimensions far below the diffraction limit. Beyond the implications for integrated nanophotonics, reconfigurable HPhP resonators could be used to match resonant frequencies to local molecular vibrational modes for the realization of dynamic surface-enhanced infrared absorption (SEIRA) spectroscopy.[41] Whilst in our case we have experimentally demonstrated these concepts using hBN on VO_2, using different combinations of PCMs (such as GeSbTe) and other hyperbolic materials (such as transition metal oxides),[31] could see expanded applications over a wide frequency range. Ultimately, we anticipate that the combination of low-loss, hyperbolic materials and latchable PCMs could see applications in lithography-free design and fabrication of optical and optoelectronic devices, whereas volatile PCMs could be used for dynamic modulation of photonic structures.

4.6 Methods

4.6.a Device Fabrication

Vanadium dioxide (VO_2) single crystals were grown by physical vapor transport in a quartz tube furnace at 810°C under 1.7 Torr Ar gas at a flow rate of 25 sccm. Vanadium pentoxide (V_2O_5) powder (~0.3 g, Sigma Aldrich 221899) was placed in a quartz boat (10 x 1 x 1 cm) upstream of the desired substrates and heated for 1 hr. Evaporated V_2O_5 was reduced to VO_2 in this process and deposited on quartz (0001) substrates. Representative crystals from each sample were investigated using Raman spectroscopy to identify the VO_2 phase and optical microscopy to verify the thermal phase transition. Smaller, loose crystals located on the substrate surface were removed by adhesion to a heated (60°C) layer of PMMA firmly brought into contact with the sample and subsequently retracted.

The isotopically enriched hBN crystals were grown from high-purity elemental ^{10}B (99.22 at%) powder by using the metal-flux method. A Ni-Cr-B powder mixture at respective 48 wt%, 48 wt%, and 4 wt% was loaded into an alumina crucible and placed in a single-zone furnace. The furnace was evacuated and then filled with N_2 and forming gas (5% hydrogen in balance argon) to a constant pressure of 850 Torr. During the reaction process, the N_2 and forming gases continuously flowed through the system with rates of 125 sccm and 25 sccm, respectively. All the nitrogen in the hBN crystal originated from the flowing N_2 gas. The forming gas was used to minimize oxygen and carbon impurities in the hBN crystal. After a dwell time of 24 hours at 1550 °C, the hBN crystals were precipitated onto the metal surface by cooling at a rate of 1°C /h to 1500 °C, and then the system was quickly quenched to room temperature. Bulk crystals were exfoliated from the metal surface using thermal release tape. Crystals were subsequently mechanically exfoliated onto a PMMA/PMGI polymer bilayer on silicon. Flakes were then transferred from the polymer substrate onto VO_2 single crystals using a semi-dry technique, and the polymer membrane was removed using acetone and isopropyl alcohol.

4.6.b Numerical Simulations

Numerical simulations were conducted in CST Studio Suite 2017 using the frequency domain solver with plane waves incident at 45° and Floquet boundary conditions. In these simulations, polariton modes were only launched by scattering from edges in the simulation, and field profiles were extracted using frequency monitors. All results used thicknesses consistent with that measured in topographic maps of the samples. Dielectric functions were taken from Ref. 18 for isotopically enriched hBN, from Ref. [47] for VO_2 and from Ref. [48] for GeSbTe.

4.6.c s-SNOM Measurements

Near-field nano-imaging experiments were carried out in a commercial (www.neaspec.com) scattering-type, scanning near-field optical microscope (s-SNOM) based around a tapping-mode atomic-force microscope (AFM). A metal-coated Si-tip of apex radius $R \approx 20$ nm that oscillates at a frequency of $\Omega \approx 280$ kHz and tapping amplitude of about 100 nm is illuminated by monochromatic quantum cascade laser (QCL) laser beam at a wavelength $\lambda=6.9$ µm and at an angle 45° to the sample surface. Scattered light launches hBN HPhPs in the device, and the tip then re-scatters light (described more completely in the main text) for detection in the far-field. Background signals are efficiently suppressed by demodulating the

detector signal at the second harmonic of the tip oscillation frequency and employing pseudo-heterodyne interferometric detection.

4.7 References

1.   Yu, N.; Capasso, F., Flat optics with designer metasurfaces. *Nature Materials* **2014,** *13*, 139-150.
2.   Staude, I.; Schilling, J., Metamaterial-inspired silicon nanophotonics. *Nat. Photonics* **2017,** *11* (5), 274-284.
3.   Kildishev, A. V.; Boltasseva, A.; Shalaev, V. M., Planar photonics with metasurfaces. *Science (Washington)* **2013,** *339* (12), 1232009.
4.   Meinzer, N.; Barnes, W. L.; Hooper, I. R., Plasmonic meta-atoms and metasurfaces. *Nat. Photonics* **2014,** *8* (12), 889-898.
5.   Khurgin Jacob, B., Relative merits of phononics vs. plasmonics: the energy balance approach. *nanoph* **2018,** *7* (1), 305-316.
6.   Wuttig, M.; Bhaskaran, H.; Taubner, T., Phase-change materials for non-volatile photonic applications. *Nat. Photonics* **2017,** *11* (8), 465-476.
7.   Yang, Z.; Ramanathan, S., Breakthroughs in Photonics 2014: Phase Change Materials for Photonics. *IEEE Photonics Journal* **2015,** *7* (3), 1-5.
8.   Abate, Y.; Marvel, R. E.; Ziegler, J. I.; Gamage, S.; Javani, M. H.; Stockman, M. I.; Haglund, R. F., Control of plasmonic nanoantennas by reversible metal-insulator transition. *Sci Rep* **2015,** *5*, 8.
9.   Liu, M.; Sternbach, A. J.; Basov, D. N., Nanoscale electrodynamics of strongly correlated quantum materials. *Rep. Prog. Phys.* **2017,** *80* (1), 27.
10.   McGahan, C.; Gamage, S.; Liang, J.; Cross, B.; Marvel, R. E.; Haglund, R. F.; Abate, Y., Geometric constraints on phase coexistence in vanadium dioxide single crystals. *Nanotechnology* **2017,** *28* (8), 085701.
11.   Qazilbash, M. M.; Brehm, M.; Chae, B.-G.; Ho, P. C.; Andreev, G. O.; Kim, B.-J.; Yun, S. J.; Balatsky, A. V.; Maple, M. B.; Keilmann, F.; Kim, H.-T.; Basov, D. N., Mott Transition in VO_2 Revealed by Infrared Spectroscopy and Nano-Imaging. *Science* **2007,** *318* (5857), 1750.
12.   Li, P.; Yang, X.; Maß, T. W. W.; Hanss, J.; Lewin, M.; Michel, A.-K. U.; Wuttig, M.; Taubner, T., Reversible optical switching of highly confined phonon–polaritons with an ultrathin phase-change material. *Nature Materials* **2016,** *15*, 870-875.
13.   Yin, X. H.; Steinle, T.; Huang, L. L.; Taubner, T.; Wuttig, M.; Zentgraf, T.; Giessen, H., Beam switching and bifocal zoom lensing using active plasmonic metasurfaces. *Light-Sci. Appl.* **2017,** *6*, 7.
14.   Karvounis, A.; Gholipour, B.; MacDonald, K. F.; Zheludev, N. I., All-dielectric phase-change reconfigurable metasurface. *Appl. Phys. Lett.* **2016,** *109* (5), 051103.
15.   Guo, P. J.; Weimer, M. S.; Emery, J. D.; Diroll, B. T.; Chen, X. Q.; Hock, A. S.; Chang, R. P. H.; Martinson, A. B. F.; Schaller, R. D., Conformal Coating of a Phase Change Material on Ordered Plasmonic Nanorod Arrays for Broadband All-Optical Switching. *Acs Nano* **2017,** *11* (1), 693-701.
16.   Kats, M. A.; Sharma, D.; Lin, J.; Genevet, P.; Blanchard, R.; Yang, Z.; Qazilbash, M. M.; Basov, D. N.; Ramanathan, S.; Capasso, F., Ultra-thin perfect absorber employing a tunable phase change material. *Appl. Phys. Lett.* **2012,** *101* (22), 221101.
17.   Krishnamoorthy, H. N. S.; Zhou, Y.; Ramanathan, S.; Narimanov, E. E.; Menon, V. M., Tunable hyperbolic metamaterials utilizing phase chane heterostructures. *Appl. Phys. Lett.* **2014,** *104*, 121101.
18.   Giles, A. J.; Dai, S.; Vurgaftman, I.; Hoffman, A. J.; Liu, S.; Lindsay, L.; Ellis, C. T.; Assefa, N.; Chatzakis, I.; Reinecke, T. L.; Tischler, J. G.; Fogler, M. M.; Edgar, J. H.; Basov, D. N.; Caldwell, J. D., Ultra-low-loss Polaritons in Isotopically Pure boron nitride. *Nature Materials* **2017,** *17*, 134-139.
19.   Vuong, T. Q. P.; Liu, S.; Van der Lee, A.; Cusco, R.; Artus, L.; Michel, T.; Valvin, P.; Edgar, J. H.; Cassabois, G.; Gil, B., Isotope engineering of van der Waals interactions in hexagonal boron nitride. *Nature Materials* **2018,** *17*, 152-158.

20.   Caldwell, J. D.; Kretinin, A.; Chen, Y.; Giannini, V.; Fogler, M. M.; Francescato, Y.; Ellis, C.; Tischler, J. G.; Woods, C.; Giles, A. J.; Hong, M.; Watanabe, K.; Taniguchi, T.; Maier, S. A.; Novoselov, K. S., Sub-diffractional, Volume-confined Polaritons in the Natural Hyperbolic Material Hexagonal Boron Nitride. *Nat. Commun.* **2014,** *5*, 5221.

21.   Dai, S.; Fei, Z.; Ma, Q.; Rodin, A. S.; Wagner, M.; McLeod, A. S.; Liu, M. K.; Gannett, W.; Regan, W.; Thiemens, M.; Dominguez, G.; Castro Neto, A. H.; Zettl, A.; Keilmann, F.; Jarillo-Herrero, P.; Fogler, M. M.; Basov, D. N., Tunable phonon polaritons in atomically thin van der Waals crystals of boron nitride. *Science (Washington)* **2014,** *343* (6175), 1125-1129.

22.   Korzeb, K.; Gajc, M.; Pawlak, D. A., Compendium of natural hyperbolic materials. *Optics Express* **2015,** *23* (20), 25406-25424.

23.   Low, T.; Chaves, A.; Caldwell, J. D.; Kumar, A.; Fang, N. X.; Avouris, P.; Heinz, T. F.; Guinea, F.; Martin-Moreno, L.; Koppens, F. H. L., Polaritons in layered two-dimensional materials. *Nature Materials* **2017,** *16*, 182-194.

24.   Sun, J.; Litchinitser, N. M.; Zhou, J., Indefinite by Nature: From Ultraviolet to Terahertz. *ACS Photonics* **2014,** *1* (4), 293-303.

25.   Duan, J.; Chen, R.; Li, J.; Jin, K.; Sun, Z.; Chen, J., Launching Phonon Polaritons by Natural Boron Nitride Wrinkles with Modifiable Dispersion by Dielectric Environments. *Advanced Materials* **2017,** *29* (38), 1702494.

26.   Poddubny, A.; Iorsh, I.; Belov, P.; Kivshar, Y., Hyperbolic metamaterials. *Nat. Photonics* **2013,** *7*, 948-957.

27.   Vakil, A.; Engheta, N., Transformation Optics Using Graphene. *Science (Washington)* **2011,** *332*, 1291-1294.

28.   Yang, X.; Yao, J.; Rho, J.; Xiaobo, Y.; Zhang, X., Experimental realization of three-dimensional indefinite cavities at the nanoscale with anomalous scaling laws. *Nat. Photonics* **2012,** *6*, 450-453.

29.   Dai, S.; Tymchenko, M.; Yang, Y.; Ma, Q.; Pita-Vidal, M.; Watanabe, K.; Taniguchi, T.; Jarillo-Herrero, P.; Fogler, M. M.; Alù, A.; Basov, D. N., Manipulation and Steering of Hyperbolic Surface Polaritons in Hexagonal Boron Nitride. *Advanced Materials* **2018,** *30* (16), 5.

30.   Li, P.; Dolado, I.; Alfaro-Mozaz, F. J.; Casanova, F.; Hueso, L. E.; Liu, S.; Edgar, J. H.; Nikitin, A. Y.; Vélez, S.; Hillenbrand, R., Infrared hyperbolic metasurface based on nanostructured van der Waals materials. *Science* **2018,** *359* (6378), 892-896.

31.   Zebo, Z.; Jianing, C.; Yu, W.; Ximiao, W.; Xiaobo, C.; Pengyi, L.; Jianbin, X.; Weiguang, X.; Huanjun, C.; Shaozhi, D.; Ningsheng, X., Highly Confined and Tunable Hyperbolic Phonon Polaritons in Van Der Waals Semiconducting Transition Metal Oxides. *Advanced Materials* **2018,** *30* (13), 1705318.

32.   Fei, Z.; Rodin, A. S.; Andreev, G. O.; Bao, W.; McLeod, A. S.; Wagner, M.; Zhang, L. M.; Zhao, Z.; Thiemens, M.; Dominguez, G.; Fogler, M. M.; Castro Neto, A. H.; Lau, C. N.; Keilmann, F.; Basov, D. N., Gate-tuning of graphene plasmons revealed by infrared nano-imaging. *Nature* **2012,** *487*, 82-85.

33.   Chen, J.; Badioli, M.; Alonso-Gonzalez, P.; Thongrattanasiri, S.; Huth, F.; Osmond, J.; Spasenovic, M.; Centeno, A.; Pesquera, A.; Godignon, P.; Elorza, A. Z.; Camara, N.; Garcia de Abajo, F. J.; Hillenbrand, R.; Koppens, F. H. L., Optical nano-imaging of gate-tunable graphene plasmons. *Nature* **2012,** *487*, 77-81.

34.   Dai, S.; Ma, Q.; Yang, Y.; Rosenfeld, J.; Goldflam, M. D.; McLeod, A. S.; Sun, Z.; Andersen, T. I.; Fei, Z.; Liu, M.; Shao, Y.; Watanabe, K.; Taniguchi, K.; Thiemens, M.; Keilmann, F.; Jarillo-Herrero, P.; Fogler, M. M.; Basov, D. N., Efficiency of launching highly confined polaritons by infrared light incident on a hyperbolic material. *Nano Lett.* **2017,** *17* (9), 5285-5290.

35.   Dai, S.; Ma, Q.; Anderson, T.; McLeod, A. S.; Fei, Z.; Liu, M. K.; Wagner, M.; Watanabe, K.; Taniguchi, T.; Thiemens, M.; Keilmann, F.; Jarillo-Herrero, P.; Fogler, M. M.; Basov, D. N., Subdiffractional focusing and guiding of polaritonic rays in a natural hyperbolic material. *Nat. Commun.* **2015,** *6*, 6963.

36.   Li, P.; Lewin, M.; Kretinin, A. V.; Caldwell, J. D.; Novoselov, K. S.; Taniguchi, T.; Watanabe, K.; Gaussmann, F.; Taubner, T., Hyperbolic Phonon-Polaritons in Boron Nitride for near-field optical imaging and focusing. *Nat. Commun.* **2015,** *6*, 7507.

37.   Alonso-González, P.; Nikitin, A. Y.; Golmar, F.; Centeno, A.; Pesquera, A.; Vélez, S.; Chen, J.; Navickaite, G.; Koppens, F.; Zurutuza, A.; Casanova, F.; Hueso, L. E.; Hillenbrand, R., Controlling graphene plasmons with resonant metal antennas and spatial conductivity patterns. *Science* **2014,** *344* (6190), 1369-1373.
38.   Yu, N.; Genevet, P.; Kats, M. A.; Aieta, F.; Tetienne, J.-P.; Capasso, F.; Gaburro, Z., Light Propagation with Phase Discontinuities: Generalized Laws of Reflection and Refraction. *Science* **2011,** *334* (6054), 333-337.
39.   Brown, L. V.; Davanco, M.; Sun, Z.; Kretinin, A.; Chen, Y.; Matson, J. R.; Vurgaftman, I.; Sharac, N.; Giles, A. J.; Fogler, M. M.; Taniguchi, T.; Watanabe, K.; Novoselov, K. S.; Maier, S. A.; Centrone, A.; Caldwell, J. D., Nanoscale Mapping and Spectroscopy of Nonradiative Hyperbolic Modes in Hexagonal Boron Nitride Nanostructures. *Nano Lett.* **2018,** *18* (3), 1628-1636.
40.   Giles, A. J.; Dai, S.; Glembocki, O. J.; Kretinin, A. V.; Sun, Z.; Ellis, C. T.; Tischler, J. G.; Taniguchi, T.; Watanabe, K.; Fogler, M. M.; Novoselov, K. S.; Basov, D. N.; Caldwell, J. D., Imaging of Anomalous Internal Reflections of Hyperbolic Phonon-Polaritons in Hexagonal Boron Nitride. *Nano Lett.* **2016,** *16* (6), 3858-3865.
41.   Autore, M.; Li, P.; Dolado, I.; Alfaro-Mozaz, F. J.; Esteban, R.; Atxabal, A.; Casanova, F.; Hueso, L. E.; Alonso-Gonzalez, P.; Aizpurua, J.; Nikitin, A. Y.; Velez, S.; Hillenbrand, R., Boron nitride nanoresonators for phonon-enhanced molecular vibrational spectroscopy at the strong coupling limit. *Light: Science & Applications* **2018,** *7* (2), 15.
42.   Caldwell, J. D.; Glembocki, O. J.; Francescato, Y.; Sharac, N.; Giannini, V.; Bezares, F. J.; Long, J. P.; Owrutsky, J. C.; Vurgaftman, I.; Tischler, J. G.; Wheeler, V. D.; Bassim, N. D.; Shirey, L. M.; Kasica, R.; Maier, S. A., Low-Loss, Extreme Subdiffraction Photon Confinement via Silicon Carbide Localized Surface Phonon Polariton Resonators. *Nano Lett.* **2013,** *13* (8), 3690-3697.
43.   Ocelic, N.; Hillenbrand, R., Subwavelength-scale tailoring of surface phonon polaritons by focused ion-beam implantation. *Nature Materials* **2004,** *3*, 606-609.
44.   Bassim, N. D.; Giles, A. J.; Ocola, L. E.; Caldwell, J. D., Fabrication of phonon-based metamaterial structures using focused ion beam patterning. *Appl. Phys. Lett.* **2018,** *112*, 091101.
45.   Chen, Z.; Wang, X.; Qi, Y.; Yang, S.; Soares, J. A. N. T.; Apgar, B. A.; Gao, R.; Xu, R.; Lee, Y.; Zhang, X.; Yao, J.; Martin, L. W., Self-Assembled, Nanostructured, Tunable Metamaterials via Spinodal Decomposition. *ACS Nano* **2016,** *10* (11), 10237-10244.
46.   Takahashi, T.; Itoh, H.; Takeuchi, A., Chemical vapor deposition of hexagonal boron nitride thick film on iron. *J. Cryst. Growth* **1979,** *47* (2), 245-250.
47.   Kats, M. A. Optics at interfaces: ultra-thin color coatings, perfect absorbers, and metasurfaces. PhD, Harvard University, Harvard University, 2014.
48.   Kremers, S. Optical properties of phase change materials for novel optical and electrical storage applications. RWTH Aachen, 2009.

4.8 Acknowledgements

4.9 Supplementary Information

4.9.a Launching and Reflecting Hyperbolic Polaritons at Interfaces

Our sample presents three different interfaces, each of which can have distinctive properties in terms of launching polaritons in the s-SNOM experiment. Observing a tip-launched mode requires a strong reflection from an interface, while observation of an edge-launched mode demands strong scattering off the sample edge. First, we consider the edge of the hBN flake. The polariton cannot propagate past the edge of the flake and therefore nearly 100% is reflected, leading to a strong tip-launched mode. On the other hand, these hBN flakes are thin (24 nm), and therefore interact only weakly with incident waves, suppressing the edge-launched mode (similar to Ref 25 main text).[1] Thus, we only observe the tip-launched mode near the hBN crystal edge.
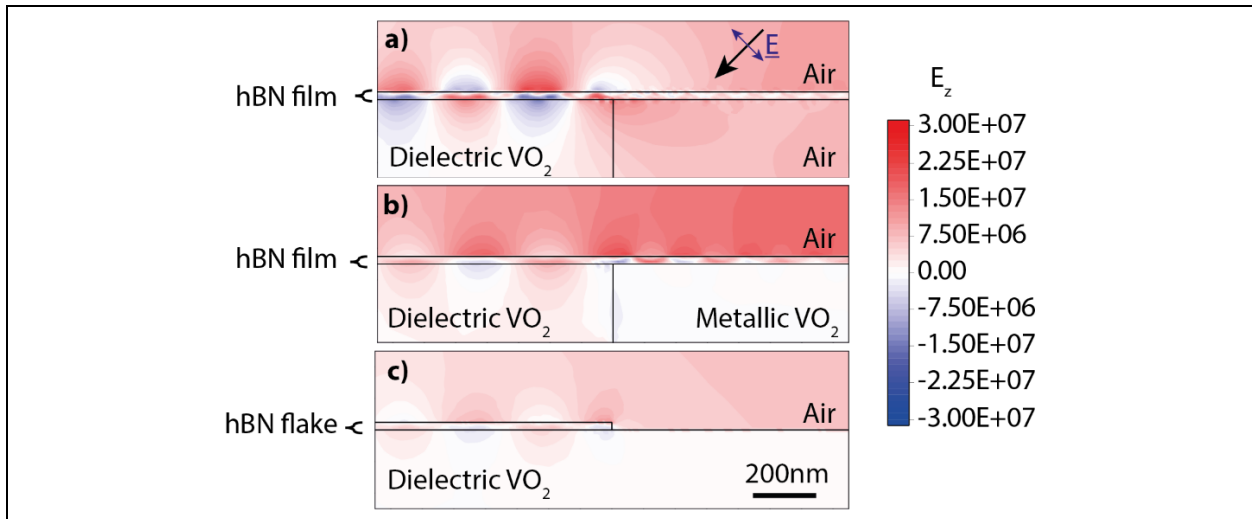
Figure 4.S1: Cross sectional plot of electromagnetic fields from hyperbolic polaritons launched at the interface between a) dielectric VO_2 and vacuum, b) dielectric VO_2 and metallic VO_2 and c) at the edge of a hBN flake on VO_2. The peak electromagnetic fields launched above the dielectric domain are $\sim 2.3 \cdot 10^7$ V/m, $\sim 1.8 \cdot 10^7$ V/m and $\sim 1.2 \cdot 10^7$ V/m, indicating the strongest fields are launched at the edge of the VO_2 flake, however, these simulations clearly show that edge-launched modes are highly suppressed in c).

Second, there is an interface where the hBN extends over the edge of the VO_2 crystal. As the films of hBN are continuous across the VO_2 edge, tip-launched modes can propagate over this interface and will only be weakly reflected. This has been observed in earlier experiments,

for example Ref. 25 of the main text.[1] On the other hand, the VO_2 crystal itself strongly scatters incident waves to launch polaritons from the VO_2 crystal edges. Therefore, we only see the edge-launched modes at the interfaces between hBN and the VO_2 crystal.

The third type of interface is the domain boundaries between dielectric and metallic VO_2. Due to the relatively small size of the domains in this sample, these show much weaker s-SNOM signals, however, the same arguments as for the edge of the VO_2 crystal hold. Therefore, we mainly see the edge-launched polaritons. This hypothesis is qualitatively supported by electromagnetic simulations of plane waves incident on these three types of boundaries, presented in Supplementary Fig. 1. The results show that polaritons launched from the VO_2 crystal edge (Supplementary Fig. 1a) or dielectric-metal domain boundaries (Supplementary Fig. 1b) are relatively strong, whilst those initiated from the edge of the hBN flake (Supplementary Fig. 1c) are relatively weak in intensity.

For the experimental efforts exploring the changes in polariton wavelength, refraction and propagation over the two VO_2 domain types, we employed a series of heating and cooling cycles with s-SNOM measurements performed at various temperatures and incident frequencies. The generalized process for these measurements is summarized in Fig. S2, whereby the sample was initial measured using S-SNOM at room temperature, then heated to various temperatures just below, within and then above the phase-change temperature, with s-SNOM measurements performed at specific temperatures within this range. Following these efforts, the sample was cooled, thereby resetting the VO_2 to the dielectric phase, where the process could be repeated with different phase transition domain structures. Multiple heating and cooling cycles were performed for the experiments discussed in this work, with no changes in the response of the dielectric functions of the constituent materials observed, thereby illustrating the reproducibility of this process.
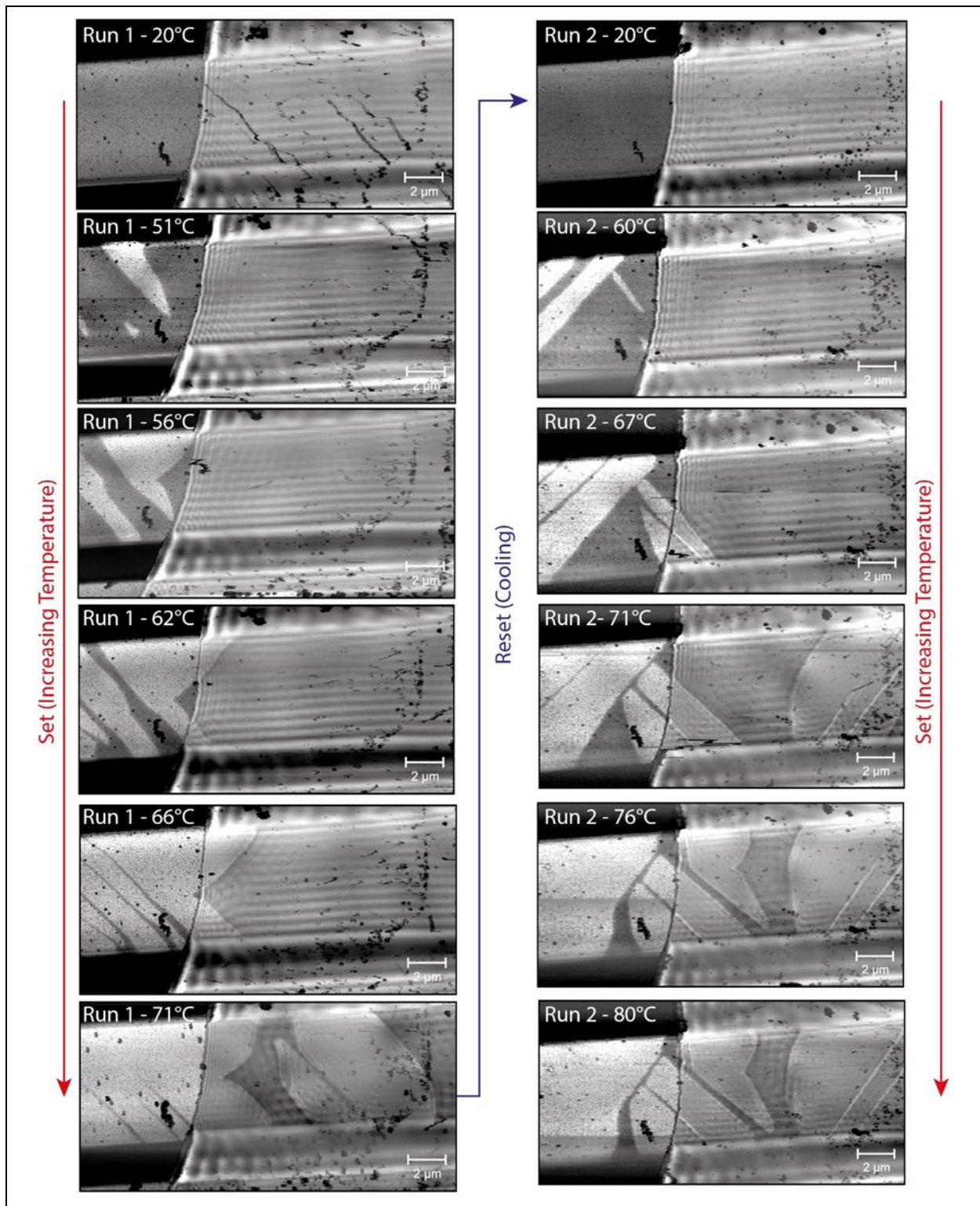
Figure 4.S2: Thermally induced phase transition in VO_2 for reconfigurable metasurfaces. Here we show a series of s-SNOM images taken at the same position as the sample temperature is increased, showing the growth of metallic VO_2 domains, which manipulate polariton propagation in hBN. By cooling the device back to room temperature the device is reset to its dielectric state, and, upon reheating, form a different phase domain pattern.

4.9.b Absence of Out-of-Plane Topographic Change during Crystal VO₂ Phase Transition

Figure 4.S3: Topographic variation upon phase transition. Near-field 2nd Harmonic IR amplitude (left top) and topography (left bottom), with the correlated line profiles provided on the right (red - IR amplitude and black - topography).
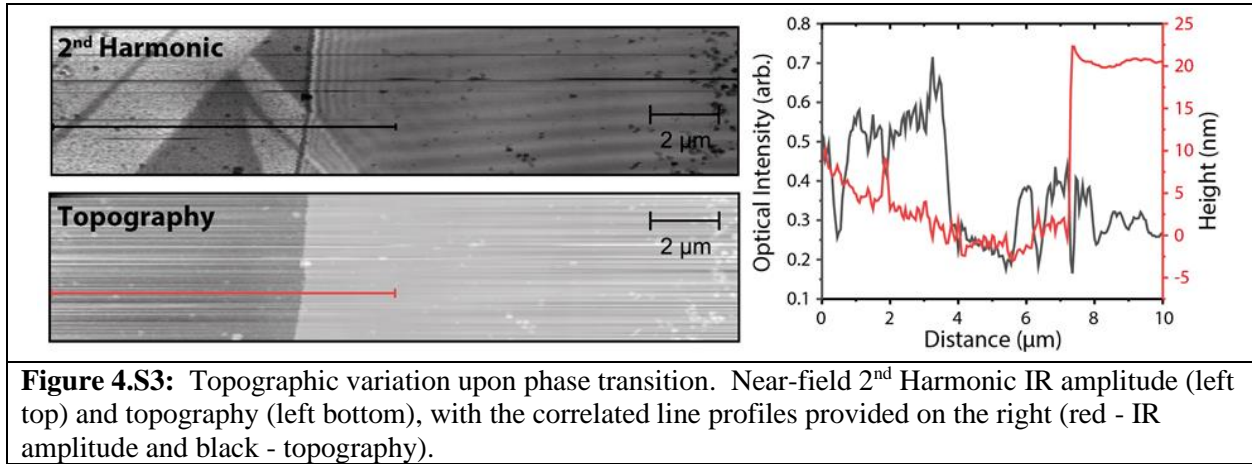
To show that the observed optical effects are attributable to changes in the dielectric environment and not to topographical changes along the out-of-plane axis, we compared spatial maps of the sample with optical s-SNOM measurements (Supplementary Fig. 3). Comparing line scans at the same topographical location in both 2nd harmonic IR amplitude s-SNOM signal and topographical height, we see that while there appears to be small topographic variations (due to noise induced at elevated temperatures, and residual contaminants from the device fabrication process), these do not correlate with the location of domains in the IR s-SNOM amplitude maps. This clearly demonstrates that the domains observed in the IR s-SNOM maps are due to the change in the phase change material (PCM) dielectric function, not to changes in the topography of the sample surface.

4.9.c Additional Images of Polariton Refraction and Determination of Dispersion
Experimental demonstration of HPhP refraction for polaritons transmitted across a dielectric-metallic domain was presented in Fig. 2a,b of the main text. For completeness and to demonstrate the how the additional refraction angles that were reported in Fig. 3c, we provide three additional s-SNOM maps that were collected at the same incident frequency as Fig. 2a,b, but were collected during different thermal cycles, providing different domain angles with respect to the VO₂ crystal edge. In all cases, the HPhP launching within the metallic domain from the VO₂ crystal edge is designated with the red lines, while the refracted HPhP by the black lines. The corresponding linescans extracted from these images are provided below each s-SNOM map and demonstrate again that despite the refracted wave propagated at a direction that is non-normal to either the VO₂ crystal or PCM domain edge that it has the same HPhP wavelength (black curves) as the edge-launched mode in the same domain (red curves).

Figure 4.S4: Additional images of polariton refraction in S-SNOM experiments. Dark patches on the images are contaminants that built up on the sample due to continuous imaging at high temperatures. The s-SNOM maps were collected at 1450cm^{-1} frequency and 65.5,58 and 55.7°C temperatures.
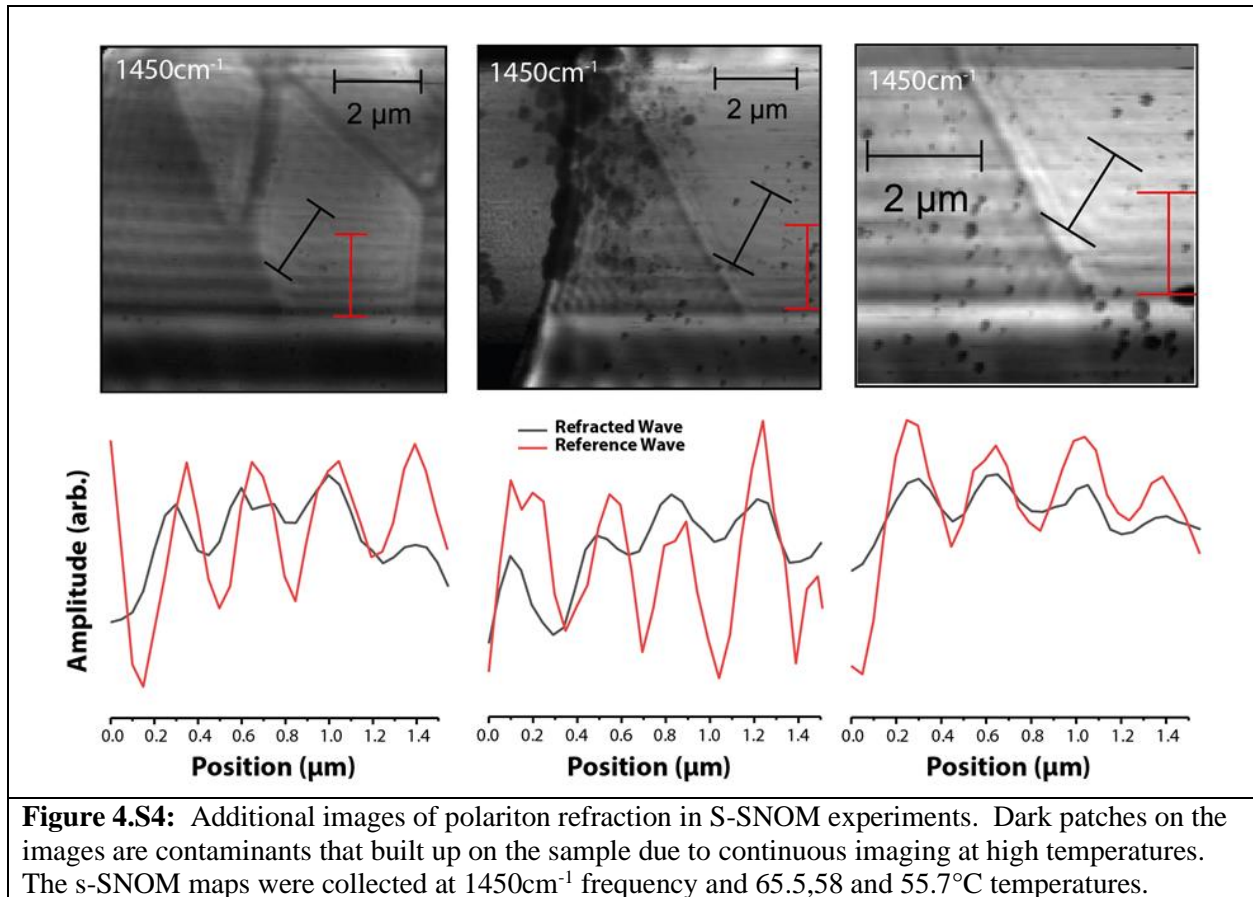
The extraction of the HPhP wavelength was performed as described within the main text and methods sections. This is also illustrated in Supplementary Fig. 5, where we present a) the s-SNOM maps collected at two different incident frequencies (as labelled) when the underlying VO$_2$ was in the dielectric (top two) and metallic (bottom two) phase. Linescans were collected along the trajectories designated by the white lines in Supplementary Fig. 5a, and are presented for each plot in Supplementary Fig. 5b. Through implementing a discrete Fourier transform (FFT) of these linescans, the frequency component of the HPhP propagation and thus, the HPhP wavelength within these domains can be extracted (Supplementary Figure 5c). By plotting the frequency dependence of this wavelength for both VO$_2$ phases, the dispersion plots presented in Fig. 3a and b, respectively, were realized.
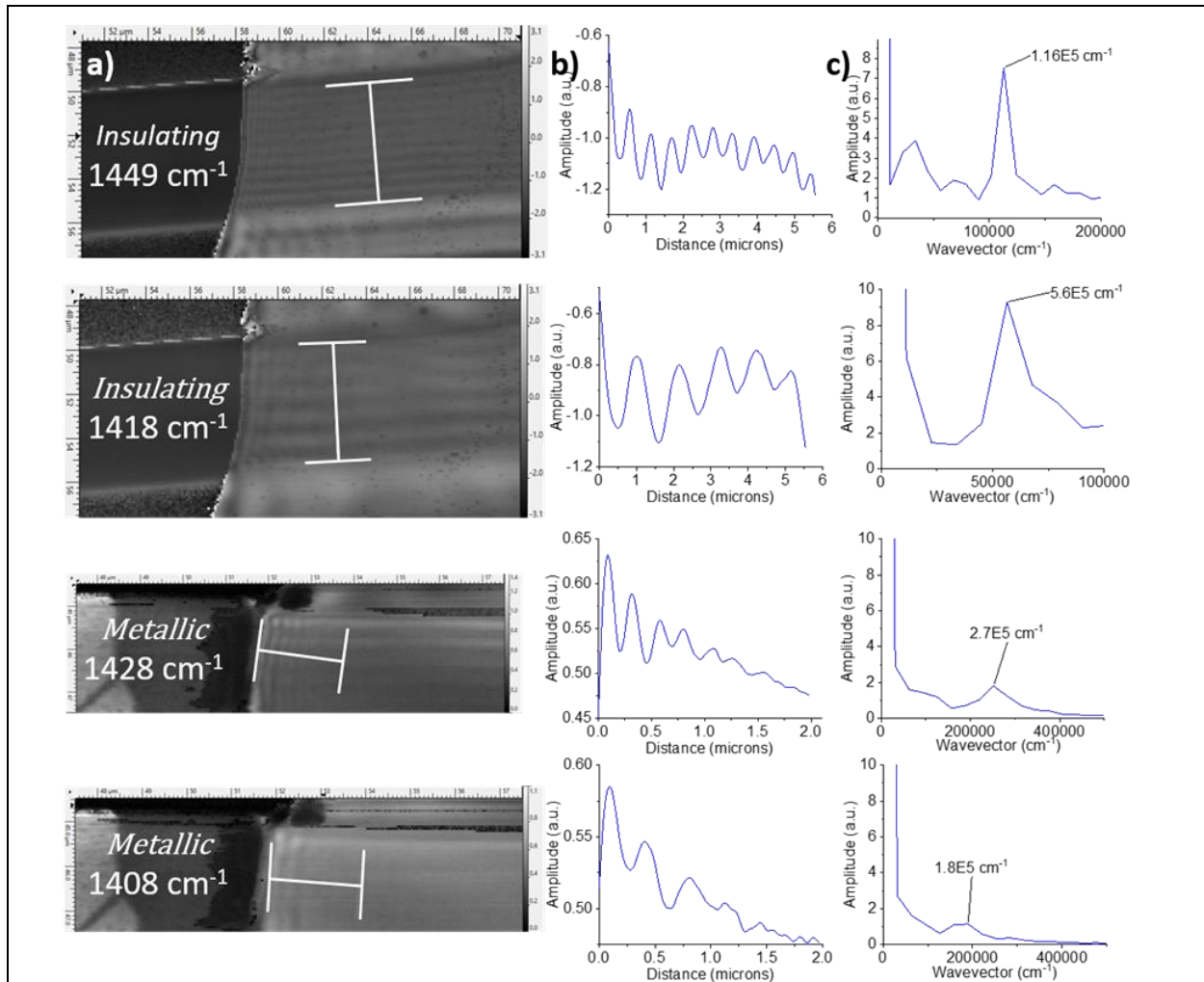
Figure 4.S5: Determining the polariton wavelength for given VO$_2$ phases and laser frequencies. a) The s-SNOM amplitude corresponds to line-scan markers perpendicular to the dominant propagating wave. b) The line-scan profiles, taken where shown in **a**). c) The frequency component of each line scan was extracted using fast Fourier transforms (FFTs) with a rectangular window, and normalizing amplitude to the mean-square amplitude (MSA). The peaks show the dominant frequencies in the line scan. Peak positions were converted to wavevector and used to plot the dispersions in Fig. 3.

4.9.d Electromagnetic Simulations of Polariton Refraction:

To supplement experimental results on polariton refraction, we conducted electromagnetic simulations for various metallic-dielectric domain angles and frequencies, identical to Fig. 2c, and present them in Supplementary Fig. 6a. In each simulation, the angle of the refracted wave was determined by inspection, from which we plotted Supplementary Fig. 6b, analogous to Fig. 3c. Lines in Supplementary Fig. 6b were extracted by calculating n_1 and n_2 for the polaritons propagating over both the metallic and dielectric domains from the polariton wavelength. As a result, the plots in Supplementary Figure 6b contains no fitting, and shows excellent agreement with Snell's law.
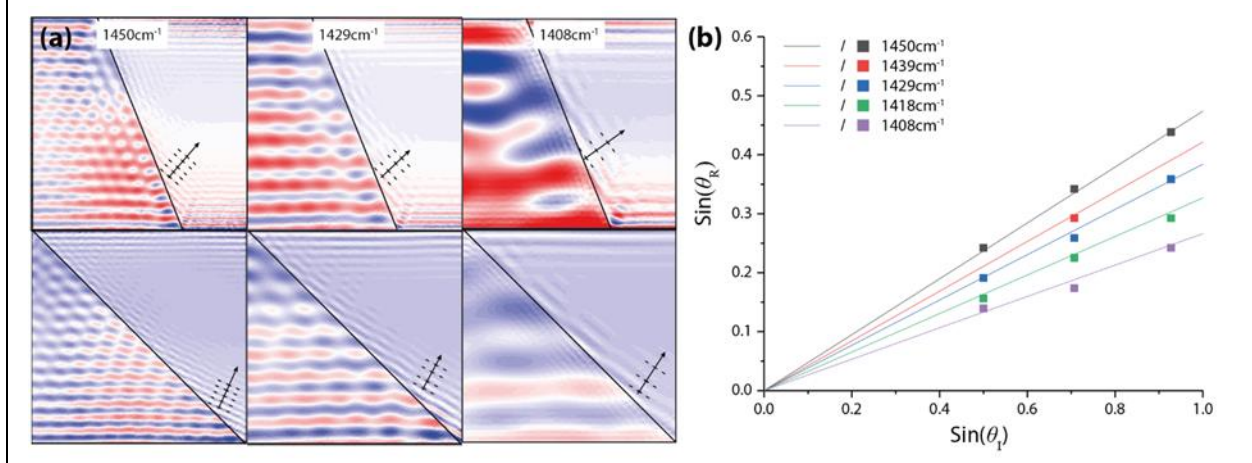
Figure 4.S6: a) Electromagnetic simulations of polariton refraction at 68˚ and 45˚ with respect to the surface normal. Each image shows the refracted wave, and was used to create the data points in b). b) Snell's law tested using electromagnetic simulations. The calculations follow Snell's law closely, with discrepancies due to uncertainties in accurately determining refraction angles.

4.9.e VO$_2$ and hBN Rewritable Metasurface

In Fig. 4a of the main text, we present the simulated reflectance spectrum of a hBN film on top of VO$_2$ patterned into metallic and dielectric domains (hereafter referred to as VO$_2$ resonators). Here we address the frequency tuning of the resonances observed in these spectra. We address two approaches to achieving frequency tuning – changing resonator size L (L=250 nm in Fig. 4a) with fixed pitch P (P=500 nm in Fig. 4a) and changing pitch with fixed filling fraction (f = L/P). The reflectance spectrum of such reconfigurable resonators as a function of the resonator size, is provided in Supplementary Fig. 7a and illustrates both a variation in reflectance, and small changes in the spectral positions of the resonant modes. The change in the overall reflectance can be attributed largely to changes in the reflectance of the VO$_2$ resonators, with larger resonators exhibiting higher reflection. The spectral mode shifts are approximately 3.34, 3.34, 4 and 2 cm^{-1} from lowest to highest modal wavenumbers, which is much lower than what would be expected for localized resonances. The reason for this becomes clear when we consider the influence of grating pitch with a constant fill fraction in Supplementary Fig. 7b. Here we see that each mode red-shifts significantly (approximately 30 cm^{-1} for the mode around 1525 cm^{-1}) with increasing grating pitch. Note that here the overall reflectance does not change significantly, as the fraction of metallic vs dielectric VO$_2$ remains approximately constant when we fix the fill fraction. Our resonant tuning behaviour is consistent with our metasurface effectively acting as a grating coupler, as HPhPs can freely propagate through the hBN film. We note that while here we do not show significant absorption or reflection resonances induced by the metasurface design, this could potentially be achieved by optimizing the combination of hBN thickness, VO$_2$ crystal thickness and lateral size, along with the designed metallic domain pitch and size.

Figure 4.S7: Frequency tuning of hyperbolic modes for the metasurface presented in Fig 4a. a) Shows tuning of the resonant modes for different metallic domain sizes at constant pitch, b) the tuning of the resonant modes for variable domain pitch.
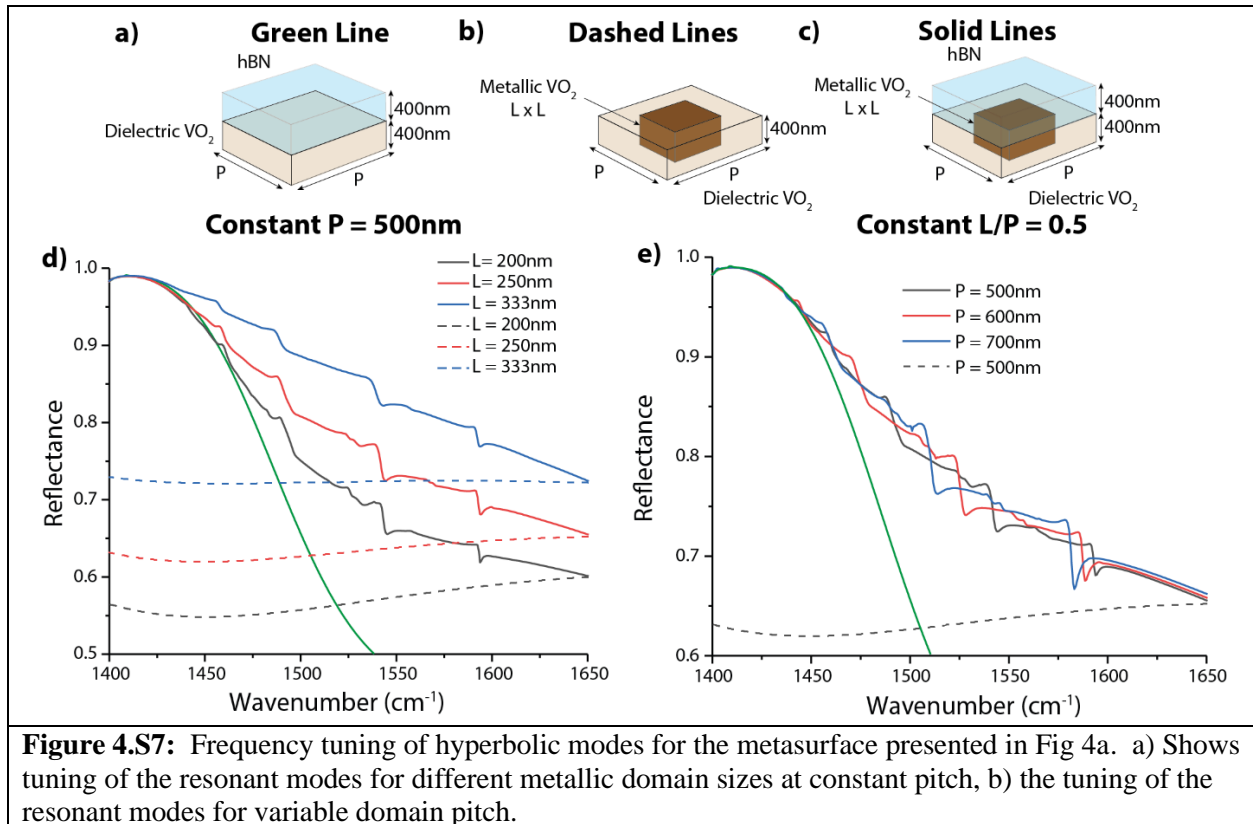
4.9.f VO₂ and GeSbTe Hyperbolic Waveguides

Here we compare the performance of VO_2 and GeSbTe PCMs for applications in creating hyperbolic polariton waveguides. Whilst the phases of VO_2 are discussed in the main text, GeSbTe also possesses both metallic and dielectric phases, which can be cycled by heating and cooling. In contrast to VO_2, the dielectric phase of GeSbTe is amorphous (α-phase), and the metallic phase is cubic (c-phase). To simulate a hyperbolic waveguide in both materials, a 300 nm metallic/c-phase domain was formed within a dielectric/α-phase of VO_2/GeSbTe (see Supplementary Fig. 8). This forms a lateral waveguide, where the high refractive index of the polariton within the strip prevents light from escaping. A small gap in the metallic phase (500 nm wide) creates an antenna that couples far-field waves into both the laterally confined waveguide mode and a radially propagating mode. For the VO_2 structure the radial wave propagates a significant distance over the dielectric domain, due to low losses inherent to the dielectric medium. However, in metallic VO_2 the guided wave is suppressed after just a few oscillations, with a $1/e$ propagation length of $\gamma = 0.57$ µm extracted by fitting a decaying sine wave. In contrast, for GeSbTe the waveguide mode appears to propagate a longer distance than the radial mode, with a decay length of $\gamma = 1.57$µm. This shows that the phenomena reported in this paper should be observable in GeSbTe films, and that this PCM might be better suited to some waveguide applications, In principle, by optimizing the waveguide width, hBN and PCM thickness it may be possible to optimize this structure to achieve long range ($>\lambda$) propagation of the polariton mode.

Figure 4.S8: Simulation of a near-field waveguide achieved using phase-change materials. Bottom shows E_z electric field profiles taken from the centre of the hBN, with extracted line profiles from the centre of the waveguide. Red lines show fitting of a damped sine wave to the simulated data.
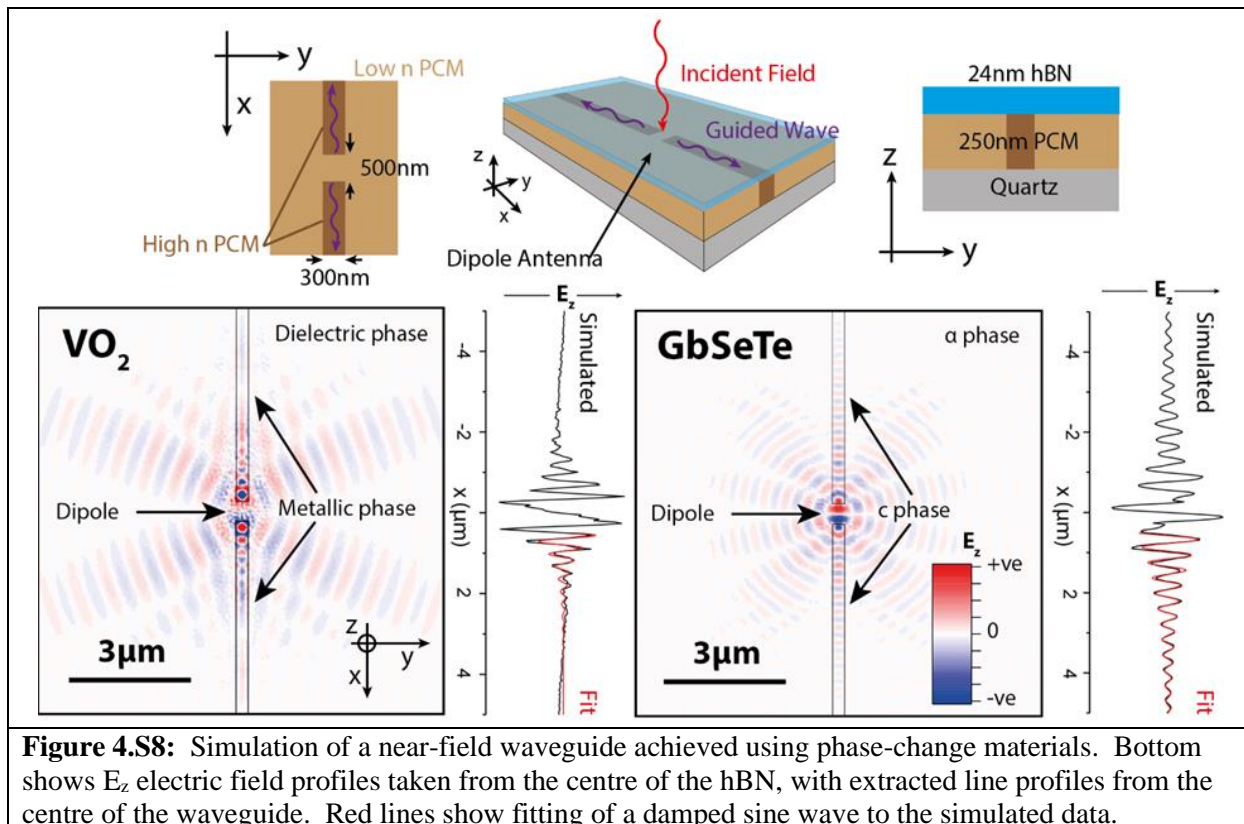
4.9.g SI References

1.   Duan, J.; Chen, R.; Li, J.; Jin, K.; Sun, Z.; Chen, J., Launching phonon polaritons by natural boron nitride wrinkles with modifiable dispersion by dielectric environments. *Advanced Materials* **2017,** *29* (38), 1702494.

CHAPTER 5

REFRACTIVE INDEX-BASED CONTROL OF HYPERBOLIC PHONON-POLARITON PROPAGATION

5.1 Publication Citation

Material in this chapter has been published as follows:

It is reproduced here, with minor formatting changes, with the permission of all authors and the publisher.

5.2 Abstract

Hyperbolic phonon polaritons (HPhPs) are generated when infrared photons couple to polar optic phonons in anisotropic media, confining long-wavelength light to nanoscale volumes. However, to realize the full potential of HPhPs for infrared optics, it is crucial to understand propagation and loss mechanisms on substrates suitable for applications from waveguiding to infrared sensing. In this paper, we employ scattering-type scanning near-field optical microscopy (s-SNOM) and nano-Fourier transform infrared (FTIR) spectroscopy, in concert with analytical and numerical calculations, to elucidate HPhP characteristics as a function of the complex substrate dielectric function. We consider propagation on suspended, dielectric and metallic substrates to demonstrate that the thickness-normalized wavevector can be reduced by a factor of 25 simply by changing the substrate from dielectric to metallic behavior. Moreover, by incorporating the imaginary contribution to the dielectric function in lossy materials, the wavevector can be dynamically controlled by small local variations in loss or carrier density. Counterintuitively, higher-order HPhP modes are shown to exhibit the same change in polariton wavevector as the fundamental mode, despite the drastic differences in the evanescent ranges of these polaritons. However, because polariton refraction is dictated by the *fractional* change in the wavevector, this still results in significant differences in polariton refraction and reduced sensitivity to substrate-induced losses for the higher-order HPhPs. Such effects may therefore be used to spatially separate hyperbolic modes of different orders, and indicates that for index-based sensing schemes that HPhPs in thin flakes of hBN are more sensitive than surface polaritons only when the analyte material is itself very thin. Our results advance our understanding of fundamental hyperbolic polariton excitations and their potential for on-chip photonics and planar metasurface optics.

5.3 Introduction

Due to the long free-space wavelength of mid- to far-infrared (IR) light, the field of IR nanophotonics has employed polariton effects to confine light to dimensions well below the diffraction limit. This has advanced the state of the art in on-chip photonics, [1] polariton waveguides[1-2] and nanolasers. The hyperbolic polariton offers significant promise in many nanophotonic applications[3-4] because it offers volume-confined electromagnetic near-fields,[5-12] a restricted propagation angle dictated by the hyperbolic dielectric function,[9, 13-14] and a dramatically expanded photon density of states[4, 11] due to the inclusion of higher-order polaritons with diminishing wavelengths (increasing wavevectors) at the same frequency.[5-6, 10] Applications of these properties include hyperlensing,[7, 12, 15-16] metasurface-based optical components,[1-2, 17-18] quantum optics[19] and probes of nanoscale defects.[20-21]

In 2014 hBN was first reported as a naturally hyperbolic material with exceptionally low optical losses, [5-6] because it supports polaritons derived from optic phonons[22] rather than scattering from free carriers. Since then, an extensive list of naturally hyperbolic materials have been cataloged;[23-25] one of the most promising is MoO_3[18, 26-28] given its record polariton lifetimes (up to 20 ps)[26] and in-plane hyperbolicity. Unlike surface-confined polaritons,[29] volume-confined hyperbolic polariton fields can interact with the local environment with minimal additional loss.[1, 30] Thus, hyperbolic polariton properties can be potentially tuned without substantially reducing propagation lengths.

Previously, we demonstrated planar meta-optics in heterostructures comprising hBN and the phase-change material (PCM) vanadium dioxide (VO_2) by showing that refraction of HPhPs in hBN obeys Snell's law at boundaries between rutile and monoclinic domains of VO_2.[1] Refraction, induced by a large (1.6x change) wavevector mismatch between principal HPhP modes in hBN supported over the two domains, opens pathways to reconfigurable metasurfaces, rewritable designer planar optics and waveguides, and tunable optical resonators. The volume confinement of the HPhPs guaranteed that although the polaritons are sensitive to the local environment, the polaritonic near-fields will propagate primarily within the low-loss hyperbolic material. This not only provided a first demonstration of a reconfigurable, hyperbolic metasurface, but also illustrated the strong sensitivity of the hyperbolic polaritons to the local dielectric environment, unlike earlier studies with hBN frustums,[5] however, the strong SEIRA enhancement reported for HPhPs in hBN nanostructures inferred the environment played a significant role in response.[31] While the effects of substrate dielectric function on HPhPs have been investigated for several different individual substrates, no systematic comparison has been performed from which broad conclusions can be drawn.[32-37] A recent study of HPhPs in suspended hBN by real-space nanoimaging[33, 35] showed that the propagation figure of merit (FoM) was significantly reduced for hBN supported on SiO_2.[33] Furthermore, for wrinkled hBN on gold, the polariton wavelength is compressed by a factor two.[36-37] For advanced applications featuring the growing library of natural hyperbolic materials,[23-25] such as reconfigurable planar optics, the role of the substrate in dictating the room-temperature HPhP dissipation and propagation on the principal and higher-order HPhP modes must be ascertained. Thus, it is critical to quantify how the local dielectric environment of the substrate modifies propagating hyperbolic polariton modes, and to analyze how this propagation is affected by dielectric losses in the substrate.

To this end, we have explored the effects of substrates with varying refractive indices on HPhPs in isotopically enriched hBN, on suspended, metallic, dielectric and phase-change
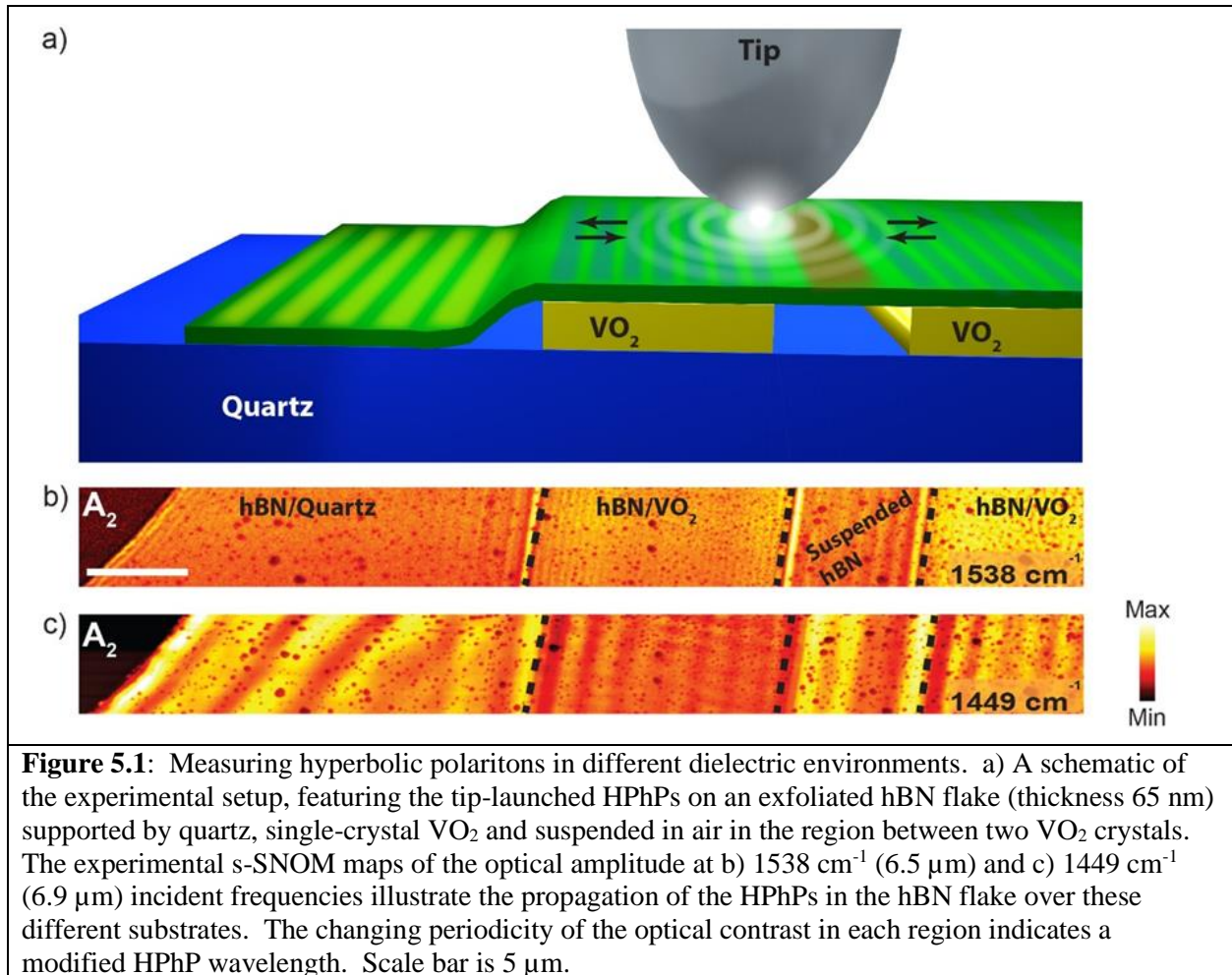
substrates. Employing the analytical model first proposed by Dai et al.,[6] we show that the complex substrate dielectric function has non-trivial consequences for hyperbolic polariton propagation. The model specifically predicts that in the limit of small real substrate permittivity that the wavelength of the lowest-k hyperbolic polariton can be modified by up to a factor of 25, simply by transitioning from a metallic to a dielectric substrate. The trends of all hyperbolic polariton wavelengths as a function of the real part of the substrate permittivity are inverted, with metallic (dielectric) substrates exhibiting shrinking (expanding) polariton wavelength with increasing substrate permittivity. Counterintuitively, despite the increasing confinement of the polariton fields to the volume of the hyperbolic medium, the influence of such changes in the substrate permittivity upon the wavelength of the higher-order hyperbolic modes is equivalent to that of the fundamental polariton. Our experiments and calculations also highlight that the imaginary part of the substrate permittivity plays a critical role in dictating hyperbolic polariton propagation. While we report these results using hBN, the findings discussed can be generalized to the broader class of hyperbolic media. Based on our findings, we highlight their technological implications, illustrating that this offers the potential for spatially separating the fundamental from the higher order HPhP modes within planar geometries and offers promise for advanced index-based sensing modalities by controlling the substrate dielectric function at a local level.

5.4 Results

To quantify the role of the substrate complex refractive index on the hyperbolic polariton wavevector, we prepared several hBN flakes (see Methods) of similar thicknesses on silicon, quartz, VO$_2$ (insulating and metallic) and silver. We then probed the HPhPs in the hBN using a scattering-type scanning near-field optical microscope (s-SNOM) coupled to a line-tunable quantum cascade laser or a broadband IR source (Methods). When laser light is scattered from the AFM tip, HPhPs are launched by the evanescent fields induced at the tip apex, which is located in near-field proximity to the hBN surface (Fig. 1a). These HPhPs propagate radially outward from the tip, confined within the volume of the hBN flake. Upon reaching a boundary, such as a sharp flake edge or a local domain with significant index contrast, the HPhP is reflected. This reflected polariton wave interferes with the outgoing mode to generate a pattern that can be directly probed by the s-SNOM tip, which for "tip-launched" polaritons this results in an interference pattern with a periodicity that is half of that of the incident polariton wavelength. Other HPhPs can be directly launched by IR light scattered by the flake edge, which is out-coupled to the detector via the s-SNOM tip. These "edge-launched" modes exhibit a different interference pattern with the periodicity of the incident polariton wavelength.[1, 6, 10, 38] Thus, by probing polariton wavelength and propagation length as a function of incident frequency and the complex dielectric constant of the substrate, it is possible to extract quantitatively the substrate-modified HPhP dispersion.

The HPhPs propagating within the hBN flake can be observed in the spatial profiles of s-SNOM amplitude (Fig. 1b and c) collected at ω=1538 and ω=1449 cm^{-1}. The exfoliated 65 nm thick hBN flake is supported on quartz and draped over two VO$_2$ single crystals, resulting in three regions where the hBN is suspended in air (Fig. 1a). The near-field amplitude maps collected at both incident laser frequencies show that the separation between interference fringes, and thus the wavelength of the principal HPhP mode, is strongly modified by the refractive index of the medium over which the mode is propagating, consistent with recent reports.[32-37] The

polariton wavelength was similarly substrate dependent in a second hBN flake supported between a Si substrate and VO$_2$ crystal (Fig. S1).

Figure 5.1: Measuring hyperbolic polaritons in different dielectric environments. a) A schematic of the experimental setup, featuring the tip-launched HPhPs on an exfoliated hBN flake (thickness 65 nm) supported by quartz, single-crystal VO$_2$ and suspended in air in the region between two VO$_2$ crystals. The experimental s-SNOM maps of the optical amplitude at b) 1538 cm^{-1} (6.5 µm) and c) 1449 cm^{-1} (6.9 µm) incident frequencies illustrate the propagation of the HPhPs in the hBN flake over these different substrates. The changing periodicity of the optical contrast in each region indicates a modified HPhP wavelength. Scale bar is 5 µm.

To capture the dispersion of the propagating HPhPs on different substrates, we collected s-SNOM amplitude images, similar to those in Fig. 1b and c, at several incident laser frequencies. From these images we extracted line-scans parallel to the propagation direction, and then utilized a fast Fourier transform (FFT) to extract the HPhP wavelength (λ_{HPhP}), then plotting the dependence of this wavelength on laser excitation frequency (ω) for each substrate (dispersion relation). We extracted the magnitude of the in-plane wavevector k, using $k=2\pi/\lambda_{HPhP}$. The experimental substrate-dependent dispersion relations were then determined by plotting k as a function of ω (circles in Fig. 2), for HPhP modes within hBN (a) suspended in air between the two VO$_2$ crystals, (b) on quartz, (c) on insulating VO$_2$ and (d) on metallic VO$_2$.
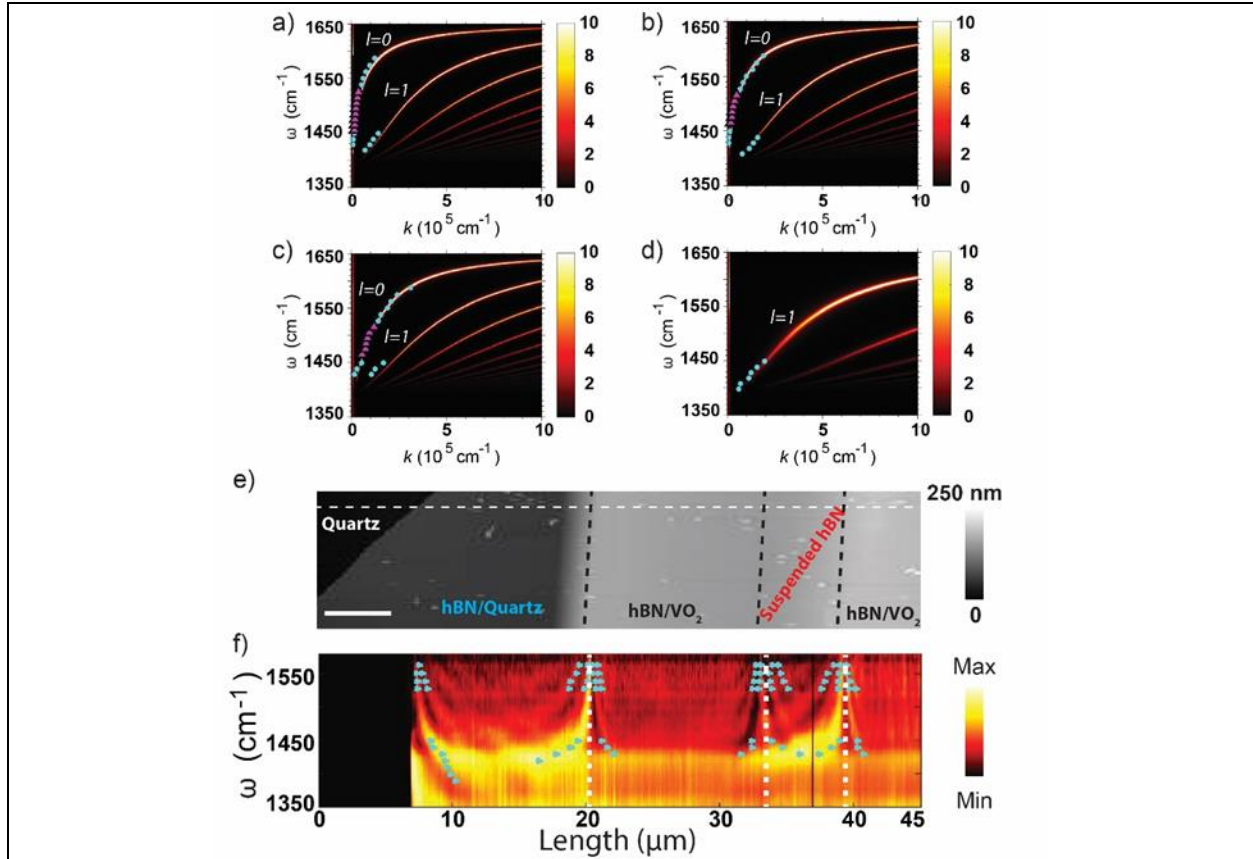
Figure 5.2: Measurements of the dispersion relations of HPhPs in 65 nm thick hBN on different substrates. The polariton wavelengths (ω, wavevectors) for each incident frequency were extracted using fast Fourier transforms of linescans extracted from the s-SNOM amplitude plots for the HPhP modes collected over the various substrates. The dispersion in these values for HPhPs propagating within hBN over a) air (suspended), b) quartz, c) insulating VO_2 and d) metallic VO_2. Circles indicate data points from s-SNOM and triangles are similar results derived from nano-FTIR spectral linescans (results from f) and are superimposed upon analytical calculations of the HPhP dispersion. The z-scale is the imaginary part of the p-polarized reflection coefficient, $Im(r_p)$ (e) Topographic maps of the sample illustrate the lack of surface features. (f) Corresponding nano-FTIR spectral linescans illustrate the HPhP properties at every position along the broken white line in e). Solid points in f) are experimental data points extracted from monochromatic polariton images (as in Figures 1b and c).

To supplement these results and provide experimental data in the spectral gap between 1450 to 1480 cm^{-1}, we acquired a nano-FTIR linescan that yields the relationship between the momentum k and the excitation frequency ω at every pixel. The nano-FTIR data were acquired by collecting a broadband spectrum along the white dashed line shown in Fig. 2e and displaying the resulting spectra in a 2D plot where the x-axis (length) is pixel location and the y-axis is the frequency (ω) covering the polariton spectral range, as shown in Fig. 2f. The line-scan covers all of the substrate environments, including suspended hBN, as well as regions where the hBN was in direct contact with quartz and VO_2, providing a k vs ω spatial map over the various substrates in a single scan. This enabled us to extract data points outside of the range of our available monochromatic laser sources (in purple triangles in Figures 2a-c).[6] The experimental data are in excellent agreement with the analytical dispersion relations, as shown by the solid lines for all

substrates. These calculations were performed using the analytical model reported in Ref.[6] In the limit where the HPhP wavelength is much shorter than the wavelength within the underlying substrate, this analytic expression can be derived from the Fabry-Perot resonance condition:

$$kd = [Re(k) + iIm(k)]d = -\psi \left[tan^{-1} \left(\frac{\varepsilon_0}{\varepsilon_t \psi} \right) + tan^{-1} \left(\frac{\varepsilon_s}{\varepsilon_t \psi} \right) + \pi l \right], \psi = -i \sqrt{\frac{\varepsilon_z}{\varepsilon_t}}$$

(Equation 1)

where d is the hBN thickness, $\varepsilon_0, \varepsilon_s, \varepsilon_t$ and ε_z are the complex dielectric functions of air, the substrate, and hBN for both in- and out-of-plane directions, respectively, and l is the mode order of the HPhP. For dielectric substrates, l=0,1, 2... however, on metallic substrates the mode $l = 0$ is not supported, due to the influence of the image charge generated in the substrate.[32] Throughout, we compare the $l = 0$ mode HPhPs on dielectric substrates to the $l = 1$ mode HPhPs on metallic substrates, because these represent the lowest-k modes supported on the respective substrates. The three terms in Eq. 1 represent the phase shift accumulated from reflection of the HPhPs from the top and bottom of the flake, and during propagation within the layer, respectively.[6, 14] In this approximate equation, the polariton wavelength is normalized to the hBN thickness, facilitating direct comparison of the HPhP dispersion in hBN flakes of varying thickness on different substrates. This is especially important for the work presented here, as identifying flakes with the exact same thickness suitable for transfer to the various substrates studied would be a considerable difficulty. In addition to the substrates already discussed, similar measurements were made on silver and silicon. The HPhP images and dispersion plots of hBN on these substrates are provided in the Supporting Information, (Fig. S2).

The dispersion relations plotted in Fig. 2 and Fig. S2 show that the wavelength of the propagating HPhPs can be altered by the choice of substrate and incident frequency, as explored in prior work.[32-37] However, in this study the range of substrate dielectric properties is broader, enabling a systematic examination of the variation of the HPhP wavelength with substrate dielectric function, referenced to the intrinsic properties of suspended hBN. To compare our experimental results and theory, we plot the polariton wavevector as a function of the absolute value of the real part of the dielectric function of the substrate $[|Re(\varepsilon_s)|]$ at a single frequency (similar plots at other incident frequencies are provided in the Supporting Information, Fig. S6) to draw general conclusions about the dependence of HPhP modes on substrate dielectric function.

To make consistent comparisons between theoretical and experimental results on hBN flakes of varying thicknesses between the different substrates, we make two simplifications. First, we consider the dimensionless HPhP wavevector *kd*, calculated by multiplying the HPhP momentum by the flake thickness, to normalize the dispersion relationship, as in Eq. 1. The thickness dependence of hyperbolic polariton dispersion is a consequence of the Fabry-Perot behavior of hyperbolic modes in thin slabs.[6, 14] Second, we make assumptions about the relative magnitudes of the real and imaginary parts of the substrate dielectric function to account for absorption. Lossless IR dielectrics such as silicon have $Im(\varepsilon_s) = 0$; however for metals and polar materials, the real and imaginary parts of the dielectric function are coupled by the Kramers-Kronig relations. For many metals, in the spectral regions we probe, the imaginary part of the dielectric function satisfies $0.1 \leq Im(\varepsilon_s)/|Re(\varepsilon_s)| \leq 0.3$,[39] whereas for polar dielectrics $0.01 \leq Im(\varepsilon_s)/|Re(\varepsilon_s)| \leq 0.1$.[22] In certain classes of poor metals, as well as non-crystalline materials, $Im(\varepsilon_s) \gg |Re(\varepsilon_s)|$,[40] with $Im(\varepsilon_s)/|Re(\varepsilon_s)|$~10 being typical. Thus $Im(\varepsilon_s)/|Re(\varepsilon_s)|$ (the loss tangent) is a good measure of substrate loss properties.
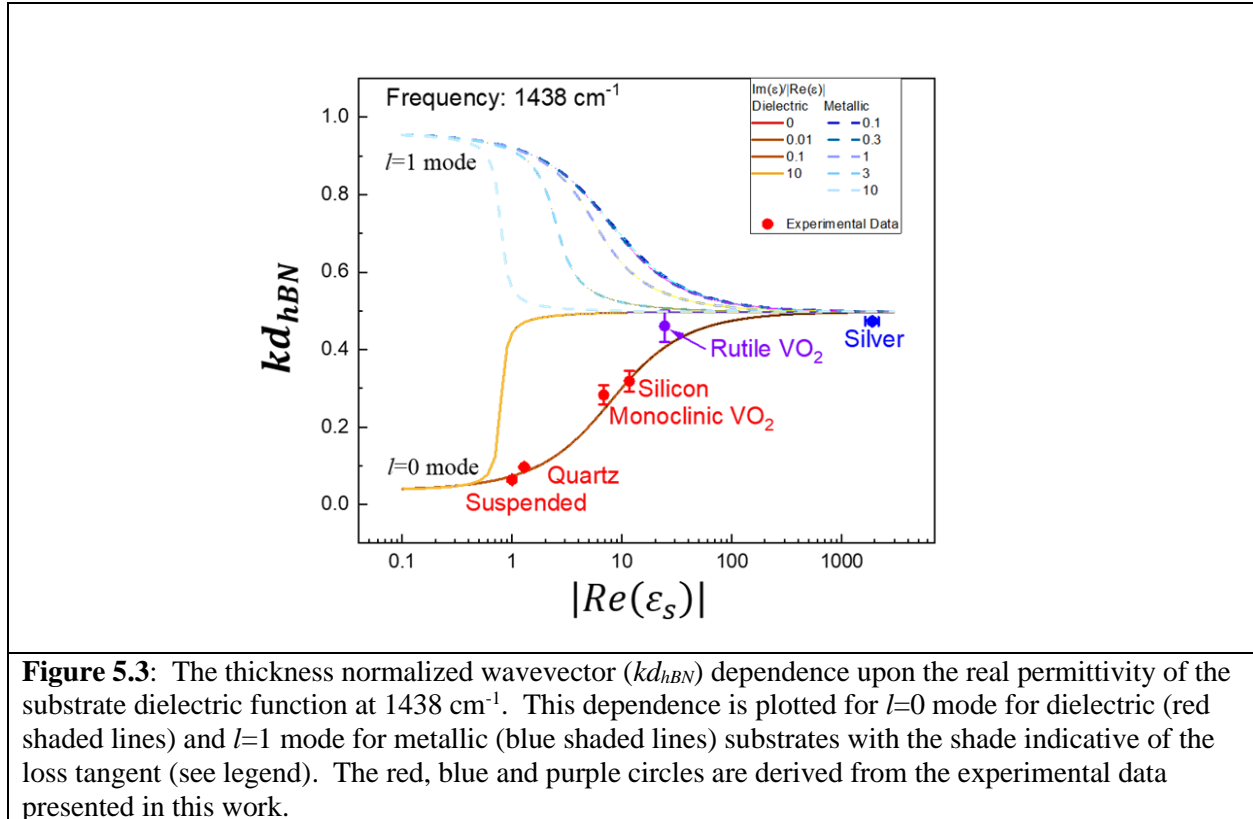
Figure 5.3: The thickness normalized wavevector (kd_{hBN}) dependence upon the real permittivity of the substrate dielectric function at 1438 cm^{-1}. This dependence is plotted for $l=0$ mode for dielectric (red shaded lines) and $l=1$ mode for metallic (blue shaded lines) substrates with the shade indicative of the loss tangent (see legend). The red, blue and purple circles are derived from the experimental data presented in this work.

The analytical (Eq. 1 with $l=0$ for dielectric and $l=1$ for metallic substrates) and experimental results for the normalized wavevector as a function of $|Re(\varepsilon_s)|$ are plotted in Fig. 3. The absolute magnitude of the real part is chosen to ensure metallic and dielectric species can be compared on the same scale. A range of analytical curves representing different $Im(\varepsilon_s)/|Re(\varepsilon_s)|$ ratios, for both positive (dielectric) and negative (metallic) $Re(\varepsilon_s)$ at 1438 cm^{-1} are provided. Experimental data are represented as solid points, with error bars derived from the range of dielectric functions for each substrate for the x-axis [39, 41-44] and from measurement uncertainty in the hBN flake thickness and wavevector for the y-axis. (The error estimates are discussed in SI). We compare theory and experiment by considering dielectrics [$Re(\varepsilon_s) > 1, Im(\varepsilon_s) \ll Re(\varepsilon_s)$], metals [$Re(\varepsilon_s) < 0, Im(\varepsilon_s) < Re(\varepsilon_s)$] and highly absorbing materials [$Im(\varepsilon_s) > Re(\varepsilon_s)$] separately. If there is little dispersion in the substrate dielectric function, the trends measured at the specific frequency reported in Fig. 3 will be generic to other frequencies. More pronounced effects can occur in the presence of absorption bands, where strong spectral dispersion occurs and could be treated by applying this analysis at other frequencies, as in the Supporting Information, Fig. S6.

First, we consider dielectric substrates. Analytical results (solid lines) indicate that the HPhP wavevector increases monotonically as a function of substrate permittivity $Re(\varepsilon_s)$, with only minimal influence from substrate-induced absorption loss. Red points indicate experimental data for HPhP modes within hBN on dielectric substrates in this experiment (suspended, quartz, silicon and monoclinic VO$_2$), which offer good quantitative agreement with the analytical model. This demonstrates that hyperbolic polaritons will exhibit a larger polariton wavevector (smaller wavelength) on higher permittivity dielectric substrates and is nominally

insensitive to substrate loss within the range of typical loss tangents for such materials, $Im(\varepsilon_s)/|Re(\varepsilon_s)| < 0.1$. We also emphasize that as $Re(\varepsilon_s)$ tends towards infinity, the value of kd tends to a frequency-dependent constant (ψ), which can be interpreted using Eq. 1. The only term that includes the substrate dielectric function is $tan^{-1}\left(\frac{\varepsilon_s}{\varepsilon_t\psi}\right)$, which defines the influence of the phase accumulated upon reflection of the hyperbolic wave from the substrate surface. As the dielectric function becomes larger, the phase of the reflected polariton tends towards $\pi/2$. We attribute the increase in phase shift to the reduced penetration depth in substrate, with a large real part of the dielectric function, which appears analogous to the Goos-Hänschen shift.[45] The longest absolute HPhP propagation length, compared to all the substrates considered in this study, is over the suspended region between the two VO$_2$ crystals, as confirmed by analytical calculations, and measured in prior work,[33] while the shortest is observed over metallic substrates.[35]

The propagation characteristics of the HPhP modes on metallic substrates are less intuitive. Analytical predictions for metallic substrates are shown as dashed lines in Fig. 3. For negative permittivity substrates, the tan^{-1} term in Eq. 1 becomes negative, resulting in a negative shift in the reflected phase. To provide a direct comparison between dielectric and metallic substrates, we set the minimum l=1. As the substrate becomes more metallic (i.e.. $Re(\varepsilon_s)$ becomes more negative) the magnitude of the HPhP wavevector is reduced. In the limit of large absolute values of the dielectric permittivity, the wavevectors of HPhPs in hBN over both metallic and dielectric substrates converge. For metals, this occurs when the plasma frequency is significantly larger than that of the HPhP mode, and thus the complex dielectric constant of the substrate comprises a large negative real permittivity and correspondingly large imaginary part. From the analytical calculations shown in Fig. 3, it would appear at first glance that the dispersion is more sensitive to losses for metallic substrates; however, this is due simply to the higher loss tangents associated with metals. This is consistent with our calculations for dielectrics, as no light can enter any material in which $Re(\varepsilon_s) \ll 0$, and hence experiences a $\pi/2$ phase shift upon reflection. In this study, we compared the analytical model to a single noble metal (silver), with the experimentally extracted wavevector quantitatively matching with our calculations at multiple incident frequencies.

Finally, we consider a highly absorbing material, represented by rutile (metallic) VO$_2$. The dielectric function of rutile VO$_2$ has not been measured extensively in this frequency range for single crystals, however, a recent paper has addressed this deficiency for certain types of deposited films.[40] Reference [46] indicates, however, that VO$_2$ is properly classified as a 'bad metal' as it fails to satisfy the Wiedemann-Franz law; therefore, we take it to be an overdamped material with $Im(\varepsilon_s) > |Re(\varepsilon_s)|$. If we assume a large loss tangent, $\frac{Im(\varepsilon_s)}{|Re(\varepsilon_s)|} \sim 10$, we find that regardless of whether rutile VO$_2$ is considered a bad metal or a lossy dielectric, there is minimal influence upon the normalized wavevector. To highlight the ambiguity in this case, we plot the wavevector of HPhPs supported in hBN on rutile VO$_2$ as a purple circle.

The good quantitative agreement between experiment and the analytical model clearly indicates the broad applicability of this approach for HPhPs, demonstrating that it is indeed capable of reproducing the influence of the substrate, regardless of loss or magnitude or sign of the permittivity in a generalized fashion for all hyperbolic media. However, it is important to note that the analytical model of Eq. 1 is only appropriate in the large k limit; that is when $k \gg k_s$. Outside of this regime numerical methods more accurately describe dispersion. However, the general trends for both the analytical and numerical models are nearly identical regardless of

regime, with the numerical results being required for conditions where k and $2\pi n_s/\lambda_0$ are of the same order, as shown in the Fig. S3 and S4 of the Supporting Information. Thus, conclusions drawn from the analytical model are representative of the mode behavior in hBN even for thicker flakes.
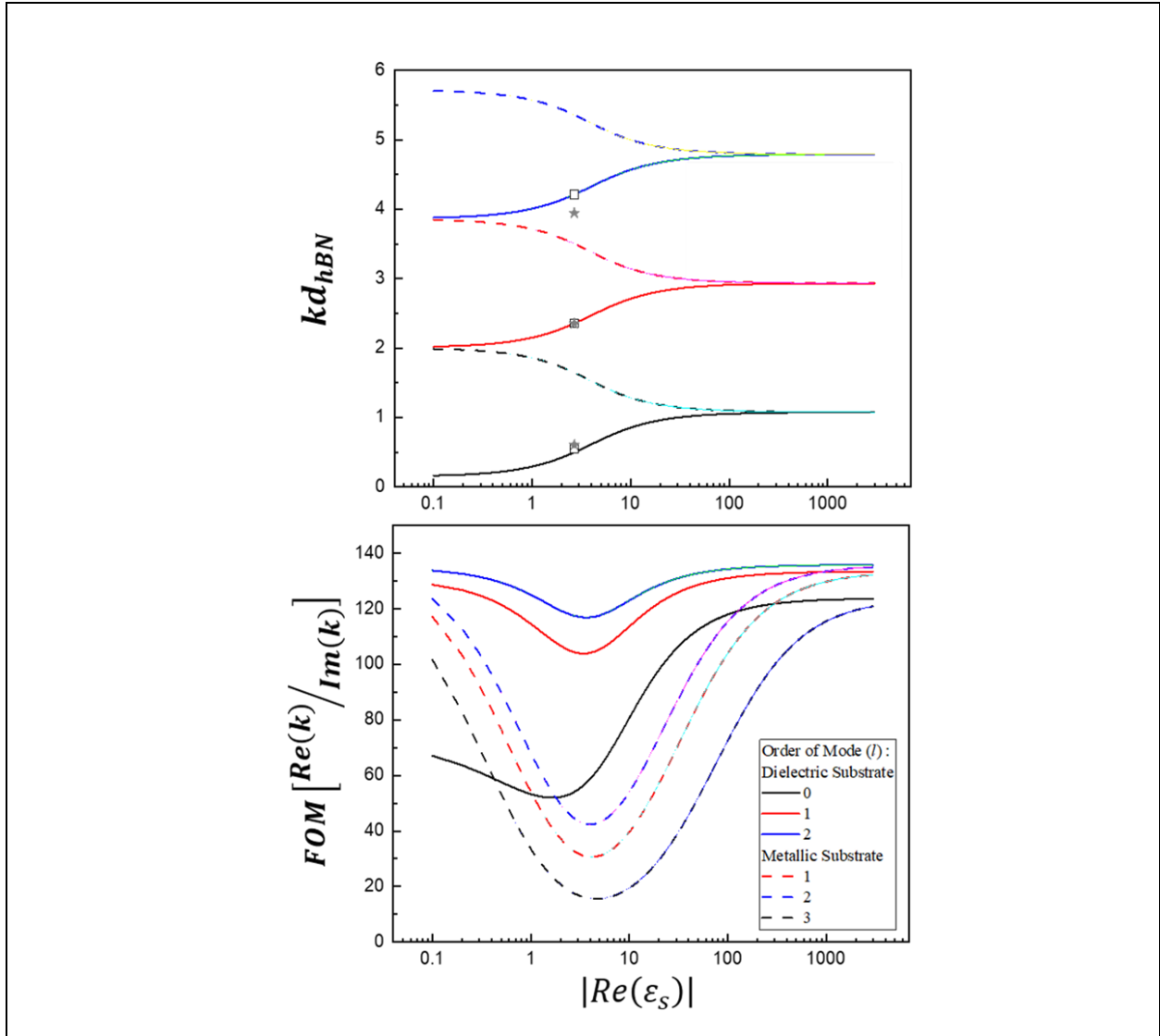
Figure 5.4: Influence of substrate dielectric function upon high-order HPhP modes of hBN at 1510 cm^{-1}, for dielectric (metallic) substrates, with the loss tangent fixed at 0.01 (0.3). a) $k \cdot d$ was plotted versus $|Re(\varepsilon_s)|$, and gray stars are experimental data in Ref. [10], while open boxes are numerical solutions for 120 nm thick hBN. b) FOM of the first three orders of HPhPs in this same thickness flake of hBN as a function of the $|Re(\varepsilon_s)|$.

To investigate the effect of the substrate refractive index on higher-order modes, we again plot the analytical dispersion relation in Fig. 4, including now the $l=1(2)$ and $l=2(3)$ modes at 1510 cm^{-1} and a loss tangent of 0.01 (0.3) for dielectric (metallic) substrates. These higher-

order branches correspond to shorter-wavelength polariton modes that are supported within the hyperbolic medium at the same incident frequency[4, 10] (Fig. 2). As with the principal HPhP mode, these high-order polaritons are also affected by the substrate dielectric function; however, due to the reduced range of the evanescent field associated with the shorter polariton wavelengths, one would expect this effect to be significantly reduced. However, the change in wavevector $\Delta k = k(\varepsilon_{s1}) - k(\varepsilon_{s2})$, from a low ε_s substrate with wavevector $k(\varepsilon_{s1})$ to a high ε_s substrate with wavevector $k(\varepsilon_{s2})$ is actually the same for all hyperbolic modes. Naively, this suggests that the substrate will have the identical influence on all higher-order modes in the hyperbolic material, with no significant change in the properties of different modes other than the degree of volume confinement.

However, the *fractional* change in wavevector $\frac{k(\varepsilon_s)}{k(\varepsilon_{s\prime})} = 1 + \frac{\Delta k}{k(\varepsilon_s)}$ is often a more useful metric in comparing HPhP propagation, where $\varepsilon_{s\prime}$ refers to a second substrate to which the first is compared. This is because phenomena such as refraction are entirely dependent on the fractional change in wavector, as indicated by Snell's law. For higher-order modes, with larger initial values of k, this fractional change becomes smaller, approaching unity—i.e. the higher-order modes are less sensitive to the substrate dielectric function. For example, between air and silicon (at 1510 cm^{-1}) the wavelength changes by factors of 7.4 and 3.1 for the first- ($l = 0$) and second- ($l = 1$) order modes, respectively. This has significant implications for the behavior of HPhP propagation across substrate boundaries; for example, lower-order modes are more strongly refracted at such boundaries, an effect that could be exploited to separate the different higher-order modes as demonstrated below (Fig. 5). While the experimental methods deployed here precluded observation of higher-order modes due to the thinness of the hBN flakes - chosen to ensure the validity of the analytical model – we have added data from Ref. [10] as well as numerical solutions from the model in Ref. [6] to validate these conclusions (Fig. 4a). The experimental data agree well with predicted mode positions, with slight deviations for the $l = 2$ mode attributed to the challenges associated with launching high wavevector modes and the concomitant error in extracting the polariton wavelength given the correspondingly short propagation lengths.

To compare propagation properties of HPhP modes on different substrates we use a figure of merit (FOM) [10] related to the real and imaginary parts of the wavevector:

$$FOM = \frac{Re(k)}{Im(k)} \qquad \text{(Equation 2)}$$

This FOM offers a better descriptor of the behavior than the propagation length as it to accounts for the stronger confinement of the polaritonic fields typical of correspondingly shorter propagation lengths. Furthermore, while long propagation lengths can be realized for weakly confined polaritons, it is only within the limit of strong modal confinement that the intrinsic benefits of sub-diffractional wavelengths associated with polaritons can be exploited. Specifically, $Im(k)$ determines the propagation length $L_p = \frac{1}{2 \cdot Im(k)}$,[33] and $Re(k)$ defines the polariton wavelength $\lambda = \frac{2\pi}{Re(k)}$, and thus the FOM can be expressed as:

$$FOM = \frac{2\pi}{\lambda} \times 2L_p = 4\pi Q \qquad \text{(Equation 3)}$$

where λ is polariton wavelength, L_p is propagation length, and Q is the quality factor that defines the number of cycles that the polariton wave oscillates before the amplitude decreases to $1/e$ of its initial value. The relationship between this FOM and the substrate dielectric function is plotted in Fig. 4b, using the loss tangents from Fig. 4a.

From the general trends, the FOM clearly decreases rapidly with increasing substrate dielectric constant, reaching a minimum at approximately $|\varepsilon_s| = 3$, and then increasing again. This effect is especially pronounced for the principal ($l = 0$) mode on dielectric substrates, as high-index substrates yield stronger confinement and longer propagation lengths. This contrasts with, and goes well beyond, prior results,[33] which showed only that FOM increased for suspended hBN compared to hBN on silicon. For metallic substrates, the effect is similar; however, the FOM is approximately symmetric about the minimum with respect to the dielectric response. Interestingly, this implies that when the substrate permittivity is close to the epsilon-near-zero (ENZ) condition rather than a metallic or dielectric value, the FOM for lossy substrates might actually be higher than that for a low-loss dielectric substrate.

For both dielectric and metallic substrates, the FOM of the higher-order modes is always improved with reference to the principal ($l = 0$ for dielectric, $l = 1$ for metallic) mode, though the trends with substrate permittivity are generally similar. Overall, the results of Fig. 4 indicate that the choice of substrate is a complicated issue for hyperbolic polaritons. While low-index substrates produce long-wavelength propagating modes, very high index substrates actually produce the highest FOMs for such polaritons. In the Supporting Information we discuss the effect of the substrate loss tangent on the principal and higher-order modes, (see Fig. S5).

These results have significant implications for device designs based on HPhPs, in particular for both polariton refraction in planar metasurface-based optics[1-2, 18] and hBN-based sensors.[5, 31] Previously we showed that HPhPs refract when propagating across a boundary between metallic and dielectric regions of a phase-change material.[1] The fact that each successively higher-order mode exhibits a smaller change in wavelength due to the changing dielectric environment promises the potential for spatial sorting of hyperbolic polaritons featuring different modal orders. To illustrate the potential for using the local dielectric function to control HPhP propagation, we consider a hypothetical device capable of spatially separating different mode orders by refraction at dielectric boundaries (Fig. 5a and b). The simulations are configured with a 120 nm thick hBN flake that is partly suspended and partly supported on a Si substrate. The HPhPs are launched from an array of dipole emitters above the suspended hBN, with the HPhPs propagating within the hBN towards the air-Si interface at a 45° angle of incidence. To suppress HPhP reflections from the simulated boundaries, we surrounded the region of interest by a border of highly lossy (20x increased damping) hBN. The z-component of the electric field at a position 10 nm above the hBN surface is provided to demonstrate the varied refraction of $l = 0$ and higher-order modes leading to spatial separation (Fig. 5b). The HPhPs launched from the emitter array are refracted at the air-Si interface due to the wavevector mismatch across the boundary, but since the $l = 0$ mode is significantly more sensitive to the surrounding dielectric environment, it is more strongly refracted (transmitted angle 13°, orange arrow) and is thus spatially separated from the $l = 1$ mode (transmitted angle 34°, green arrow). Therefore, using such approaches, high wavevector, higher-order HPhPs featuring increased spatial information could be spatially separated from the longer wavelength principal modes in a planar film.
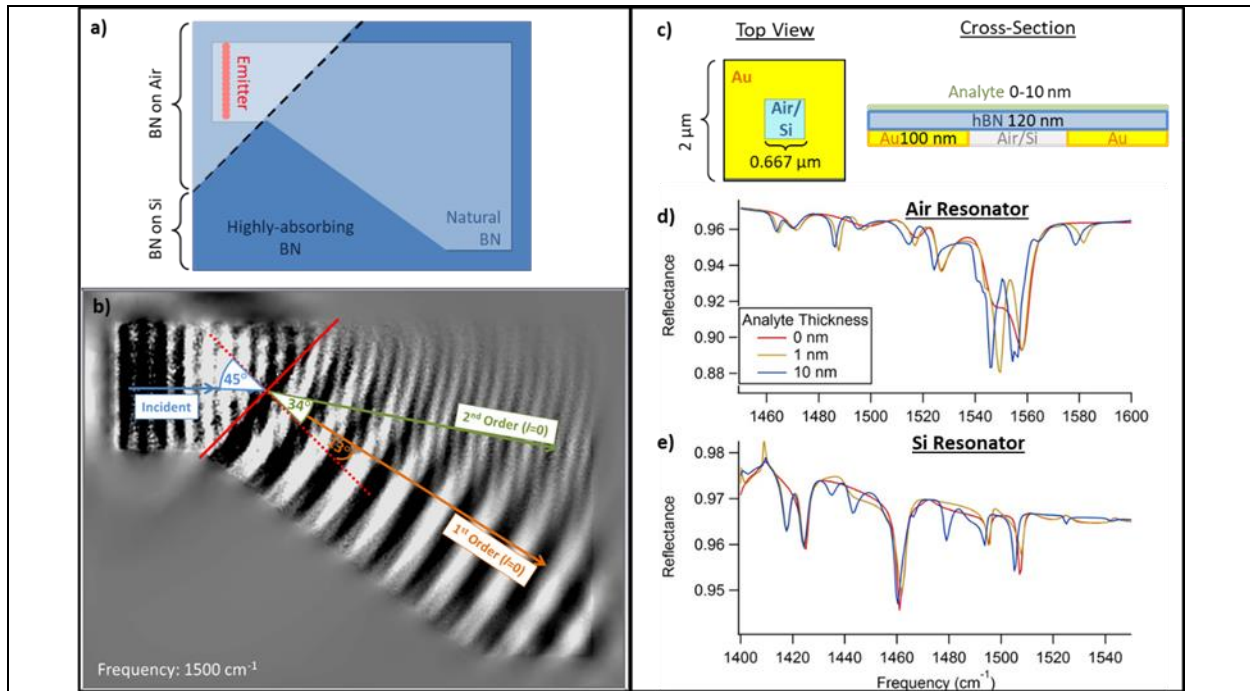
Figure 5.5: Simulations of spatial separation of the HPhP modes and applications of HPhPs through dielectric enviornment control. a) A schematic diagram of the proposed HPhP spatial separator device, with the corresponding b) simulated electric field (E_z) for HPhP modes separated due to refraction resulting from HPhP transmission over a Si-air interface aligned at 45º with respect to the propagation direction. To eliminate complexities in the image due to back reflections, a notional highly-absorbing hBN border with a 20-fold increase in the damping constant was added. The corresponding refraction of the l=0 (orange) and l=1 order (green) HPhPs are provided. c) Schematic diagram of a proposed hBN HPhP-based SEIRA or index-sensing resonant device induced due to large index contrast in spatial regions underneath the hBN flake as designated. The corresponding reflection spectra for this resonant structure fabricated from a hBN flake over an empty d) or Si-filled e) resonant chamber (e.g. hole). The calculated resonance spectra are highly sensitive to the presence and thickness of an analyte layer on top of the hBN surface; suspended hBN films have the highest degree of sensitivity.The spectra provided for both cases in d) and e) as a function of analyte layer thickness are labeled.

To discuss the implications for index-based sensing,[47] where the change in frequency of polaritonic resonance indicates a change in the local dielectric environment, we consider the analytical model for both surface phonon polaritons (SPhPs) and HPhPs. At mid-IR frequencies, strongly confined HPhPs enabled the environmental sensitivity necessary to realize hBN enabled surface-enhanced infrared absorption (SEIRA)[31, 48] spectroscopy and suggested a basis for planar metaoptics structures [1] that have since been reduced to practice.[2] These new results also have implications for deploying hBN in thin-film sensing applications. Thin film sensing operates in two main regimes: index-based sensing (which relies on the change in local dielectric environment to change the mode frequency), or surface enhanced infrared absorption (SEIRA, which exploits local field enhancements). Our results are most obviously relevant in the field of the former, as they consider the properties of a substrate without significant spectral dispersion. As shown in Fig. 3, the presence of a nearby analyte significantly affects the properties of suspended hBN – resulting in a measurable shift in resonance frequencies. Thus, it is critical that

hBN be suspended or on a low-permittivity substrate to function as an effective index sensor (see Supporting Information Fig. S7).

To demonstrate how such a device could be realized, a device consisting of 120 nm thick hBN atop a 100 nm thick gold structure surrounding a resonant cavity filled with air or Si is simulated in Fig. 5b. Since HPhPs in hBN are sensitive to the surrounding dielectric environment, the resonant mode of this structure will be sensitive to the presence of an analyte on top of the hBN layer. Simulated reflectance spectra for an array of such resonators under far-field radiation incident at 45°, p-polarized light are provided in Fig. 5d and e, with the structure covered by a hypothetical analyte layer of $Re(\varepsilon)$=2.25 of variable thickness. For both air- and Si-filled resonators, sharp dips appear corresponding to resonant absorption in the cavity defined by the gold. These resonant frequencies are sensitive to as little as 1 nm of analyte placed on the hBN, demonstrating the high degree of sensitivity akin to efforts with SPhPs in SiC.[49] However, using suspended hBN significantly increases the magnitude of the observed shifts to well over 10 cm^{-1}.

Whilst these simulations suggest that hBN can act as a surface sensor, it is instructive to benchmark against other index-based sensing schemes. In the Supporting Information (Fig.s S8 and S9) we compare a hBN film against a notional isotropic SPhP material operating with the same TO, LO and damping frequencies. Surprisingly, we find that for thick films of the analyte material ($>\lambda_{HPhP}$), the SPhP mode is much more effective as an index sensor. However, taking into account the strong confinement of HPhPs in hBN, we find that hyperbolic modes are indeed much more effective for sensing thin films, especially close to the LO phonon (where HPhP modes are extremely confined). This is reflected in the results of Fig. 5d, where the peak shifts are largest close to the LO phonon energy.

5.5 Conclusion

We have investigated the interaction of HPhP with substrates encompassing a wide range of complex refractive indices. While substrates with small real parts of the dielectric function support long-wavelength propagating modes, large permittivity substrates result in polaritons exhibiting the highest propagating FOMs. Furthermore, our results demonstrate that longer wavelength principal hyperbolic modes can be used as extremely sensitive subwavelength sensors. While all modes show an equal change in wavevector (Δk), the corresponding fractional change in wavevector $k(\varepsilon_{s1})/k(\varepsilon_{s2})$ for higher-order modes implies that they are less influenced by the local dielectric environment than the principal. Most significantly, the substrate permittivity can induce spatial mode separation of these higher-order modes. This effect could be used as a tool to optimize planar refractive optics and reconfigurable metasurfaces. Our results therefore provide a deeper understanding of HPhP interactions with the surrounding environment, a necessary step for implementing practical applications in on-chip molecular sensing and nanophotonics.

5.6 Methods

5.6.a Sample Preparation

For the purposes of these experiments, we employed isotopically pure hBN flakes (>99% h^{10}BN) to minimize the intrinsic polariton losses.[10] These were grown as described in reference,[50] then subsequently exfoliated and transferred onto the appropriate substrate. Single crystals of VO$_2$ were grown on quartz from vanadium pentoxide powder (V$_2$O$_5$) by physical vapor transport.[51] Due to the presence of multiple VO$_2$ crystals on the substrate we were able to suspend the hBN between adjacent VO$_2$ crystals. This resulted in flakes which were supported by VO$_2$ and quartz or alternatively suspended between VO$_2$ crystals (as shown in Figure 1). Silver films were deposited on Si substrates, while SiO$_2$ and Si substrates were obtained commercially.

5.6.b s-SNOM

In s-SNOM a platinum-coated probe tip is used both to map the topography and to probe the optical near fields. Monochromatic infrared near field imaging at selected laser excitation frequencies is performed via a combination of phase interferometric detection and demodulation of the detector signal at the second harmonic (2Ω) of the tip oscillation frequency.[52] The nano-FTIR data were acquired using a combination of s-SNOM and a broad-band infrared light source (neaspec.com).

5.7 Acknowledgements

5.8 References

1.	Folland, T. G.; Fali, A.; White, S. T.; Matson, J. R.; Liu, S.; Aghamiri, N. A.; Edgar, J. H.; Haglund, R. F.; Abate, Y.; Caldwell, J. D., Reconfigurable infrared hyperbolic metasurfaces using phase change materials. *Nat. Commun.* **2018,** *9*, 4371.
2.	Chaudhary, K.; Tamagnone, M.; Yin, X.; Spägele, C. M.; Oscurato, S. L.; Li, J.; Persch, C.; Li, R.; Rubin, N. A.; Jauregui, L. A.; Watanabe, K.; Taniguchi, T.; Kim, P.; Wuttig, M.; Edgar, J. H.; Ambrosio, A.; Capasso, F., Polariton nanophotonics using phase-change materials. *Nat. Commun.* **2019,** *10* (1), 4487.
3.	Jacob, Z., Hyperbolic phonon–polaritons. *Nat. Mater.* **2014,** *13*, 1081-1083.
4.	Poddubny, A.; Iorsh, I.; Belov, P.; Kivshar, Y., Hyperbolic metamaterials. *Nat. Photonics* **2013,** *7*, 948-957.
5.	Caldwell, J. D.; Kretinin, A. V.; Chen, Y.; Giannini, V.; Fogler, M. M.; Francescato, Y.; Ellis, C. T.; Tischler, J. G.; Woods, C. R.; Giles, A. J.; Hong, M.; Watanabe, K.; Taniguchi, T.; Maier, S. A.; Novoselov, K. S., Sub-diffractional volume-confined polaritons in the natural hyperbolic material hexagonal boron nitride. *Nat. Commun.* **2014,** *5*, 5221.
6.	Dai, S.; Fei, Z.; Ma, Q.; Rodin, A. S.; Wagner, M.; McLeod, A. S.; Liu, M. K.; Gannett, W.; Regan, W.; Watanabe, K.; Taniguchi, T.; Thiemens, M.; Dominguez, G.; Neto, A. H. C.; Zettl, A.; Keilmann, F.; Jarillo-Herrero, P.; Fogler, M. M.; Basov, D. N., Tunable Phonon Polaritons in Atomically Thin van der Waals Crystals of Boron Nitride. *Science* **2014,** *343* (6175), 1125-1129.
7.	Dai, S.; Ma, Q.; Andersen, T.; McLeod, A. S.; Fei, Z.; Liu, M. K.; Wagner, M.; Watanabe, K.; Taniguchi, T.; Thiemens, M.; Keilmann, F.; Jarillo-Herrero, P.; Fogler, M. M.; Basov, D. N., Subdiffractional focusing and guiding of polaritonic rays in a natural hyperbolic material. *Nat. Commun.* **2015,** *6*, 6963.
8.	Dai, S.; Ma, Q.; Liu, M. K.; Andersen, T.; Fei, Z.; Goldflam, M. D.; Wagner, M.; Watanabe, K.; Taniguchi, T.; Thiemens, M.; Keilmann, F.; Janssen, G. C. A. M.; Zhu, S. E.; Jarillo-Herrero, P.; Fogler, M. M.; Basov, D. N., Graphene on hexagonal boron nitride as a tunable hyperbolic metamaterial. *Nat. Nanotechnol.* **2015,** *10*, 682.
9.	Giles, A. J.; Dai, S.; Glembocki, O. J.; Kretinin, A. V.; Sun, Z.; Ellis, C. T.; Tischler, J. G.; Taniguchi, T.; Watanabe, K.; Fogler, M. M.; Novoselov, K. S.; Basov, D. N.; Caldwell, J. D., Imaging of Anomalous Internal Reflections of Hyperbolic Phonon-Polaritons in Hexagonal Boron Nitride. *Nano Lett.* **2016,** *16* (6), 3858-3865.
10.	Giles, A. J.; Dai, S.; Vurgaftman, I.; Hoffman, T.; Liu, S.; Lindsay, L.; Ellis, C. T.; Assefa, N.; Chatzakis, I.; Reinecke, T. L.; Tischler, J. G.; Fogler, M. M.; Edgar, J. H.; Basov, D. N.; Caldwell, J. D., Ultralow-loss polaritons in isotopically pure boron nitride. *Nat. Mater.* **2018,** *17*, 134-139.
11.	Jacob, Z.; Kim, J.-Y.; Naik, G. V.; Boltasseva, A.; Narimanov, E. E.; Shalaev, V. M., Engineering photonic density of states using metamaterials. *Applied Physics B* **2010,** *100* (1), 215-218.
12.	Li, P.; Lewin, M.; Kretinin, A. V.; Caldwell, J. D.; Novoselov, K. S.; Taniguchi, T.; Watanabe, K.; Gaussmann, F.; Taubner, T., Hyperbolic phonon-polaritons in boron nitride for near-field optical imaging and focusing. *Nat. Commun.* **2015,** *6*, 7507.
13.	Ishii, S.; Kildishev, A. V.; Narimanov, E. E.; Shalaev, V. M.; Drachev, V. P., Sub-wavelength interference pattern from volume plasmon polaritons in a hyperbolic medium. *Laser and Photonics Reviews* **2013,** *7*, 265-271.
14.	Caldwell, J. D.; Aharonovich, I.; Cassabois, G.; Edgar, J. H.; Gil, B.; Basov, D. N., Photonics with hexagonal boron nitride. *Nat. Rev. Mater.* **2019,** *4* (8), 552-567.
15.	Liu, Z.; Lee, H.; Xiong, Y.; Sun, C.; Zhang, X., Far-Field Optical Hyperlens Magnifying Sub-Diffraction-Limited Objects. *Science* **2007,** *315* (5819), 1686-1686.
16.	Xiong, Y.; Liu, Z.; Zhang, X., A simple design of flat hyperlens for lithography and imaging with half-pitch resolution down to 20 nm. *Appl. Phys. Lett.* **2009,** *94* (20), 203108.

17.   Li, P.; Dolado, I.; Alfaro-Mozaz, F. J.; Casanova, F.; Hueso, L. E.; Liu, S.; Edgar, J. H.; Nikitin, A. Y.; Vélez, S.; Hillenbrand, R., Infrared hyperbolic metasurface based on nanostructured van der Waals materials. *Science* **2018,** *359* (6378), 892-896.
18.   Folland, T. G.; Caldwell, J. D., Precise Control of Infrared Polarization Using Crystal Vibrations. *Nature* **2018,** *562* (7728), 499-501.
19.   Rivera, N.; Rosolen, G.; Joannopoulos, J. D.; Kaminer, I.; Soljačić, M., Making two-photon processes dominate one-photon processes using mid-IR phonon polaritons. *Proc. Natl. Acad. Sci. U. S. A* **2017,** *114* (52), 13607-13612.
20.   Dai, S.; Tymchenko, M.; Xu, Z.-Q.; Tran, T. T.; Yang, Y.; Ma, Q.; Watanabe, K.; Taniguchi, K.; Jarillo-Herrero, P.; Aharonovich, I.; Basov, D. N.; Tao, T. H.; Alu, A., Internal Nanostructure Diagnosis with Hyperbolic Phonon Polaritons in Hexagonal Boron Nitride. *Nano Lett.* **2018,** *18* (8), 5205-5210.
21.   Hauer, B.; Marvinney, C. E.; Lewin, M.; Mahadik, N. A.; Hite, J. K.; Bassim, N.; Giles, A. J.; Stahlbush, R. E.; Caldwell, J. D.; Taubner, T., Exploiting Phonon-Resonant Near-Field Interaction for the Nanoscale Investigation of Extended Defects. *Adv. Funct. Mater.* **2020,** *30* (10), 14.
22.   Caldwell, J. D.; Lindsey, L.; Giannini, V.; Vurgaftman, I.; Reinecke, T.; Maier, S. A.; Glembocki, O. J., Low-Loss, Infrared and Terahertz Nanophotonics with Surface Phonon Polaritons. *nanoph* **2015,** *4*, 44-68.
23.   Low, T.; Chaves, A.; Caldwell, J. D.; Kumar, A.; Fang, N. X.; Avouris, P.; Heinz, T. F.; Guinea, F.; Martin-Moreno, L.; Koppens, F., Polaritons in layered two-dimensional materials. *Nat. Mater.* **2017,** *16*, 182-194.
24.   Sun, J.; Litchinitser, N. M.; Zhou, J., Indefinite by Nature: From Ultraviolet to Terahertz. *ACS Photonics* **2014,** *1* (4), 293-303.
25.   Korzeb, K.; Gajc, M.; Pawlak, D. A., Compendium of natural hyperbolic materials. *Optics Express* **2015,** *23* (20), 25406-25424.
26.   Ma, W.; Alonso-Gonzalez, P.; Li, S.; Nikitin, A. Y.; Yuan, J.; Martin-Sanchez, J.; Taboada-Gutierrez, J.; Amenabar, I.; Li, P.; Velez, S.; Tollan, C.; Dai, Z.; Zhang, Y.; Sriram, S.; Kalantar-Zadeh, K.; Lee, S.-T.; Hillenbrand, R.; Bao, Q., In-plane anisotropic and ultra-low-loss polaritons in a natural van der Waals crystal. *Nature* **2018,** *562*, 557-562.
27.   Zheng, Z.; Xu, N.; Oscurato, S. L.; Tamagnone, M.; Sun, F.; Jiang, Y.; Ke, Y.; Chen, J.; Huang, W.; Wilson, W. L.; Ambrosio, A.; Deng, S.; Chen, H., A mid-infrared biaxial hyperbolic van der Waals crystal. *Sci. Adv.* **2019,** *5* (5), eaav8690.
28.   Zheng, Z.; Chen, J.; Wang, Y.; Wang, X.; Chen, X.; Liu, P.; Xu, J.; Xie, W.; Chen, H.; Deng, S.; Xu, N., Highly confined and tunable hyperbolic phonon polaritons in van der Waals semiconducting transition metal oxides. *Advanced Materials* **2018,** *30*, 1705318.
29.   Li, P.; Yang, X.; Maß, T. W. W.; Hanss, J.; Lewin, M.; Michel, A.-K. U.; Wuttig, M.; Taubner, T., Reversible optical switching of highly confined phonon–polaritons with an ultrathin phase-change material. *Nature Materials* **2016,** *15*, 870-875.
30.   Folland, T. G.; Maβ, T. W. W.; Matson, J. R.; Nolen, J. R.; Liu, S.; Watanabe, K.; Taniguchi, K.; Edgar, J. H.; Taubner, T.; Caldwell, J. D., Probing Hyperbolic Polaritons Using Infrared Attenuated Total Reflectance Micro-Spectroscopy. *MRS Communications* **2018,** *8* (4), 1418-1425.
31.   Autore, M.; Li, P.; Dolado, I.; Alfaro-Mozaz, F. J.; Esteban, R.; Atxabal, A.; Casanova, F.; Hueso, L. E.; Alonso-Gonzalez, P.; Aizpurua, J.; Nikitin, A. Y.; Velez, S.; Hillenbrand, R., Boron nitride nanoresonators for phonon-enhanced molecular vibrational spectroscopy at the strong coupling limit. *Light: Science & Applications* **2018,** *7* (2), 15.
32.   Ambrosio, A.; Tamagnone, M.; Chaudhary, K.; Jauregui, L. A.; Kim, P.; Wilson, W. L.; Capasso, F., Selective excitation and imaging of ultraslow phonon polaritons in thin hexagonal boron nitride crystals. *Light: Science & Applications* **2018,** *7*, 27.
33.   Dai, S.; Quan, J.; Hu, G.; Qiu, C.-W.; Tao, T. H.; Li, X.; Alu, A., Hyperbolic Phonon Polaritons in Suspended Hexagonal Boron Nitride. *Nano Lett.* **2019,** *19*, 1009.
34.   Dai, S.; Zhang, J.; Ma, Q.; Kittiwatanakul, S.; McLeod, A. S.; Chen, X.; Gilbert Corder, S.; Watanabe, K.; Taniguchi, K.; Lu, J. C.; Dai, Q.; Jarillo-Herrero, P.; Liu, M.; Basov, D. N., Phase-Change

Hyperbolic Heterostructures for Nanopolaritonics: A Case Study of hBN/VO$_2$. *Advanced Materials* **2019,** *31* (18), 1900251.

35.   Kim, K. S.; Trajanoski, D.; Ho, K.; Gilburd, L.; Maiti, A.; van der Velden, L.; de Beer, S.; Walker, G. C., The Effect of Adjacent Materials on the Propagation of Phonon Polaritons in Hexagonal Boron Nitride. *J. Phys. Chem. Lett.* **2017,** *8* (13), 2902-2908.

36.   Duan, J.; Chen, R.; Li, J.; Jin, K.; Sun, Z.; Chen, J., Launching phonon polaritons by natural boron nitride wrinkles with modifiable dispersion by dielectric environments. *Advanced Materials* **2017,** *29* (38), 1702494.

37.   Ciano, C.; Giliberti, V.; Ortolani, M.; Baldassarre, L., Observation of phonon-polaritons in thin flakes of hexagonal boron nitride on gold. *Appl. Phys. Lett.* **2018,** *112*, 153101.

38.   Folland, T. G.; Nordin, L.; Wasserman, D.; Caldwell, J. D., Probing Polaritons in the Mid- to Far-Infrared. *J. Appl. Phys.* **2019,** *125*, 191102.

39.   Yang, H. U.; D'Archangel, J.; Sundheimer, M. L.; Tucker, E.; Boreman, G. D.; Raschke, M. B., Optical dielectric function of silver. *Phys. Rev. B: Condens. Matter Mater. Phys.* **2015,** *91* (23), 235137.

40.   Wan, C.; Zhang, Z.; Woolf, D.; Hessel, C. M.; Rensberg, J.; Hensley, J. M.; Xiao, Y.; Shahsafi, A.; Salman, J.; Richter, S.; Sun, Y.; Qazilbash, M. M.; Schmidt-Grund, R.; Ronning, C.; Ramanathan, S.; Kats, M. A., On the Optical Properties of Thin-Film Vanadium Dioxide from the Visible to the Far Infrared. *Ann. Phys.-Berlin* **2019,** *531* (10), 1900188.

41.   Winsemius, P.; Kampen, F. F. v.; Lengkeek, H. P.; Went, C. G. v., Temperature dependence of the optical properties of Au, Ag and Cu. . *J. Phys. F: Met. Phys.* **1976,** *6* (8), 1583-1606.

42.   Johnson, P. B.; Christy, R. W., Optical Constants of the Noble Metals. *Phys. Rev. B: Condens. Matter Mater. Phys.* **1972,** *6* (12), 4370-4379.

43.   Abelès, F., *Optical Properties and Electronic Structure of Metals and Alloys: Proceedings of the International Colloquim*. Amsterdam, North-Holland Pub. Co.; New York, Wiley, Interscience Publishers Division **1966**.

44.   Kischkat, J.; Peters, S.; Gruska, B.; Semtsiv, M.; Chashnikova, M.; Klinkmuller, M.; Fedosenko, O.; Machulik, S.; Aleksandrova, A.; Monastryrskyi, G.; Flores, Y.; Masselink, W. T., Mid-infrared optical properties of thin films of aluminum oxide, titanium dioxide, silicon dioxide, aluminum nitride and silicon nitride. *Applied Optics* **2012,** *51* (28), 6789.

45.   Snyder, A. W.; Love, J. D., Goos-Hanchen Shift. *Applied Optics* **1976,** *15* (1), 236-238.

46.   Lee, S.; Hippalgaonkar, K.; Yang, F.; Hong, J.; Ko, C.; Suh, J.; Liu, K.; Wang, K.; Urban, J. J.; Zhang, X.; Dames, C.; Hartnoll, S. A.; Delaire, O.; Wu, J., Anomalously low electronic thermal conductivity in metallic vanadium dioxide. *Science* **2017,** *355* (6323), 371-374.

47.   Neuner, B.; Korobkin, D.; Fietz, C.; Carole, D.; Ferro, G.; Shvets, G., Midinfrared Index Sensing of pL-Scale Analytes Based on Surface Phonon Polaritons in Silicon Carbide. *J. Phys. Chem. C.* **2010,** *114* (16), 7489-7491.

48.   Osawa, M., Surface-enhanced infrared absorption. In *Near-Field Optics and Surface Plasmon Polaritons*, Springer Berlin **2001**; Vol. 81, pp 163-187.

49.   Berte, R.; Gubbin, C. R.; Wheeler, V. D.; Giles, A. J.; Giannini, V.; Maier, S. A.; De Liberato, S.; Caldwell, J. D., Sub-nanometer thin oxide film sensing with localized surface phonon polaritons. *ACS Photonics* **2017,** *5* (7), 2807-2815.

50.   Hoffman, T. B.; Clubine, B.; Zhang, Y.; Snow, K.; Edgar, J. H., Optimization of Ni-Cr Flux Growth for Hexagonal Boron Nitride Single Crystals *J. Cryst. Growth* **2014,** *393*, 114-118.

51.   McGahan, C.; Gamage, S.; Liang, J. R.; Cross, B.; Marvel, R. E.; Haglund, R. F.; Abate, Y., Geometric constraints on phase coexistence in vanadium dioxide single crystals *Nanotechnology* **2017,** *28*, 085701.

52.   Keilmann, F.; Hillenbrand, R., Near-field microscopy by elastic light scattering from a tip. *Philosophical Transactions of the Royal Society of London, Series A* **2004,** *362*, 787-805.

5.9 Supporting Information

5.9.a Additional Example of HPhP Wavelength Modulation across Multiple Substrates

Another exfoliated hBN flake draped over a VO$_2$ single crystal, here on top of a Si substrate, is presented in Figure S1. Again, we observe HPhPs of different wavelengths in hBN in three different environments: on Si substrate, suspended above the substrate, and on VO$_2$. As discussed in the main text, the dielectric properties of the surrounding environment modulate the HPhP propagation in hBN.
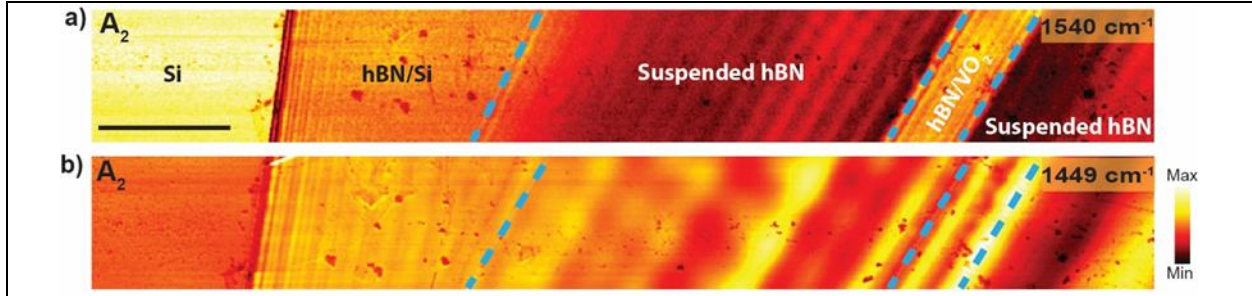
Figure 5.S1: Substrate-dependent modulation of the polariton wavelength in an hBN flake draped over a Si substrate and VO$_2$ crystal. (a) and (b) HPhP amplitude near field images taken at 1540 cm^{-1} and 1449 cm^{-1}, respectively. Scale bar is 5 µm.

5.9.b SNOM Images and Polariton Dispersion on Silver and Silicon Substrates
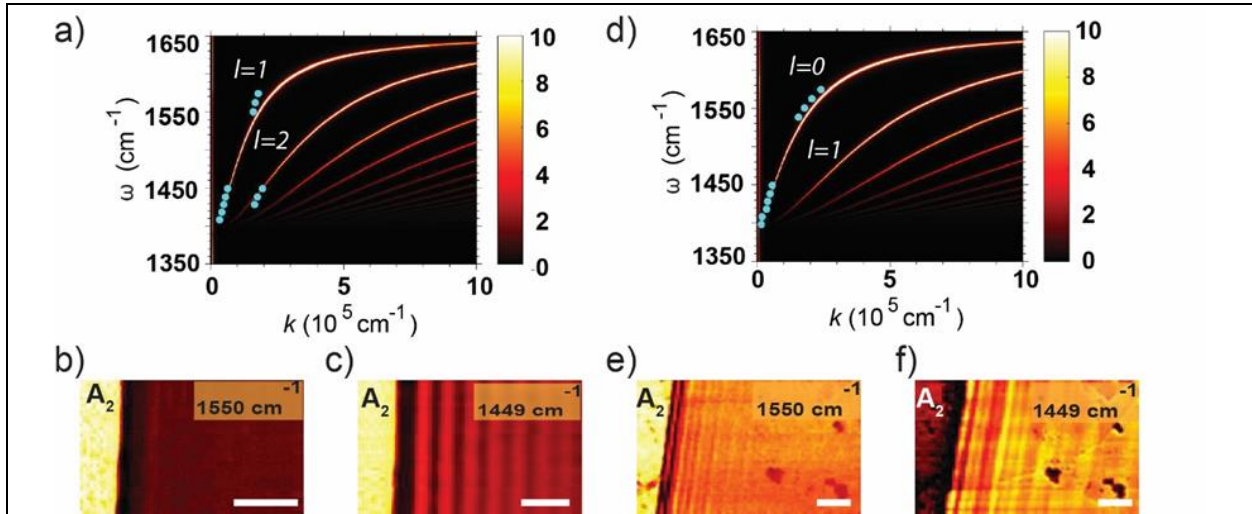
Figure 5.S2: Dispersion relation of HPhP of hBN: (a) a 85 nm thick hBN flake on silver (b) and (c) HPhP amplitude near field images taken at 1550 cm^{-1} and 1449 cm^{-1}. (d) a 65 nm thick hBN flake on silicon (e) and (f) HPhP amplitude near field images taken at 1550 cm^{-1} and 1449 cm^{-1}. Experimental data points (extracted from monochromatic) are shown superimposed on analytical calculation. Scale bar is 1 µm.

Figure 2 of the main text shows calculated and experimental dispersion relations for HPhPs in hBN suspended in air, on quartz, or on metallic or insulating VO_2. The corresponding data for the two other substrates discussed in the paper (silicon and silver) are shown in Figure S2. Solid curves in the dispersion plots [Figure S2(a) and (d)] are calculated from the analytical formula Eq. 1; solid blue circles are experimental data points derived from s-SNOM images such as those presented in Figure. S2 (b-c) and (e-f).

5.9.c Systematic Error in the Analytical Calculations

As mentioned in the main text discussion regarding Figure 3, the analytical solution is based on the approximation that k is much larger in hBN than in the surrounding environment (i.e. substrate and air), so that k can be neglected in those environments. Numerical simulations, on the other hand, do not rely on such assumptions. When the hBN is sufficiently thin (e.g. 20 nm), the field is highly confined, k is large, and the analytical and numerical solutions are identical (Figure S3, open red boxes and red line). For thicker hBN (e.g. 100 nm), where k is smaller at a given frequency, the analytical solution is less accurate: it yields a k lower than the experimental value[1] (grey star), whereas the numerical simulation agrees well (Figure S3, open grey boxes).
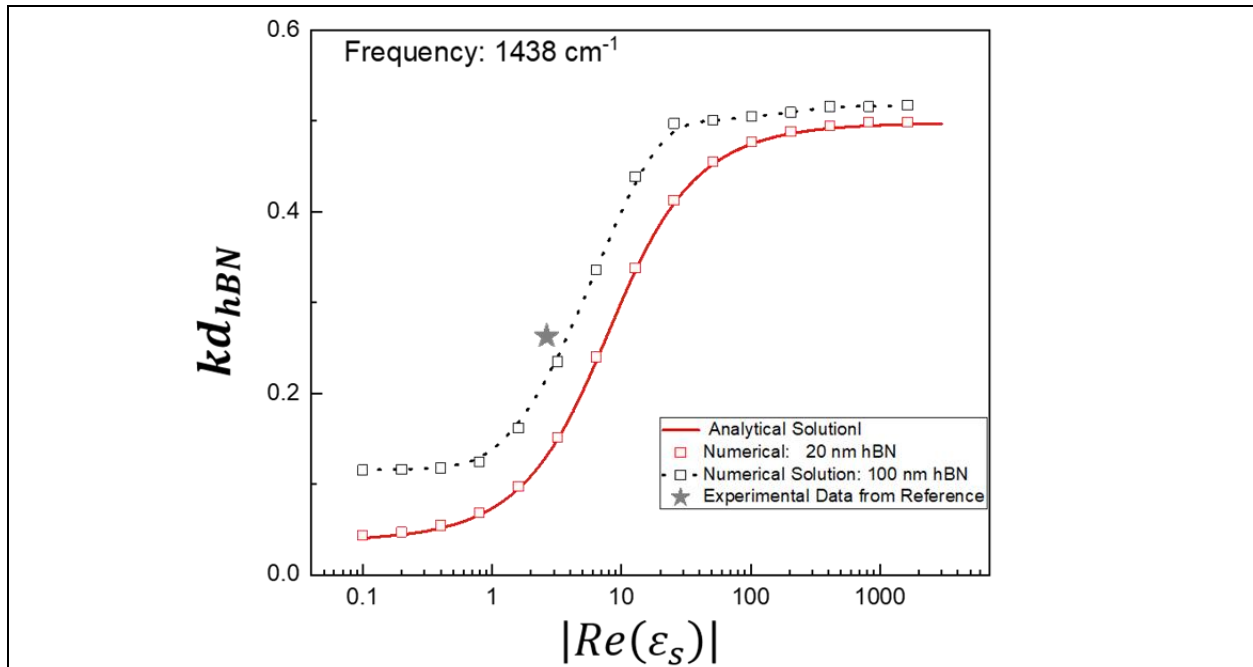
Figure 5.S3: The thickness-normalized wavevector kd versus substrate dielectric function, at 1438 cm^{-1}, for the l=0 mode on dielectric substrates [$Im(\varepsilon_s)/Re(\varepsilon_s) = 0.01$]. Red line is the analytical solution. Red(grey) open boxes are numerical solutions for 20 nm (100 nm) hBN. Grey star is an experimental datum from reference [1].

This error is more pronounced at low frequencies, where k is small, but disappears as frequency increases and k becomes arbitrarily large, even for thick hBN. Figure S4 illustrates this behavior by plotting the thickness-normalized dispersion curves (l=0) for suspended and Si-supported

hBN. For thin (20 nm) hBN, the analytical and numerical solutions agree at all frequencies; for thick (120 nm) hBN, they agree at high frequencies, but diverge as the frequency decreases, the analytical solution consistently yielding a too-small k value. Thus, the analytical approximation holds well as long as the hBN is thin, or the frequency is high.
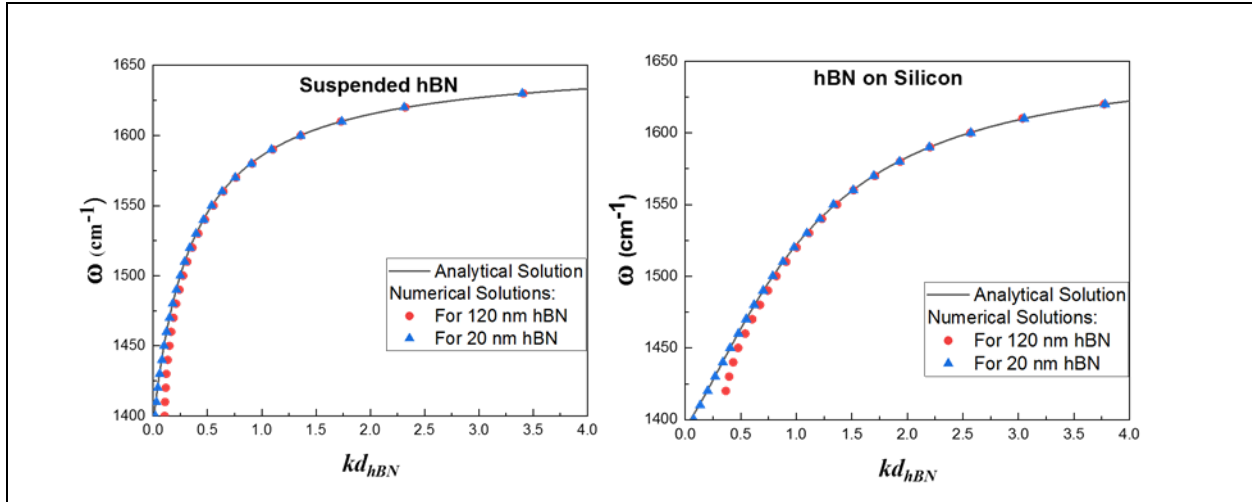
Figure 5.S4: Comparison of numerical and analytical solutions as a function of frequency, for different hBN thicknesses, suspended (left) and on Si (right). The thickness-normalized wavevector kd is plotted to suppress the influence of hBN thickness. Blue (red) triangles (circles) are numerical solutions at 20nm (120nm). The analytical solutions (solid lines) diverge from the numerical solutions in thick flakes at low frequencies.

5.9.d The Dependence of FOM on Substrate Loss
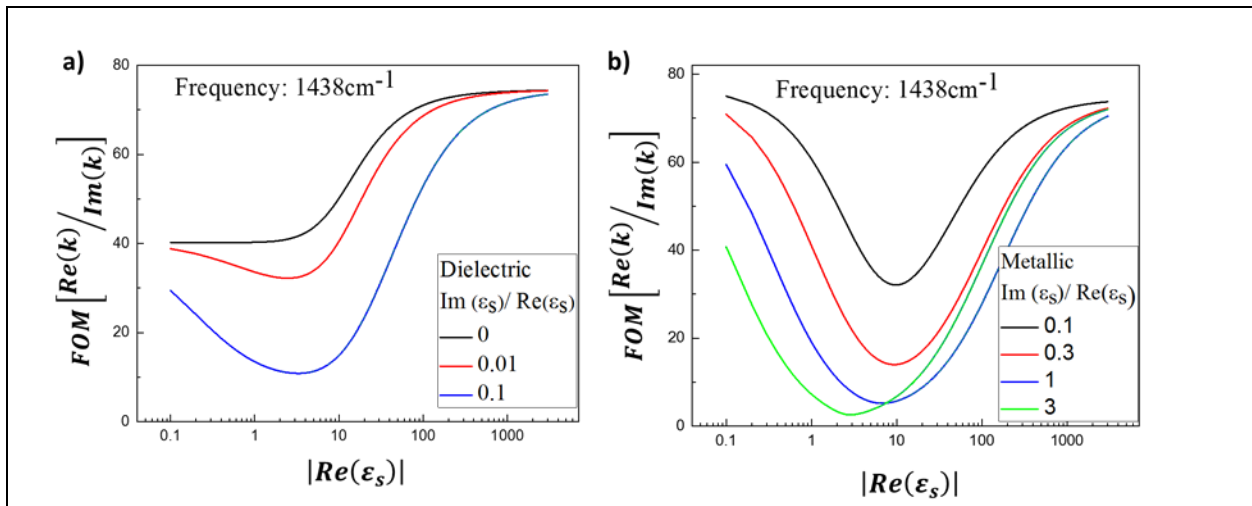
Figure 5.S5: FOM of HPhPs in hBN on (a) dielectric ($Re(\varepsilon_s) > 0$) and (b) metallic ($Re(\varepsilon_s) < 0$) substrates with different loss tangents at 1438 cm^{-1}, based on the analytical solution. Mode is l=0 for dielectric substrate and l=1 for metallic substrate.

Figure S5 illustrates the dependence of FOM on the substrate loss tangent, considering the same values of the loss tangent as in the main text, Figure 2. For loss-free dielectric substrates $[\text{Im}(\varepsilon_s) = 0, Re(\varepsilon_s) > 0]$, the FOM increases monotonically with $Re(\varepsilon_s)$. For lossy dielectrics, on the other hand, the FOM decreases to a minimum and then increases, asymptotically approaching a limiting value at high $Re(\varepsilon_s)$. For metallic substrates $[Re(\varepsilon_s) < 0]$, the trend is similar to that for lossy dielectrics, except that in metallic substrates the low-$Re(\varepsilon_s)$ limiting value of FOM is higher than in dielectrics. As a result, for epsilon-near-zero (ENZ) materials, the FOM of hBN is higher on metallic substrates (despite their greater loss), due to the larger k (see main text Figure 4(a)).

Generally, the FOM decreases as the loss tangent increases, though for high levels of loss, the FOM minimum shifts, so that for a given value of $Re(\varepsilon_s)$, it is possible for FOM to increase with loss tangent. In summary, the relationship between ε_s and the HPhP FOM can be complex and non-intuitive, and these computations will help identify the ideal substrate for a given purpose.

5.9.e Standard Deviation Analysis of Dielectric Function

In Figure 3 of the main text, x-axis error bars represent the standard deviation (STD) in ε_s of the substrates as reported in the literature, the error arising from inconsistencies across these reports. The values of ε_s for silver[2-7] and quartz[8-9] in this frequency range have been reported several times with little deviation, as shown in Table S1. The silicon substrate we used is diced from wafer-size silicon grown at foundry level, and should have negligible error.

Table 5.S1: Values and standard deviations for dielectric functions of different substrates at 1438 cm^{-1}, used in Figure 3 of the main text. Dielectric functions are averaged from values drawn from literature, with standard deviations representing differences across reports.

	$Re(\varepsilon_s)$	STD of $Re(\varepsilon_s)$	$\text{Im}(\varepsilon_s)$	STD of $\text{Im}(\varepsilon_s)$	Loss Tangent	STD of Loss Tangent
Silver[2-7]	-2580	58	590	104	0.228	0
Quartz[8-9]	1.23	0.06	0.006	0.004	0.005	0.000020
Rutile VO$_2$ [10]	13	15	91	17	7.1	2.5
Monoclinic VO$_2$ [10]	6.67	0.43	0.33	0.16	0.05	0.00060

However, for VO$_2$, especially for rutile VO$_2$, the dielectric functions from literature are inconsistent. Reference [10] reported refractive index and extinction coefficient of four different VO$_2$ films, grown by different methods and on Si and sapphire substrates. As VO$_2$ grown on sapphire is very different from that grown on Si, we use only the data sets for VO$_2$ grown on Si wafer. For monoclinic VO$_2$, ε_s is 6.67 with an STD of 0.43, or merely 6%. In rutile VO$_2$, on the other hand, the variation in ε_s is so large we cannot be sure whether it is metallic $[Re(\varepsilon_s) < 0]$ or dielectric $[Re(\varepsilon_s) > 0]$—at this frequency, rutile VO$_2$ is either an extremely lossy metal or

extremely lossy dielectric. However, this would have negligible influence on the HPhP dispersion, as mentioned in the main text.

5.9.f Substrate Dependence for Different Frequencies

As mentioned in the discussion of Figure 3 in the main text, the normalized wavevector kd and its change as a function of $Re(\varepsilon_s)$ is sensitive to the frequency of the polariton mode. To show the influence of polariton mode frequency we plot the kd over $[Re(\varepsilon_s)]$ for a range of frequencies (Figure S6). Generally speaking, at higher frequencies the HPhP is more sensitive to the local dielectric environment, resulting in a larger change in the polariton wavelength. This can be attributed to the change in the HPhP propagation angle within the hBN (main text Ref. 5,15), which results in a stronger interaction with the surrounding dielectric environment.
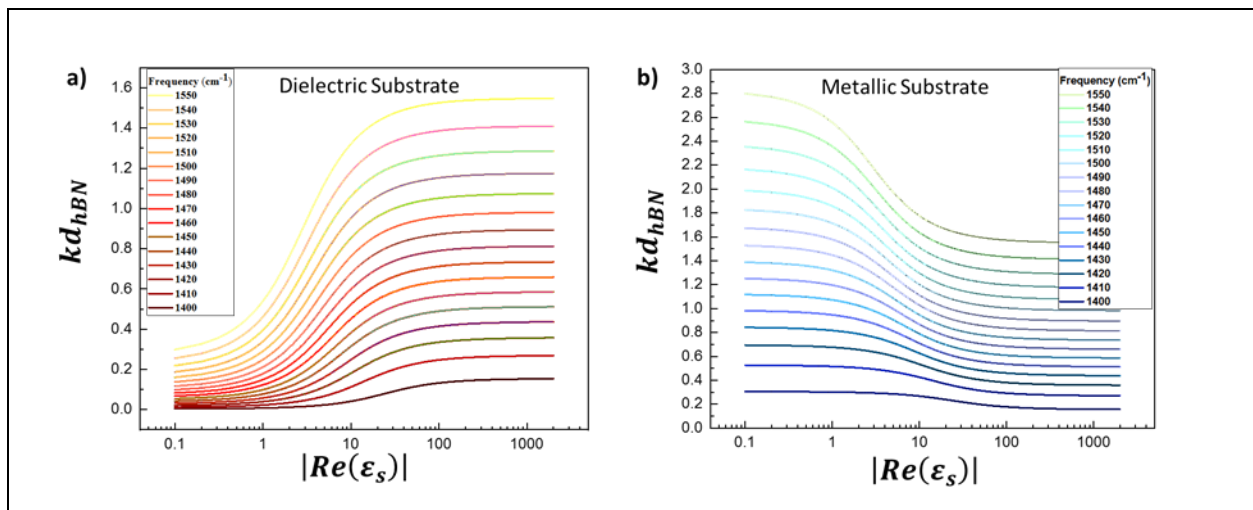
Figure 5.S6: The relationship between kd and $Re(\varepsilon_s)$ at different frequencies for (a) dielectric substrates (l=0), and (b) metallic substrates (l=1).

5.9.g Analytical Analysis of HPhP vs SPhP Sensing on a Semi-Infinite Half Space

For index-based surface sensing experiments, we wish to assess how much the frequency changes ($\partial\omega$) when exposed to a small change in the dielectric function of an analyte material on top of the hBN ($\partial\varepsilon_t$). We treat the analyte as semi-infinite, which allows us to use the dispersion relation of Eq (1). The result will be inherently dependent on the substrate dielectric function ε_s, as well as the incident frequency and the initial value of ε_t. To calculate $\partial\omega/\partial\varepsilon_t$, we write $\partial\omega/\partial\varepsilon_t = (\partial\omega/\partial k) \cdot (\partial k/\partial\varepsilon_t)$, where the derivative ($\partial\omega/\partial k$) represents the group velocity, and ($\partial k/\partial\varepsilon_t$) represents the change in wavevector upon a change in the dielectric environment. For simplicity, we here assume that the substrate and analyte have little dispersion, so their dependence on frequency may be neglected.

Results from this calculation are presented in Figure S7(a). If the hBN is suspended ($Re(\varepsilon_s) = 1$), the change in frequency could be as high as 32 cm^{-1} per unit change in ε_t. If ε_t starts as a higher value, this sensitivity is reduced. Crucially, $\partial\omega/\partial\varepsilon_t$ is always much higher for hBN suspended than on substrates like Si, by nearly an order of magnitude. Furthermore, if the analyte surrounds hBN rather than lying on one side only, $\partial\omega/\partial\varepsilon_t$ can be nearly doubled, as

shown in Figure S7 (b). These calculations illustrate that hBN on a low-$Re(\varepsilon_s)$ material is preferable for sensing purposes (as noted in the main text). We note that the parameter $\partial\omega/\partial\varepsilon_t$ is invariant on the thickness of the hBN film, as discussed below.

Figure 5.S7: The sensitivity of HPhPs to surrounding dielectric environment for index sensing. The rate of change of ω with respect to $Re(\varepsilon_t)$ is plotted over incident frequency for (a) suspended or Si-supported hBN covered with analyte or (b) hBN surrounded by analyte.

Figure 5.S8: Comparison of sensing benchmark for SPhPs and HPhPs, assuming that the analyte material is semi-infinite with $Re(\varepsilon_s) = 1$. (a) $\partial\omega/\partial\varepsilon_t$ for 20-nm thick hBN on air, and a hypothetical isotropic SPhP-supporting material; (b) $\partial\omega/\partial k$ and $\partial k/\partial\varepsilon_t$ for hBN on air, 20-nm (solid line) or 100-nm (broken line) flakes; (c) $\partial\omega/\partial k$ and $\partial k/\partial\varepsilon_t$ for the SPhP material.

To compare this index sensing to prior work, particularly to that employing surface phonon polaritons (SPhP), we simulate an artificial 'isotropic hBN', with the same phonon energies along all crystal axes, and perform a similar analysis to that presented above. With this assumption, we compare $\partial\omega/\partial\varepsilon_t$ for both SPhP and HPhP systems used to sense a material with $[Re(\varepsilon_s)]$ close to 1 (Figure S8). Surprisingly, the max $\partial\omega/\partial\varepsilon_t$ of SPhP modes is almost 10 times higher than that of HPhP modes, as shown in figure S8(a). To understand this difference, we plot the two constituent derivatives $\partial\omega/\partial k$ and $\partial k/\partial\varepsilon_t$, for both SPhP [Figure S8(b)] and

HPhP [Figure S8(c)] systems. Examining $\partial k / \partial \varepsilon_t$ (red curves), we find that k is much more sensitive to ε_t in HPhPs than in SPhPs. However, due to the highly dispersive nature of the HPhPs, and consequently low group velocity, of hyperbolic materials, $\partial \omega / \partial k$ (black curves) is much smaller. Overall, $\partial \omega / \partial \varepsilon_t$ is smaller in the HPhP material than in the SPhP material.

      Note, while we chose 20-nm thick hBN for comparison to the SPhP system, the result is valid for other hBN thickness. For example, in 100-nm hBN [dashed lines in Figure S3(b)] $\partial \omega / \partial k$ is 5 times larger (its dispersion is smaller, v_g is higher); but $\partial k / \partial \varepsilon_t$ would be 5 times smaller, since kd is fixed for a given surrounding environment and frequency. Thus, the changes in $\partial \omega / \partial k$ and $\partial k / \partial \varepsilon_t$ due to thickness variation would compensate for each other, leaving $\partial \omega / \partial \varepsilon_t$ unchanged.

      However, the above discussion assumes that the analyte is semi-infinite; for analyte films which are only a few atomic layers thick, the relatively low confinement of SPhPs away from the LO-phonon energy could lead to reduced sensitivity. To account for the improved confinement of hyperbolic polaritons, we compute $\partial \omega / \partial \varepsilon_t$ multiplied by the polariton wavevector (Figure S9). Due to the significantly enhanced confinement of HPhPs, they show improved sensitivity close to the LO-phonon energy. This is particularly pronounced for thin flakes of hBN, illustrating that a thin hyperbolic material may offer the best sensitivity for index-based sensing applications.
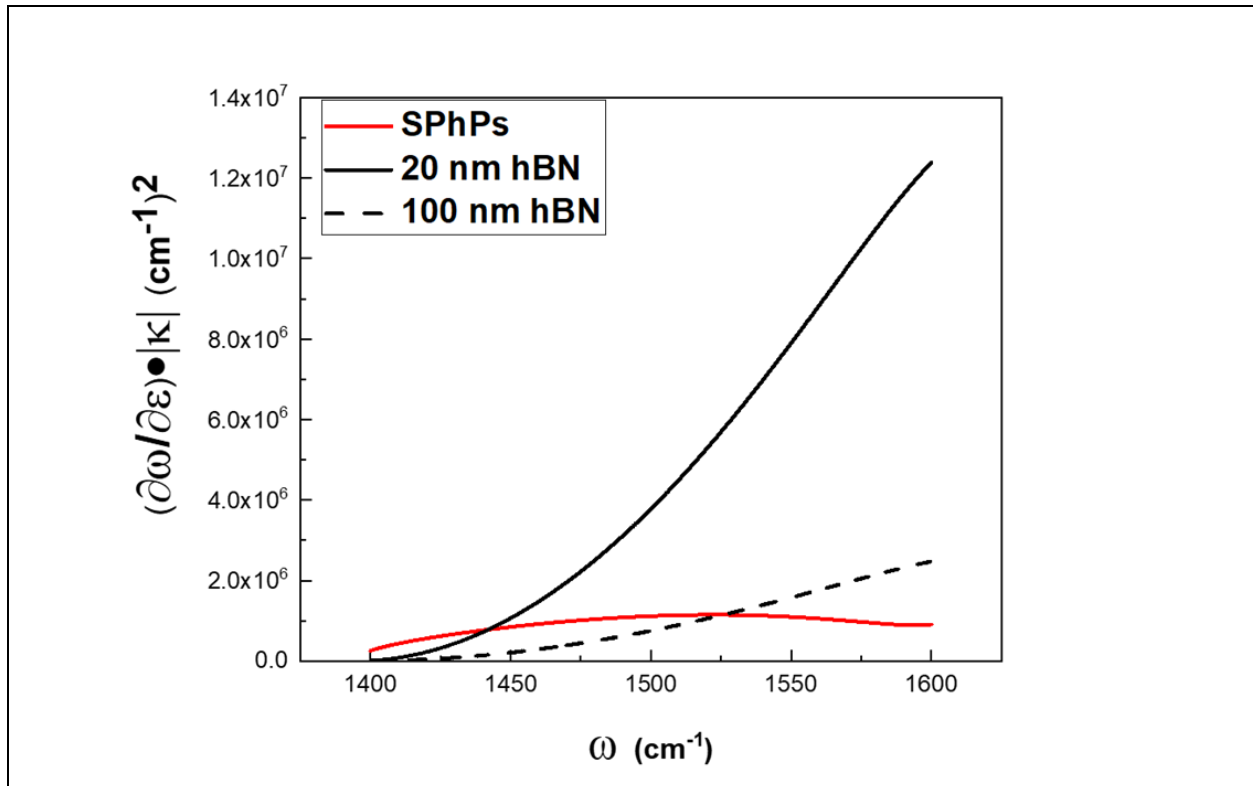
Figure 5.S9: Confinement-normalized sensitivity to dielectric environment. SPhP modes (red line) are more sensitive at low frequencies, near the TO phonon, but HPhP modes (black lines) become more sensitive as the frequency increases, approaching that of the LO-phonon.

5.9.h SI References

1. Giles, A. J.; Dai, S.; Vurgaftman, I.; Hoffman, T.; Liu, S.; Lindsay, L.; Ellis, C. T.; Assefa, N.; Chatzakis, I.; Reinecke, T. L.; Tischler, J. G.; Fogler, M. M.; Edgar, J. H.; Basov, D. N.; Caldwell, J. D., Ultralow-loss polaritons in isotopically pure boron nitride. *Nat. Mater.* **2018,** *17*, 134-139.
2. Yang, H. U.; D'Archangel, J.; Sundheimer, M. L.; Tucker, E.; Boreman, G. D.; Raschke, M. B., Optical dielectric function of silver. *Phys. Rev. B: Condens. Matter Mater. Phys.* **2015,** *91* (23), 235137.
3. Winsemius, P.; Kampen, F. F. v.; Lengkeek, H. P.; Went, C. G. v., Temperature dependence of the optical properties of Au, Ag and Cu. . *J. Phys. F: Met. Phys.* **1976,** *6* (8), 1583-1606.
4. Johnson, P. B.; Christy, R. W., Optical Constants of the Noble Metals. *Phys. Rev. B: Condens. Matter Mater. Phys.* **1972,** *6* (12), 4370-4379.
5. Dold, B.; Mecke, R., Optische eigenschaften von edelmetallen ubergangsmetallen und deren legierungen im infrarot. 1. *Optik* **1965,** *22* (6), 435.
6. Dold, B.; Mecke, R., Optische eigenschaften von edelmetallen ubergangsmetallen und deren legierungen im infrarot. 2. *Optik* **1965,** *22* (7), 453.
7. Abelès, F., *Optical Properties and Electronic Structure of Metals and Alloys: Proceedings of the International Colloquim.* Amsterdam, North-Holland Pub. Co.; New York, Wiley, Interscience Publishers Division **1966**.
8. Kischkat, J.; Peters, S.; Gruska, B.; Semtsiv, M.; Chashnikova, M.; Klinkmüller, M.; Fedosenko, O.; Machulik, S.; Aleksandrova, A.; Monastyrskyi, G.; Flores, Y.; Ted Masselink, W., Mid-infrared optical properties of thin films of aluminum oxide, titanium dioxide, silicon dioxide, aluminum nitride, and silicon nitride. *Applied Optics* **2012,** *51* (28), 6789-6798.
9. Hafeli, A. K.; Rephaeli, E.; Fan, S.; Cahill, D. G.; Tiwald, T. E., Temperature dependence of surface phonon polaritons from a quartz grating. *J. Appl. Phys.* **2011,** *110* (4), 043517.
10. Wan, C.; Zhang, Z.; Woolf, D.; Hessel, C. M.; Rensberg, J.; Hensley, J. M.; Xiao, Y.; Shahsafi, A.; Salman, J.; Richter, S.; Sun, Y.; Qazilbash, M. M.; Schmidt-Grund, R.; Ronning, C.; Ramanathan, S.; Kats, M. A., On the Optical Properties of Thin-Film Vanadium Dioxide from the Visible to the Far Infrared. *Annalen der Physik* **2019,** *0* (0), 1900188.

VANADIUM DIOXIDE METAMATERIAL FILMS FOR PASSIVE THERMAL CONTROL OF SPACECRAFT

6.1 Introduction

Controlling the temperature of designated spaces and of particular objects is a perennial challenge, generally addressed either by pumping heat into or out of the space/object, or by changing its ability to exchange heat with its surroundings. Thermochromic films,[1-2] which have optical properties that vary as a function of temperature, exemplify the latter strategy. Requiring no energy input or control signal beyond the ambient temperature, and having low mass due to their micron or sub-micron dimensions, thermochromic thin films are ideal for passive thermal control in small spacecraft, where weight- and energy-budgets are critical. In the near-vacuum environment of space, the primary mechanisms for energy exchange are absorption of sunlight and thermal emission of radiation; thus, the critical parameters for such a thermal control film are absorptance α_{sol}, weighted by the solar spectrum, emittance ε relative to that of a blackbody, and switching temperature T_c. Ideally, α_{sol} will be minimized regardless of temperature, ε will be high in the hot state and low in the cold state, and T_c will be at or near the ideal operating temperature of the spacecraft. The change in ε is often characterized by the difference $\Delta\varepsilon=\varepsilon_{hot}-\varepsilon_{cold}$; it is also helpful to define the "turndown ratio", $Q\varepsilon=\varepsilon_{hot}/\varepsilon_{cold}$ Figure 1 illustrates the solar spectrum, the blackbody spectra of interest, and the ideal device behavior.
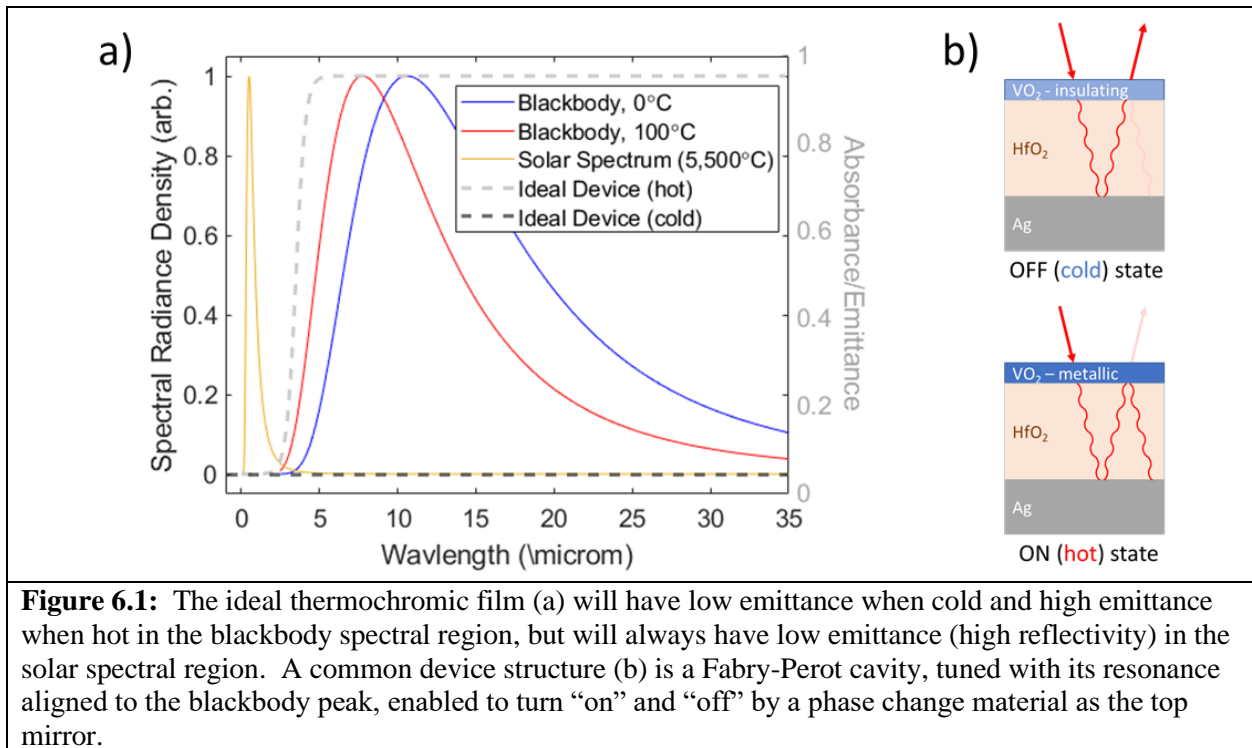
Figure 6.1: The ideal thermochromic film (a) will have low emittance when cold and high emittance when hot in the blackbody spectral region, but will always have low emittance (high reflectivity) in the solar spectral region. A common device structure (b) is a Fabry-Perot cavity, tuned with its resonance aligned to the blackbody peak, enabled to turn "on" and "off" by a phase change material as the top mirror.

Thermochromic films by definition derive their optical properties from a material with a thermally-driven phase transition. Vanadium dioxide (VO$_2$) is a popular choice, with an insulator-to-metal phase transition (IMT) occurring at $T_c \approx 68°C$ with a corresponding change in optical properties. Among IMT materials, VO$_2$ has the T_c closest to room temperature,[3] but for many applications it is desirable lower it to room -temperature or below. Tungsten doping can achieve this, but high doping levels can also cause loss of optical contrast.
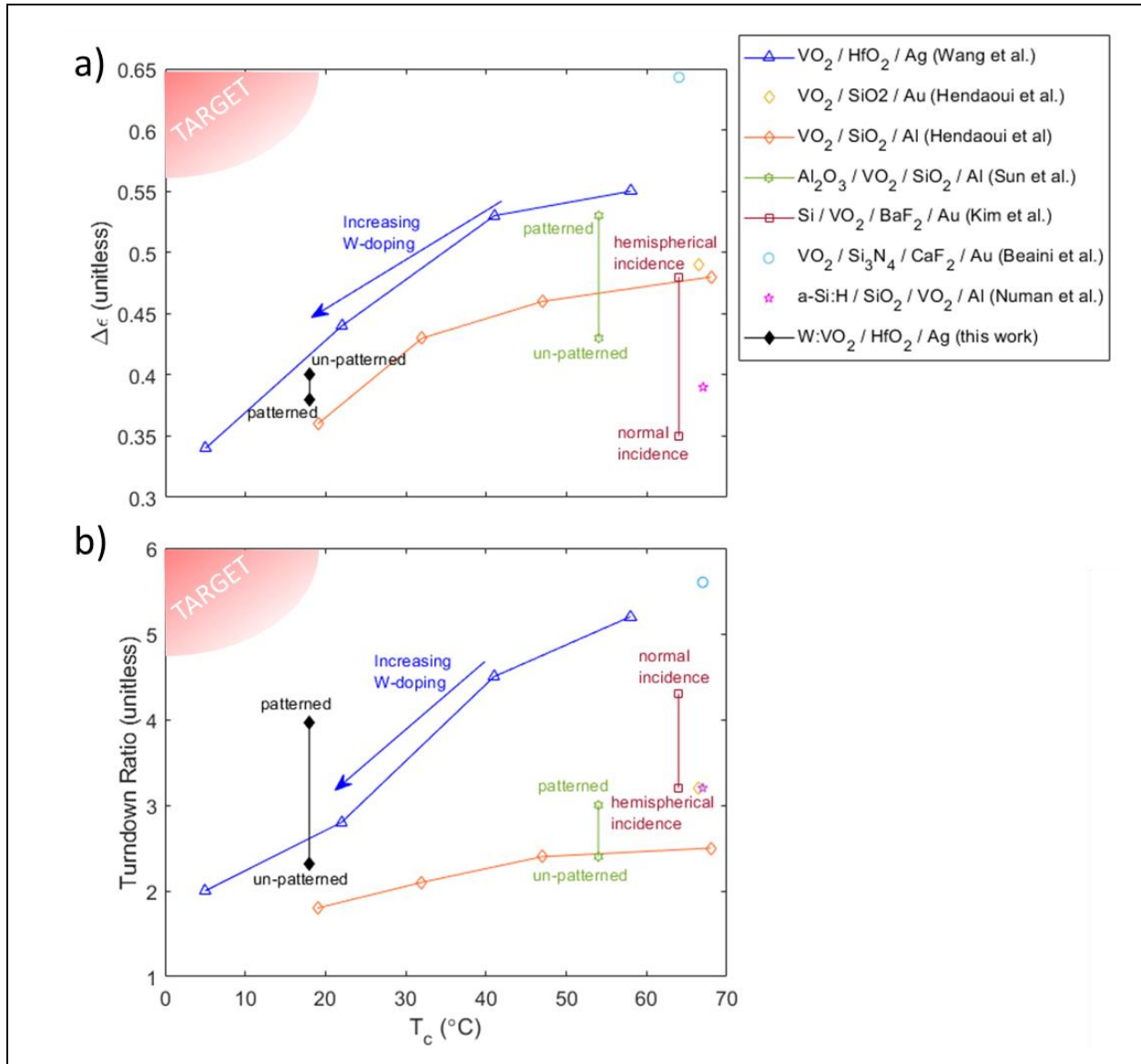
Figure 6.2: Performance metrics $\Delta\varepsilon$ (a) and $Q\varepsilon$ (b) plotted vs T_c for various thermochromic films reported in the literature show the state-of-the-art for these devices. The target behavior, high turndown ratio at low T_c, has yet to be demonstrated.

A VO$_2$ film alone, however, does not satisfy the desired thermochromic behavior. In the metallic (high-temperature) phase, a VO$_2$ film is more reflective (thus less emissive), opposite

the desired change. Several studies have explored metamaterial devices consisting of thin film stacks and/or patterned surfaces in order to achieve and optimize the desired spectral behavior. The typical strategy (illustrated in Figure 1b) is to build a Fabry-Perot resonant cavity with a transparent spacer layer bounded by a highly-reflective mirror on the back side and VO_2 film on the front. The resonant cavity can effectively be turned "on" ("off") to a highly emissive (reflective) states by switching to metallic (insulating) VO_2. Adjusting the thicknesses of the spacer and VO_2 layers allows fine-tuning of the spectral response. Figure 2 and Table S1 in the Supporting Information summarize some prominent results of VO_2-based thermochromic films from the literature.[4-10] Two studies have demonstrated a lowered T_c by using W-doped films,[6, 10] but at the cost of lower $\Delta\varepsilon$ and $Q\varepsilon$ as doping level increases (blue and orange curves). It has also been shown[9] that patterning the VO_2 film into a switchable plasmonic metasurface can further tune the spectral response to improve $\Delta\varepsilon$ and $Q\varepsilon$ (green).

 The goal of this present and ongoing work is to develop a flexible thermochromic thin film device employing micro-patterned, tungsten-doped VO_2 to achieve both large $\Delta\varepsilon/Q\varepsilon$ and low T_c.

6.2 Experimental Methods

Hafnia films were deposited by radio-frequency magnetron sputtering at 125 W from a 3 in hafnia target under 1 mtorr Ar (49 sccm) and O_2 (1 sccm). Silver films on Ti adhesion layers were deposited by e-beam evaporation of Ag or Ti metal, respectively. Undoped (VO_2) and tungsten-doped ($W:VO_2$) films were deposited via radio-frequency magnetron sputtering at ~280 W from pure vanadium metal and tungsten-vanadium alloy (8:92 wt.%) 5.08-cm-diameter targets, under 6 mtorr Ar (20 sccm) and O_2 (1 sccm). After deposition, VO_2 and $W:VO_2$ films were annealed at 450°C under 250 mtorr O_2 for 10 min.

A photolithographic process was used to create the Fabry-Perot cavity using a bi-layer resist of positive photoresist S1805 on polymer LOR-1A. The photomask (custom made by Photomask Portal) consisted of a 4-in-by-4-in square array of hexadecagons with 5-μm radius and 6-μm center-to-center spacing. The resist was exposed in a Karl Suss MA6 mask aligner at a dose of 47-56 mJ/cm^2 and developed in MF319 for 30-60 sec (see Supporting Information, section b, for a discussion of optimizing exposure and develop times). Liftoff was effected by sonication in acetone for ~30 min (except where otherwise noted).

Silicon substrates (P-type, B-doped, 0.1-1.0 Ωcm, (100) cut) were obtained from MTI Corporation and W-foils (0.05mm thick, 99.95\%) from Alfa Aesar. FTIR spectra were measured on a Bruker Tensor 27 with 4 cm^{-1} resolution and 128 scans per measurement, using an ~100-nm thick Au film as a reference. Except where otherwise noted, FTIR spectra were measured in reflection geometry with a 10° angle of incidence. A custom-built heater stage was used to control the sample temperature; during any given measurement, the temperature varied less than ±2°. Reflectance hysteresis was measured using a white-light tungsten-halogen lamp source and InGaAs photodiode detector.

Turndown ratio ($Q\varepsilon$) is calculated as the ratio of integrated hot-state emittance (ε_{hot}) to cold-state emittance (ε_{cold}). For comparing device behavior at intermediate temperatures, we can consider $Q\varepsilon$ to be a function of temperature

$$Q\varepsilon(T) = \frac{\varepsilon(T)}{\varepsilon_{cold}}$$
(Equation 1)

Similarly for the difference $\Delta\varepsilon$

$$\Delta\varepsilon(T) = \varepsilon(T) - \varepsilon_{cold} \tag{Equation 2}$$

FTIR measurements yield the spectral reflectance $R(\lambda,T)$. Assuming transmission and scattering are negligible, the spectral emittance is

$$\varepsilon(\lambda,T) = 1 - R(\lambda,T) \tag{Equation 3}$$

the total emittance is then calculated from the spectral emittance as

$$\varepsilon(T) = \frac{\int_{\lambda_1}^{\lambda_2} \varepsilon(\lambda,T)B_\lambda(\lambda,T)\,d\lambda}{\int_{\lambda_1}^{\lambda_2} B_\lambda(\lambda,T)\,d\lambda} = \frac{\int_{\nu_1}^{\nu_2} \varepsilon(\nu,T)B_\nu(\nu,T)\,d\nu}{\int_{\nu_1}^{\nu_2} B_\nu(\nu,T)\,d\nu} \tag{Equation 4}$$

where

$$B_\lambda(\lambda,T) = \frac{2hc^2}{\lambda^5}\frac{1}{e^{hc/(\lambda k_B T)}-1} \quad \text{and} \quad B_\nu(\nu,T) = 2hc^2\nu^3\frac{1}{e^{hc\nu/(k_B T)}-1} \tag{Equation 5}$$

are the wavelength- and wavenumber-parametrized blackbody spectral radiance densities, respectively. For practical purposes, it is only necessary to integrate over the spectral region where B is appreciably non-zero. This range depends on temperature, but is approximately 3-35 μm for the temperatures of interest here. For the purposes of this study, we integrate from 1.3 to 27 μm (368 to 7497 cm^{-1}), the full spectral range of our FTIR spectrometer.

Expected behavior of our unpatterned devices was calculated using the Fresnel reflection/transmission coefficients and the multi-beam interference formula discussed in the Appendix, Section A.1. Optical constants for Ag, HfO$_2$, and W-doped VO$_2$ were taken from literature.[11-13] To account for the possibility that the VO$_2$ films had air gaps, defects, and surface roughness, an additional Bruggeman effective medium approximation (EMA) was applied to mix the VO$_2$ optical constants with those of vacuum with some fill fraction:

$$fill = \frac{volume\ VO_2}{volume\ VO_2 + volume\ air\ gaps} \tag{Equation 6}$$

6.3 Results and Discussion

6.3.a Simple Fabry-Perot Device: Calculations

Our device (illustrated in Figure 1b) consists of a VO$_2$ film, an HfO$_2$ film, and a Ag backplane. It is instructive to consider first the HfO$_2$-on-Ag without VO$_2$. In a first-order approximation, best performance will be achieved when the first-order Fabry-Perot resonance of the cavity overlaps the peak of the blackbody spectrum (~8-11 μm at 0-100°C). This resonance corresponds to destructive interference between light reflected from the HfO$_2$ surface and from the HfO$_2$-Ag interface. Assuming normal incidence, a π phase shift at the air-HfO$_2$ and HfO$_2$-Ag interfaces, and no reflection phase shift at the HfO$_2$-air interface, resonant modes should be expected when

$$2n_{HfO_2}d_{HfO_2} = \frac{(2m-1)}{2}\lambda \qquad \text{(Equation 7)}$$

where d_{HfO_2} is the thickness of the HfO$_2$ layer, n_{HfO_2} is the index of refraction of HfO$_2$, and m is a positive integer.

Figure 3 shows calculated reflectance spectra for HfO$_2$ films of varying thicknesses on Ag. Two distinct sets of spectral features are observed—those arising due to the HfO$_2$ absorption band (orange box, grey curve is HfO$_2$ extinction coefficient k_{HfO_2}) and those arising due to Fabry-Perot resonances (green box). As expected, the resonances shift to longer wavelengths and the absorption features become stronger as the film thickness increases. The reflection minima corresponding to the first-order Fabry-Perot modes for each structure are marked with solid lines, and the predictions from Eq. 7 with dashed lines (Figure 3b). The slight differences between these can be attributed to the fact that the reflection phase shift is not exactly 0 or π for materials with nonzero absorption coefficients.

Figure 6.3: Evaluating different-thickness films of HfO$_2$ on Ag (without VO$_2$) helps identify two different types of spectra features (a): those arising from HfO$_2$ absorption (orange box) and those arising from Fabry-Perot resonances (green box). The Fabry-Perot features (b) vary strongly with HfO$_2$ thickness, as expected. The first-order modes for each thickness are marked with solid lines and the predictions from Eq. 7 with dashed lines.

Adding a thin layer of VO$_2$ to the structure provides a "top mirror" for the Fabry-Perot structure and deepens the resonances (Figure 4). For these calculations, we use the optical constants for 8 wt.% W-doped VO$_2$, to correspond to the devices shown below. Switching the VO$_2$ from insulating (blue) to metallic (red) phase further deepens the resonance, and also shifts it slightly to longer wavelengths (black vertical lines mark the predictions obtained from Eq. 7). Figure 4 illustrates how varying different structure parameters affects the device spectrum. Increasing VO$_2$ film thickness (a) or fill fraction (b) has a similar effect, deepening the Fabry-Perot resonances and shifting them to higher wavelengths. Increasing HfO$_2$ thickness, on the other hand, does not significantly affect the resonance depth, has an even stronger effect on resonance position, and decreases the overall reflectance beyond ~15 μm due to HfO$_2$ absorption.
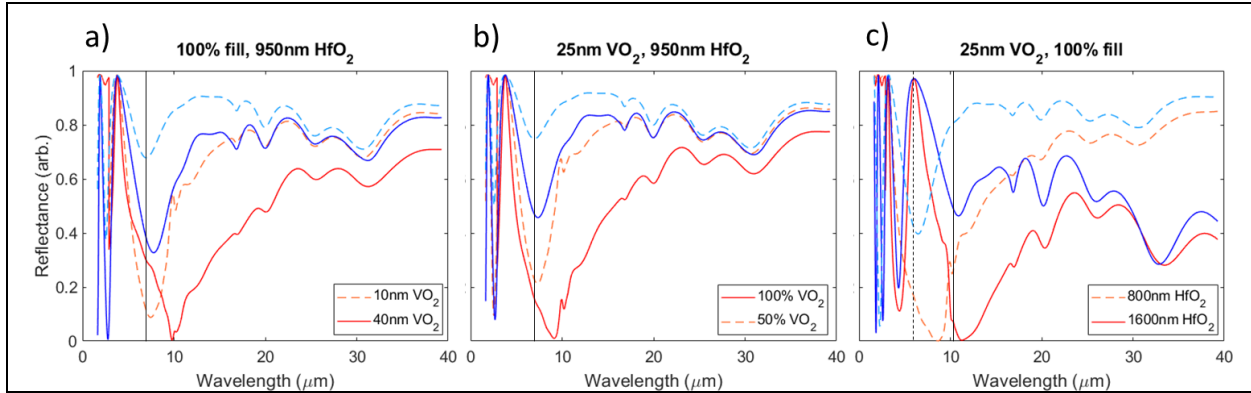
Figure 6.4: Varying device structure affects performance. VO$_2$ film thickness (a) and fill fraction (b) both have similar effects; increasing either deepens the Fabry-Perot resonance (in cold or hot state) and slightly shifts it to longer wavelengths, and increases contrast in the >20-micron spectral region. Increasing hafnia thickness (c) on the other hand, strongly shifts the Fabry-Perot resonance and decreases reflectance in the >20-micron spectral region (due to absorptive losses). Black vertical lines indicate the resonance positions predicted by Eq. 7.
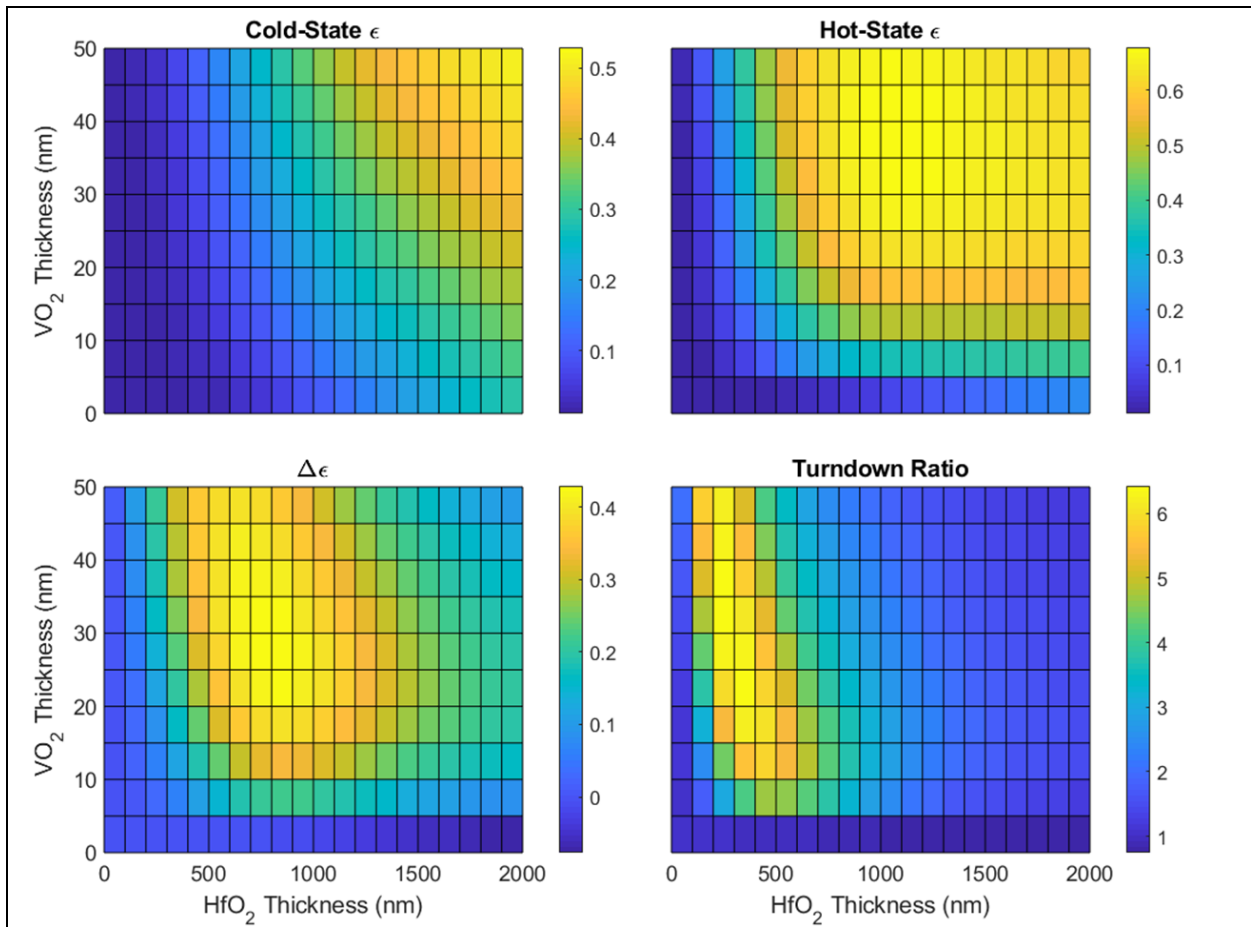
Figure 6.5: Both the cold-state and hot-state emissivity increase with increasing VO$_2$ or HfO$_2$ thickness. Notably, $\Delta\varepsilon$ and Qε are maximized for different device parameters.

124

To optimize device performance, we examine how ε_{hot}, ε_{cold}, $\Delta\varepsilon$, and $Q\varepsilon$ with these device structure parameters. Figure 5 shows how each metric depends on thickness of the VO_2 and HfO_2 films (assuming 100% fill fraction). Both ε_{hot} and ε_{cold} increase monotonically with increasing film thickness. Note that the two measures of performance, $\Delta\varepsilon$ and $Q\varepsilon$, are optimized in different regions of parameter space, with $Q\varepsilon$ peaking where both ε_{hot} and ε_{cold} are small. However, maxima for both occur for ~25-35 nm VO_2 films, which presumably provide a balance of high reflectivity and low absorption.

Figure 6 shows similar plots, with VO_2 thickness replaced with VO_2 fill fraction (with a 50-nm-thick VO_2 film). For fill fractions above ~50%, the behavior is very similar to that with respect to thickness, but at ~40% and below, device performance degrades rapidly, becoming almost indistinguishable from a device with no VO_2 at all. It is also interesting to note that $\Delta\varepsilon$ and $Q\varepsilon$ are optimized at fill fractions slightly less than 100%, presumably because they approximate the slightly thinner films that optimize those metrics.

Figure 6.6: For fill fractions above ~50%, varying VO_2 fill fraction has the same effect as varying VO_2 film thickness; however, below ~40%, devices cease to function entirely.
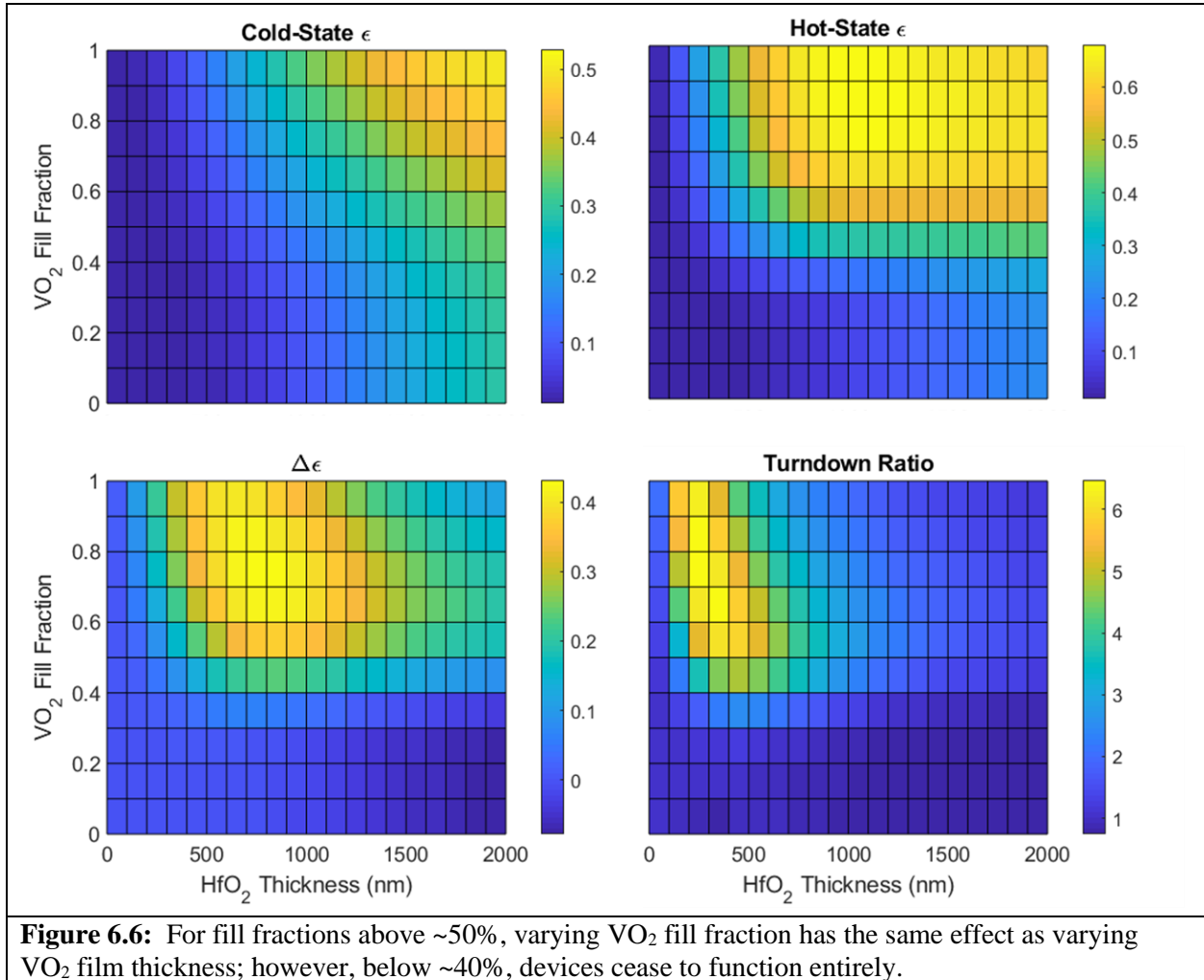
6.3.b Simple Fabry-Perot Device: Experiment

Figure 7 compares calculated (dashed lines) and experimental (solid lines) reflection spectra for a set of actual devices. The device structures and performance metrics are listed in Table 1. These use W-doped VO_2 films, patterned and un-patterned (samples *a* and *g* respectively). Supporting Information, section *d*, compares behavior of samples using doped and un-doped VO_2. They behave very similarly, though with slightly different hot/cold contrast, leading to slightly different values of the metrics.

Figure 6.7: An actual HfO_2 film (a) compares well with the calculations, though the hafnia absorption feature at ~20 μm is stronger, and additional features appear around 13-17 μm, possibly due to non-normal (~10°) incidence of experimental data. The device with a VO_2 film (b) has the expected switching behavior. The spectrum is modeled well by assuming ~75% VO_2 fill fraction, due to surface roughness. The device with microdisks (c) has better contrast than predicted, due to the plasmonic response. Right-side panels are zoomed in on the first-order Fabry-Perot resonance (green box).

A control device with no VO_2 (Fig. 7a) agrees well with the calculation (black dashed curve), with a few additional features. The HfO_2 absorbance at ~20 μm is stronger and sharper in the actual sample, probably due to a slight difference in HfO_2 optical constants for our film relative to the those used in our calculations. There is also a broad feature around 13-17 μm (which may arise due to non-normal incidence of the experimental measurement, see further discussion in the Supporting Information, section *e*), and smaller features overlaid on the first-order Fabry-Perot resonance (Fig. 7a, right panel).

The full device (Fig. 7b) exhibits the expected behavior, except that the Fabry-Perot resonances are shallower than would be expected for a fully dense VO_2 film. The reflectance spectrum is fit excellently by assuming a 75% fill fraction (Fig. 7b, broken curves). This is much lower than the expected film density (see RBS measurements in Supporting Information, section *f*), and arises because the peak-to-valley roughness of the hafnia layer is on the order of the VO_2 film thickness (see discussion in Supporting Information, section *g*).

ID	Structure	α_{sol}	ε_{hot}	ε_{cold}	$Q\varepsilon$	$\Delta\varepsilon$	T_c (°C)
q	58nm W:VO_2 / 950nm HfO_2 / 97nm Au 2.0at% W, 10° incidence, 1.3-27 μm, 17 to 54°C	-	0.706	0.306	**2.3**	**0.40**	11
c	58nm W:VO_2 / 950nm HfO_2 / 97nm Au 2.0at% W, 10° incidence, 1.3-27 μm, 7 to 66°C **patterned** VO_2 (~4.7 μm disks, 1μm spacing)	-	0.508	0.127	**4.0**	**0.38**	15

Table 6.1: Performance of VO_2-based thermochromic films from this study.

6.3.c Patterned Fabry-Perot Devices

Finally, we consider a device with lithographically-patterned VO_2 microdisks. Figure 8 shows a schematic of the complete device unit cell (a) and an atomic force microscope (AFM) image of the patterned disks (b). Analysis of the AFM image using ImageJ software shows that the average disk diameter is 4.7 μm (slightly less than intended) for a total surface coverage of 48%. This pattern was designed to decrease the cold-state emittance by decreasing the amount of VO_2 present, while producing hot-state plasmonic resonances (active only in the metallic phase) which should add resonant absorption in the spectral vicinity of the first-order Fabry-Perot peak, thus increasing hot-state emittance. Our collaborators at Triton Systems are carrying out EM-wave simulations to characterize the expected plasmonic behavior.

Figure 7c shows the response of our patterned device, which has strong hot-vs-cold contrast in the spectral region of interest. Given an effective film density of ~75% (obtained by manually fitting the response for an un-patterned device, above) and a surface coverage of ~50%, we estimate an effective fill fraction of ~0.75*0.50=0.38. The calculated spectrum (dotted line in Figure 7c) matches well in the cold state, but has too high a reflectance in the hot state. In order to get a good fit to the hot-state spectrum, the fill fraction must be increased to 0.5, which results in the cold-state reflectance being too low. The calculations presented here (based simply on Fresnel reflection coefficients) cannot accurately account for patterned structures on the order of the wavelength; the cold-state reflectance is fit well by the model and the expected fill fraction, but the hot-state plasmonic resonances increase the contrast beyond what the calculations can predict. This suggests that the patterning has the intended effect, which can only be confirmed by comparison to full EM-simulations.

Performance metrics for these patterned and un-patterned devices are compared to similar devices from the literature in Figure 2. Our present devices are comparable to other devices with a similar transition temperature, and our patterned device has a $Q\varepsilon$ exceeding the others. For the present device structure, the patterning increases $Q\varepsilon$, but slightly decreases $\Delta\varepsilon$. By further tuning the structure (HfO_2 thickness, VO_2 thickness, and disk diameter) according to the calculations in Figures 5 and 6, it should be possible to increase $Q\varepsilon$ and $\Delta\varepsilon$ still further.
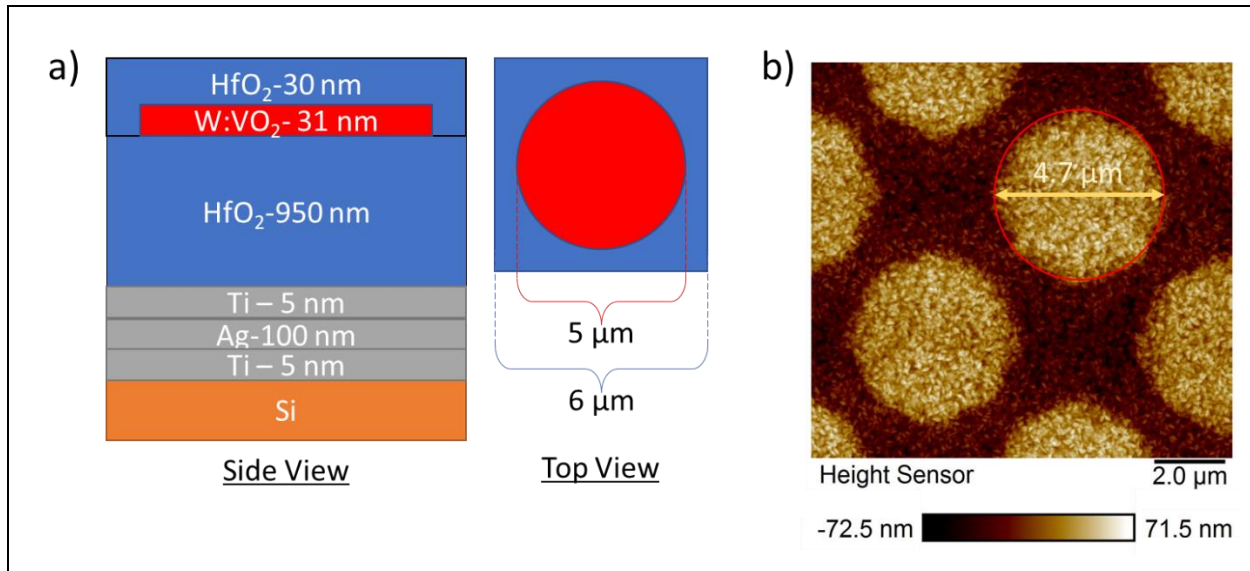
Figure 6.8: The patterned device consists of the same thin-film stack described above, but with the VO₂ film patterned into a square array of disks with a 5-μm diameter and 6-μm center-to-center spacing (a). Atomic force microscopy (b) shows that the actual disks are slightly smaller (4.7-μm diameter) than intended.

6.4 Conclusions

VO₂-based thermochromic films are a promising solution for passive thermal control in various systems with stringent weight and power limits, such as unmanned spacecraft. A switchable Fabry-Perot cavity design has been demonstrated by several groups, but has yet to achieve the required performance levels to be truly viable. It has also been shown that W-doping can decrease T_c (though at the cost of $\Delta\varepsilon$ and $Q\varepsilon$); and that patterning plasmonic structures can increase $\Delta\varepsilon$ and $Q\varepsilon$. By combining W-doping and patterning, and carefully tuning structural parameters, we should be able to improve upon the performance of devices produced heretofore and bring this technology one step closer to deployment. Our current devices are already competitive with others reported in literature, and our calculations show how we can fine-tune our structure to further increase performance. Finally, we note that the loss of contrast intrinsic to W-doped VO₂ films might be overcome by using encapsulated VO₂ nanoparticles, shown to retain large contrast with high doping levels.[14]

6.5 Acknowledgements

6.6 References

1.   Lang, F. P.; Wang, H.; Zhang, S. J.; Liu, J. B.; Yan, H., Review on Variable Emissivity Materials and Devices Based on Smart Chromism. *Int. J. Thermophys.* **2018,** *39* (1), 20.
2.   Ulpiani, G.; Ranzi, G.; Shah, K. W.; Feng, J.; Santamouris, M., On the energy modulation of daytime radiative coolers: A review on infrared emissivity dynamic switch against overcooling. *Sol. Energy* **2020,** *209*, 278-301.
3.   Yang, Z.; Ko, C. Y.; Ramanathan, S., Oxide Electronics Utilizing Ultrafast Metal-Insulator Transitions. In *Annual Review of Materials Research, Vol 41*, Clarke, D. R.; Fratzl, P., Eds. Annual Reviews: Palo Alto, 2011; Vol. 41, pp 337-367.
4.   Beaini, R.; Baloukas, B.; Loquai, S.; Klemberg-Sapieha, J. E.; Martinu, L., Thermochromic VO_2-based smart radiator devices with ultralow refractive index cavities for increased performance. *Sol. Energy Mater. Sol. Cells* **2020,** *205*, 7.
5.   Hendaoui, A.; Emond, N.; Chaker, M.; Haddad, E., Highly tunable-emittance radiator based on semiconductor-metal transition of VO_2 thin films. *Appl. Phys. Lett.* **2013,** *102* (6), 4.
6.   Hendaoui, A.; Émond, N.; Dorval, S.; Chaker, M.; Haddad, E., VO_2-based smart coatings with improved emittance-switching properties for an energy-efficient near room-temperature thermal control of spacecrafts. *Sol. Energy Mater. Sol. Cells* **2013,** *117*, 494-498.
7.   Kim, H.; Cheung, K.; Auyeung, R. C. Y.; Wilson, D. E.; Charipar, K. M.; Pique, A.; Charipar, N. A., VO_2-based switchable radiator for spacecraft thermal control. *Sci Rep* **2019,** *9*, 8.
8.   Numan, N.; Mabakachaba, B.; Simo, A.; Nuru, Z.; Maaza, M., VO_2-based active tunable emittance thermochromic flexible coatings. *J. Opt. Soc. Am. A-Opt. Image Sci. Vis.* **2020,** *37* (11), C45-C49.
9.   Sun, K.; Riedel, C. A.; Urbani, A.; Simeoni, M.; Mengali, S.; Zalkovskij, M.; Bilenberg, B.; de Groot, C. H.; Muskens, O. L., VO_2 Thermochromic Metamaterial-Based Smart Optical Solar Reflector. *ACS Photonics* **2018,** *5* (6), 2280-2286.
10.   Wang, X.; Cao, Y. Z.; Zhang, Y. Z.; Yan, L.; Li, Y., Fabrication of VO_2-based multilayer structure with variable emittance. *Appl. Surf. Sci.* **2015,** *344*, 230-235.
11.   Bright, T. J.; Watjen, J. I.; Zhang, Z. M.; Muratore, C.; Voevodin, A. A., Optical properties of HfO2 thin films deposited by magnetron sputtering: From the visible to the far-infrared. *Thin Solid Films* **2012,** *520* (22), 6793-6802.
12.   Marvel, R. E.; Earl, S. K.; White, S. T.; Tiwald, T. E.; Wang, B.; Roberts, A.; Haglund, R. F., Optical Constants for Pure and Tungsten-Doped Vanadium Dioxide from 0.5-40μm. *TBD* **In preparation**.
13.   Rakić, A. D.; Djurišić, A. B.; Elazar, J. M.; Majewski, M. L., Optical properties of metallic films for vertical-cavity optoelectronic devices. *Applied Optics* **1998,** *37* (22), 5271-5283.
14.   Lopez, R.; Haynes, T. E.; Boatner, L. A.; Feldman, L. C.; Haglund, R. F., Temperature-controlled surface plasmon resonance in VO_2 nanorods. *Opt. Lett.* **2002,** *27* (15), 1327-1329.

6.7 Supporting Information

6.7.a Device Performance Drawn from Literature

The performance metrics for several similar devices reported in the literature are summarized in Table S1. The values $\Delta\varepsilon$ and $Q\varepsilon$ reported here are plotted in Figure 2, to contextualize our results with the state of the art.

Table 6.S1: Performance of selected VO_2-based thermochromic films taken from the literature. All emissivity measurements at near-normal unless otherwise noted.

Ref.	Structure	α_{sol}	ε_{hot}	ε_{cold}	$Q\varepsilon$	$\Delta\varepsilon$	T_c (°C)
1	30nm VO_2 / 850nm SiO_2 / 350nm Au 2.5-25 μm, 25 to 100°C	-	0.71	0.22	**3.2**	**0.49**	66.5
2	30nm VO_2 / 1340nm SiO_2 / 350nm Al 2.5-25 μm, 25 to 100°C	-	0.80	0.32	**2.5**	**0.48**	68
	30nm $W:VO_2$ (1.0at% W) / 1340nm SiO_2 / 350nm Al 2.5-25 μm, 5 to 100°C	-	0.80	0.34	**2.4**	**0.46**	47
	30nm $W:VO_2$ (2.1at% W) / 1340nm SiO_2 / 350nm Al 2.5-25 μm, -5 to 100°C	-	0.81	0.38	**2.1**	**0.43**	32
	30nm $W:VO_2$ (2.9at% W) / 1340nm SiO_2 / 350nm Al 2.5-25 μm, -10 to 100°C	-	0.81	0.45	**1.8**	**0.36**	19
3	50nm VO_2 / 800nm HfO_2 / 200nm Ag 2.5-25 μm, 30 to 80°C	-	0.68	0.13	**5.2**	**0.55**	58
	50nm $W:VO_2$ (1at% W) / 800nm HfO_2 / 200nm Ag 2.5-25 μm, 15 to 65°C	-	0.68	0.15	**4.5**	**0.53**	41
	50nm $W:VO_2$ (2.2at% W) / 800nm HfO_2 / 200nm Ag 2.5-25 μm, -25 to 40°C	-	0.69	0.25	**2.8**	**0.44**	22
	50nm $W:VO_2$ (3at% W) / 800nm HfO_2 / 200nm Ag 2.5-25 μm, -25 to 35°C	-	0.68	0.34	**2.0**	**0.34**	5
4	6nm Al_2O_3 / 50nm VO_2 / 1200nm SiO_2 / 80nm Al / 50nm Al_2O_3 patterned VO_2 (2.8μm squares, 0.5μm spacing) 2.5-25μm, 25 to 80°C	0.44 to 0.52	0.79	0.26	**3.0**	**0.53**	54
	6nm Al_2O_3 / 50nm VO_2 / 1200nm SiO_2 / 80nm Al / 50nm Al_2O_3 no patterning 2.5-25μm, 25 to 80°C	0.45 to 0.57	0.74	0.31	**2.4**	**0.43**	-
5	bulk Si / 40nm VO_2 / 1500nm BaF_2 / 200nm Au near-normal, 2.5-25μm, 27 to 100°C	-	0.63	0.15	**4.3**	**0.48**	64
	bulk Si / 60nm VO_2 / 1500nm BaF_2 / 200nm Au hemispherical, 2.5-25μm, 27 to 100°C	-	0.51	0.16	**3.2**	**0.35**	64
6	40nm VO_2 / 31nm Si_3N_4 / 1240nm CaF_2 / Au 10° incidence, 3-25μm, 25 to 100°C	0.38	0.782	0.139	**5.6**	**0.643**	-
7	448nm amorphous hydrogenated Si / 101nm SiO_2 / 263nm VO_2 / Al 5-25μm, 25 to 97°C	-	0.57	0.18	**3.2**	**0.39**	67

6.7.b Optimizing Photolithography Processing Parameters

In order to achieve the desired pattern, a dose test was performed to optimize photolithography processing parameters. This dose test was performed on the S1805 resist alone (without the LOR-1A underlayer), but since S1805 is the photo-sensitive layer, these results correspond closely to the bi-layer case. Figure S1 shows the patterned resist (before VO_2 deposition) for different exposure times and develop times. At low exposure and dose (upper left), the pattern is severely underdeveloped, with the disks too small (white circle shows desired disk size) and square in shape. At high exposure and develop times (lower right), the resist is severely over-developed; the disks have "bled" into one another, leaving small "plus-shaped" patches of resist behind. We achieve the best results with a 56.6 mJ/cm^2 exposure dose and a 90 second develop time. The exposure time has a much stronger effect on pattern than develop time. In adjusting the process parameters, it is useful to consider exposure time as a coarse adjustment and develop time as a fine adjustment.
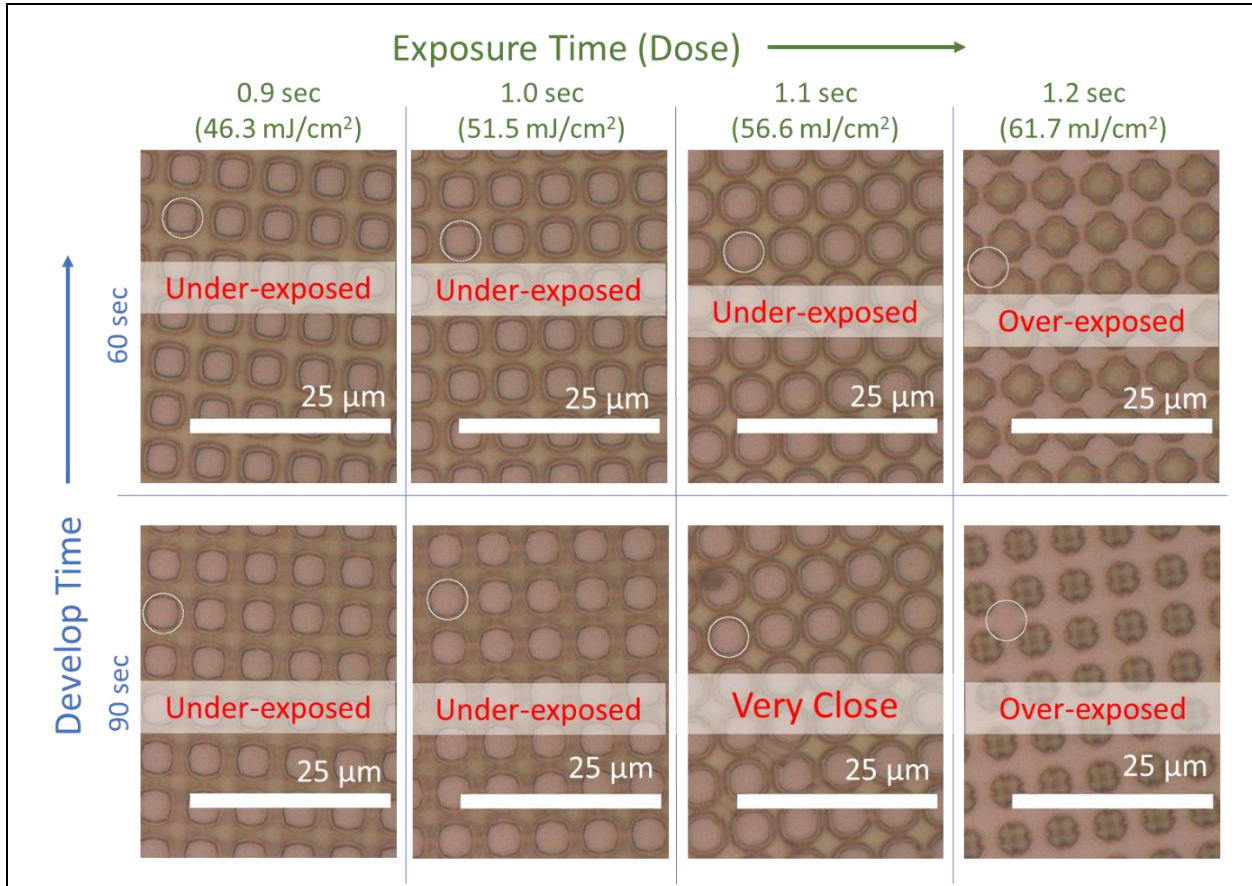
Figure 6.S1: Photolithographic patterns in resist films are sensitive to the exposure and develop time, which must be tuned to achieve the desired pattern. Disk size is greatly sensitive to exposure time, and only slightly sensitive to develop time.

6.7.c Device Aging

VO_2 has a tendency to degrade over time when exposed to oxygen and moisture,[8-9] thus it is important to characterize the stability of our devices over time. Figure S2 compares FTIR

spectra for older devices, collected four years apart. These devices consist of 53-nm-thick W-VO$_2$ (7 wt.% W) on 1000 nm HfO$_2$ (prepared by Triton Systems) on a 10:90 Al:Ag alloy backplane. Samples were annealed in the sputter chamber at ~380°C for ~50 min under 100 mtorr O$_2$. Initial measurements were performed in June 2017, less than a month after fabrication; measurements were repeated November 2021, over four years later. Two pieces were cut from the same wafer, one (S14-1) was stored under ambient conditions, the other (S14-3) in a vacuum desiccator (pumped down to below ~100 mtorr, filled with Ar to a few torr). The desiccator is known to leak (over the course of several months, its pressure will rise above 200 torr) and was re-evacuated periodically over the four-year period, but a thorough record of its pressure over that period was not maintained. Nevertheless, there is a clear difference in device behavior: the sample stored at ambient (Fig. S2a) showed no switching, while that stored at low pressure (Fig. S2b) still switched well, albeit with decreased contrast. This shows that our devices are subject to degradation in ambient environment, but can survive in excess of four years when stored under low vacuum. Device longevity is expected to be further improved by capping with HfO$_2$ to protect the VO$_2$.
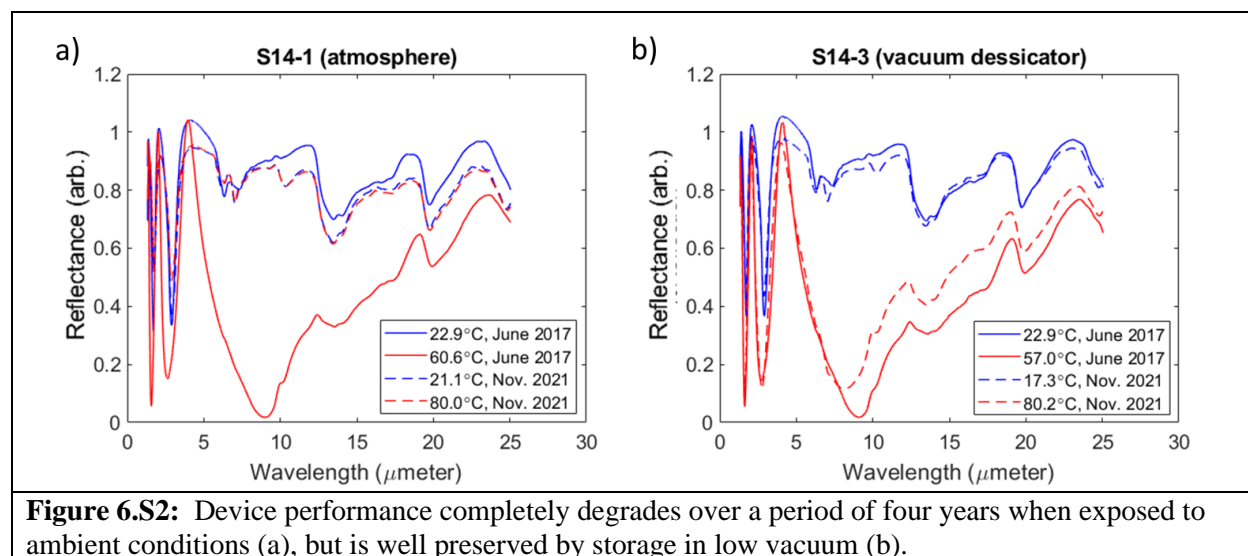
Figure 6.S2: Device performance completely degrades over a period of four years when exposed to ambient conditions (a), but is well preserved by storage in low vacuum (b).

6.7.d Undoped Devices and Effect of HfO$_2$ Capping Layer

Figure S3 compares FTIR spectra for doped and un-doped, patterned and un-patterned devices before and after deposition of a 30-nm-thick HfO$_2$ capping layer. Comparing the doped and un-doped samples (a vs. e, and g vs. h), there is very little spectral difference, only slight changes in contrast, and thus in turndown ratio. For the un-patterned films, the un-doped has better contrast, due to the expected loss of contrast with increased W-doping. In the patterned devices, on the other hand, the un-doped sample has almost no change between the hot and cold states, probably due to unusually poor film/pattern quality in that specific device. Its turndown ratio is less than 1, not because it has reversed contrast, but due to the shift of the blackbody spectrum (the weighting function in the calculation of ε) as a function of temperature.

Capping with HfO$_2$ has no effect within experimental uncertainties (see Supporting Information, section *i* for data on FTIR measurement uncertainty). The performance metrics of these devices are summarized in Table S3.

Figure 6.S3: Doped and un-doped samples have similar spectral features, but slightly different $\varrho\varepsilon$. Capping with HfO_2 has virtually no effect.
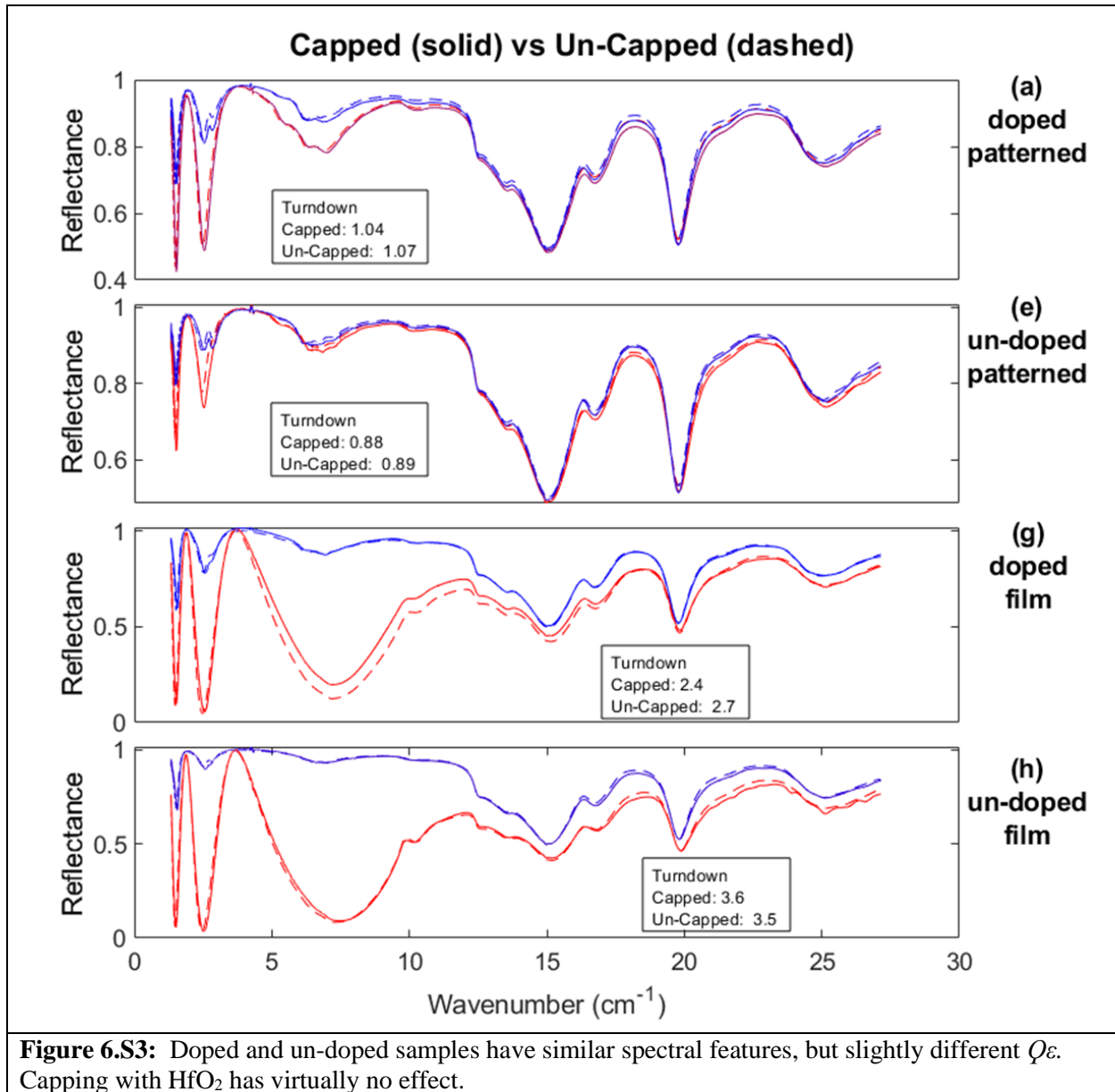
6.7.e Angular Dependence of Spectral Behavior

Since an actual device in operation will emit thermal radiation in all directions, it is important to account for the variation in device emittance as a function of angle (measured relative to the surface normal). Figure S5 shows FTIR reflectance spectra for devices without (left panel) and with (right panel) a VO_2 layer, collected at different angles of incidence ($10°$, $45°$, and $80°$). The HfO_2 absorption features (at ~17, 20 and 25 μm) do not change appreciably with incident angle. On the other hand, the Fabry-Perot resonances (marked with vertical green lines) vary in shape and depth as the incident angle is changed, with the best contrast observed at $45°$. Also, the unidentified spectral feature around 13-17 μm changes in shape and depth with incident angle. Since it does not appear in at all in our calculations (which assume normal incidence) they may represent an additional resonant mode arising at non-normal incidence. It

is unlikely that they are attributable to HfO_2 absorption, as the other HfO_2 absorption features do not exhibit the same angle-dependence.
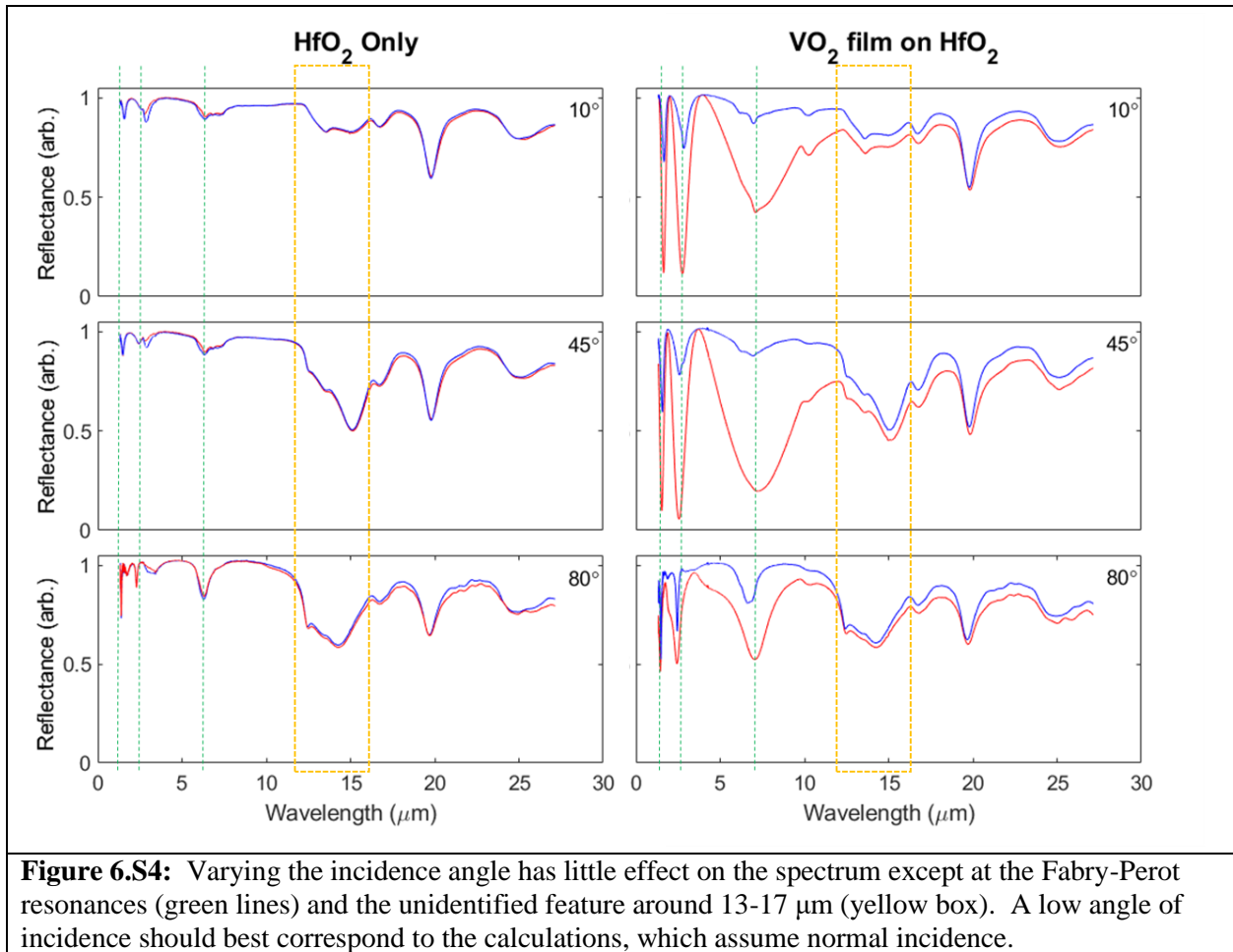
Figure 6.S4: Varying the incidence angle has little effect on the spectrum except at the Fabry-Perot resonances (green lines) and the unidentified feature around 13-17 μm (yellow box). A low angle of incidence should best correspond to the calculations, which assume normal incidence.

6.7.f Rutherford Back-Scattering Measurements

To determine the stoichiometry of un-doped and W-doped VO_2 thin films and microdisks, a set of VO_2-on-Si samples (no HfO_2 or Ag) were prepared for Rutherford backscattering (RBS) analysis. Patterning and sputter deposition for these films was the same as for those in the main text, except that liftoff required only ~3 min sonication (rather than 30 min). Measurements were performed using a 2 MeV He++ beam, with a 2mm beam spot size and an 18 keV energy resolution. Description of the samples and summary of RBS results are given in Table S3. Four separate conclusions can be drawn from these data.

First, the W:V ratio measured by RBS is slightly less than that in the sputtering target, and this difference is more pronounced as doping level increases (~6% decrease and ~15% decrease, respectively). This is likely due to different sputter rates for the W- and V-atoms in the target.

Table 6.S2: RBS measurements on VO_2 films and microdisks on Si

Sample ID		Sample Prep.					RBS Results	
Batch	Sample	Pattern?	Anneal?	at% W (target)	Pattern Coverage %	Thickness (nm)	Formula	Fill %
RBS 3	a	N	Y	0.00	100	20 ± 2	$V_{1.00} W_{0.000} O_{2.04}$	110 ± 6
	b	N	Y	0.00	100	22 ± 1	$V_{1.00} W_{0.000} O_{2.04}$	110 ± 6
	c	Y	Y	0.00	42 ± 3	22.3 ± 0.4	$V_{1.00} W_{0.000} O_{2.03}$	46 ± 3
	d	Y	Y	0.00	46 ± 4		$V_{1.00} W_{0.000} O_{2.06}$	50 ± 3
RBS 3	e	N	Y	1.44	100	32 ± 4	$V_{0.986} W_{0.014} O_{2.00}$	94 ± 12
	f	N	Y	1.44	100	44 ± 1	$V_{0.986} W_{0.014} O_{2.00}$	94 ± 12
	g	Y	Y	1.44	45 ± 9		$V_{0.987} W_{0.013} O_{2.00}$	42 ± 6
	h	Y	Y	1.44	45 ± 9	31.2 ± 0.2	$V_{0.987} W_{0.013} O_{2.00}$	42 ± 6
RBS 3	i	N	Y	2.35	100		$V_{0.981} W_{0.019} O_{2.00}$	85 ± 11
	j	N	Y	2.35	100	21 ± 4	$V_{0.980} W_{0.020} O_{2.00}$	85 ± 11
	k	Y	Y	2.35	55 ± 10		$V_{0.980} W_{0.020} O_{2.01}$	46 ± 7
	l	Y	Y	2.35	50 ± 10	26.5 ± 0.4	$V_{0.980} W_{0.020} O_{1.99}$	42 ± 6
RBS 4	a	N	N	0.00	100	28 ± 1	$V_{1.00} W_{0.000} O_{2.03}$	71 ± 4
RBS 4	b	N	N	1.44	100	37 ± 2	$V_{0.986} W_{0.014} O_{2.00}$	84 ± 5
RBS 4	c	N	N	2.35	100	24.3 ± 0.8	$V_{0.981} W_{0.019} O_{1.98}$	82 ± 5

Second, within experimental uncertainty, there is no stoichiometric difference between patterned and un-patterned samples.

Third, and somewhat surprisingly, there is no stoichiometric difference between annealed and un-annealed samples. It is generally thought that the annealing process adjusts both crystallinity and oxygen-content of VO_2 samples, but for this set of samples we observe no difference (within about ±0.09 uncertainty).

Fourth, film fill% does increase upon annealing, at least for undoped films. This occurs as grain size increases, crystallinity improves, and film defects are annealed out of the sample. In undoped films, the change in fill% with annealing is small, probably due to W-doped films requiring higher temperatures to become mobile (as discussed further in Chapter 3). It is also noteworthy that the measured fill% decreases with increasing W-concentration, which may be partially responsible for the typical loss of contrast at higher W-concentrations.

Finally, we note that the fill% values measured here are considerably higher than those needed to produce calculated responses in agreement with experimental results in the main text (Figure 7). However, the VO_2 films for RBS measurements were deposited on polished Si wafers rather than on hafnia films. The roughness of the hafnia films (discussed below) is responsible for the low apparent fill% in the full devices.

6.7.g Hafnia Roughness and VO₂ Thickness

A previous set of devices with 30-nm-thick VO₂ had much poorer performance, explicable by a very low VO₂ fill fraction. This set of devices was capped with an additional 30-nm-thick layer of HfO₂ to protect the VO₂ from oxidation (see Supporting Information, section *c* for a discussion of VO₂ aging in atmosphere). This capping layer has a negligible effect on device performance (Supporting Information, section *d*). The device structures and performances are summarized in Table S5.

The full device (Fig. S5b) exhibits the expected behavior, except that the depth of the Fabry-Perot resonances and the contrast between the hot and cold states are much smaller than expected (compare to Figure 4a-b, solid curves). This can be accounted for by reducing the fill fraction to ~45% (Fig. S5b, broken curves). However, this is much lower than the expected film density (see RBS measurements in Supporting Information, section *f*).
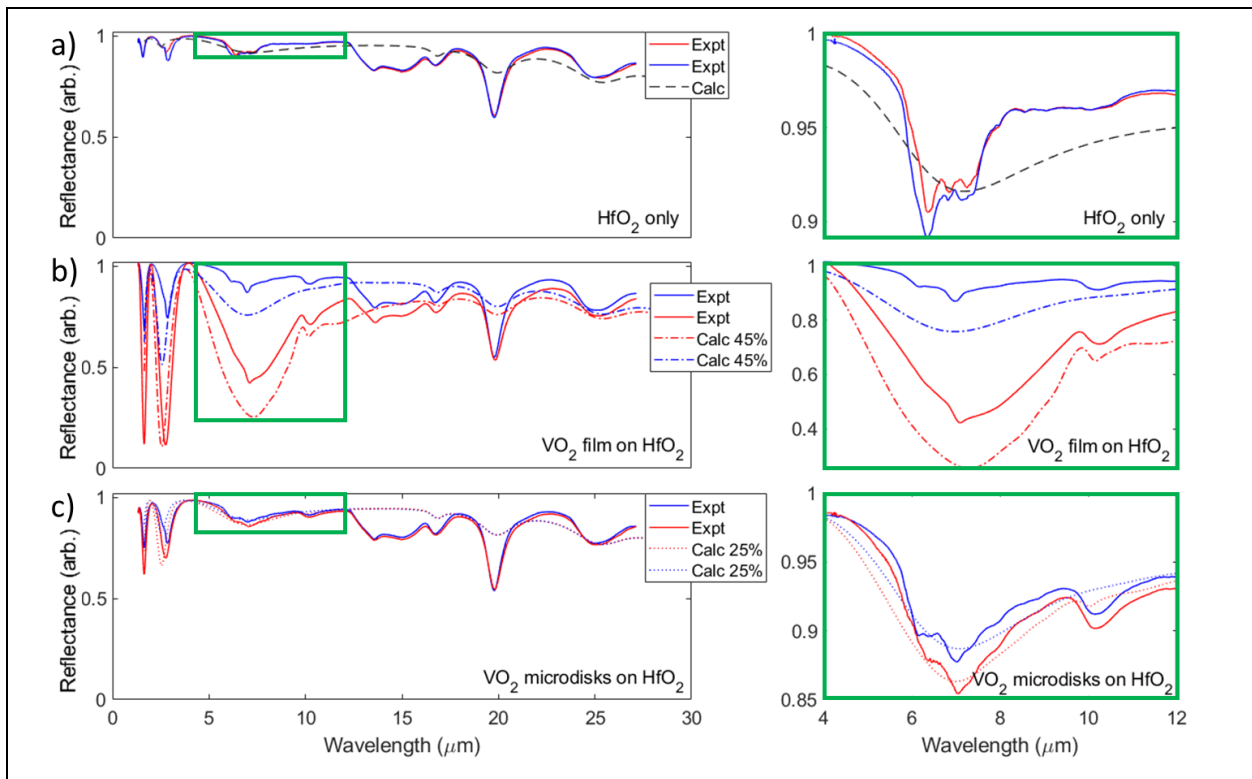
Figure 6.S5: An actual HfO₂ film (a) compares well with the calculations, though the hafnia absorption feature at ~20 μm is stronger, and additional features appear around 13-17 μm, possibly due to non-normal (~10°) incidence of experimental data. The device with a VO₂ film (b) has the expected switching behavior, but with much less contrast than expected for fully dense VO₂. The spectrum is modeled well by assuming ~45% VO₂ fill fraction. The device with VO₂ microdisks (c) has almost no contrast. Right-side panels are zoomed in on the first-order Fabry-Perot resonance (green box).

A similar problem is observed for the patterned devices. For these samples, microscope images show that the average disk diameter is 5.0 μm. Figure S5c shows the response of the patterned device. Switching behavior is observed, showing the presence of functioning VO₂, but the contrast is extremely low (from Table 1, $\Delta\varepsilon = 0.01$ and $Q\varepsilon = 1.0$) and the spectrum is almost

identical to that of a sample with no VO_2 (Fig. S5a). Although the calculations presented here (based simply on Fresnel reflection coefficients) cannot accurately account for patterned structures on the order of the wavelength, it is remarkable that using this simple formalism—assuming a 45% dense VO_2 film and ~55% areal coverage (corresponding to the ~55% coverage of our intended pattern) to give a fill fraction of 0.45*0.55=0.25—yields an extremely close match to the observed spectrum

ID	Structure	α_{sol}	ε_{hot}	ε_{cold}	$Q\varepsilon$	$\Delta\varepsilon$	T_c (°C)
Table 6.S3: Performance of thermochromic films with 30-nm-thick VO_2.							
a	30nm HfO_2 / 31nm W:VO_2 / 950nm HfO_2 / 97nm Au 2.0at% W, 10° incidence, 1.3-27 μm, 7 to 66°C **patterned** VO_2 (~5μm disks, 1μm spacing)	-	0.191	0.185	**1.0**	**0.01**	22
g	30nm HfO_2 / 31nm W:VO_2 / 950nm HfO_2 / 97nm Au 2.0at% W, 10° incidence, 1.3-27 μm, 17 to 54°C	-	0.432	0.179	**2.4**	**0.25**	22
e	30nm HfO_2 / 31nm VO_2 / 950nm HfO_2 / 97nm Au 10° incidence, 1.3-27 μm, 16 to 97°C **patterned** VO_2 (~5μm disks, 1μm spacing)	-	0.147	0.166	**0.88**	**-0.02**	71
h	30nm HfO_2 / 31nm VO_2 / 950nm HfO_2 / 97nm Au 10° incidence, 1.3-27 μm, 62 to 100°C	-	0.545	0.153	**3.6**	**0.39**	66

This lower-than-expected fill fraction can be explained by the roughness of the hafnia films. Figure S6 shows the hafnia surface roughness, measured by AFM, as a function of hafnia film thickness. Although the root-mean-squared roughness is low, the peak-to-valley roughness is larger than the VO_2 film thickness. As a result, the VO_2 layer is interrupted by voids and hafnia inclusions—effectively producing a layer of VO_2 mixed with air at a low VO_2 fill fraction. While it would be more accurate to describe this structure as a VO_2/air EMA on a VO_2 layer on a VO_2/HfO_2 EMA, our simplified model using only the VO_2/air EMA is sufficiently accurate to describe device behavior.
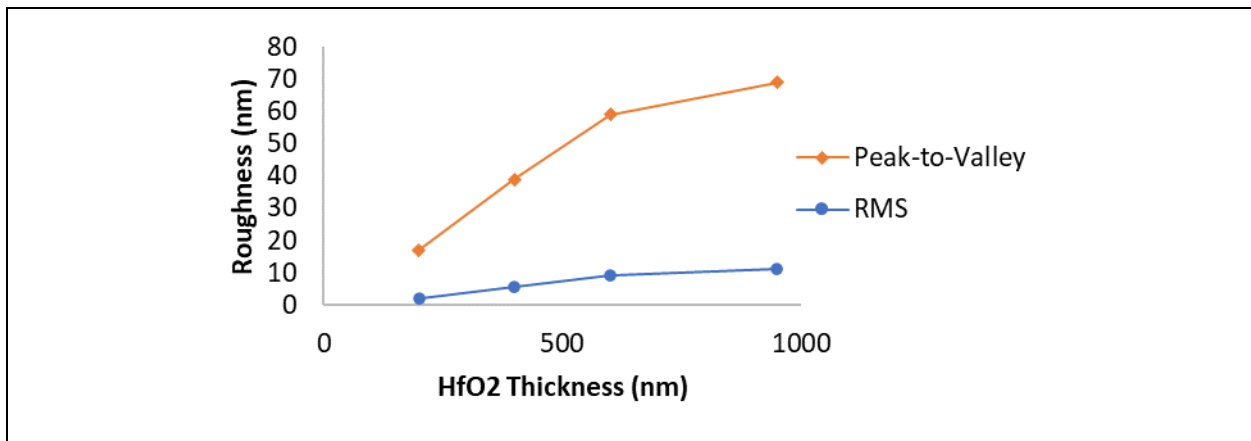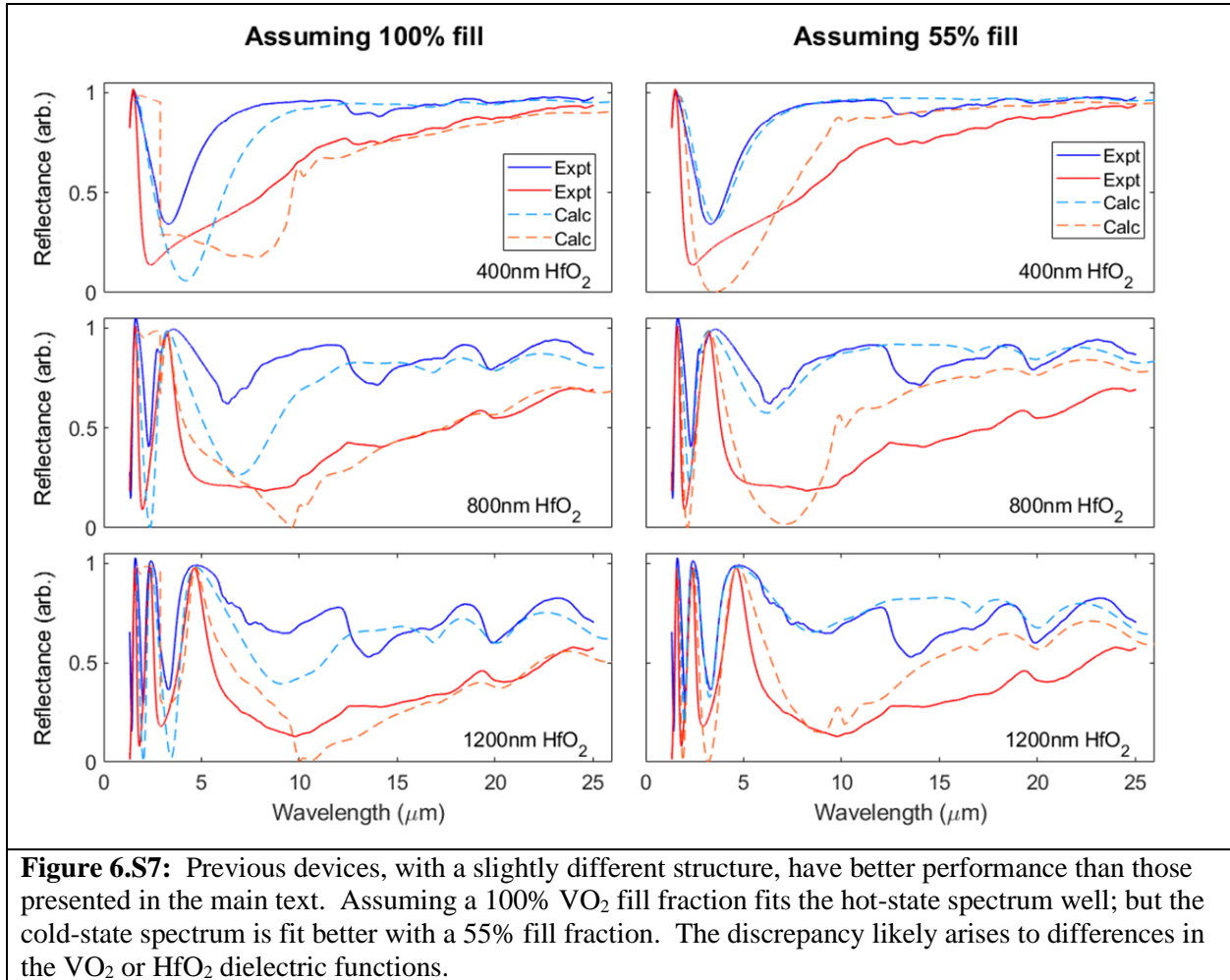

Figure 6.S6: The roughness of the hafnia film increases with film thickness. While the RMS thickness (blue) is small (<10 nm), the peak-to-valley roughness for a 950-nm-thick hafnia film is thicker than our VO_2 films.

6.7.h Performance of Older Devices

Figure 6.S7: Previous devices, with a slightly different structure, have better performance than those presented in the main text. Assuming a 100% VO₂ fill fraction fits the hot-state spectrum well; but the cold-state spectrum is fit better with a 55% fill fraction. The discrepancy likely arises to differences in the VO₂ or HfO₂ dielectric functions.

For comparison, Figure S7 presents spectra for an older set of devices (fabricated and analyzed August 2016) from before the plan of photolithographic patterning was introduced. These devices consist of 40-nm-thick 7 wt.% W-doped VO₂, on HfO₂ with a 10:90 Al:Ag alloy backplane, and the spectra were collected at a 30° angle of incidence. These HfO₂ films were prepared by Triton Systems with different deposition conditions than those listed in the main text. Overall, these devices have better $\Delta\varepsilon$ and $Q\varepsilon$ (Table S2) than those presented in the main text, possibly indicating a better VO₂ film quality (these devices were not subjected to any of the photolithographic processes, including sonication) or a smoother hafnia film. It is noteworthy that, whereas the hot-state reflectance is matched reasonably well assuming 100% VO₂ fill fraction, the cold state better matches assuming only 55% fill. This suggests that fill fraction is not responsible for the discrepancy between calculated and experimental spectra here. More likely, the disagreement is due to variance in the optical constants for VO₂ (due to a different doping level than that used in the calculations) and for HfO₂ (which is reported by Triton Systems to be

oxygen-deficient). Despite these differences, the metrics $\Delta\varepsilon$ and $Q\varepsilon$ agree well with the values and trends predicted in the main text, Figure 5.

Table 6.S4: Performance of previous, un-patterned, VO_2-based thermochromic films.

ID	Structure	α_{sol}	ε_{hot}	ε_{cold}	$Q\varepsilon$	$\Delta\varepsilon$	T_c (°C)
1	40 nm W:VO_2 / 400nm HfO_2 / 10:90 Al:Ag 1.8 at% W, 30° incidence, 1.3-27 μm	-	0.359	0.084	**4.3**	**0.28**	22
2	40 nm W:VO_2 / 800nm HfO_2 / 10:90 Al:Ag 1.8 at% W, 30° incidence, 1.3-27 μm	-	0.643	0.208	**3.1**	**0.44**	22
3	40 nm W:VO_2 / 1200nm HfO_2 / 10:90 Al:Ag 1.8 at% W, 30° incidence, 1.3-27 μm	-	0.717	0.319	**2.3**	**0.40**	71

6.7.i Measurement Reproducibility

To quantify the reproducibility of FTIR reflectance spectra, Figure S8 shows the averages and 95% confidence intervals for repeated measurements. All of these measurements were collected on the same day (June 22, 2017) for the sample S14-1 (used in the aging study above). Fig. S8a represents consecutive repeated measurements (two hot state and three cold state) made without moving the sample. The 95% confidence intervals are barely visible, showing that run-to-run variation of the instrument itself is negligible. For Fig S8b the sample was removed and rotated between each measurement. Since the sample should have no in-plane asymmetry, the variation observed here represents changes in sample position and alignment between runs. This serves as a good estimate of the uncertainty for all our FTIR measurements.
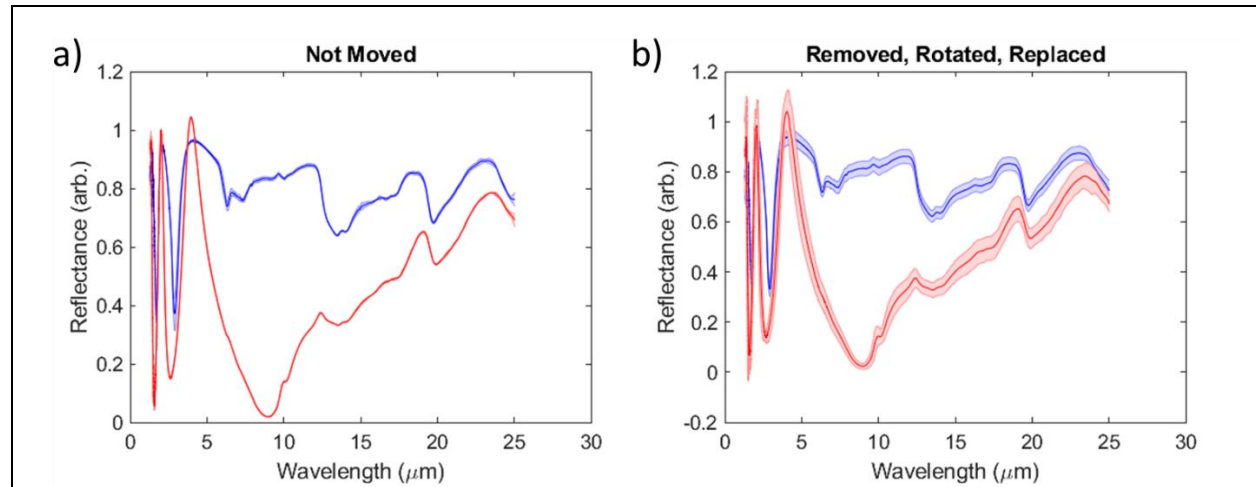

Figure 6.S8: Repeated FTIR measurements on the same sample show that uncertainty is small when the sample is not moved (a) indicating good stability of the instrument; when the sample is removed and replaced (b) uncertainty arises due to variation in alignment. Error bands represent 95% confidence intervals ($\pm 2\sigma$).

6.7.j Hafnia Characterization

The HfO_2 sputter recipe was optimized to yield a high sputter rate and low surface roughness, while yielding a film with the expected index of refraction (as measured by spectroscopic ellipsometry, JA Woollam M-2000VI). Figure S9a shows the optical constants of an HfO_2 film prepared according to the recipe followed in this work. We also performed FTIR transmission measurements on an HfO_2 film on a 2-side-polished Si substrate, using a Bruker Vertex 70v FTIR spectrometer (Figure S9b). As expected, the FTIR transmission spectra (blue) shows dips corresponding to the absorption features (black broken lines) of the HfO_2 optical constants (orange). Closely-packed oscillations in the transmission curve correspond to Fabry-Perot resonances in the Si substrate.
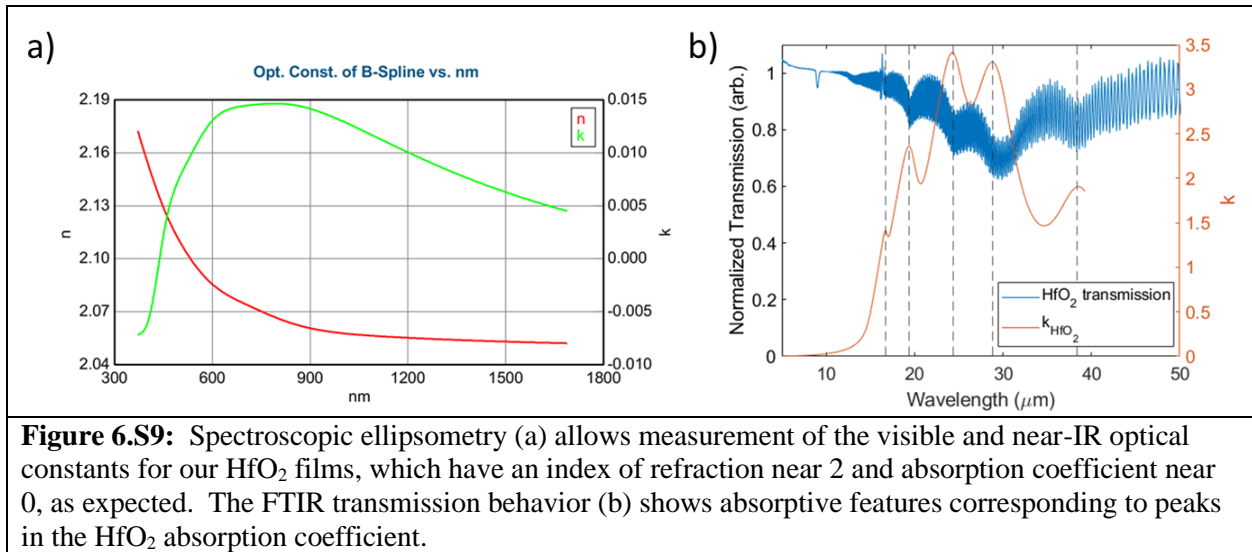

Figure 6.S9: Spectroscopic ellipsometry (a) allows measurement of the visible and near-IR optical constants for our HfO_2 films, which have an index of refraction near 2 and absorption coefficient near 0, as expected. The FTIR transmission behavior (b) shows absorptive features corresponding to peaks in the HfO_2 absorption coefficient.

6.7.k   SI References

1.   Hendaoui, A.; Emond, N.; Chaker, M.; Haddad, E., Highly tunable-emittance radiator based on semiconductor-metal transition of VO_2 thin films. *Appl. Phys. Lett.* **2013,** *102* (6), 4.
2.   Hendaoui, A.; Émond, N.; Dorval, S.; Chaker, M.; Haddad, E., VO_2-based smart coatings with improved emittance-switching properties for an energy-efficient near room-temperature thermal control of spacecrafts. *Sol. Energy Mater. Sol. Cells* **2013,** *117*, 494-498.
3.   Wang, X.; Cao, Y. Z.; Zhang, Y. Z.; Yan, L.; Li, Y., Fabrication of VO_2-based multilayer structure with variable emittance. *Appl. Surf. Sci.* **2015,** *344*, 230-235.
4.   Sun, K.; Riedel, C. A.; Urbani, A.; Simeoni, M.; Mengali, S.; Zalkovskij, M.; Bilenberg, B.; de Groot, C. H.; Muskens, O. L., VO_2 Thermochromic Metamaterial-Based Smart Optical Solar Reflector. *ACS Photonics* **2018,** *5* (6), 2280-2286.
5.   Kim, H.; Cheung, K.; Auyeung, R. C. Y.; Wilson, D. E.; Charipar, K. M.; Pique, A.; Charipar, N. A., VO_2-based switchable radiator for spacecraft thermal control. *Sci Rep* **2019,** *9*, 8.
6.   Beaini, R.; Baloukas, B.; Loquai, S.; Klemberg-Sapieha, J. E.; Martinu, L., Thermochromic VO_2-based smart radiator devices with ultralow refractive index cavities for increased performance. *Sol. Energy Mater. Sol. Cells* **2020,** *205*, 7.
7.   Numan, N.; Mabakachaba, B.; Simo, A.; Nuru, Z.; Maaza, M., VO_2-based active tunable emittance thermochromic flexible coatings. *J. Opt. Soc. Am. A-Opt. Image Sci. Vis.* **2020,** *37* (11), C45-C49.

8.   Occhiuzzi, M.; Cordischi, D.; Dragone, R., Reactivity of some vanadium oxides: An EPR and XRD study. *Journal of Solid State Chemistry* **2005,** *178* (5), 1551-1558.

9.   Yang, Y.; Wei, W.; Wang, S. X.; Huang, T. T.; Yuan, M. H.; Zhang, R.; Yang, W. L.; Zhang, T. N.; Sun, Y.; Yuan, Y. J.; Yu, Z. T.; Chen, X.; Dai, N., Suppression of Photoinduced Surface Oxidation of Vanadium Dioxide Nanostructures by Blocking Oxygen Adsorption. *ACS Omega* **2019,** *4* (18), 17735-17740.

CHAPTER 7

SUMMARY AND OUTLOOK

This dissertation has explored a fundamental question of materials science—how interactions at the substrate surface can affect VO_2 growth and behavior—and uses that knowledge to advance two specific application areas—reconfigurable 2D metastructures and passive thermal control. This final chapter (1) summarizes the conclusions we have drawn about VO_2-substrate interactions, (2) reviews our progress in the application areas and indicates possible future work, and (3) provides an outlook on the benefits and challenges of substrate-based VO_2 engineering.

7.1 Surface-Interface Effects

The interface between VO_2 and its growth substrate has pronounced effects on the morphology, composition, and phase transition of VO_2, both for thin films and single crystals, across most common growth processes. In this dissertation, we have sought to identify the fundamental interactions responsible for these various effects, in order to guide substrate choice as a tool for VO_2 engineering. The effects observed here can all be ascribed to lattice match, chemical reactions, and surface/interface energies, yielding a three-fold framework for evaluating potential substrates. Of these, lattice match has been the most thoroughly explored, producing thin films and nano-wires with uniform shape and orientation, and with transition behaviors modulated by lattice-mismatch strain. Absence of lattice match could also be useful, encouraging the growth of lower-aspect ratio microcrystals by relaxing the constraints on crystal growth. Chemical reactions have received less attention, but can lead to substrate etching, VO_2 doping, substrate-assisted reduction, and interfacial species. Molten V_2O_5 (a precursor in vapor-transport growth) in particular is reactive with many of the oxides commonly used as growth substrates. Variations in the phase and transition temperature of VO_2 crystals are often attributed to substrate-induced strain; but since dopants can affect the VO_2 phase diagram in a way similar to strain, they must be taken into account as well. Finally, surface and interface energies control the wetting and dewetting of VO_2 and its precursors, influencing the shape and size of grains and crystals.

This framework is useful for (1) interpreting behaviors observed in VO_2 growth, (2) predicting results of projected growths, and (3) identifying substrates likely to yield the desired film or crystal properties. Yttria-stabilized zirconia provides an excellent example of (1), with lattice match resulting in preferred orientation through multilayer heteroepitaxy, chemical reactions producing YVO_4, and high surface energy resulting in good surface wetting and thus large crystals. To illustrate (2), we can predict that TiO_2, with its excellent lattice match to VO_2, would result in strong preferred orientation and lattice-mismatch strain (as has been shown for both thin films and single crystals). It could result also in substrate-induced Ti-doping, which to the best of our knowledge has not been reported, but might easily have been confused with or obscured by strain effects. For (3), one of our aims is to optimize crystal growth to produce VO_2 platelets with lateral dimensions greater than 100-μm or even mm for optical experiments;

we predict that the ideal substrate for this would have poor lattice match, low reactivity with V_2O_5, and high surface energy.

7.2 Application Areas

Applications and devices that benefit from VO_2 are many and varied, and a discussion of how to engineer VO_2 to meet their different requirements and challenges is far beyond the scope of this work, but we have explored two application areas at the forefront of different fields which highlight the need for precise control of VO_2 morphology.

Two-dimensional materials, due to their extreme thinness, are highly sensitive to their environment, so that stacking them with other 2D materials or onto bulk materials can tune their properties or produce novel behaviors. Placing 2D materials in contact with phase-change materials is an attractive way to probe such interactions, as the dielectric, magnetic, or strain environment can be changed by simply triggering the phase transition—without the need to transfer the 2D material or compare to other samples (introducing sample-to-sample variations). Here, we used VO_2 to explore how HPhPs in hBN are affected by the surrounding dielectric environment as it is altered by the insulator-to-metal transition. Single-crystalline VO_2 microplatelets were pivotal in showing reconfigurable, in-plane HPhP reflection and refraction, thanks to their large-areas, flat surfaces, and sharp, straight phase domain boundaries. Using hBN-on-VO_2 as a platform for re-writeable metasurfaces still faces a major challenge in patterning the metallic/insulating domains, though laser writing, local doping, and strain engineering offer possible solutions. Beyond hBN, this scheme can be applied to study and exploit the impact of changing dielectric environment on other 2D materials. For example, transition metal dichalcogenides (TMDCs) on VO_2 thin films show enhanced photoluminescence (MoS_2 and WS_2)[1-2] and shifted exciton binding energies (WS_2)[3] when VO_2 is in the metallic phase; and a WSe_2-VO_2 heterojunction has been used to build a dual-mode photodetector.[4]

Low-energy-cost temperature control is an important problem for buildings (expensive to heat and cool) and spacecraft (subject to tight power budgets). Passive thermochromic films, which change their emittance/reflectance as a function of temperature, are a promising solution— thin, lightweight, and requiring no power to switch. The primary design challenges are to achieve (1) the desired spectral response in cold and hot states and (2) T_c near the target operating temperature. Vanadium dioxide is a strong candidate for the active component, with (1) a strong change in optical properties in the 1-10 μm spectral region (where much thermal emission occurs), and (2) T_c near room temperature and tunable by doping. Several VO_2-based thermochromic devices have been demonstrated, but performance has been limited, in part due to the complexity of optimizing structure and materials, in part due to the loss of contrast at high doping levels.

Here, we used a metamaterial design to offset the losses due to heavy W-doping, yielding the best performance yet for a device with $T_c < 20°C$. Moreover, we employed straightforward analytical calculations to examine how different performance metrics vary over the multi-dimensional space of design parameters, pointing the way to further optimizing device structure. While the fabrication methods used here (sputtering and photolithography) are feasible for small satellites (up to a few square meters of surface area), commercial viability for manned spacecraft or smart windows will require more industrially-scalable processes, such as continuous-flow processing that has been demonstrated for VO_2 nanoparticles.[5]

7.3 Outlook

Since the many applications of VO_2 all have unique, often stringent, requirements on its morphology and phase transition, it is critical to develop techniques for reproducibly controlling VO_2 growth. Substrate choice is a powerful tool for engineering VO_2 thin films nano-particles, and micro-crystals, directly affecting strain, orientation, shape, size, and doping, which in turn affect the equilibrium phase, transition temperature, and hysteretic properties. This work has examined some of these effects in specific systems and drawn from them a broader framework for understanding VO_2-substrate interactions, with a view to realizing substrate-based VO_2 engineering.

This approach, however, has one major drawback: most applications also have stringent requirements on the substrate itself. This additional constraint often conflicts with considerations of optimal VO_2 growth, but can be overcome in two primary ways. First, by growing VO_2 on one substrate and transferring it to the device. Single crystals of VO_2 are often easily detached from the growth substrate, and can be transferred by the same method used above for transferring hBN flakes. Free-standing VO_2 thin films have been prepared by etching away the substrate after growth.[6-8] Both single crystals and thin films could potentially be grown with remote-epitaxy through a 2D material, then exfoliated and transferred to another substrate. Alternatively, since the VO_2-substrate interactions are primarily surface/interface effects, the surface of a substrate (pre-defined by application requirements) could be treated to improve VO_2 growth. Hetero-epitaxial VO_2 thin films have been grown on silicon substrates by introducing a YSZ buffer layer.[9] Deposition of a thin Al or Al_2O_3 film on a substrate prior to growth has been used to Al-doped VO_2 crystals.[10] Chemical treatments of surfaces could affect substrate surface energy to manipulate VO_2 wetting behaviors.

To conclude, there has been significant progress in fabricating VO_2 thin films, micro- and nanostructures and single crystals in the past few decades, but simultaneously attaining the desired form factor, morphology, and transition behavior in a scalable, reproducible way is often still a challenge. In nearly all growth methods, substrate-surface interactions play a critical role in determining these properties. Realizing the full breadth of VO_2-based applications will require that we view VO_2-substrate interactions not only as another fabrication challenge to be overcome, but as a valuable part of the design parameter space.

7.4 References

1.   Hou, J. W.; Wang, X.; Fu, D. Y.; Ko, C.; Chen, Y. B.; Sun, Y. F.; Lee, S.; Wang, K. X.; Dong, K. C.; Sun, Y. H.; Tongay, S.; Jiao, L. Y.; Yao, J.; Liu, K.; Wu, J. Q., Modulating Photoluminescence of Monolayer Molybdenum Disulfide by Metal-Insulator Phase Transition in Active Substrates. *Small* **2016,** *12* (29), 3976-3984.
2.   Lin, Y. C.; DeLello, K.; Zhang, H. T.; Zhang, K. H.; Lin, Z.; Terrones, M.; Engel-Herbert, R.; Robinson, J. A., Photoluminescence of monolayer transition metal dichalcogenides integrated with VO2. *J. Phys.-Condens. Mat.* **2016,** *28* (50), 7.
3.   Kajino, Y.; Oto, K.; Yamada, Y., Modification of Optical Properties in Monolayer WS2 on Dielectric Substrates by Coulomb Engineering. *J. Phys. Chem. C* **2019,** *123* (22), 14097-14102.
4.   Luo, H.; Wang, B. L.; Wang, E. Z.; Wang, X. W.; Sun, Y. F.; Li, Q. Q.; Fan, S. S.; Cheng, C.; Liu, K., Phase-transition modulated, high-performance dual-mode photodetectors based on WSe2/VO2 heterojunctions. *Appl. Phys. Rev.* **2019,** *6* (4), 11.

5.   Malarde, D.; Johnson, I. D.; Godfrey, I. J.; Powell, M. J.; Cibin, G.; Quesada-Cabrera, R.; Darr, J. A.; Carmalt, C. J.; Sankar, G.; Parkin, I. P.; Palgrave, R. G., Direct and continuous hydrothermal flow synthesis of thermochromic phase pure monoclinic VO_2 nanoparticles. *J. Mater. Chem. C* **2018,** *6* (43), 11731-11739.

6.   Han, K.; Wu, L.; Cao, Y.; Wang, H. Y.; Ye, C.; Huang, K.; Motapothula, M.; Xing, H. N.; Li, X. H.; Qi, D. C.; Li, X.; Wang, X. R. S., Enhanced Metal-Insulator Transition in Freestanding VO2 Down to 5 nm Thickness. *ACS Appl. Mater. Interfaces* **2021,** *13* (14), 16688-16693.

7.   Ma, H.; Xiao, X.; Wang, Y.; Sun, Y. F.; Wang, B. L.; Gao, X. Y.; Wang, E. Z.; Jiang, K. L.; Liu, K.; Zhang, X. P., Wafer-scale freestanding vanadium dioxide film. *Sci. Adv.* **2021,** *7* (50), 9.

8.   Sim, J. S.; Zhou, Y.; Ramanathan, S., Suspended sub-50 nm vanadium dioxide membrane transistors: fabrication and ionic liquid gating studies. *Nanoscale* **2012,** *4* (22), 7056-7062.

9.   Gupta, A.; Aggarwal, R.; Gupta, P.; Dutta, T.; Narayan, R. J.; Narayan, J., Semiconductor to metal transition characteristics of VO_2 thin films grown epitaxially on Si (001). *Appl. Phys. Lett.* **2009,** *95* (11), 111915.

10.   Strelcov, E.; Tselev, A.; Ivanov, I.; Budai, J. D.; Zhang, J.; Tischler, J. Z.; Kravchenko, I.; Kalinin, S. V.; Kolmakov, A., Doping-based stabilization of the M2 phase in free-standing VO_2 nanostructures at room temperature. *Nano Lett.* **2012,** *12* (12), 6198-6205.

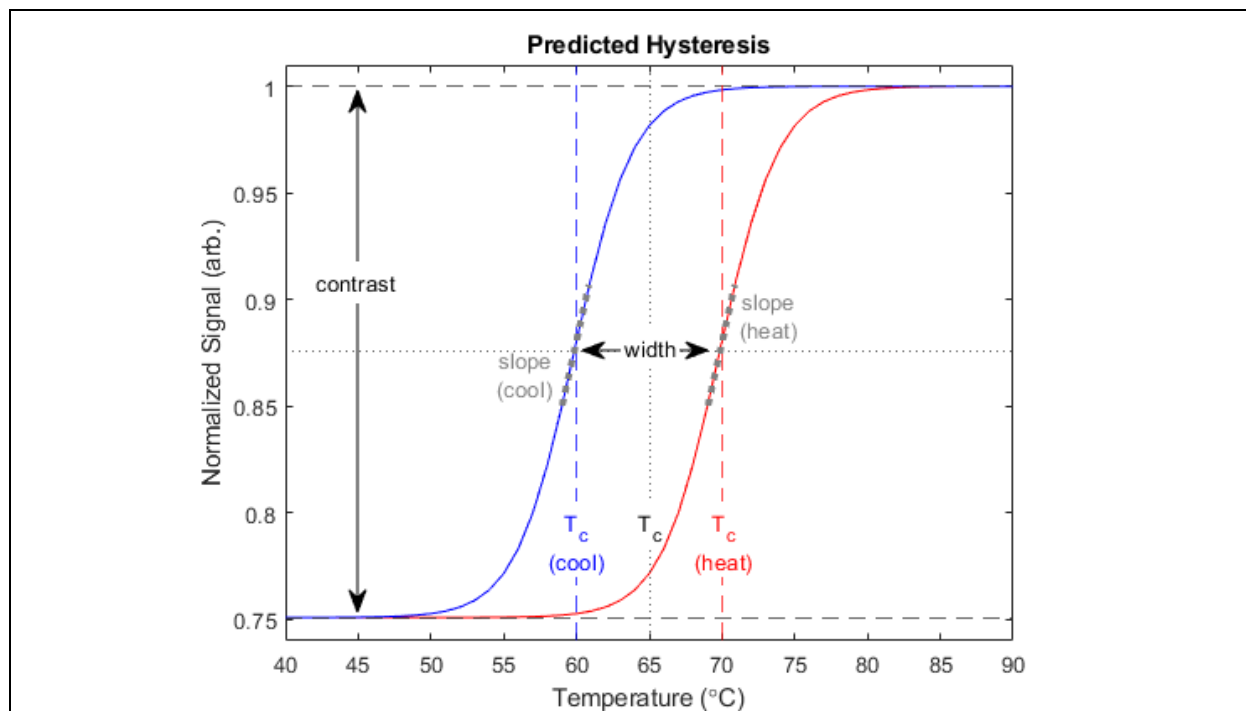## A.1 Hysteresis Measurements and Interpretation

Figure A.1: A hysteresis loop is characterized by its contrast, transition temperature, width, and slope. These quantities are of practical importance in determining device behavior, but also yield information about the VO_2 quality.

Optical reflection/transmission measurements as a function of temperature are a quick, inexpensive way to directly measure the hysteretic behavior of the VO_2 phase transition. The hysteretic behavior is critical to devices/applications, and serves as a non-specific proxy for several micro-/nano-scale VO_2 properties, including strain state, doping, defect density, grain size, film thickness, and oxidation state. Figure 1 shows an example hysteresis loop, normalized by dividing by the maximum value, with the heating curve in red and the cooling curve in blue. Several important metrics are extracted from the hysteresis curve:

- **Contrast:** the difference between the hot-state signal and the cold-state signal (in Figure 1, the contrast is ~25%). As discussed below, contrast is sensitive to VO_2 thickness and substrate, but for otherwise identical samples, contrast is a good metric of VO_2 "quality"; a lower-than-expected contrast is often indicative of a defective film.

- **Transition Temperature (T_c):** for the heating and cooling curves, respectively, $T_{c,heat}$ and $T_{c,cool}$ are each defined as the midpoint between the temperatures at which the

146

transition begins and ends. For a symmetric, monotonically increasing curve (as shown), this corresponds to the temperature at which the measured signal is halfway between its cold-state and hot-state values (in Figure 1, $T_{c,heat}=70°C$, and $T_{c,cool}=60°C$). The overall transition temperature T_c, is defined as the average of $T_{c,heat}$ and $T_{c,cool}$ ($T_c=65°C$ in Figure 1). For pure, bulk VO_2, $T_c \approx 67°C$; a shift in T_c may arise from oxygen stoichiometry, doping, or substrate strain. If the sample temperature differs appreciably from the temperature monitor, actual T_c may differ slightly from the measured.

- **Slope:** The slope for the heating or cooling curve is the tangent to that curve at its respective T_c, and the overall slope as the average of these two. Bulk, unstrained, single-crystalline VO_2 has a very steep slope; thin films have a more shallow slope, as individual grains switch at different temperatures. Unusually shallow slopes may indicate highly non-uniform samples. If the temperature is increased faster than the sample can reach thermal equilibrium, ramp rate may affect the slope as time (rather than set temperature) becomes the limiting factor.

- **Width:** The width is defined as the difference between $T_{c,heat}$ and $T_{c,cool}$ (width=10°C in Figure 1). Width is often affected by nucleation behavior in the VO_2. Films with small grains and a high density of nucleating defects have a small hysteresis width; whereas low-defect samples and nanoparticles (with few defects-per-particle) have larger width.

The hysteresis curve shown in Figure 1 is symmetric, with identical heating and cooling curves. Asymmetry between the heating and cooling transitions can occur, and is often attributed to different nucleation mechanisms in the M1-R vs. R-M1 transitions.

All the hysteresis measurements presented in this work were collected using a custom-built in-house hysteresis setup, schematically illustrated in Figure 2a. A light source is collimated, then focused onto the sample at normal incidence with a microscope objective. The transmitted or reflected light is collected with a photodiode. Sample temperature is controlled by manually varying the voltage applied to a thermoelectric heating element. Data collection is handled by a custom LabVIEW virtual instrument which collects temperature and intensity data at a rate of 2 Hz. The sample stage is enclosed in an acrylic box purged by dry nitrogen to allow for cooling below 0°C without condensation forming on the sample.

Unless otherwise noted, all hysteresis measurements in this work were performed with a tungsten-halogen lamp (effectively a blackbody at ~3000K) and with a Thorlabs PDA10CS amplified InGaAs photodiode (sensitive over 700-1800nm). Figure 2b shows the output spectrum of the light source (yellow), the sensitivity spectrum of the detector (blue), and the product of these (green) which represents the maximum signal we could obtain (for a perfectly reflective or transmissive sample). Reflectance or transmittance is calculated as

$$Signal = \frac{raw - bkg}{ref - bkg}$$
(Equation 1)

where *raw* is the unmodified detector response with sample present, *bkg* is the average detector response with the light source blocked, and *ref* is the average detector response with a reference sample (no sample for transmission, an optically thick gold film for reflection).

The signal output from the photodiode is proportional to the integral of the sample reflectance/transmittance spectrum weighted by the "max signal" spectrum (green curve in Figure 2b). For thin films (or thin film stacks), the reflectance/transmittance depends in a non-trivial way on the layer thickness(es) and optical constants, due to multi-beam interference. In

order to predict the measured hysteresis curve for a given sample, we begin by using the complex Fresnel equations[1] to calculate reflection/transmission at each interface.
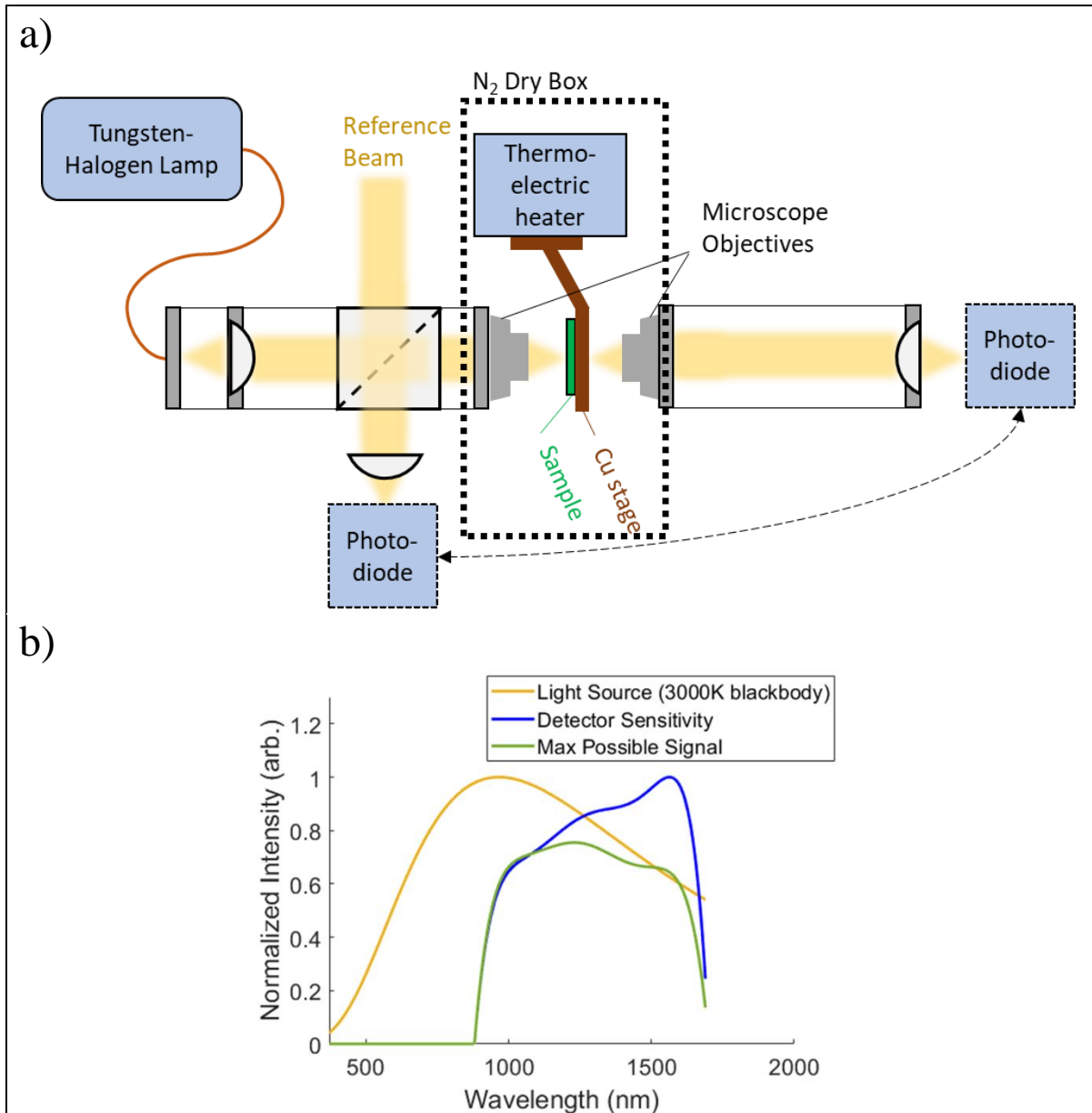
Figure A.2: Optical hysteresis measurements (a) are performed either in reflection or transmission mode, with light focused onto the sample surface at normal incidence, with data collected in real time as the sample temperature is ramped manually. The reflectance/transmission spectrum of the sample is modified (b) by the source spectrum (yellow) and detector sensitivity spectrum (blue).

For a two-layer thin film stack on a substrate, the interference of multiply-reflected beams produces a series which converges to a closed formula:[2]

$$E_r = \frac{(r_{01}+r_{12}\delta_1\delta_1)+(r_{01}r_{12}+\delta_1\delta_1)r_{23}\delta_2\delta_2}{(1+r_{01}r_{12}\delta_1\delta_1)+(r_{12}+r_{01}\delta_1\delta_1)r_{23}\delta_2\delta_2}$$ (Equation 2)

where E_r is the relative magnitude of the reflected electric field, r_{xy} is the Fresnel reflection coefficient at the interface of materials x and y, and δ_x is the phase shift occurring for a beam propagating through layer x.

Figure A.3: Reflectance spectra (left) and resulting hysteresis curves (right) are sensitive not only to VO₂ optical constants, but also to film thickness and substrate. With certain geometries, multibeam interference and spectral shifts can result in "dips" or inversions of the hysteresis loop.
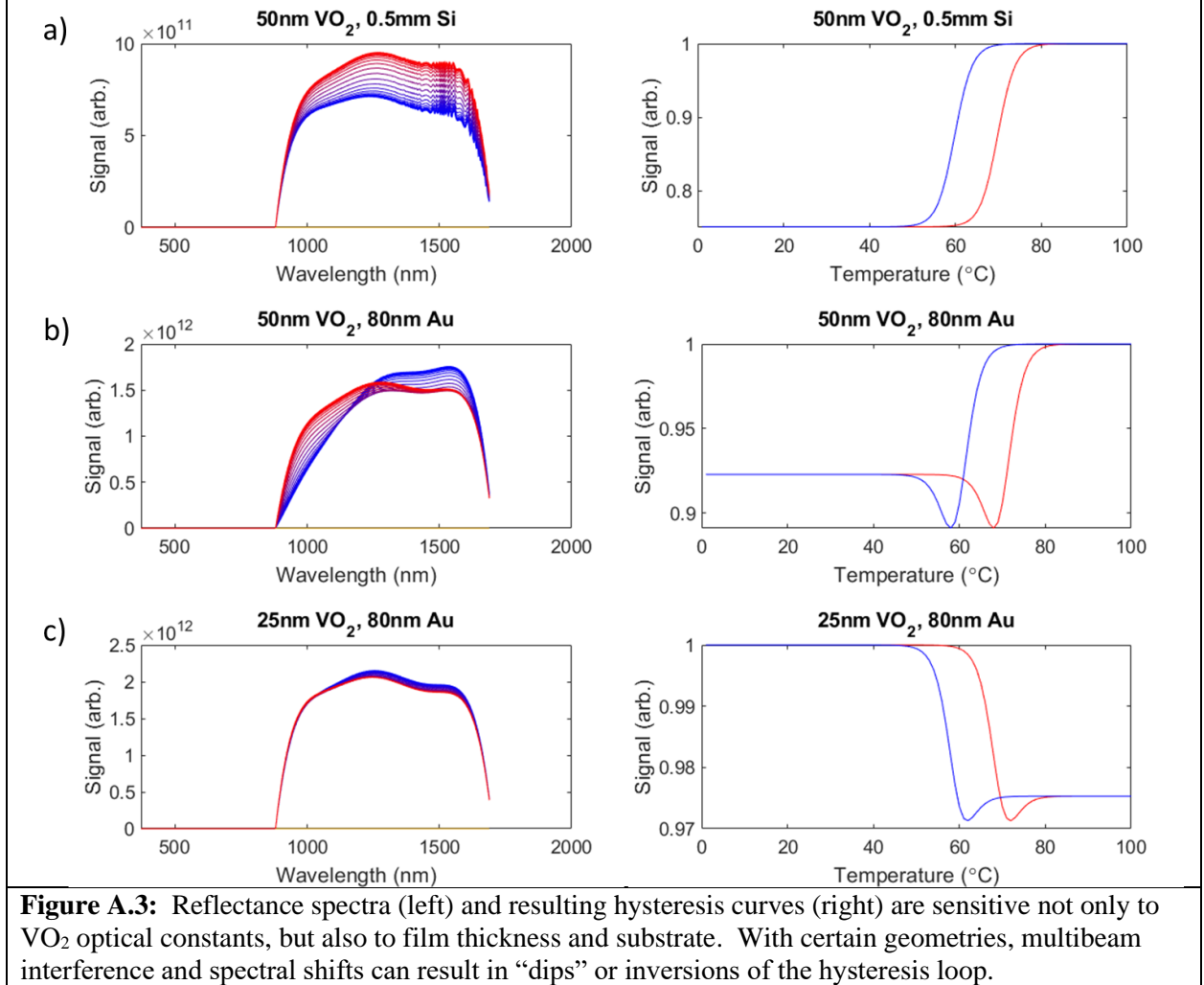
Given the optical constants of each layer, we can calculate the reflectance/transmittance spectrum of a sample. Weighting this spectrum by the "max signal" spectrum and integrating yields the expected signal. To model the phase transition behavior, the VO₂ optical constants are represented by a Bruggeman effective medium approximation (EMA) combining the optical constants of M1-phase (ε_{M1}) and R-phase (ε_R) VO₂

$$\varepsilon = \frac{1}{4}(\varepsilon_{M1}(2-3f) + \varepsilon_R(3f-1)$$
$$+\sqrt{(\varepsilon_{M1}(2-3f) + \varepsilon_R(3f-1))^2 + 8\varepsilon_{M1}\varepsilon_R})$$ (Equation 3)

where the fill fraction f varies from 0 (fully M1) to 1 (fully R) according to

$$f(T) = 1 - \frac{1}{1+e^{(T-T_c)/b}}$$

(Equation 4)

where T_c is the transition temperature for either the heating or cooling curve and b is a constant related to the slope of the hysteresis loop.

Figure 3 presents results of reflectance calculations for a few different systems. The optical constants for Si[3] and Au[4] are taken from literature; the optical constants for VO_2 are derived from ellipsometric measurements of our films. A 50-nm-thick VO_2 film on silicon (Figure 3a) shows the expected behavior, with reflectivity increasing with temperature due the higher reflectance of the metallic phase. On a highly-reflective gold substrate, however (Figure 3b), the reflectance increases in only part of the spectrum, but decreases in the other, resulting in a non-monotonic change in signal as a function of temperature (producing a "dip" in the hysteresis curve). Adjusting the film thickness (Figure 3c) can further alter the hysteretic behavior, even inverting the change in overall reflectance (high-to-low vs. low-to-high).

A.2 Additional Crystal Growth Observations

Figure A.4: Single crystal growth is carried out in a tube furnace at 810°C, under 25 sccm Ar at 1.7 torr. V_2O_5 powder is loaded into one end of a pair of quartz boats, samples are loaded into the other end. Both boats are placed end-to-end within a smaller quartz tube inside the furnace.
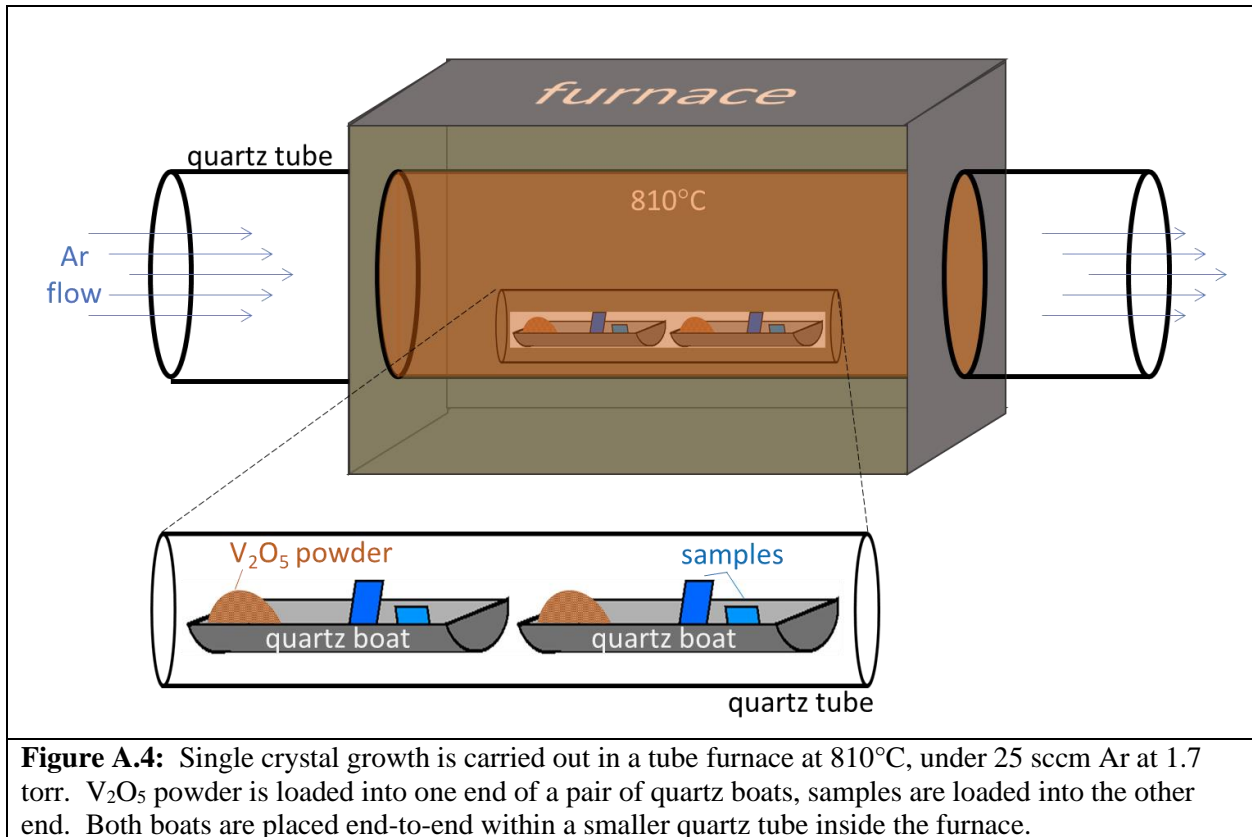
Figure 4 shows a schematic of the crystal growth setup. The crystal growth process is explained in detail in the Experimental Section of Chapter 2, which discusses the impact of substrate choice on crystal growth results. In addition to substrate, there are many other process parameters

which can be adjusted to influence crystal growth: amount of precursor powder, position and orientation of substrates, temperature, temperature ramp rate, growth time, pressure, and carrier gas flow rate. These have not been studied with great detail in this work, but some qualitative observations are described here.

A.2.a Amount of Precursor

Increasing the amount of precursor powder can increase the flux of precursor vapor incident upon the sample, which tends to produce larger and more densely packed crystals.[5] Large amounts of precursor can also lead to secondary growth on the VO_2 crystals. On sapphire, this results in a dark, "fuzzy", crystalline material coating the crystals, most likely composed of different vanadium oxides between V_2O_5 and VO_2. Figure 5 compares microscope images of sapphire substrates after growths with smaller (5a) and larger (5b) precursor volumes. With more precursor, VO_2 crystals grow larger, but are completely covered with "fuzz".
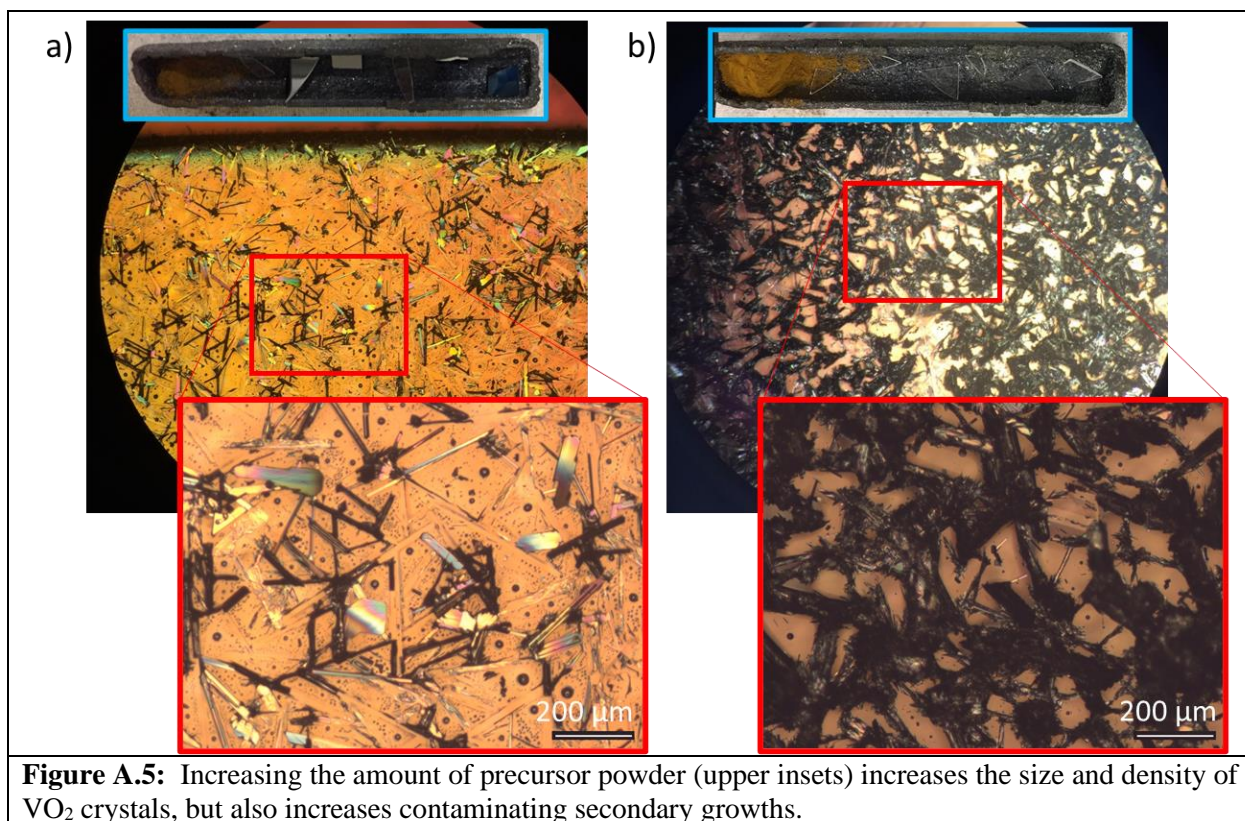
Figure A.5: Increasing the amount of precursor powder (upper insets) increases the size and density of VO_2 crystals, but also increases contaminating secondary growths.

A.2.b Position in Boat

The distance between precursor and sample, the number of samples loaded in the boat, and the orientation of samples all have the potential to impact the precursor vapor flux reaching the sample. However, we have not been able to identify a clear trend in their effects on the crystals grown.

151

A.2.c Temperature and Ramp Rate

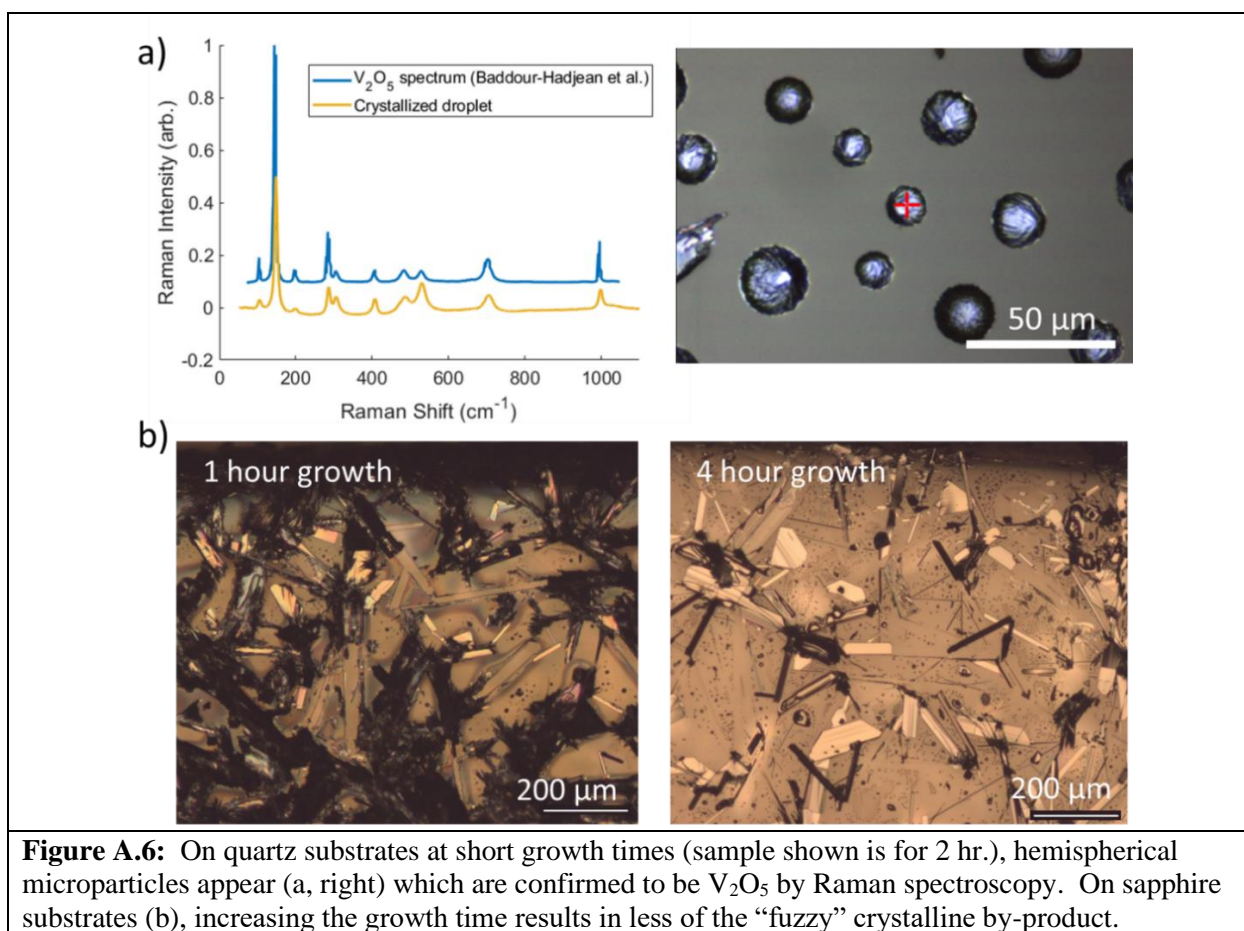These parameters were not varied in our studies. The growth temperature is chosen to be slightly above the atmospheric-pressure melting point of V_2O_5,[6-7] and the heating and cooling ramp rates are determined by the furnace's PID temperature control. To avoid temperature overshoot, the furnace is heated in two steps, first to 600°C (over ~1hr.), then to the growth temperature of 810°C (~30 min.). The quoted growth times are measured from the moment the furnace reaches 810°C to the moment the set temperature is reset to room temperature. After growth, the furnace takes approximately 3 hrs to decrease below 300°C, at which point the samples can be removed.

A.2.d Growth Time

Figure A.6: On quartz substrates at short growth times (sample shown is for 2 hr.), hemispherical microparticles appear (a, right) which are confirmed to be V_2O_5 by Raman spectroscopy. On sapphire substrates (b), increasing the growth time results in less of the "fuzzy" crystalline by-product.

Growth time has the potential to affect how much of the precursor material is carried to the substrate and subsequently reduced to VO_2. At shorter times, hemispherical particles of V_2O_5 can sometimes be observed on quartz, indicating that the growth was ended before all of the precursor droplets were reduced to VO_2 (Figure 6a). Increasing growth time can also reduce the amount of "fuzz" on crystals grown on sapphire (Figure 6b). We suggest two likely explanations for this behavior. First, it may represent an intermediate vanadium oxide which

forms during growth and later reduces to VO$_2$. Second, it may form from un-reduced precursor material when cooled prematurely, and thus never forms at all with longer growth times.

We have also examined the effects of subjecting VO$_2$ crystal samples to a second heating process, in a clean boat with no precursor material, under the same gas conditions. The results, qualitatively different from those of simply increasing the growth time, are presented in Figure 7 (the images shown before and after re-heating are not the same spatial regions, but are representative of the whole). On quartz (Figure 7, top), the crystals have become much smaller, less densely packed. Also, they have changed shape, losing their sharp edges; in some cases, holes or gaps have appeared in the crystals. It appears that a significant amount of the VO$_2$ has sublimtated away, likely due to the lower partial-pressure of V$_2$O$_5$ with no precursor present. On sapphire (Figure 7, bottom), the dark "fuzz" has largely disappeared, but left behind dark-colored traces or contaminants on the remaining VO$_2$ crystals, either residue from its sublimation, or products of its thermal decomposition.
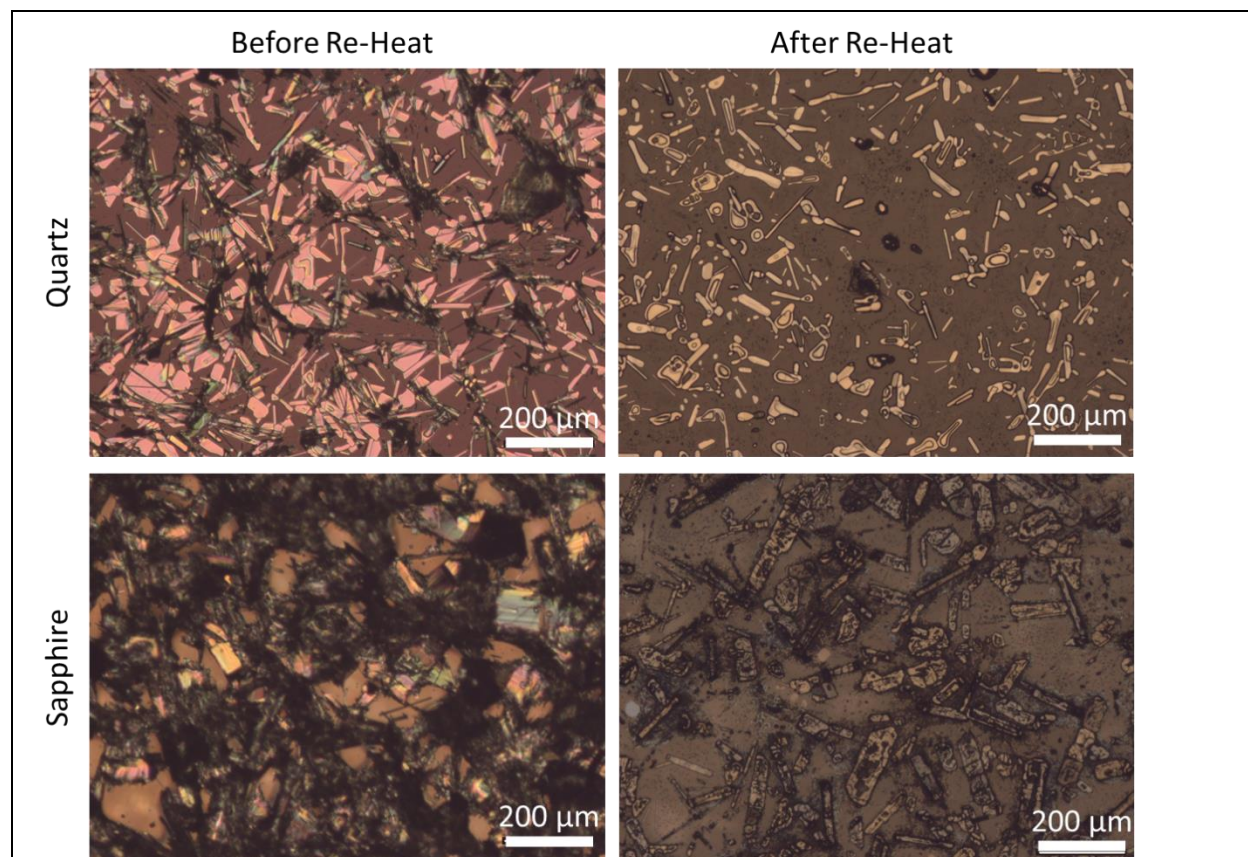

Figure A.7: Re-heating crystals under the same conditions, but in the absence of any precursor material, has a different effect than simply increasing the growth time. On quartz, crystals become smaller and lose their shape as VO$_2$ sublimates. On sapphire, the "fuzzy" material has disappeared, but left behind dark contaminants across the substrate.

A.2.e   Carrier Gas, Pressure, and Flow Rate

These were not varied in our studies, but are expected to affect the rate at which precursor vaporized, carried to the substrate, and reduced to VO$_2$. One study has shown that

better control over the growth products may be obtained by using a two-step growth process with different gas conditions at each step.[8]

A.2.f Condition of the Boat

Figure 8a compares a new, unused quartz boat (left) with one that has been used in many growths (right). Over use the boat becomes encrusted with a grey, crystalline material, most likely a composite of different vanadium oxides. The condition of the boat significantly impacts growth result; in a new boat, very few crystals grow on the sample at all. Moreover, some crystals will grow on substrates placed in an old boat even without the addition of precursor powder (Figure 8b). Notably, the crystals on the top side (Figure 8b, left) are larger, lower in aspect ratio, and less-clearly oriented than those on the bottom (right), due to the asymmetry induced by facing away from or toward the material on the boat. Clearly, the vanadium oxide material coating a well-used boat participates in the growth process by providing an additional source of growth material.
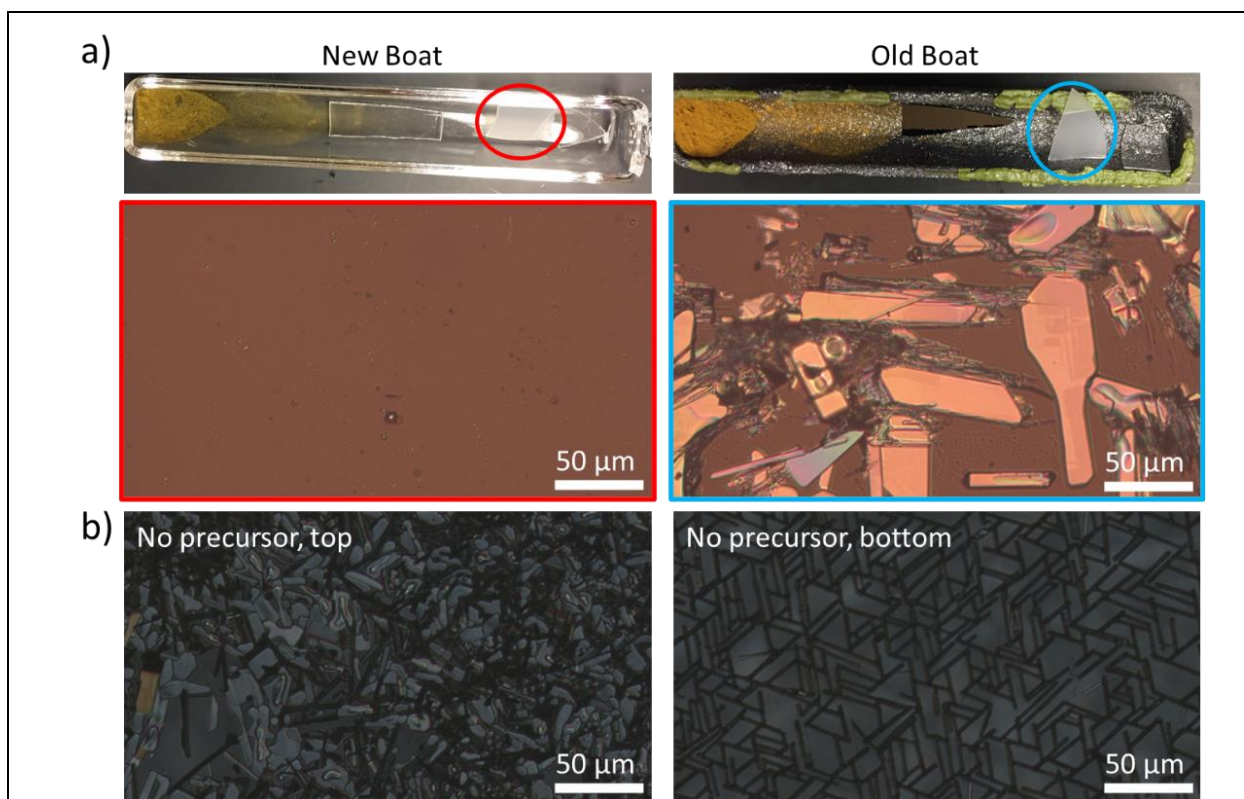

Figure A.8: With use, the boats used to contain substrates and precursors become coated with a composite of vanadium oxides (a, top). Almost no crystals grow on substrates (quartz shown here) placed in a new boat (a, left), but crystals do grow in an old boat (a, right). Moreover, VO_2 crystals can be grown (here on sapphire) in an old boat even with no precursor (b).

A.3 XRD Pole Figure Collection/Interpretation

X-ray diffraction (XRD) is a useful tool for measuring the spacing and direction of crystal planes, and thus for identifying a material, its phase, and its orientation. Figure 9a illustrates the principle of a reflection-mode XRD measurement. An x-ray beam with wavevector $\vec{k_i}$ incident upon a sample with angle of inclination θ from a set of planes will be reflected into $\vec{k_r}$, also at angle θ relative to that same set of planes, if the Bragg diffraction formula is satisfied
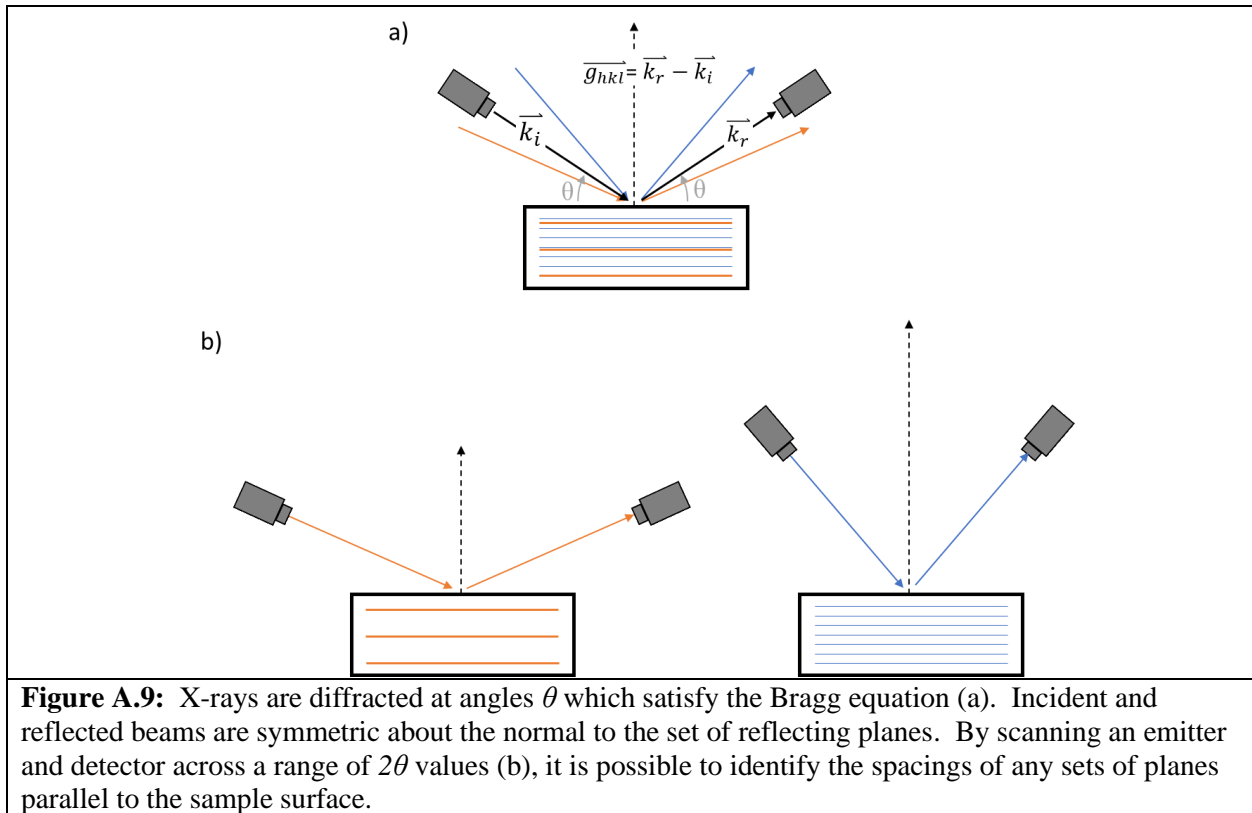
$$n\lambda = \frac{n}{k} = 2d \sin\theta \qquad \text{(Equation 5)}$$

where $\lambda = \frac{1}{k}$ is the x-ray wavelength, d is the plane spacing, and n is an integer. It also useful to note that the difference $\vec{k_r} - \vec{k_i}$ is a vector perpendicular to the set of planes with magnitude

$$\vec{k_r} - \vec{k_i} = 2\,k\sin\theta\,\hat{n} = \frac{n}{d}\hat{n} = n\overrightarrow{g_{hkl}} \qquad \text{(Equation 6)}$$

where $\overrightarrow{g_{hkl}}$ is the reciprocal lattice vector for the set of planes in question.

   A standard θ-2θ measurement consists in scanning an x-ray emitter and detector in tandem across a range of 2θ values (2θ, corresponding to the angle between $\vec{k_i}$ and $\vec{k_r}$, is commonly used instead of θ as the independent variable), keeping both at the same angle above the sample surface. Whenever 2θ satisfies the Bragg equation for a set of planes, a signal will be detected (Figure 9b).

Figure A.9: X-rays are diffracted at angles θ which satisfy the Bragg equation (a). Incident and reflected beams are symmetric about the normal to the set of reflecting planes. By scanning an emitter and detector across a range of 2θ values (b), it is possible to identify the spacings of any sets of planes parallel to the sample surface.

This measurement scheme is limited to detecting planes which are parallel to the sample surface. For a powder or a thin film with randomly-oriented grains, all the various planes will be visible to the measurement, but for a single crystal (or any sample with strong preferred orientation) only a small subset of all the planes can be detected. In order to detect a set of planes at an angle α relative to the sample surface, it is necessary to tilt the emitter/detector pair by α such that they are symmetric about this plane's reciprocal lattice vector (Figure 10a). If instead of scanning to see which planes are present, we need to find the orientation of a specific set of planes, we can fix 2θ and scan α. A signal will be detected whenever the detector and emitter are symmetric about the reciprocal lattice vector of a set of planes that satisfies the Bragg law for that value of 2θ. It is helpful to visualize a semicircle about the sample; wherever a reciprocal lattice vector intersects this semicircle, a peak will appear (Figure 10b). For easier representation, this semicircle can be projected onto a linear axis. Repeating such a measurement with a different 2θ value will reveal the locations of a different set of planes.
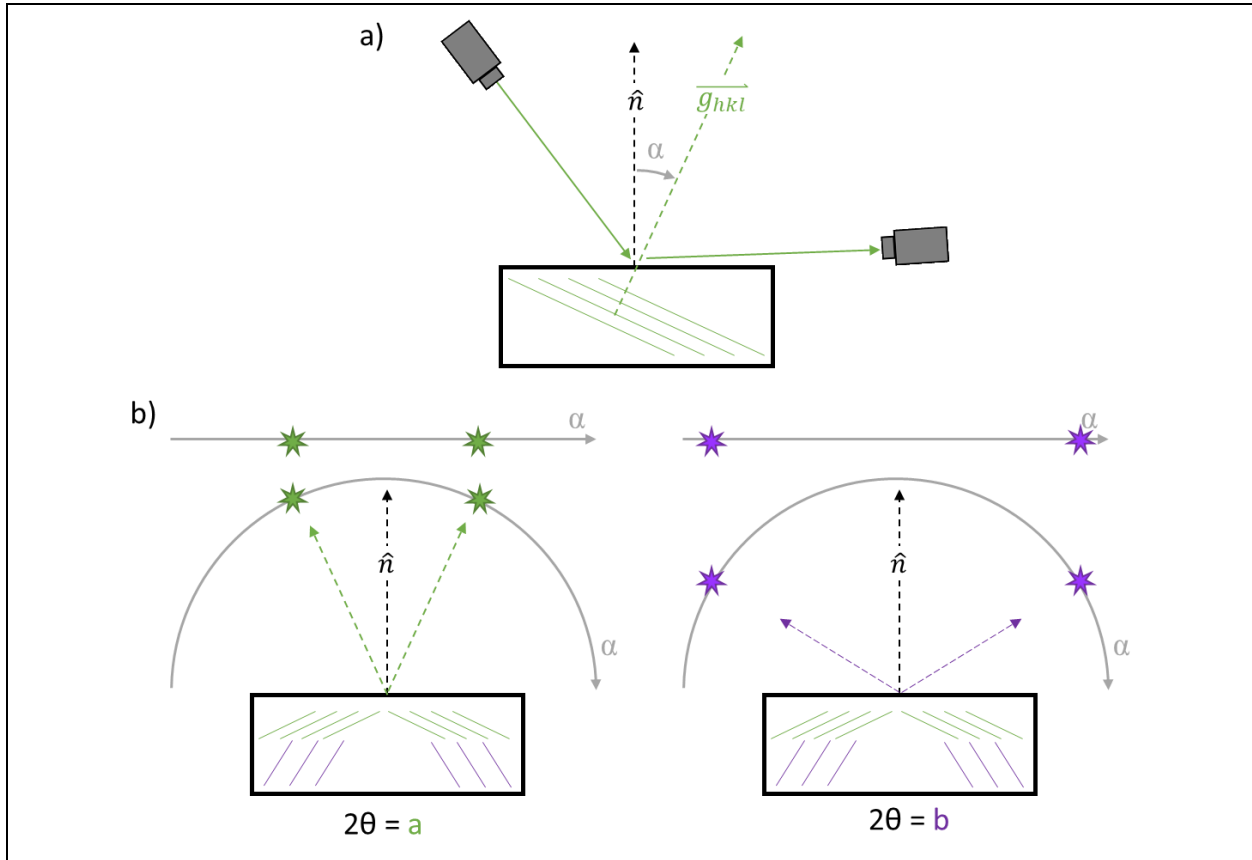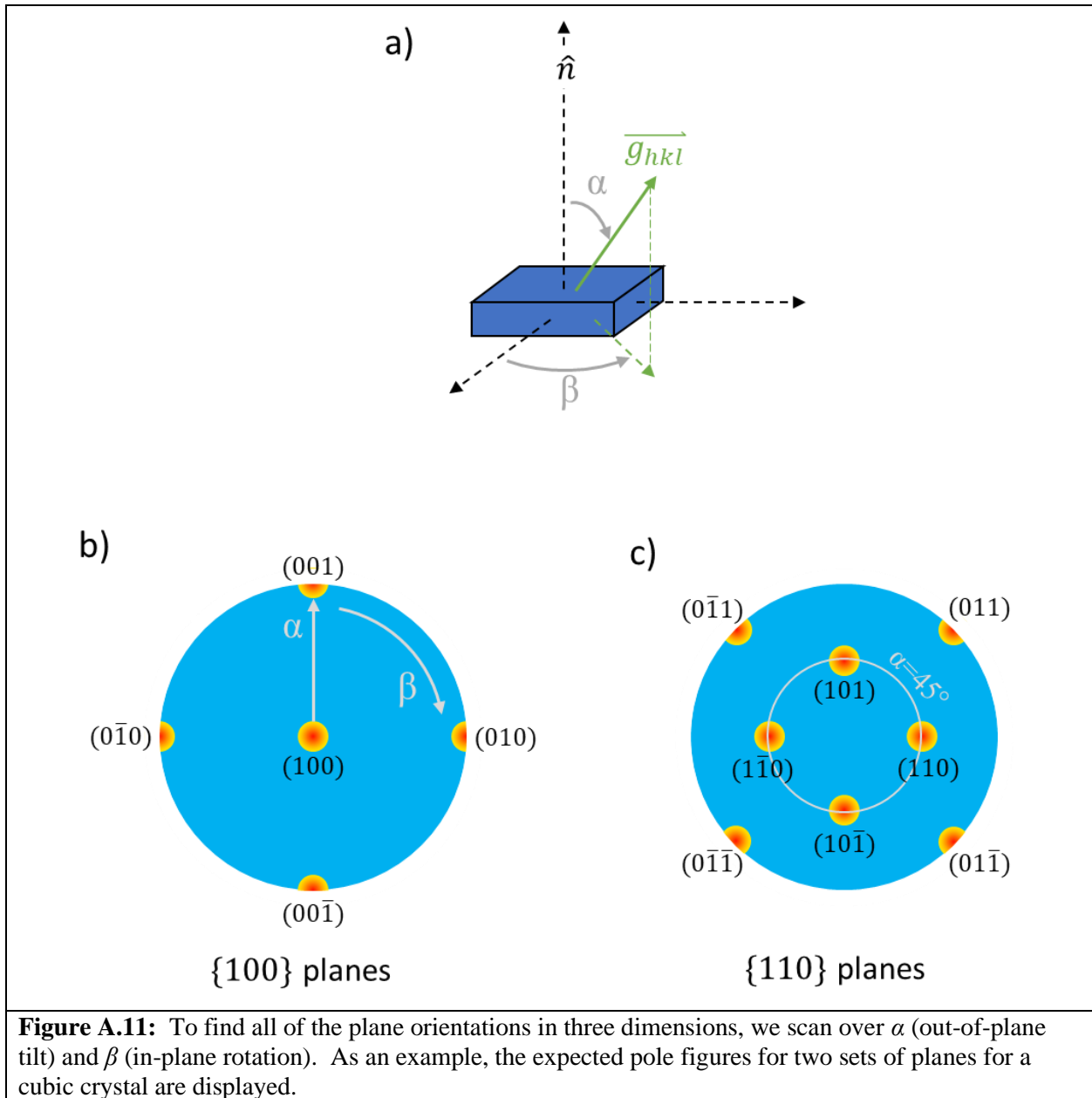

Figure A.10: To detect planes non-normal to the sample surface, the emitter/detector pair must be tilted by an angle α away from the sample surface normal (a). By fixing 2θ to a certain value and scanning over α, the orientation of a certain set of planes can be obtained.
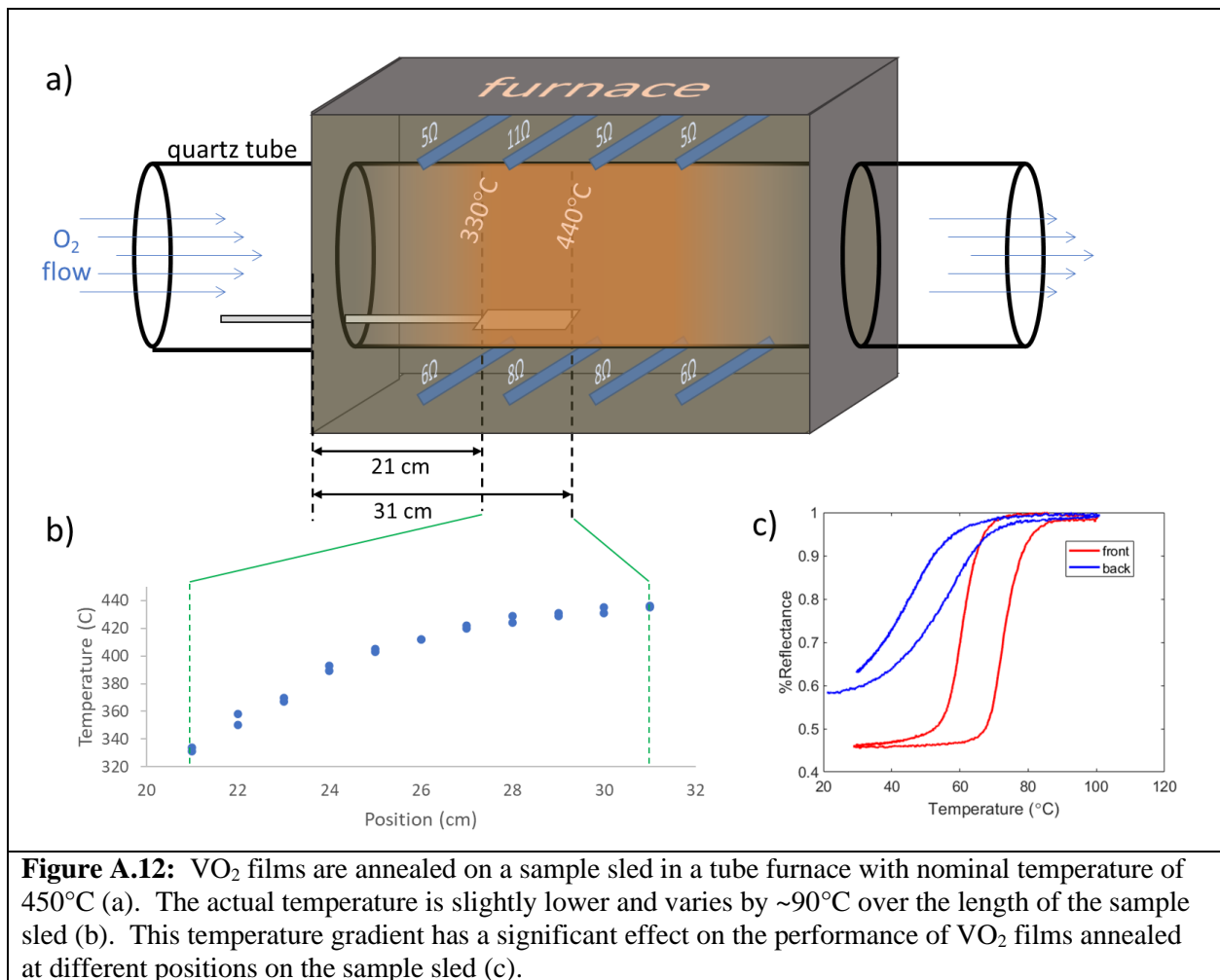
For a 3-dimension crystal, another degree of freedom is required to find all possible plane orientations. In addition to α (the tilt of the surface normal relative to the vector which bisects the emitter and detector directions), we can vary β (the in-plane rotation of the sample, see

Figure 11a). Fixing *2θ* and scanning over both *α* (0-90°) and *β* (over 0-360°) produces a pole figure. Figure 11b-c shows the expected pole figure for a single crystal with a cubic unit cell oriented with its (100) set of plane parallel to the sample surface. The (100) peak appears at *α*=90°, with other {100} family planes (all perpendicular to it) at *α*=0° and separated by *Δβ*=90° (four-fold symmetry). The {110} family of planes, corresponding to the edges of the cubic unit cell (Figure 11c), is slightly more complex, with peaks at *α*=45° and *α*=0°, but retaining four-fold rotational symmetry.

Figure A.11: To find all of the plane orientations in three dimensions, we scan over *α* (out-of-plane tilt) and *β* (in-plane rotation). As an example, the expected pole figures for two sets of planes for a cubic crystal are displayed.

A.4 VO₂ Annealing Conditions

All VO$_2$ thin film in this study are annealed after deposition to improve oxygen stoichiometry and crystallinity. Without annealing, our films do not show the expected switching behavior. Moreover, film quality and hysteretic properties are highly sensitive to anneal conditions. Unless otherwise noted, films in this work are annealed at 450°C for 10 minutes under 250 mtorr O$_2$ (flow rate ~16-17 sccm), in the same tube furnace used for crystal growth (but in a separate tube to avoid cross-contamination between the processes). The samples are introduced to the furnace at temperature with a magnetic sample sled with a 10-cm sample plate. When fully inserted, the front end of the sled sits at the furnace center. Figure 12a illustrates the process geometry.

Figure A.12: VO$_2$ films are annealed on a sample sled in a tube furnace with nominal temperature of 450°C (a). The actual temperature is slightly lower and varies by ~90°C over the length of the sample sled (b). This temperature gradient has a significant effect on the performance of VO$_2$ films annealed at different positions on the sample sled (c).

We have found that, at a set point of 450°C, a significant temperature gradient exists across the space covered by the sample sled. Figure 12b shows the measured temperature as a function of position, from ~330°C at the back of the sled (21 cm) to ~440°C at the center of the furnace (31 cm). While it is expected that the furnace temperature will fall off continuously

toward either open end, the steepness of this temperature gradient is somewhat surprising. In part, thjs likely arises because 450°C is below the intended operating temperature of this [type of furnace](#). There is also a slight asymmetry in the heating elements which exacerbates this effect. The furnace is heated by eight equally-spaced resistive heaters (four above and four below) connected in series. We have measured the resistance of each rod (labeled in Figure 12a), and found that they vary by up to a factor of 2. For resistors in series (such that the current is constant), the power consumed by each resistor is $P=I^2R$; thus the elements with higher resistivity will give off more heat than their lower-resistivity counterparts. Since the higher-resistivity rods are all near the center of the furnace, the thermal gradient is steepened.

The 90°C difference in temperature between the front and back of the sample sled is large enough to significantly impact VO_2 quality. Figure 12c show hysteresis curves for a pair of identical VO_2 samples annealed at the front and back of the sample sled. The latter has lower contrast and lower slope, indicative of poorer film quality. For this reason, all films in this study were annealed using only the front half of the sample sled.

A.5 VO₂ Sputter Deposition Uniformity

All of the sputtered VO_2 thin films used in this work were prepared in an Angstrom Amod® Multimode Deposition system. In this tool, the sputter gun is offset from the sample plate, which, despite substrate rotation, could lead to nonuniformity in film thickness based on its position on the sample plate. Here, we characterize film thickness as a function of radial position (Figure 13). Film thickness is measured by masking a Si sample with thin strips of Kapton® tape (Figure 13a), then removing the tape after deposition (Figure 13b), to leave parallel stripes of VO_2 on the sample. The thickness of each stripe is then measured with a stylus profilometer.

The substrate holder in our system is a 6-inch diameter disk. A single piece of Si, 8 cm long, was placed along the radius of this holder, and masked along its length (Figure 13c). We have found that when masking strips are placed too close together, shadowing effects (Figure 13a) can affect the resulting film thickness. Figure 13d shows thickness as a function of stripe width. At lower stripe width, the thickness varies strongly with width, but as the stripe becomes wider the measured thickness asymptotically approaches the actual deposited thickness. For this reason, all data points with width less than 700 μm (left of the broken line) are rejected. After excluding these values, we can plot film thickness as a function of position (Figure 13e). Position 0 nm corresponds to the center of the sample holder. The thickness varies only slightly with position, if at all; a linear curve fit gives a slope of -0.006 nm/mm (with a 95% confidence interval of ±0.09 nm/mm). Even taking a worst-case value of -0.1 nm/mm the film thickness should vary by less than 8 nm (2.6%).

In sputter depositions, film thickness is controlled by varying the deposition time. The sputter rate varies from target to target, and can be affected by adjustments to the sputter system (such as replacement of electronic components or realignment of mechanical components), so performing periodic rate calibrations for each target is important to maintain precise control over film thickness. Table 1 presents rates measured in our system for four different W-doped vanadium targets, within the last 7 months at the time of writing. Thickness measurements used in Table 1 are derived from both stylus profilometer and AFM measurements. These rates assume that the rate is constant throughout a deposition. This may not hold for long deposition times, but a thorough characterization of this behavior is beyond the scope of this work.
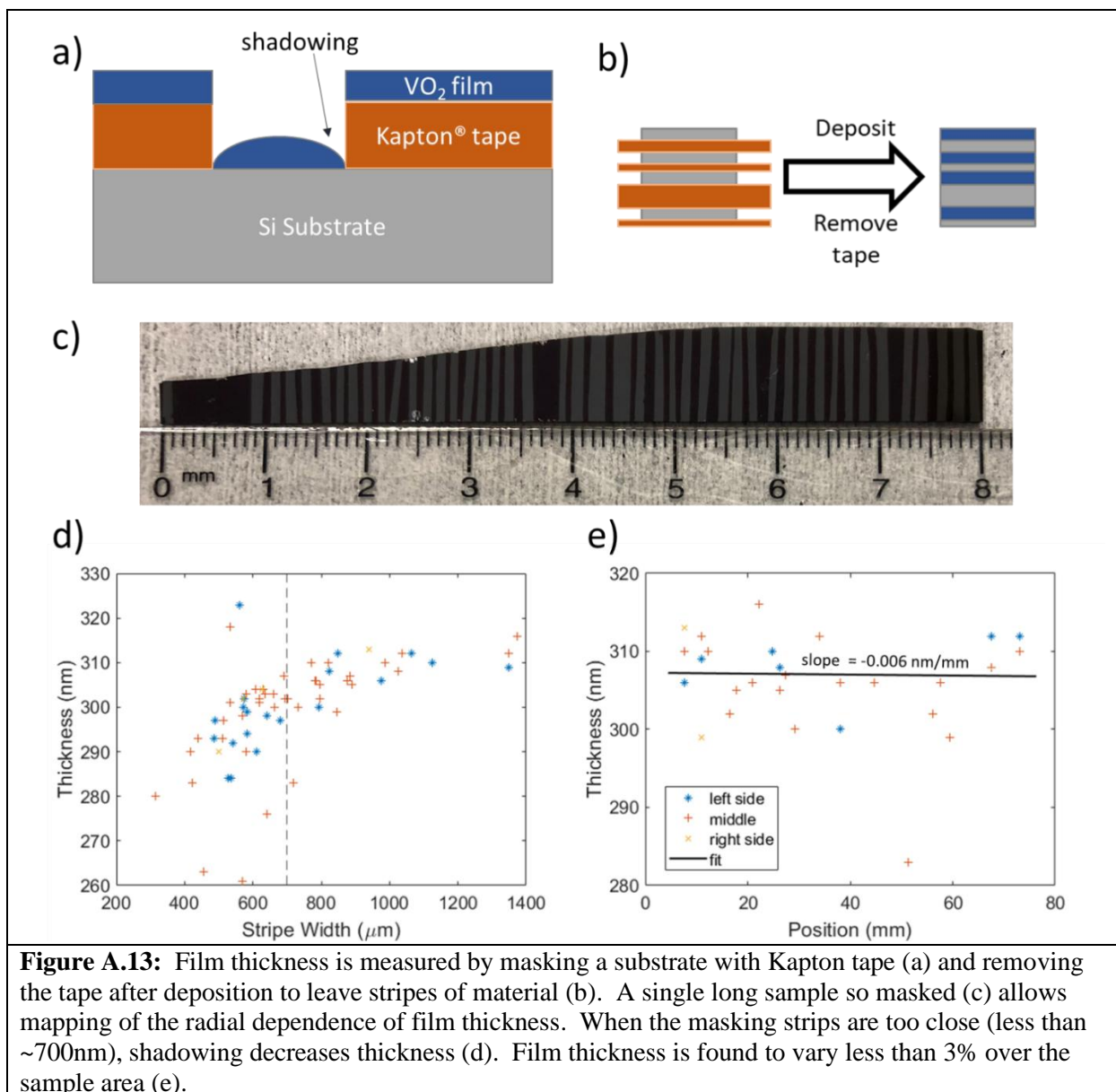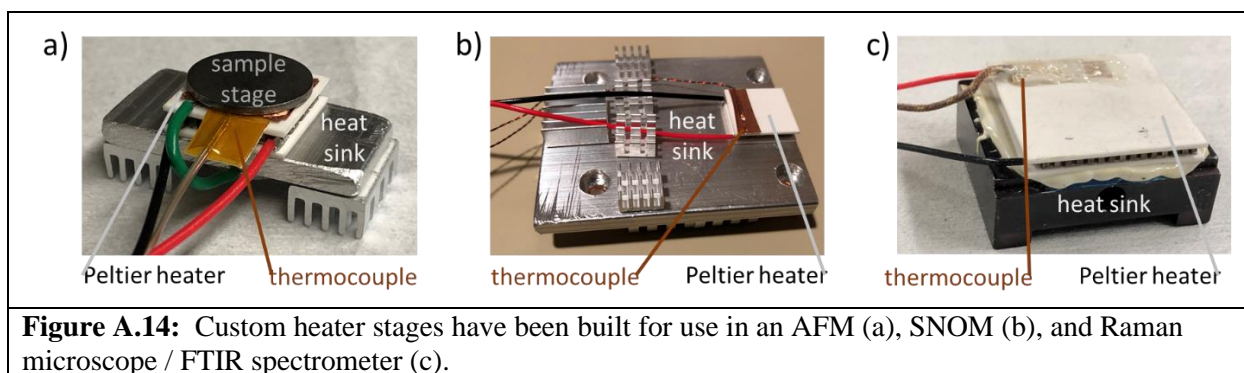
Figure A.13: Film thickness is measured by masking a substrate with Kapton tape (a) and removing the tape after deposition to leave stripes of material (b). A single long sample so masked (c) allows mapping of the radial dependence of film thickness. When the masking strips are too close (less than ~700nm), shadowing decreases thickness (d). Film thickness is found to vary less than 3% over the sample area (e).

Table A.1: VO$_2$ sputter rates measured May through November 2021. Uncertainties represent 1 standard error of the mean (SEM).

wt.% V	wt.% W	rate (nm/sec)	# measurements	# depositions
100	0	0.27±0.01	8	6
95	5	0.137±0.009	8	3
92	8	0.19±0.02	6	5
90	10	0.29	1	1

A.6 Custom Heaters

Throughout this work, heated measurements were accomplished using custom-built heater stages (with the exception of s-SNOM measurements performed at University of Georgia). These heaters all employ thermoelectric Peltier elements from TETech. Peltier heaters use the thermoelectric effect to pump heat from one side to the other, allowing for both heating and cooling. However, in order to attain significant cooling, it is necessary to remove heat from the hot side, else resistive heating will eventually cause both sides to heat. Thus cooling requires that the hot side be attached to an efficient heat sink. For the optical hysteresis setup described above, the Peltiers are clamped to an optical table, allowing for cooling to below 0°C. The temperature of the stages are monitored by type-K self-adhesive thermocouples purchased from Omega Engineering.   The stages are assembled using either thermally-conductive epoxy, or double-sided copper tape. Figure 14 exhibits three different heater stages designed for use in different commercial instruments.

Figure A.14: Custom heater stages have been built for use in an AFM (a), SNOM (b), and Raman microscope / FTIR spectrometer (c).

A.7 Acknowledgements

A.8 References

1.   Maezawa, H.; Miyauchi, H., Rigorous expressions for the Fresnel equations at interfaces between absorbing media. *J. Opt. Soc. Am. A-Opt. Image Sci. Vis.* **2009,** *26* (2), 330-336.
2.   Landry, J. P. Optical oblique -incidence reflectivity difference microscopy: Application to label-free detection of reactions in biomolecular microarrays. Ph.D., University of California, Davis, Ann Arbor, 2008.
3.   Schinke, C.; Peest, P. C.; Schmidt, J.; Brendel, R.; Bothe, K.; Vogt, M. R.; Kroger, I.; Winter, S.; Schirmacher, A.; Lim, S.; Nguyen, H. T.; MacDonald, D., Uncertainty analysis for the coefficient of band-to-band absorption of crystalline silicon. *AIP Adv.* **2015,** *5* (6), 22.

4.   Rakić, A. D.; Djurišić, A. B.; Elazar, J. M.; Majewski, M. L., Optical properties of metallic films for vertical-cavity optoelectronic devices. *Applied Optics* **1998,** *37* (22), 5271-5283.

5.   Strelcov, E.; Davydov, A. V.; Lanke, U.; Watts, C.; Kolmakov, A., In situ monitoring of the growth, intermediate phase transformations and templating of single crystal VO_2 nanowires and nanoplatelets. *Acs Nano* **2011,** *5* (4), 3373-3384.

6.   Kosuge, K., The phase diagram and phase transition of the $V_2O_3-V_2O_5$ system. *J. Phys. Chem. Solids* **1967,** *28* (8), 1613-1621.

7.   Wriedt, H. A., The O-V (Oxygen-Vanadium) system. *Bulletin of Alloy Phase Diagrams* **1989,** *10* (3), 271-277.

8.   Kim, I. S.; Lauhon, L. J., Increased yield and uniformity of vanadium dioxide nanobeam growth via two-step physical vapor transport process. *Cryst. Growth Des.* **2012,** *12* (3), 1383-1387.